FATIGUE & FRACTURE STUDIES ON ULTRAFINE GRAINED 2014 AL ALLOY

Ph.D. THESIS

by

AMIT JOSHI

DEPARTMENT OF METALLURGICAL & MATERIALS ENGINEERING
INDIAN INSTITUTE OF TECHNOLOGY ROORKEE
ROORKEE- 247667, INDIA
JULY, 2017

FATIGUE & FRACTURE STUDIES ON ULTRAFINE GRAINED 2014 AL ALLOY

A THESIS

*Submitted in partial fulfilment of the
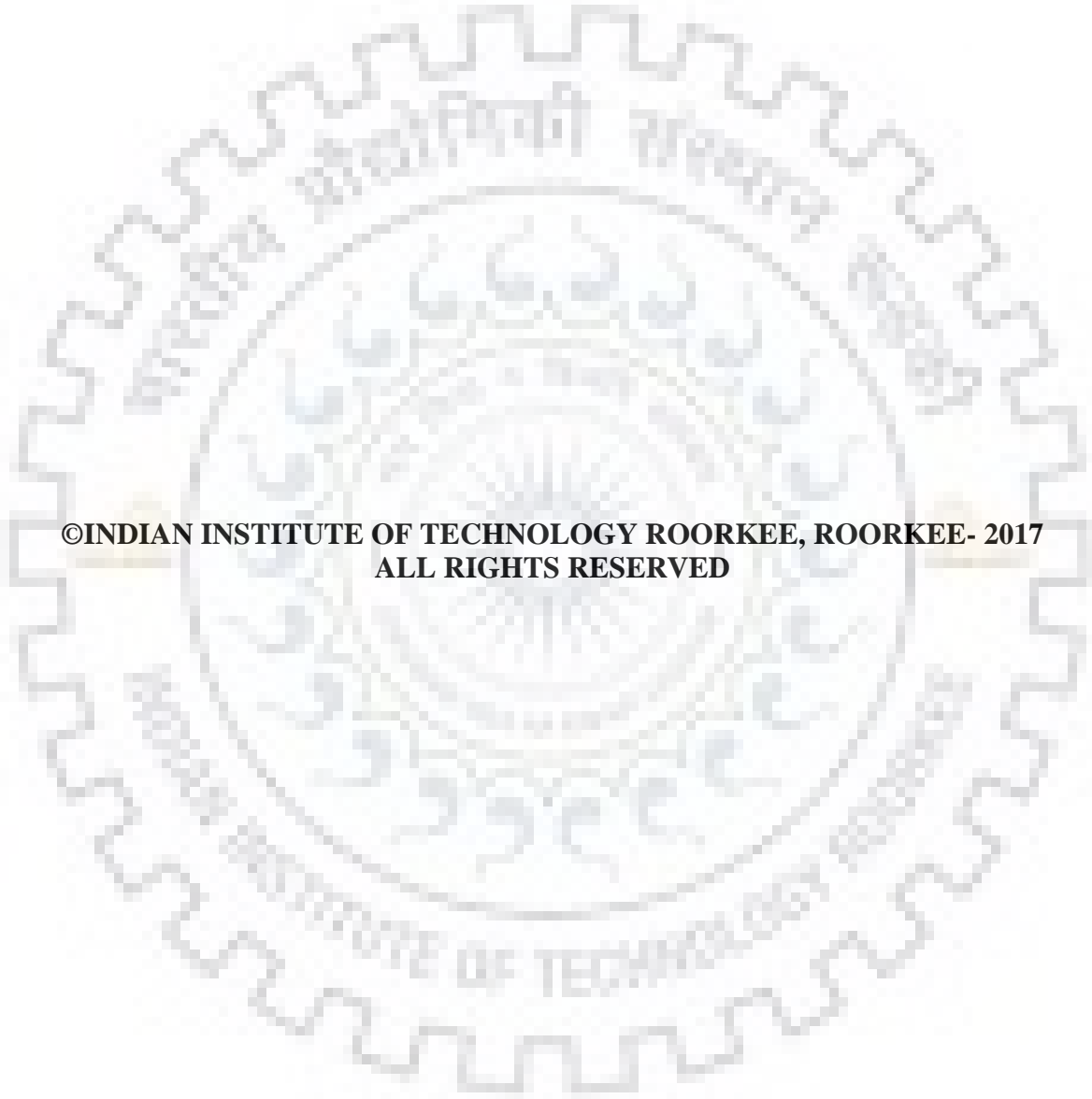requirements for the award of the degree*

of

DOCTOR OF PHILOSOPHY

in

METALLURGICAL & MATERIALS ENGINEERING

by

AMIT JOSHI

DEPARTMENT OF METALLURGICAL & MATERIALS ENGINEERING
INDIAN INSTITUTE OF TECHNOLOGY, ROORKEE
ROORKEE- 247667, INDIA
JULY, 2017

INDIAN INSTITUTE OF TECHNOLOGY ROORKEE
ROORKEE

CANDIDATE'S DECLARATION

I hereby certify that the work which is being presented in the thesis entitled **"FATIGUE & FRACTURE STUDIES ON ULTRAFINE GRAINED 2014 AL ALLOY",** in partial fulfilment of the requirements for the award of the Degree of Doctor of Philosophy and submitted in the Department of Metallurgical & Materials Engineering of the Indian Institute of Technology Roorkee, Roorkee is an authentic record of my own work carried out during a period from July, 2014 to July, 2017, under the supervision of Dr. R. Jayaganthan, Professor, Department of Metallurgical and Materials Engineering, Indian Institute of Technology Roorkee, Roorkee.

The matter presented in this thesis has not been submitted by me for the award of any other degree of this or any other institution.

(AMIT JOSHI)

This is to certify that the above statement made by the candidate is correct to the best of my knowledge.

Dated: ………..   (R. Jayaganthan)
                                                                             Supervisor

The Ph.D. Viva-Voce examination of Mr. Amit Joshi, Research Scholar has been held on
………………………

Chairman, SRC   **Signature of External Examiner**

This is to certify that the student has made all the corrections in the thesis.

Signature of Supervisor   **Head of the Department**

ABSTRACT

Al alloys are extensively used in high strength applications due to its high strength to weight ratio. Among Al alloys, Al 2014 alloy is generally used for aircraft and automobile applications and is key engineering material for aircraft fitting vessels, roof structures and bridge decks. Therefore, it is imperative to enhance the mechanical and physical properties of these alloys through different thermo mechanical techniques without changing the alloy composition in order to increase service life of the structural components. In recent years, producing ultrafine grained material (UFG) through various severe plastic deformation techniques is growing enormously for achieving significant improvement in mechanical and physical properties hitherto unachieved in their bulk materials. In addition to the primary properties of these ultrafine grain (UFG) alloys such as tensile strength and hardness, fatigue and fracture behavior are very essential for the structural components experiencing dynamic loads during service conditions. Therefore, the fatigue and fracture studies can provide comprehensive deformation behavior of material under cyclic loading as compared to monotonic loading. Cryorolling and cryoforging are the novel deformation processing techniques used widely to produce ultrafine and nanostructures in the pure metals and alloys. In this technique, dynamic recovery is suppressed to accumulate high density of dislocation in the materials during processing at liquid nitrogen temperature. The dislocation density acts as a source of nucleation sites for the formation of ultrafine grains and nanostructures in the bulk materials through dynamic recrystallisation. The literature on the effect of cryorolling & cryoforging on tensile properties, fatigue and fracture behavior of Al 2014 alloys is scarce. Thus, the present work is focused on fabricating ultrafine grained Al 2014 alloy through cryorolling and cryoforging and to investigate i) Effect of cryorolling and followed by annealing on the mechanical properties such as tensile strength, yield strength, fracture toughness, fatigue crack growth rate and high cycle fatigue of Al 2014 alloy ii) To correlate the above mechanical properties with the microstructural features obtained through optical microscopy, SEM, TEM and EBSD characterization techniques iii) To identify the optimum processing conditions for the bulk UFG Al 2014 alloy usable in high strength structural applications iv) Development of ultrafine grain microstructure in coarser grained Al 2014 alloy through multidirectional room temperature and cryoforging v) A comparative study of

mechanical properties (Ultimate tensile strength, yield strength and Fracture toughness) and microstructure of bulk UFG Al 2014 developed by multidirectional room temperature forging and cryoforging vi) To study the influence of annealing on the tensile properties, strain hardening behavior, fracture toughness, and fracture mechanism of bulk UFG Al 2014 alloy produced by multidirectional cryoforging. The key results obtained in each piece of work are discussed below.

To understand the effect of cryorolling and followed by annealing on microstructural evolution, precipitation sequence, tensile properties and fracture toughness of Al 2014 alloy, the sample was solutionised (ST) and subjected to cryorolling (CR) up to effective true strain of 2.3. The CR Al 2014 alloy samples were annealed (AN) at temperatures ranging from 100°C to 350°C for the duration of 45 minutes. Study reveals the improvement in ultimate tensile strength (245 MPa - 447 MPa) and fracture toughness K_{ee} (23.06 MPa$\sqrt{m}$ - 37.8 MPa$\sqrt{m}$) of cryorolled Al 2014 alloy as compared to solution treated alloy with reduction in ductility from 18.5% to 4.8%. When cryorolled samples were annealed in the temperature range of 100°C to 350°C, the strength and fracture toughness were retained up to 200°C, while continuous drop in these properties were observed when samples were annealed beyond 200°C. However, the ductility was improved with increasing annealing temperature when cryorolled samples were annealed from 100°C to 350°C due to softening facilitated by dynamic recovery and recrystallisation, which led to formation of dislocation free grains. The improvement in mechanical properties of cryorolled Al 2014 alloy at low temperature annealing from 100°C to 200°C is attributed to formation of GP zones and metastable phase θ' in this temperature range, while the reduction in mechanical properties beyond temperature 200°C is observed due to combined recovery, recrystallisation and formation of stable coarser phase θ and λ.

Studies on the effect of cryorolling and followed by annealing on high cycle fatigue behaviour of bulk UFG Al 2014 alloy revealed the improved high cycle fatigue (HCF) strength of cryo rolled (CR) alloy as compared to solution treated (ST) alloy due to grain refinement. The improvement in high cycle fatigue properties of cryorolled followed by annealed alloy up to 200°C as compared to ST alloy observed is due to improved crack tip plasticity facilitated by crack tip/precipitate interaction at grain boundaries (GBs).The high cycle fatigue (HCF) strength is observed to be maximum on annealing at 100°C, while beyond

this temperature, a gradual decrease on high cycle fatigue (HCF) strength is observed as compared to sample annealed at 100°C due to gradual coarsening of metastable precipitate (θ' phase), which transformed in to stable coarser precipitate 'θ' phase at 250°C.

On investigating the fatigue crack growth (FCG) behaviour of cryorolled and followed by annealed alloy at low stress intensity factor (ΔK) range, fatigue crack growth rate (FCGR) of cryorolled (CR) alloy was observed to be more as compared to coarser grain solution treated (ST) alloy due to formation of UFG microstructure resulting reduced crack path tortousity, while on annealing in the temperature range 100°C to 250°C, the fatigue crack growth rate (FCGR) decreases significantly and it was observed to be minimum for sample annealed at 100°C. The decrease in fatigue crack growth rate (FCGR) at 100°C is attributed to evolution of fine metastable spherical phase θ', which obstructs the crack growth during FCGR testing.

To investigate the effect of multidirectional room temperature forging and cryoforging on the microstructure evolution, tensile properties and fracture toughness, Al 2014 alloy is multidirectional forged (MDFed) at room temperature and cryogenic temperature up to cumulative true strains of 1.2 (2 cycles), 1.8 (3 Cycles) and 2.4 (4 cycles). This study revealed that, multidirectional cryoforged sample up to cumulative strain of 2.4 showed an improvement of ultimate tensile strength, hardness and apparent fracture toughness (K_Q) from 245 MPa to 470 MPa, 115 HV to 171 HV, and 23.93 MPa$\sqrt{m}$ to 37.7 MPa$\sqrt{m}$, respectively, with decrease in ductility from 18.5% to 6% as compared to solution treated alloy. The substantial improvement in the ultimate tensile strength (7%), yield strength (3%) and hardness (3%) of multidirectional cryoforged Al 2014 alloy is observed as compared to room temperature forged alloy due to suppression of dynamic recovery at liquid nitrogen temperature.

To understand the effect of multidirectional cryoforging (MDCF) and followed by annealing on the tensile properties, strain hardening behavior, fracture toughness, and fracture mechanism in MDCFed Al 2014 alloy, the sample is post annealed in the temperature range from 150°C to 350°C with the interval of 50°C for the duration of 1 hour. The mechanical properties are correlated with the microstructural evolution during deformation and post deformation annealing through optical microscopy and TEM studies, while fracture mechanism in processed and annealed alloy is established using macrograph analysis and SEM studies. The study reveals that strain hardening ability, fracture mechanisms and fracture

toughness of deformed and post annealed samples are influenced by the shear banding, combined recovery /recrystallisation process, and evolution of second phase precipitates during annealing treatment at various temperatures. Significant improvement in the ultimate tensile strength (UTS) and fracture toughness is observed on annealing the processed alloy at 100°C, while beyond this temperature, a gradual drop in these properties is seen as compared to sample annealed at 100°C. Macroscale fracture behaviour in tensile testing of multidirectional cryoforged (MDCFed) alloy consists of shear fracture while upon annealing, it is transformed gradually in to mixed mode of fracture consisting of shear plus necking. Finally, it was concluded that fine spherical semi coherent phase θ' is responsible for improving the mechanical properties of bulk UFG Al 2014 alloy.

Finally, strengthening contributions to the yield strength from different strengthening mechanism were evaluated for the multidirectional cryoforged (MDCFed) and MDCFed followed by annealed Al 2014 alloy. The study revealed that grain boundary strengthening (σ_{Gbs}), is dominating strength contributor for raising the yield strength of MDCFed Al 2014 alloy, while for annealed samples up to the temperature range 350°C, the grain boundary (σ_{Gbs}) and precipitation strengthening (σ_{ps}) are found to be dominating strengthening mechanism in raising the yield strength of bulk UFG Al 2014 alloy.

ACKNOWLEDGEMENTS

Kumar Tiwari, Praveen Kumar Tiwari for their true blessings and support during my Ph.D work. Especially I am very much thankful to Pawan Kumar Tiwari who looked after my mother carefully in my home town Srinagar during my absence there.

I would like to show my gratitude from the depth of my heart to my wife Arundhati Joshi, who always appreciated my efforts and provided me cheerful encouragement and unconditional support throughout my research work. Her true love, continuous encouragement, and support in all aspects played a vital role in the completion of this Ph.D work. I especially thank my elder daughter Aditi and younger daughter Arohi for sacrificing many times they desired to spend time with me. Their innocent love and cute smile inspired me to complete this research work well within the time.

AMIT JOSHI

TABLE OF CONTENTS

LIST OF FIGURES

xviii

LIST OF TABLES

LIST OF ABBREVIATIONS AND SYMBOLS

SPD	Severe Plastic Deformation
UFG	Ultra-Fine Grained
NC	Nanocrystalline
HCP	Hexagonal Closed Packed
BCC	Body Centered Cubic
Al	Aluminium
FCC	Face Centered Cubic
TEM	Transmission Electron Microscopy
FESEM	Field Emission Scanning Electron Microscope
XRD	X –Ray Diffraction
EBSD	Electron Back Scattered Diffraction
HCF	High Cycle Fatigue
LCF	Low Cycle Fatigue
FCGR	Fatigue Crack Growth Rate
GNBs	Geometrically Necessary Boundaries
IDBs	Incidental Dislocation Boundaries
CR	Cryorolling
CR+AN	Cryorolled followed by Annealed
K_Q	Apparent Fracture Toughness
K_{ee}	Equivalent Energy Fracture Toughness
MDCF	Multidirectional Cryoforging
ECAP	Equal Channel Angular Pressing
HPT	High Pressure Torsion
ARB	Accumulative Roll Bonding
MAF	Multi Axial Forging
TE	Twist Extrusion
ASR	Asymmetric Rolling
C2S2	Continuous confined strip shearing
I-ECAP	Incremental ECAP
PC-ECAP	Parallel Channel ECAP

CCDF	Cyclic Close Die Forging
RCS	Repetitive Corrugation and Straightening
CRCS	Continuous Repetitive corrugating and straightening
TCP	Tube Channel Pressing
RTR	Room Temperature Rolling
DPD	Dynamic Plastic Deformation
CT	Cryogenic Temperature
CF	Cryoforged
UTM	Universal Testing Machine
K_{IC}	Plain Strain Fracture Toughness
$\frac{\Delta\varepsilon_{el}}{2}$	Elastic Strain Amplitude
$\frac{\Delta\varepsilon_{t}}{2}$	Total Strain Amplitude
GPa	Giga Pascal
MPa	Mega Pascal
$\overset{\circ}{A}$	Armstong
HV	Hardness Vickers
LAGBs	Low angle grain boundaries
HAGBs	High angle grain boundaries
GBs	Grain Boundaries
PFZs	Precipitate Free Zones
GOS	Grain Orientation Spread
3PBT	3 Point Bend Test
MDFed	Multidirectional Forged
LEFM	Linear Elastic Fracture Mechanics
μm	Micro Meter
CTOD	Crack Tip Opening Displacement
Annld	Annealed
EPFM	Elasto Plastic Fracture Mechanics
J- Integral	J Integral
Cu	Copper
Si	Silicon

Mg	Magnesium
Mn	Maganese
Fe	Iron
Ni	Nickel
Ti	Titanium
Zn	Zinc
K	Kelvin
T_m	Melting temperature
^oC	Degree Celsius

LIST OF PUBLICATIONS

Refereed International Journals

[1] **Amit Joshi,** Yogesha K. K., Nikhil Kumar, R. Jayaganthan, "Influence of Annealing on Microstructural Evolution, Precipitation Sequence, and Fracture Toughness of Cryorolled Al–Cu–Si Alloy." *Metallography, Microstructure, and Analysis* 5(6) (2016), 540-556.

[2] **Amit Joshi,** Nikhil Kumar, Yogesha K. K., R. Jayaganthan, S. K. Nath, (2016). "Mechanical Properties and Microstructural Evolution in Al 2014 Alloy Processed Through Multidirectional Cryoforging" *Journal of Materials Engineering and Performance*, *25*(7), 3031-3045

[3] **Amit Joshi,** Yogesha K. K, R. Jayaganthan, "Influence of cryorolling and followed by annealing on high cycle fatigue behavior of ultrafine grained Al 2014 alloy" *Materials Characterization* 127 (2017): 253-271.

[4] **Amit Joshi,** Yogesha K. K, R. Jayaganthan, "Fatigue crack growth behavior of bulk UFG Al 2014 alloy after annealing treatment" *(Materials &Design,2017* **(Under Review)**

[5] **Amit Joshi, Yogesha K. K, R. Jayaganthan, "** Investigation of strain hardening and fracture behaviour of multidirectional cryoforged (MDCFed) Al 2014 alloy", *Materials Science and Engineering: A*, **2017 (Under Review)**

National and International Conferences

[1] **Amit Joshi**, Nikhil Kumar, Yogesha K. K., R. Jayaganthan, Tensile and Fracture properties of Al 2014 alloy processed through multidirectional Forging , **NMD ATM- 2015 Coimbatoor, 13th to 16th Nov, 2015**

[2] **Amit Joshi**, Nikhil Kumar, Yogesha K. K., R. Jayaganthan, Effect of deformation temperature on mechanical properties and microstructural evolution in Al 2014 alloy processed through multidirectional Cryoforging, **ICMR 2016 IISC Banglore, 21 Jun 2016 – 23 Jun 2016**

[3] **Amit Joshi**, Yogesha K. K., Raviraj Verma, R. Jayaganthan, " High cycle fatigue behavior of bulk UFG Al 2014 alloy processed through cryorolling" **ICMAT 2017 Singapore, 18 Jun 2017 – 23 Jun 2017**

INTRODUCTION

Aluminum alloys have been key structural material for aircraft, automobile, structural and construction sectors due to their unique combination of good mechanical properties such as high specific strength, excellent ductility, good machinability, and a high corrosion resistance [1.1]. The conventional strengthening methods used for improving the strength of these alloys are strain hardening, solid-solution strengthening and precipitation hardening [1.2]. However, the precipitation hardening method is the most cost effective method to strengthen the Al alloys and widely used in automobile and aerospace sectors. In age hardenable Al alloy, strength is improved through impeding the dislocation motion by fine precipitates during the deformation [1.3]. For precipitation hardening to occur, the second phase must be soluble at high temperature but must exhibit decreasing solubility with decreasing temperature. The short term and long term annealing treatment (aging) are the primary methods for precipitating the secondary phase in the supersaturated solid solution. During these treatments, secondary phases come out from the matrix in the form of nano clusters along with various meta stable precipitate phases, which after while transform in to stable precipitates/phases [1.4].

An ever growing demand for high specific weight materials in aircraft and automobile sectors is a prime concern for the researchers and scientists worldwide due to the need for reducing fuel consumptions. The excellent mechanical properties of nanostructured (NS) (having grain size < 100 nm) and bulk ultrafine grained (UFG) materials (having grain size < 1000 nm) as compared to coarser grain (CG) materials have attracted the immense interest of material scientists and engineers, globally [1.5-1.6]. However, the major issues/challenges for the scientists and engineers lie in developing the ultrafine or nano grain microstructure in bulk product so as to be used in high strength structural applications. Severe plastic deformation (SPD) techniques have been identified as promising routes for developing bulk ultrafine grain microstructure in coarser grain metals/alloys. Usually, SPD process involves imposition of severe plastic strain without any significant modification of the dimensions of the sample [1.8]. The important feature of these processing techniques includes retention of shape of workpiece with the help of special tools and fixtures resulting imposition of substantial

hydrostatic pressure on the sample [1.9]. This hydrostatic pressure is responsible for imposing severe plastic strain and generating the high densities of lattice defects essential for extraordinary grain refinement. In the past, various processes such as equal channel angular pressing (ECAP) [1.10], high pressure torsion (HPT) [1.11], accumulative roll bonding (ARB) [1.12], hydrostatic extrusion (HE) [1.13], cyclic extrusion and compression (CEC) [1.14], repetitive corrugation and straightening (RCS) [1.15] have been well developed for refining the grain size well below than 1µm. Most of these techniques (ECAP, HE, HPT and RCS) produces ultrafine grain microstructure in the coarser grain metals without significant changes in the initial shape/dimensions of the object. The grain refinement through these techniques depends upon the deformation strain, processing method and processing temperature. During the deformation, defects are continuously generated in coarser grain (CG) metals in the form of dislocations, which further multiply and subsequently rearranged to form the sub grains with dense dislocation walls (DDWs) resulting UFG microstructure in coarser grain (CG) metals/ alloy [1.16]. Some of the processes such as equal channel angular pressing (ECAP) and multidirectional forging (MDF) involves formations and intersection of microshear bands (MSBs). The finer grains are recrystallised at the intersection of theses microshear bands with the transformation of low angle grain boundaries (LAGBs) to higher angle grain boundaries (HAGBs). Such mechanism is known as continuous dynamic recrystallisation (CDRX) [1.17].

Grain fragmentation process in high or medium stacking fault metals such as Al or Cu through dislocation subdivision mechanism does not provide grain size within nanometer regime (less than 100 nm) or slightly above nanometer regime in the range of 100 nm - 200 nm. This is due to the fact that dynamic recovery is associated in high or medium stacking fault energy (S.F.E) metals, which accelerate the dislocation annihilation process by facilitating cross slip and climb in these metals/alloys [1.18]. This limits the formation of new dislocation boundaries and hinders further grain refinement. Now, it has been generally agreed that grain fragmentation is not only depends upon the deformation strain but it is the deformation temperature especially cryogenic temperature, which plays a significant role in refining the grain size. Processing at cryogenic temperature for high stacking fault energy (S.F.E.) Al alloys is a favourable condition to produce ultrafine grained microstructure. At this temperature, strain required for grain fragmentation becomes very low due to suppression of dynamic recovery resulting very high dislocation density [1.19].

High strength and good ductility is the primary requirement for the metals/alloys to be

used for high strength structural applications and can be achieved by microstructural modification. Severe plastic deformation techniques generally led to the high strength but the ductility of SPDed materials significantly decreased due to the lack of strain hardening ability upon processing. In last two decades, various strategies have been developed for improving the strength of material without loss of ductility [1.20]. Various strategies such as bimodal grain size distribution, introducing nano size precipitates and modifying grain boundary characters have been proposed by various researchers for improving the uniform tensile elongation of UFG material fabricated by SPD methods. Out of these three strategies, bimodal grain size distribution is simplest and most commonly used method for improving the ductility of UFG materials fabricated by cryodeformed SPDed methods [1.21]. Post deformation annealing treatment has been identified as another unique strategy for improving the mechanical properties in UFG metals/alloy. This strategy is far more important and useful for enhancing the mechanical properties in age hardenable Al alloys because post deformation annealing of age hardenable Al alloys leads to the evolution of fine second phase precipitates, which helps in hindering the dislocation motion during deformation. In addition to this, these second phase fine precipitates impart the drag force on grain boundaries (GBS) and improves the thermal stability of UFG alloy as reported in the literature [1.20-1.21]

However, along with the ductility which can be evaluated/measured by simple tensile experiments, the high cycle fatigue (HCF), fatigue crack growth rate (FCGR), and fracture toughness is also important and have a significant role in damage safe design of automobile, aerospace and structural applications. In general, these tests involve significant stress triaxiality as compared to simple tension test where material is subjected to unidirectional stresses [1.22-1.23]. Fatigue and fracture toughness test provide a broader and diversified view of the fracture behavior of metals/alloys when they are subjected to multiaxial stress system. In addition, the presence of pre-existing crack might be dangerous for many engineering situations. Hence, it is very important to monitor the crack growth to identify the condition at which this crack grows significantly leads to unstable failure before giving previous warning. Therefore, fatigue and fracture behavior of metals/alloys especially bulk UFG Al alloys produced through SPD methods ought to be thoroughly investigated to use these material for high strength applications.

Cryorolling and cryoforging are low temperature plane strain deformation techniques, which are widely reported in the literature. Cryorolling is one of the classic deformation

processing methods used to produce UFG microstructure in Al alloy sheets. The production of UFG microstructure by cryorolling requires a limited amount of total strain (~2.3) due to the suppression of dynamic recovery. While, multidirectional forging (MDF) on the other hand is a conventional SPD technique, which produces UFG structures in the bulk metals and alloys by imparting very large strains to the materials. MDF at cryogenic temperature utilized the collective results of very low temperature and very high plastic strain generated during processing for the productive fabrication of UFG structure in the alloys.

The literature on the influence of cryorolling and cryoforging on the fatigue and fracture properties of Al 2014 alloy is limited. Therefore, the present work has been focused on producing ultrafine grained Al 2014 alloy, with improved mechanical properties, from its coarse-grained alloy using the various thermo mechanical processing such as cryorolling and multidirectional cryoforging (MDCF). The effect of post processing annealing treatment on the microstructural evolution and mechanical properties such as tensile strength, high cycle fatigue (H.C.F.) , fatigue crack growth and fracture toughness of bulk UFG Al 2014 alloy produced through these methods has been studied in the present work.

References

[1.1] M. Gavgali, B. Aksakal, Effects of various homogenisation treatments on the hot workability of ingot aluminium alloy AA2014, 1998, Mater.Sci. Eng.A, Vol. 254(1), pp.189-199

[1.2] E. A. Starke, J. T. Staley, Application of modern aluminum alloys to aircraft, 1996, Prog. Aerosp Sci, Vol 32(2), pp. 131-172

[1.3] P. N. Rao, D. Singh, R. Jayaganthan, Effect of annealing on microstructure and mechanical properties of Al 6061 alloy processed by cryorolling, 2013, Mater.Sci.Tech Vol 29(1), pp. 76-82

[1.4]   S. K. Panigrahi, R. Jayaganthan, Development of ultrafine grained Al–Mg–Si alloy with enhanced strength and ductility, 2009, J Alloy Compd, Vol 470(1), pp. 285-288

[1.5] Y. Estrin, A. Vinogradov, Extreme grain refinement by severe plastic deformation: a wealth of challenging science, 2009, Acta Mater, Vol 61(3), pp. 782-817

[1.6] R. B. Figueiredo, T. G. Langdon, Using severe plastic deformation for the processing of advanced engineering materials,   2009, Mater trans, Vol 50 (7), pp. 1613-1619

[1.7] V. M. Segal, Severe plastic deformation: simple shear versus pure shear, Mater. Sci. Eng. *A,* 2002, Vol 338 (1), pp. 331-344

[1.8] D. Fuloria, S. Goel, R. Jayaganthan, D. Srivastava, G.K. Dey, N. Saibaba, Mechanical Properties and Microstructural Evolution of Ultrafine Grained Zircaloy-4 Processed Through Multiaxial Forging at Cryogenic Temperature, 2015, T. Nonferr. Metal Soc, Vol 25, pp. 2221-2229.

[1.9] R.Z. Valiev, A.V. Korznikov, R.R. Mulyukov, Structure and Properties of Ultrafine-Grained Materials Produced by Severe Plastic Deformation, 1993, Mater.Sci. Eng.A, Vol 168, pp. 141- 148.

[1.10] R. Z. Valiev, T. G. Langdon, Principles of equal-channel angular pressing as a processing tool for grain refinement, 2006, Prog. Mater. Sci , Vol 51, pp. 881-981

[1.11] A. P. Zhilyaev, T. G. Langdon, Using high-pressure torsion for metal processing: fundamentals and applications, 2008, Prog. Mater Sci , Vol. 53, pp. 893-979.

[1.12] Y. Saito, H. Utsunomiya, N. Tsuji, T. Sakai, Novel Ultra-High Straining Process for Bulk Materials -Development of the Accumulative Roll-Bonding (ARB) Process, 1999, Acta Mater, Vol 47, pp. 579-583.

[1.13] W. Chrominski, S. Wenne, C. D. Marioara, R. Holmestad, M. Lewandowska, Strengthening mechanisms in ultrafine grained Al-Mg-Si alloy processed by hydrostatic extrusion–Influence of ageing temperature, 2016, Mater. Sci Eng; A. Vol 669, pp. 447-58.

[1.14] M. Richert, Q. Liu, N. Hansen, Micro structural Evolution Over a Large Strain Range in   Aluminium Deformed by Cyclic-Extrusion–Compression, 1999, Mater. Sci. Eng., A, Vol 260 pp. 275-283.

[1.15] J.Y. Huang, Y.T. Zhu, H. Jiang, T.C. Lowe, Microstructures and Dislocation Configurations in Nanostructured Cu Processed by Repetitive Corrugation and Straightening, 2001, Acta Mater, Vol 49 , pp. 1497-1505.

[1.16] X. An, Q. Lin, S. Qu, G. Yang, S. Wu, F. Z. Zhang, Influence of stacking-fault energy on the accommodation of severe shear strain in Cu-Al alloys during equal-channel angular pressing. 2009, Journal of materials research Vol 24, pp. 3636-3646.

5

[1.17] O. Sitdikov, T. Sakai, A. Goloborodko, H. Miura, R. Kaibyshev, Effect of Pass Strain on Grain Refinement in 7475 Al Alloy During Hot Multidirectional Forging, 2004, Mater. Transac. Vol 45, pp. 2232-2238.

[1.18] S. K. Panigrahi, R. Jayaganthan, Effect of rolling temperature on microstructure and mechanical properties of 6063 Al alloy, 2008, Mater. Sci. Eng. A, Vol 492, pp. 300-305.

[1.19] N. Rangaraju, T. Raghuram, B.V. Krishna, K.P. Rao, P. Venugopal, Effect of Cryo-rolling and Annealing on Microstructure and Properties of Commercially Pure Aluminium, 2005, Mater. Sci. Eng. A, Vol 398, pp. 246-251.

[1.20] A. Dhal, S.K. Panigrahi, and M.S Shunmugam, Influence of Annealing on Stain Hardening Behaviour and Fracture Properties of a Cryorolled Al 2014 Alloy, 2015, Mater. Sci. Eng. A, Vol 645, pp. 383-392.

[1.21] Y. Wang, M. Chen, F. Zhou, and E. Ma, High Tensile Ductility in a Nanostructured Metal, 2002, Nature, Vol 419, pp. 912-915.

[1.22] A. Hohenwarter, R. Pippan, Fracture Toughness Evaluation of Ultrafine-Grained Nickel, 2011, Scripta Mater, Vol 64, pp. 982-985,

[1.23] A. Hohenwarter, R. Pippan, Anisotropic fracture behavior of ultrafine-grained iron, Mater Sci Eng: A, 2010, Vol 527(10), pp. 2649-2656

.

Chapter 2   LITERATURE REVIEW

This chapter provides a brief introduction of aluminium and its alloys describing various strengthening mechanisms, ultrafine grained/nano-crystalline materials, material development and different techniques used for producing ultrafine and nano-crystalline materials. Further, literature related to ultrafine grained Al alloys obtained by cryorolling and other severe plastic deformation (SPD) techniques is discussed. Finally, based on the above discussion, formulation of the problem along with the scope, objectives and outline of the work has been made in this chapter.

2.1 Severe Plastic Deformation

In the polycrystalline metals/alloys, grain size has a significant effect on the mechanical properties such as tensile strength, hardness, ductility, fatigue and fracture toughness. In conventional coarser grain (CG) materials, grain size lies in the range of several micron meters. The mechanical behavior of coarser grained materials has already been well studied in the literature. In ultrafine grained (UFG) materials, grain size lies in the range of 100 nm- 1µm [2.1]. These materials show exceptional physical, mechanical and chemical properties with respect to its bulk coarser grain counterparts. The term nanostructured (NS) materials have also been defined for the materials for which microstructural features are within the size range of 1-100 nm [2.2].

Bulk UFG/NS materials can be produced by two methods, one is the "Bottom up" approach in which individual atoms which are nanoscale building block (nanoparticles) are assembled by the help of various bottom up methods such as inert gas condensation, high energy ball milling, chemical and physical deposition technique to form UFG/NS materials [2.3].The another method is known as "top down "approach, in which bulk coarser grain materials is subjected to severe plastic deformation (SPD) to develop ultrafine grain microstructure. SPD induces high density of dislocations within the coarser grains, which then rearranges to dislocation cells, subgrains and dense dislocation walls (DDWs) to evolve ultrafine grain microstructure in metals/alloys [2.1-2.3]. One of the most important characteristics of SPD method is such that original dimensions, shape and size of the work piece are not affected and remains same after the processing. This feature is

helpful in inducing and accumulating high plastic strain during the processing. Top down approach has certain advantages over the bottom up approach which are listed in following points.

i) Bulk UFG/NC materials can be produced through SPD methods.

ii) Conventional metal forming techniques are employed for SPD methods which are easy to implement in the industry for mass production.

iii) Defect produced during casting can be removed without affecting the dimension of the specimen.

2.2 SPD techniques

The various SPD methods used for refining grain size well below than 1μm are ECAP, HPT and MDF [2.4-2.6]. Bulk material can be processed at high temperature using MDF and ECAP. The other popular SPD techniques are accumulative roll bonding, continuous confined strip shearing, twist extrusion and constrained groove pressing [2.7-2.10]. Among conventional sheet metal forming techniques, cryorolling and asymmetric rolling have been widely used to develop UFG/Nano grain structure in the material. Various SPD techniques are as follows.

1. Multiaxial Forging (MAF) [2.11-2.13]
    i. Channel Die Forging (CDF) [2.14]
    ii. Cyclic Close – die forging (CCDF) [2.15]
2. Equal Channel Angular Pressing (ECAP) [2.16-2.18]
    i. Repetitive Side Extrusion [2.19-2.20]
    ii. Rotary – die ECAP [2.21-2.22]
    iii. Parallel channel ECAP (PC – ECAP) [2.23-2.24]
    iv. Con-shearing [2.25]
    v. ECAP – conform [2.26-2.28]
    vi. Incremental ECAP (I – ECAP) [2.29-2.30]
    vii. Continuous Confined Strip Shearing (C2S2) [2.31-2.33]
    viii. Continuous Manufacturing of Bolts [2.34]
3. High Pressure Torsion (HPT) [2.35-2.37]
    i. Continuous High – Pressure Torsion [2.38]
    ii. Hollow cone – HPT process [2.39]

4. Extrusion based Techniques
    i. Twist extrusion [2.40-2.42]
    ii. Pure Shear extrusion [2.43]
    iii. Tube Channel Pressing (TCP) [2.44]
5. Rolling based Techniques
    i. Accumulative roll Bonding (ARB) [2.45-2.47]
    ii. Asymmetric rolling[2.48-2.49]
    iii. Cryorolling [2.50-2.51]
    iv. Wavy rolling [2.52-2.53]
6. Other Techniques
    i. Repetitive Corrugation and Straightening (RCS) [2.54-2.55]
    ii. Continuous Repetitive corrugating and straightening [2.56-2.57].

2.2.1 Multi Axial Forging

Multi-Directional Forging (MDF) is one of the novel SPD techniques, which was used during the first half of the 1990s for the fabrication of UFG structures in bulk alloys [2.11-2.13]. The continuous dynamic recrystallisation is the main mechanism responsible for the grain refinement during the multidirectional forging. The schematic of multidirectional forging is shown in Figure 2.1 and it involves multiple repeats of free-forging operations including setting and pulling with changes of the axes of the applied load [2.58]. The strain produced by this process is less homogeneous as compared to strain produced in ECAP and HPT. Since this process is generally carried out at elevated temperatures, therefore, this can be applied in brittle materials to obtain a nanostructured state. The proper selection of the temperature and strain rate of deformation results in the desired grain refinement. The process is generally performed over the temperature range of 0.1–0.5 Tm, where Tm is the absolute melting temperature, and this method produces large-sized billets with nanocrystalline structures. The process of multiaxial forging for microstructural refinement has been reported in the literature from liquid nitrogen/cryogenic temperature (-196˚C) to elevated temperature (600˚C) for various alloys such as Al 6061 alloy [2.59], Cu [2.58], Mg alloys [2.60-2.62], Fe-32%Ni alloy [2.63], AISI 1016 steel [2.64], Al-Mg alloy [2.65], titanium alloy [2.66], pure aluminum (AA1100) [2.67], Plain low carbon steel [2.68].
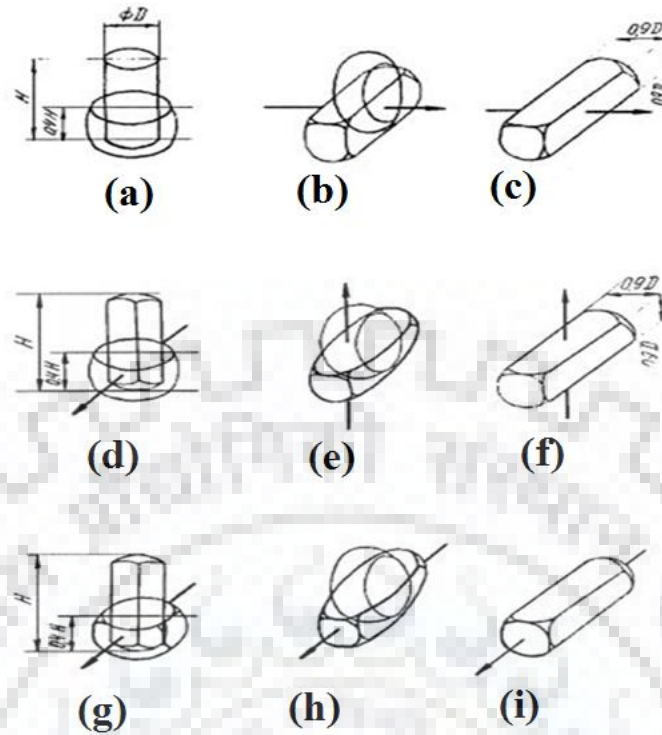
Figure 2.1: Process of multiaxial forging showing setting and pull broaching along the first axis (a – c), along the second axis (d – f), and along the third axis (g – i) [2.11-2.13]

2.2.2 Cryorolling

Cryorolling has been identified as a promising method for producing a UFG microstructure in coarser grained metals/alloys due to various advantages as compared to other SPD methods. Processing at cryogenic temperature reduces the amount of strain required for the development UFG microstructure in metals/alloys [2.69]. In addition, at very low temperature, high density of dislocations/defects can be generated inside the sample due to suppression of dynamic recovery resulting significant improvement in the mechanical properties [2.70]. Further, owing to the several advantages such as no requirement of a die, lesser wear problems, low maintenance cost, simple and economical process associated with cryorolling, makes it highly recommendable process for fabrication of UFG and NC structures in the bulk alloys. Cryorolling can be performed by using conventional rolling machine and liquid nitrogen. The starting material which is to be cryorolled must be in the form of sheet. During the process, samples are dipped in liquid nitrogen for 15-30 min to attain the sample temperature to liquid nitrogen temperature and conventional rolling is performed.

10

2.2.3 Equal channel angular pressing

ECAP for the production of ultrafine grain/nanostructured materials was first developed by Segal and his co-workers in 1981 [2.71]. After their work, interest in the production of UFG/NS materials through SPD has been ever growing. In this technique, a material with uniform cross section is forced through a intersecting channels of the same cross section (Figure 2.2) under minimum friction conditions [2.72-2.73]. During this process, material undergoes shear localization along a fixed plane under steady state [2.72]. This process is repeated by rotating orientation of the material blank along the length direction after every pass. The amount of imposed strain can be increased by applying back pressure at the end of the sample and by increasing number of passes. The grain refinement takes place through simple shear.
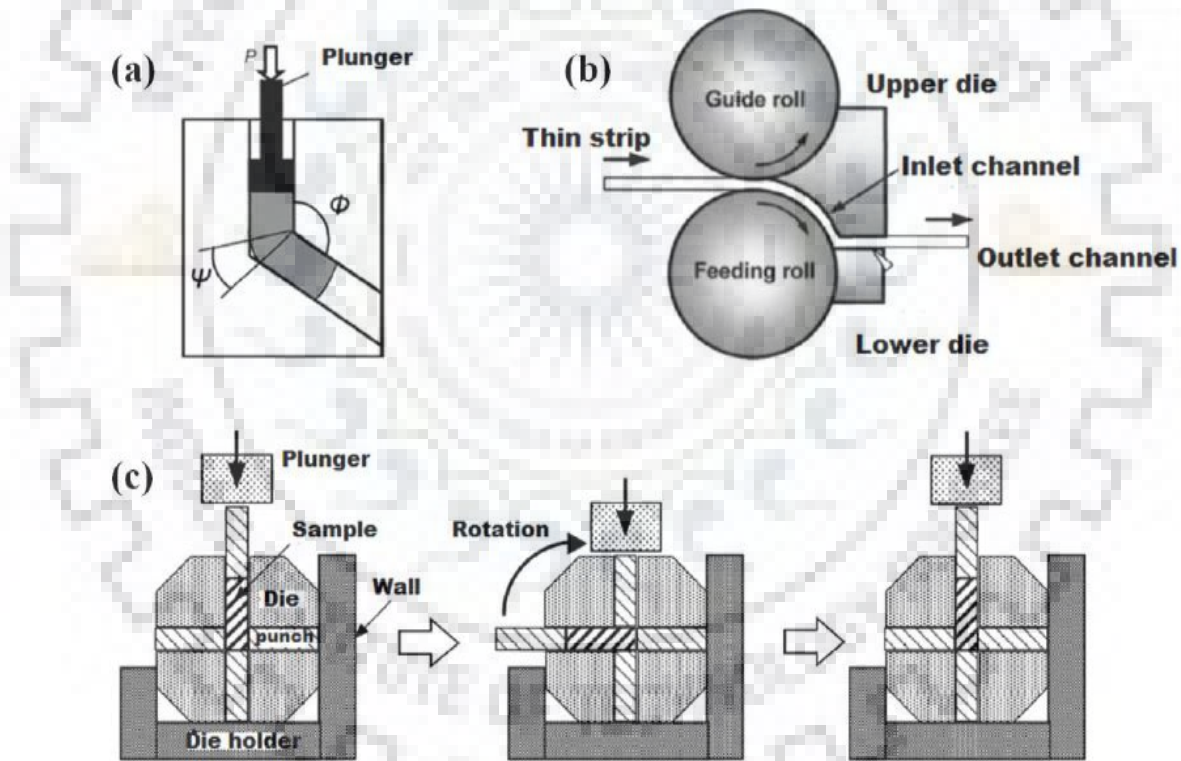
Figure 2.2: Schematic representation of equal channel angular processing (ECAP) [2.71]; (a) Conventional ECAP [2.72-2.74], (b) Conventional Equal channel angular rolling (ECAR) [2.75], (c)Rotary die ECAP [2.75]

With increasing number of passes, the average misorientation of the grain boundaries increases, this leads to formation of high angle grain boundaries in the material [2.72-2.74]. ECAP with four different routes are used to produce material with different microstructure. The sample is pressed without rotation in route A, rotated by 90˚ in alternate directions (Route B$_A$) and rotated by 90˚ in clock or anticlockwise direction (Route B$_C$). The sample is rotated by 180° between passes (route B$_C$). This technique is a suitable because load requirement is very less and simple tool geometry resulting low tool pressure to develop new microstructure with improved strength in the material at applied strain. Fig. 2.2 shows the schematic of various ECAP techniques.

2.2.4 High pressure torsion (HPT)

HPT technique is derived from Bridgman technique which was used to increase the torsional strength of the samples by applying compressive and torsional forces simultaneously (Figure 2.3) [2.35-2.37].
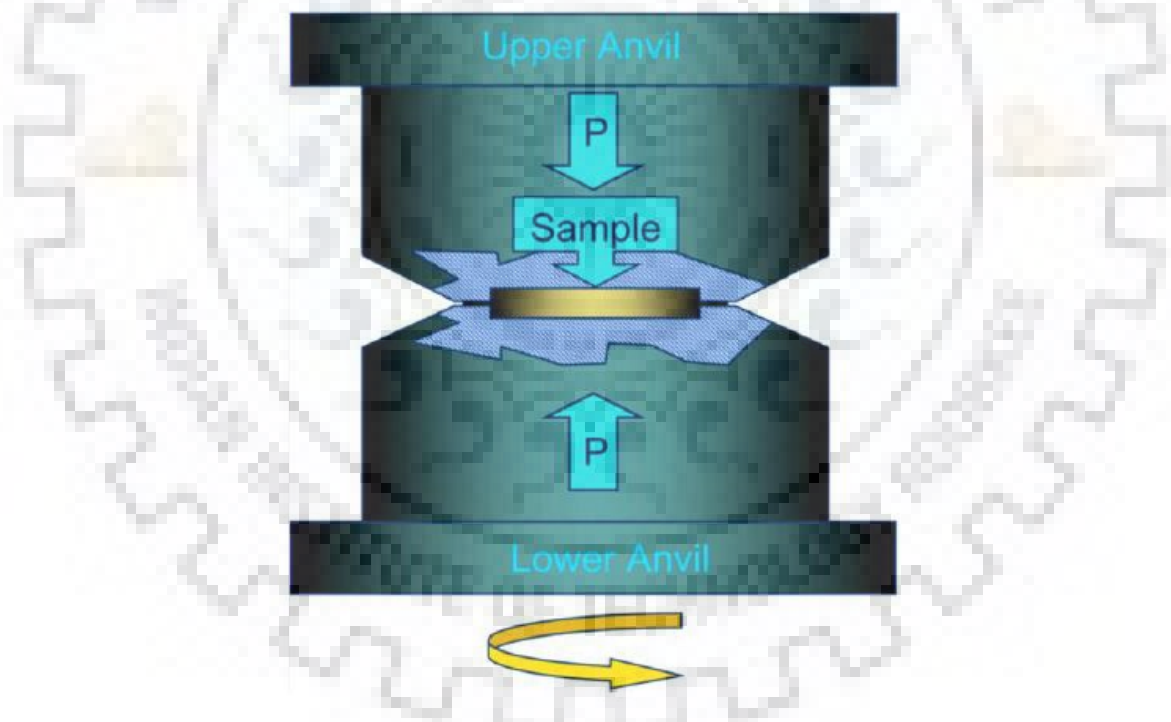
Figure 2. 3: Schematic representation of Bridgman apparatus [2.35-2.37]

The typical shape of the sample that can be produced through this technique is in disc form. Improved mechanical properties have been realized through this process [2.35-2.37]. The major advantages of HPT process is due to its ability to produce materials with exceptionally small grains sizes, often lying in the lower sub micrometer or nanometer range. It often

produces grain boundaries with high fraction of high angle grain boundaries. The limitations of the HPT are as follows; i) The microstructure and property in the samples processed through HPT is not homogeneous due to inhomogeneous strain distribution in the samples, ii) It is limited to produce small scale samples only, iii) The tooling and equipment cost is relatively high.

2.2.5 Accumulative roll bonding (ARB)

At first, Saito et al. [2.76] have proposed this technique to produce UFG structure in the various metals and alloys. The process involves stacking of two strips one above another and subjected to conventional rolling process with reduction per pass by ~50%.
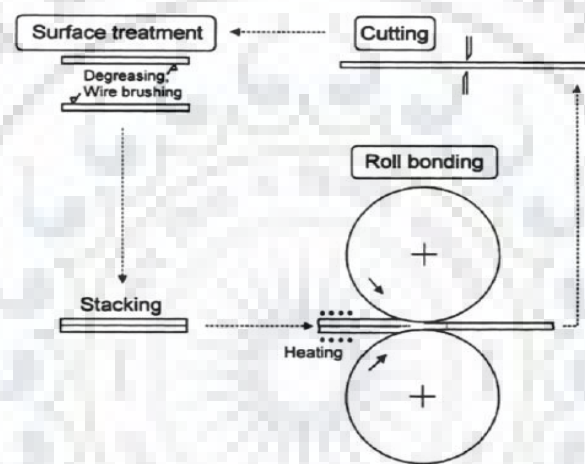
Figure 2. 4: Schematic representation of ARB process [2.76]

Here, conventional rolling process is used to produce bond between two layers. For a sound bonding between two layers, the surface of the strips was properly surface treated. The obtained sheet after rolling is cut into two halves in length direction. The sectioned pieces are stacked again after surface treatment and rolled again. The whole process is repeated again to induce severe strain in the material. The grain refinement takes place in the material through pure shear [2.45- 2.46]. Figure 2.4 shows the schematic representation of the ARB process. Later this process has been successfully used to produce metallic multi layered composites by performing roll bonding between dissimilar metals and alloys [2.77-2.79]. The advantages of this process are simplicity, cheap, and easy adoptability in industrial process.

2.2.6 Asymmetric rolling

Asymmetric rolling (ASR) process was developed by Kim and Lee [2.80] to produce shear texture in the material through shear deformation. Later Jin and Lloyd [2.81], Cui and Ohori [2.82] have applied ASR at room temperature to develop fine grained structure in the AA 5754 alloy and pure Al, respectively. Grain sizes with 1-2 μm were obtained in pure Al alloy due to dynamic continuous recrystallization and in AA 5754 after static recrystallization. ASR also known as differential speed rolling (DSR), in which the diameter of the rolls is different or the rotating speeds of the upper and lower rolls are different from each other. It can employ additional shear strain to the material in addition to compressive force [2.83]. It has been successfully used for various metals and alloys for grain refinement and texture modifications [2.80-2.82].The advantages of ASR over symmetric rolling are ; i) It can introduce much more redundant shear deformation, ii) Promotes the deformation to extend to the centre regions of the rolled sheets. Schematic of asymmetric rolling for various roll diameter is shown in Fig. 2.5.
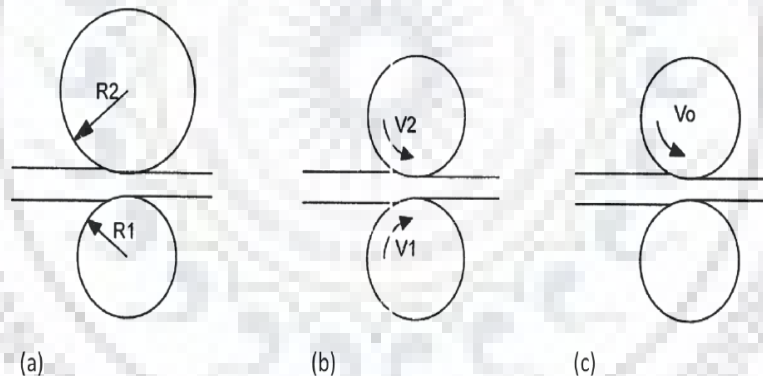
Figure 2.5: Schematic representation of asymmetric rolling due to (a) Non-unity roll radius ratio (b) Non-unity roll speed ratio and (c) Single roll drive rolling [2.81].

2.2.7 Cyclic Extrusion Compression (CEC)

Cyclic extrusion compression (CEC) is well known process to produce UFG materials and devised by Richert et al. [2.84], and represented schematically in Fig. 2.6 (c). It involves the cyclic flow of metal between the blinking extrusion and compression chambers. The sufficient counter pressure is given to the samples to cause plastic deformation by alternating extrusion and compression by touching the work piece cyclically between the two die

chambers to build up desired plastic strain. The accumulated equivalent strain is approximately given by;

$$\varepsilon = 4\,n\,ln\left(\frac{D}{d}\right) \qquad (2.1)$$

Where; D is the chamber diameter, d is the channel diameter and n is the number of deformation cycles. An elevated hydrostatic pressure is imposed due to cyclic extrusion and compression, resulting in higher loads, which require special tooling. This process is most appropriate for processing of soft material such as aluminium alloys.
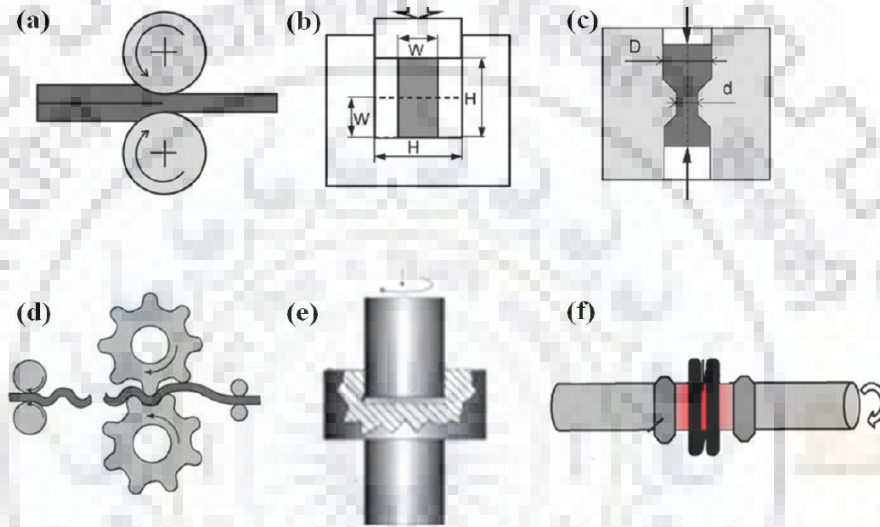
Figure 2.6: Schematic representation of few common SPD processes; (a) ARB [2.46], (b) MAF [2.11-2.13], (c) CEC [2.84], (d) RCS [2.85], (e) HPT [2.35], (f) STS [2.6]

2.2.8 Repetitive Corrugation and Straightening (RCS)

This method was developed by Huang et al. [2.85], and represented schematically in Fig. 2.6 (d). The method consists of continually bending and straightening of a billet with ridged tools and then straightening the billet with flat tools without changing the cross-sectional area of the billet, imposing high strain into the material. The equivalent strain per one sequence is given by;

$$\varepsilon = 4\,n\,\frac{\left[\frac{r+t}{r+0.5t}\right]}{\sqrt{3}} \qquad (2.2)$$

Where, t is the thickness of sample and r is the curvature of bent zone. By repeating this process in a cyclic manner, severe plastic strain can be introduced in to the work piece, which results in grain refinement.

2.2.9 Specification applications and comparative study of cryorolling/cryoforging

Specification applications of cryorolling includes production of lengthy product in the form of continuous sheet, mass production of threaded part like screw and bolt, used in construction material, roofing panels, partition beams and most importantly used in automobile industries for manufacturing of various parts. However the specific application of cryoforging includes the production of large size high strength billets which can be used for structural applications. However Cryorolling requires less strain as compared to cryoforging due to which UFG microstructure can be easily developed in the metals/alloy. In addition the strain produced by cryoforging is less homogeneous as compared to strain produced by cryorolling. The another disadvantage of cryoforging is the use of complex die, tooling and fixtures due to which cost associated with cryoforging is much higher than cryorolling.

2.3 Aluminium Alloys

Aluminium is widely used materials for the applications in foils and cables. In its pure form, it is light and soft and shows a yield strength of about 8-11 MPa only. Pure form of an aluminium has a limited applications and used in packaging and electrical applications. However, for the better use of aluminium for high strength applications, it is essential to alloy aluminium with other elements. Based on the alloying elements, Al alloys can be classified in to cast and wrought alloys. These alloys can further be classified in to heat treatable and non heat treatable alloys and classification is shown in Fig. 2.7.

16
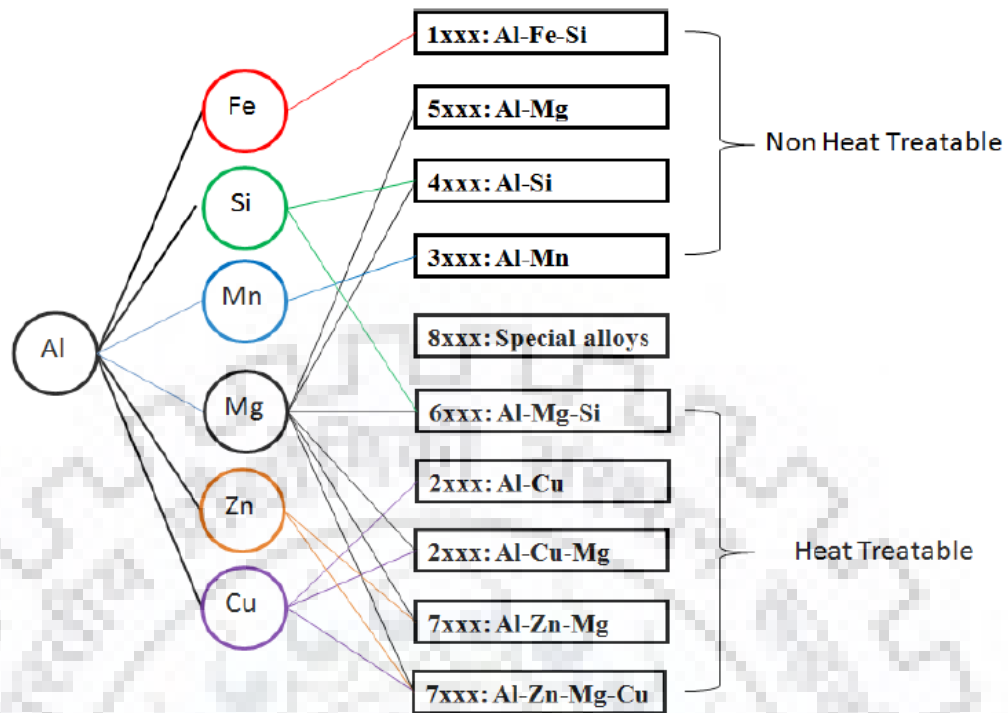
Figure 2.7: Principal alloying elements and the families of alloy derived from them [2.89]

2.3.1 Heat treatable alloys

These are the alloys in which mechanical properties can significantly be altered by heat treatment and precipitation hardening. In heat treatable Al alloys, the concentration of solute atoms at room temperature exceeds the equilibrium solubility due to which when these alloys are heat treated excess amount of solutes comes out from the matrix in the form of precipitates. These precipitates strengthen the alloys and the mechanism is known as precipitation hardening.

2.3.2 Non heat treatable alloys

These are the alloys which derive their properties from strain hardening and solid solution strengthening. Al 1xxx, 3xxx, 4xxx, and 5xxx series alloys are non heat treatable alloys. Cold rolling methods are used for improving the mechanical properties of non heat treatable alloys. These alloys are not suitable for high strength and high temperature applications because strengthening achieved from cold working process is lost at high temperature.

17

2.4   Strengthening mechanisms for Al alloys

There are several mechanisms associated with strengthening of Al alloys. These mechanisms are grain boundary strengthening, solid-solution strengthening, strain hardening, precipitation hardening and dispersion- hardening [2.86]. These mechanisms are discussed in detail in following section.

2.4.1   Grain boundary strengthening

Grain boundary is the area where the lot of lattice perturbation exists. When the dislocation faces grain boundary, its motion gets hindered. It leads to pile up of dislocations at the grain boundaries. Grain boundary act as an obstacle for dislocation motion, resulting in high strength. When the grain size is fine, the distance travelled by the mobile dislocations before reaching grain boundary decreases, so the pile up of dislocation will be more rapid due to which strength is significantly improved for finer grain materials. If the grain boundary is low angle, grain boundary hindering of dislocations is less, while high angle grain boundary completely hinders the dislocation motion, thus strength of the material increases. The Fig. 2.8 (a) shows dislocation moving along a slip plane approaching grain boundary. Fig. 2.8 (b) shows low and high-angle grain boundaries with respect to atom positions adjacent to it. In coarse grained aluminium alloy, the grain size is in the range of few microns to several microns (three digits). Coarse grained aluminium alloys shows normal yielding and work hardening behavior, whereas UFG materials shows sharp yield point. In the early 1950s, Hall and Petch has proposed a relation between yield stress (σ_y) to the grain size (d) of the undeformed material [2.87-2.88] as ascribed by following equation

$$\sigma_y = \sigma_o + \frac{k}{\sqrt{d}} \qquad (2.3)$$

18
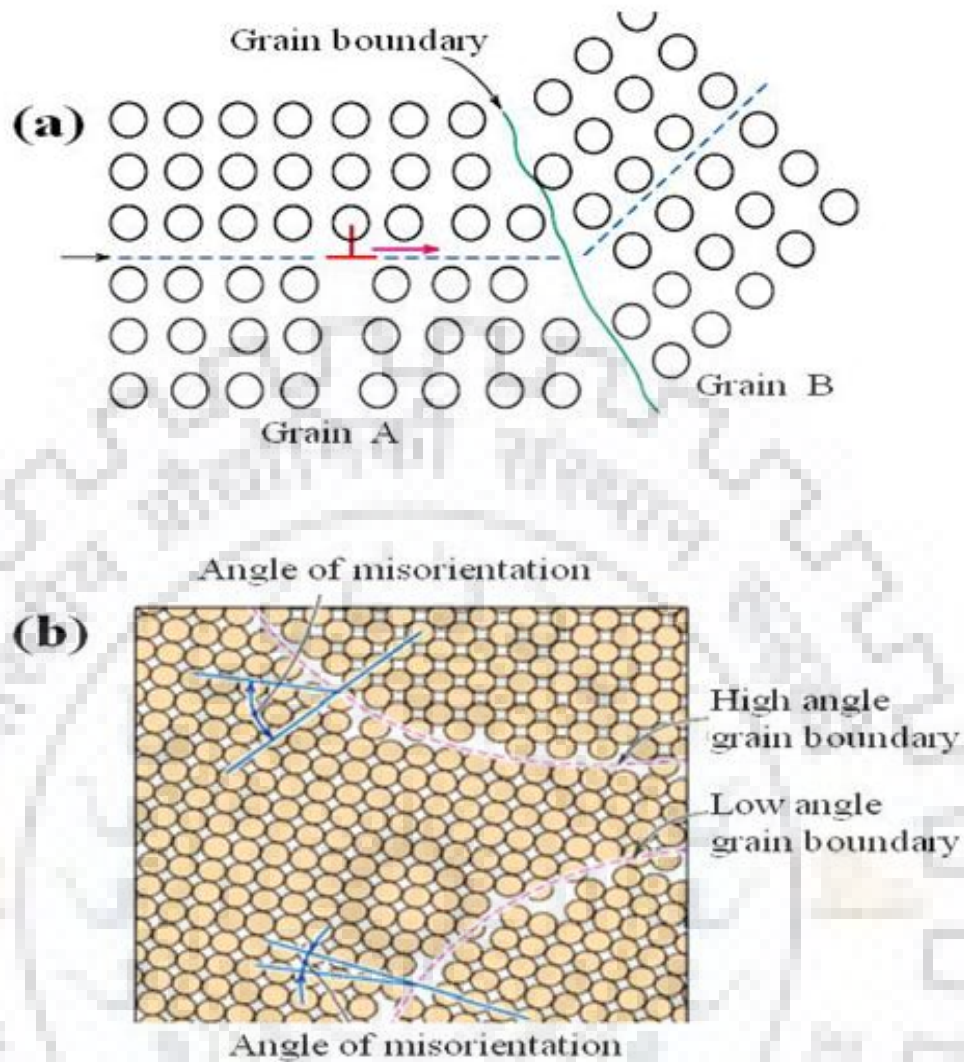
Figure 2.8: (a) Interaction of dislocations and grain boundaries   (b) Low and high angle grain boundaries with respect to atom position [2.87-2.88]

Where σ_y is the yield stress, σ_o is the lattice friction stress, k is the Hall-Petch constant and D is the grain size. From above equation (2.3), it is clear that   yield strength of the material is inversely proportional to its grain size; this means that as the grain size decreases, the strength of the material will increase.

2.4.2   Solid solution strengthening

In the category of non-heat treatable Aluminium alloys, the strengthening mainly comes from solid solution strengthening and grain boundary strengthening. Al1xxx (Al- small amounts of Fe and Si), 3xxx (Al-Mn) and the 5xxx (Al-Mg) alloys are under this category. These alloys are widely used in the range of applications where a low to medium strength, a

good formability, and a good corrosion resistance are desirable [2.89]. A systematic work has been carried out on the effect of solid solution on strengthening of the matrix in coarse grained Al alloys.
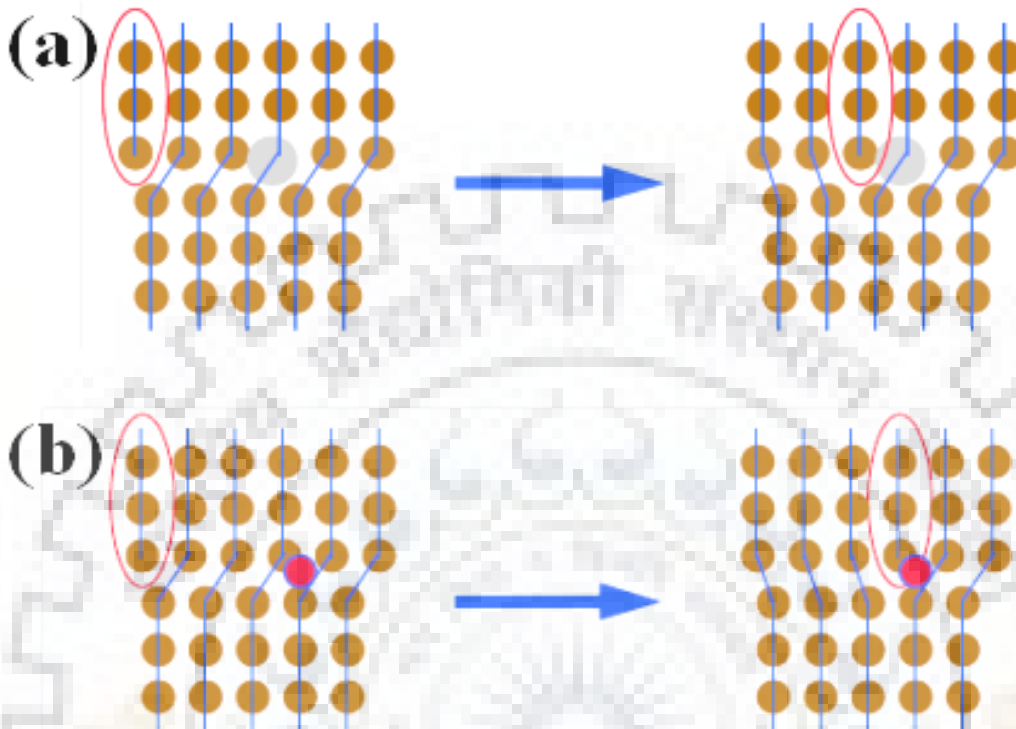
Figure 2.9: Representation of a dislocation stopped by; (a) Substitutional atom (b) Interstitial atom

It has been observed that the strength by solid solution is directly proportional to the concentration (C) of solute in the matrix. This relation can be expressed as per following equation

$$\sigma_{ss} = HC^n \qquad (2.4)$$

Where H and n are the constants. A higher concentration of solute atoms will obstruct more dislocation as compared to low solute concentration, thus increasing strength of metals/alloys. Fig. 2.9 (a) and (b) shows the effect of substitutional and interstitial atoms on the dislocation motion.

2.4.3   Strain hardening

One of the key characteristics of the plastic deformation of metals is the fact that shear stress required to produce slip increases with increasing shear strain. The increase in the stress required to cause slip due to plastic deformation is known as strain hardening [2.90]. Strain

20

hardening is caused by dislocation interacting with each other and with barriers which impede their motion through the crystal lattice. Hardening due to dislocation interaction is a complicated problem because it involves large group of dislocations.

2.4.4   Precipitation strengthening

Small second phase particles distributed in a ductile matrix are a common source of alloy strengthening. Precipitation hardening is produced by solution treating and quenching an alloy in which a second phase is in solid solution at the elevated temperature but precipitates upon quenching and aging a lower temperature. For precipitation hardening to occur, the second phase must be soluble at elevated temperature but must exhibit decreasing solubility with decreasing temperature [2.91]. Precipitation hardening is most useful strengthening mechanisms of aluminium alloys in 2xxx, 6xxx and 7xxx series, where the strength of aluminium alloys is improved by the formation of fine and uniformly dispersed second-phase particles of the solute atoms in matrix. The process consists mainly of three steps; i) Homogenization or Solution heat treatment of the alloy, where the alloy is heated above the solvus temperature and soaked, until solute dissolves properly and homogeneous solid solution is produced; ii) Quenching, where this solid solution cools rapidly to a lower temperature forming a supersaturated solid solution and the solute does not immediately diffuse out of a phase; iii) Finally, precipitation of small sized precipitates occurs when super saturated solid solution is brought below the solvus temperature. Fig. 2.10 shows temperature versus time plot for precipitation hardening mechanism.
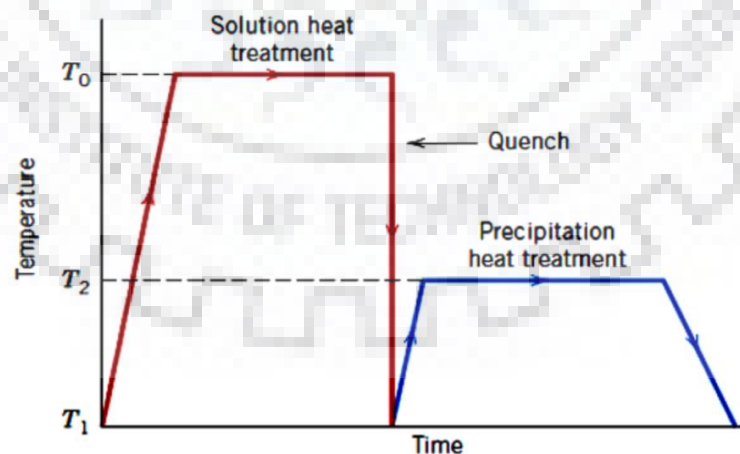
Figure 2.10: Schematic of temperature-time plot showing precipitation hardening mechanism

21

2.5   Strategies for improving Ductility of Ultrafine grained Al alloy

2.5.1   Duplex microstructure

Wang et al [2.92] studied the influence of bimodal microstructure on the ductility without sacrificing the strength of nanostructure Cu produced by cryorolling and found that post deformation annealing is a suitable method for improving the ductility of UFG metals/alloys. Annealing leads to formation of micron sized grains in matrix of UFG/NS, which attributes for increased tensile ductility. Since then, there are several attempts made on different metals to achieve the similar effect. However, the improvement in ductility was observed with the expense of strength. Recently, Panigrahi et al. [2.93] have developed a new strategy for improving the ductility of precipitation hardenable Al 6063 alloy without loss of strength. The proposed strategy is short annealing followed by aging after cryorolling as reported in their work. Cryorolling after solid solution treatment results in improved strength by accumulation of high density of dislocations and formation of subgrain boundaries in the material. Short annealing leads to formation of recovered or partially recrystallized grains, which would act as empty rooms for newly generate dislocations to accommodate plastic deformation. Further, low temperature ageing leads to increase in strength by precipitation hardening effect. The selection of short annealing temperature and time is critical to observe the enhanced ductility without affecting strength. However, it is obvious that by performing short annealing results in restoration process through recovery and recrystallization. It will have definite negative influence on strength. In precipitation hardenable alloys, it is not observable due to nullifying effect by cluster strengthening effect. It can be noted that the increase in ductility through this route is with the cost of ductility.

2.5.2   Introducing nano-sized precipitates

This is an effective approach for enhancing the ductility of bulk UFG Al alloy without sacrificing the strength. Zhao et al. [2.94] studied the influence of nanosized precipitates on ductility of UFG Al 7075 alloy and found that generation of nano precipitates in UFG microstructure helps in improving the ductility of UFG Al 7075 alloy. The proposed strategy as reported by Zhao et al. [2.94] is (i) Allowing second phase particles to dissolve in to the matrix in coarse grained material; ii) Producing UFG structure through deformation at supersaturated solid solution state, and (iii) Proper ageing treatments to form nano sized precipitates in the UFG microstructure. Generation of nano precipitates alone will not help to

enhance the ductility of the material. During ageing process, the microstructure undergoes recovery process, thus the dislocation density will be reduced. The annihilation of dislocations during recovery process will leave a space for dislocations that generate during deformation. Thus, ductility of the material is increased. To enable the material to undergo stable plastic flow, the nano-sized precipitates play a major role and also they accumulate more dislocations; thus the work hardening rate of the material gets improved. The drop in strength due to annihilated dislocations is compensated by the nano sized precipitates, but it also enhances the strength further.

2.5.3   Modifying Grain Boundary Characters

The microstructure that develops during SPD generally is characterized by nature of the grain boundaries. If the misorientation with the neighbour grains is less than 15°, then it is called as low angle grain boundaries (LAGBs). If it is greater than 15°, then it is called high angle grain boundaries (HAGBs). It has been observed that the misorientation of the adjacent grains directly influences the mechanical properties [2.95-2.96]. Grain boundaries render strength to the material by behaving as an obstacle to the gliding of mobile dislocations. However, the amount of strength that can be imparted to the material is dependent on the grain boundary character. In the material with HAGBs, activation of slip between the adjacent grains is difficult and it requires more energy [2.95-2.96]. Thus, the strength of the material increases. Increase in strength with the expense of ductility is not desirable as high strength with reasonable ductility of materials is essential for engineering applications. In contrast to HAGBs, LAGBs shows poor resistance to the gliding of mobile dislocations. This property can be utilized to improve the ability of plastic deformation in UFG/NS materials. Hu et al., [2.95] have recently reported increased ductility and uniform elongation while retaining high strength by engineering.

2.6   Microstructural Characteristics of SPD processed Al alloys

2.6.1   Dislocations

In SPD process, dislocations are the building blocks for the evolution of new grains. Dislocations induced during deformation facilitate evolution of new grains. They may exist in the form of tangles zones or rather random structures [2.97]. In high stacking fault energy materials, faster dynamic recovery takes place through annihilation of dissimilar type

dislocation. Dislocation accumulation can be enhanced by performing cryogenic deformation. A material deformed at cryogenic temperatures possesses high dislocation tangled zones due to reduced dynamic recovery.

2.6.2   Dislocations cells and subgrains

Dislocation cell or subgrain boundary is the primary element in the evolution of new ultrafine grain through plastic deformation. These are the smallest volume elements in the deformed microstructure [2.97]. The boundaries of dislocation cell or subgrain form through the rearrangement of similar type of dislocations. Materials that undergo deformation at very low temperature possess thick dislocation walls with dislocation tangled zones. The interior of the dislocation possesses relatively lower dislocation density than the boundaries.

2.6.3   Geometrical necessary dislocations (GND)

Huajian and Yonggang [2.98] have defined geometrically necessary dislocations as, "An extra storage of dislocations that are required to accommodate the lattice curvature that arises whenever there is a non-uniform plastic deformation." These dislocations will contribute for work hardening by acting as an obstacle to the motion of statically stored dislocations. GND densities are estimated by using EBSD technique.

2.6.4   Non equilibrium grain boundaries

The evolution of UFG/NS in SPD process involves generation of high densities of dislocations followed by formation of cellular structure and its continuous transformation to granular structure by the interaction of generated dislocations with cell walls and grain boundaries [2.99]. The grain boundaries that form in SPD process contain very high density of extrinsic dislocations, which results in high energies and high internal stresses.
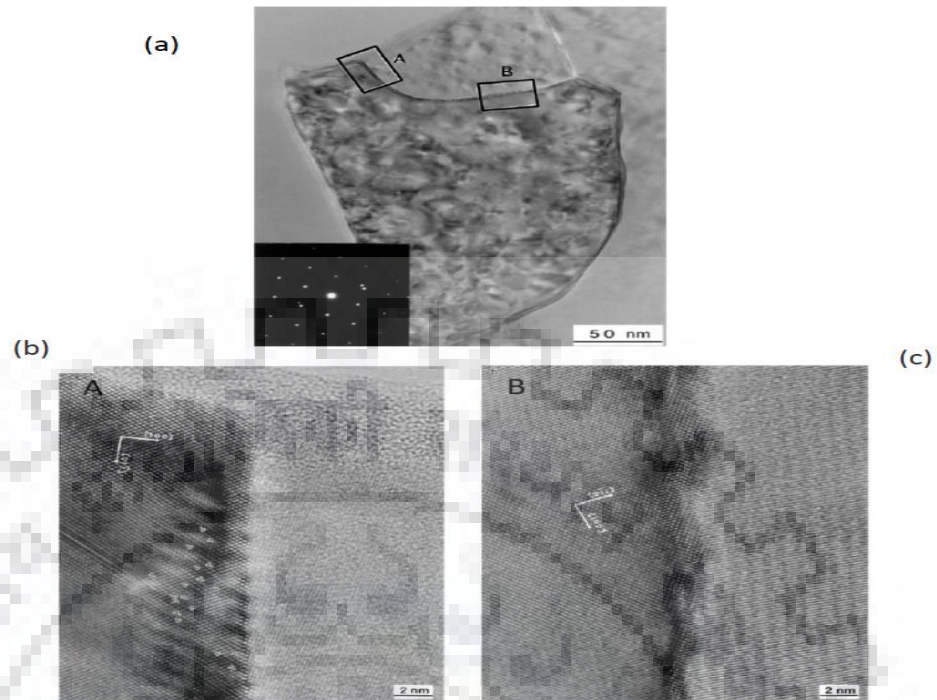
Figure 2.11: TEM micrographs of Al–3% Mg alloy sample after HPT at room temperature; a) UFG grains with non-equilibrium grain boundaries, b) HRTEM image taken at location'A'shown in **Figure 2.11(a)**, c) HRTEM image taken at location B shown in **Figure 2.11(b).** This image is taken from the reference [2.101].

These boundaries are called non-equilibrium grain boundaries. Figure 2.11 shows the TEM micrograph of Al–3% Mg alloy sample after HPT at room temperature. It is evident from the image that presence of distorted and diluted grain boundaries with the presence of high densities of extrinsic dislocations makes the grain boundaries non-equilibrium [2.99]. The extrinsic dislocations present in the grain boundaries in SPD processed material influence the mechanical properties. These can easily move in the grain boundaries leading to negative Hall-Petch effect [2.100-2.101]. From the ductility point of view, non-equilibrium grain boundaries might be favourable to achieve decent elongations in UFG/NS materials processed through SPD.

2.7 Applications of ultrafine grained (UFG) materials

UFG/NS materials can be used as potential materials for structural and functional applications in many engineering sectors such as aerospace, automotive, defence, electronics,

constructions, biomedical, etc. [2.102-2.103]. The process of commercialization of UFG/NS materials is hindered due to small size of SPD processed material and their cost of production. However, the recent developments in SPD techniques, allowed scaling up of the processing up to industry production level.

2.7.1   Micromechanical systems (MEMS)

In order to have a better mechanical strength of the micro parts in MEMS, the average grain size should be less than the part dimension. UFG/NS materials are suitable candidates for these applications. Latest developments in SPD by miniaturizing the processing technique allows to produce micron scale products with desired grain size to enhance the strength and fracture toughness of the material [2.104].

2.7.2   Biomedical applications

The metals such as Fe, Mg, and Ti are widely used for biomedical applications as body implants. The field of biomaterials is significantly growing due to ever increasing demand for bio implants. The physical properties that are generally considered for biomaterials includes hardness, tensile strength, modulus, elongation, fatigue strength, impact properties, wear, dimension stability, biodegradability, biocompatibility [2.105]. Materials for permanent implants such as bone and tooth replacements should possess inert behavior in body fluids, whereas for temporary implants, material must degrade at a suitable rate for the targeted application [2.106].Titanium alloys are widely used as permanent body implants due to its excellent combination of physical and electrochemical properties. Implants with pure Fe and Mg are highly biodegradable. Recent studies have proven that UFG materials processed through SPD can be used as suitable candidates for biomedical applications [2.107-2.109]. The reported literature shows that the commercial pure Ti with UFG structure developed through SPD will be better replacement for Ti alloys. By nano sizing the microstructure of CP Ti, the mechanical behavior and biocompatibility have increased [2.110-2.111]. The materials processed through SPD have shown better corrosion resistance in body fluids over coarse grained materials. Fine grained Mg has shown significant enhancement of fatigue life and endurance limit as well as reduction in corrosion rate in Hanks solution [2.112].

2.8 Precipitation phenomenon in 2xxx series Al alloys

Aluminum 2xxx series alloy are high strength alloy and they are strengthened by precipitation hardening and strain hardening. Materials can be hardened by inhibiting the motion of crystal defects called dislocations. In pure metals, the presence of defects (such as vacancies, interstitials, dislocations and grain boundaries) can enhance the strength. In single phase alloys, additional resistance to deformation may arise from the presence of foreign atoms. In two-phase alloys, additional stress is needed to enable the dislocation to intersect the second-phase particles.
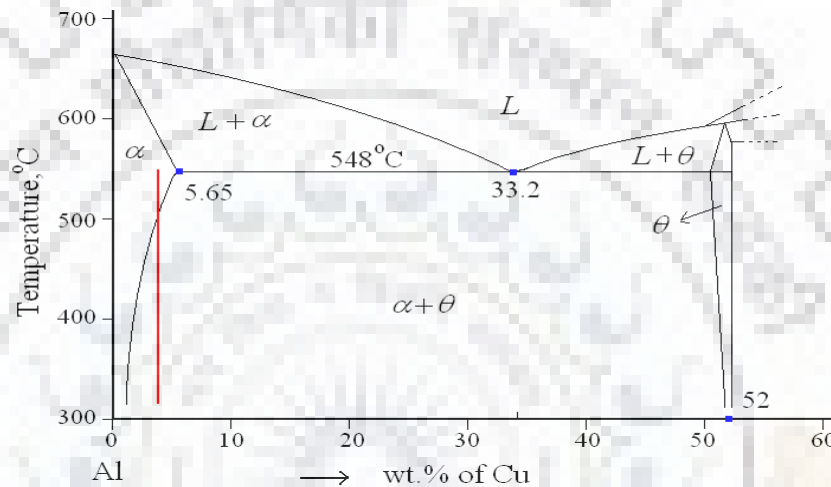
Figure 2.12: Phase Diagram of Al- 4% Cu alloy

A finely dispersed precipitate may, therefore, strengthen the material. This phenomenon is termed **precipitation hardening.** When the aluminum-copper alloy of less than 5 wt% copper is heated to a temperature just above the **solvus line (Fig. 2.12)**, only one phase is thermodynamically stable. Other solid phases dissolve (disappear). This process is called **solution treatment**. The only requirement is that the specimen must be kept at this temperature for a long enough time. By rapidly cooling the alloy, a supersaturated solution can be obtained at room temperature. As a function of time at room temperature, and at higher temperatures up to 200^0 C, the diffusion of Cu atoms may take place and the precipitate particles can form. For this particular alloy, Al-4% Cu, five sequential structures can be identified: (a) supersaturated solid solution α, (b) GP1 zones, (c) GP2 zones (θ'' phase), (d) θ' phase and (e) θ phase, CuAl$_2$. Not all these phases can be produced at all aging temperatures. GP1 and GP2 zones are produced at lower temperatures, and θ' and θ phases occur at higher temperatures. The initial stages of precipitation are the most difficult to analyze because of the

27

extremely small size of the particles and their relatively uniform distribution. GP zones meant for *Guinier-Preston* zones which have a definite composition and structure that is not the same as that of the final stable precipitate. Evidently, these particles are easier to nucleate than the final precipitate, as a result, form first. Eventually, they disappear as later more stable phases appear. θ'' and θ' are meta-stable transition precipitates with distinct crystal structure of their own, while θ is the equilibrium stable precipitate of $CuAl_2$. When the crystals are solution treated and quenched so that alloy contains all of the copper in supersaturated solid solution, the yield stress is raised significantly over that for pure aluminium. The rate of strain hardening is low and it is characteristics of easy glide. Slip bands are broad and widely spaced. When the crystal is aged to form coherent GP zones, the yield stress is raised significantly but rate of strain hardening is still low. Low rate of strain hardening suggests that dislocation cut through the zones, once the stress reaches a high enough value. Crystal which is aged to peak hardness will have a slight decrease in yield strength as well as increasing rate of strain hardening.. This suggests that dislocations are moving around particles so as to by pass them. In the over aged condition, where particles are noncoherent and relatively coarse, the yield strength will be low but rate of strain hardening is high. This promotes slip on secondary slip systems and promotes strain hardening of the matrix.

2.9 Mechanical properties of UFG Al alloys

Aluminum alloys have been processed by several SPD methods to achieve UFG microstructure in coarser grain counterparts.

Panigrahi et al. [2.113] investigated the effect of deformation temperature on mechanical properties of Al 6063 alloy and found the improved strength (257 MPa) cryorolled Al 6063 alloy over the room temperature rolled (232 MPa) Al 6063. The improved strength of cryorolled Al 6063 alloy is attributed to the accumulation of higher dislocation density at cryogenic temperature.

Krishna et al. [2.114] compared the mechanical properties of Al-Cu alloy processed through cryorolling and room temperature rolling and observed the 7 % increase in the tensile strength of cryorolled alloy with respect to room temperature rolled alloy due to suppression of dynamic recovery at cryogenic temperature.

Chatterjee et al. [2.115] investigated the mechanical properties and microstructural evolution in Al-Mg alloy subjected to ECAP (route B_c) at cryogenic temperature and observed the significant improvement (55 %) in the hardness of ECAP processed Al-Mg alloy as compared to its coarser grain counterpart due to formation of UFG microstructure. **Rao et al.** [2.116] studied the effect of aging and combined treatment of short annealing and aging on the mechanical properties of cryorolled Al 6061 alloy and found that short annealing and aging treatment is an optimum method for improving the ductility without the expense of strength of Al 6061 alloy.

Kumar et al. [2.117] studied the effect of cryorolling and annealing on tensile and corrosion behavior of Al 6082 alloy and observed the improvement in strength and hardness of cryorolled alloy as compared to solution treated alloy due formation of ultrafine grains. Post annealing of deformed alloy at 150^0C exhibited the maximum strength and hardness due to precipitation of fine needle and spherical phases as reported in their work.

Mohamed et al. [2.118] studied the effect of age hardening on the mechanical properties of Al- Cu alloy processed by high pressure torsion and observed the significant improvement in strength (820 MPa) and hardness (205 HV) of Al –Cu alloy after HPT processing as compared to solution treated alloy (205 MPa) due to Hall- Petch strengthening and precipitation of Al_2Cu phase.

Mazurina et al. [2.119] investigated the the role of deformation temperature on the microstructure evolution in Al 2219 alloy and reported that microstructural evolution at low strain has little significance on the temperature while at high strain up to 12 passes depends upon the density of deformation bands along with continuous dynamic recrystallisation, which facilitates the formation of new finer grains at high strain.

Shanmugasundarum et al. [2.120] developed the ultrafine grained microstructure in Al- Cu alloy by cryorolling and reported the effect of short annealing and aging treatment on the mechanical properties of cryorolled Al- Cu alloy. The significant improvement in the strength (540 MPa) along with ductility was observed as reported in their work due to precipitation hardening and combined recovery and recrystallisation phenomenon, which facilitates duplex microstructure with enhanced dislocation density.

Goodarzy et al. [2.121] investigated the effect of aging on the mechanical properties of ECAP processed 2024 Al alloy and found the significant improvement in yield strength and hardness of Al 2024 alloy due to enhanced dislocation density resulting from precipitation hardening effect and grain refinement.

Venkatachalam et al. [2.122] compared the mechanical properties of Al 2014 alloy processed through different ECAP routes A, B_a, B_c, and C up to 5 passes and found an optimum route B_c for improving the strength (602 MPa) and hardness (184 MPa) of Al 2014 alloy. The equiaxed microstructural evolution after ECAP processing through route B_c was responsible for improving the mechanical properties of Al 2014 alloy as reported in their work. Various routes of ECAP process has been shown in Fig. 2.13.
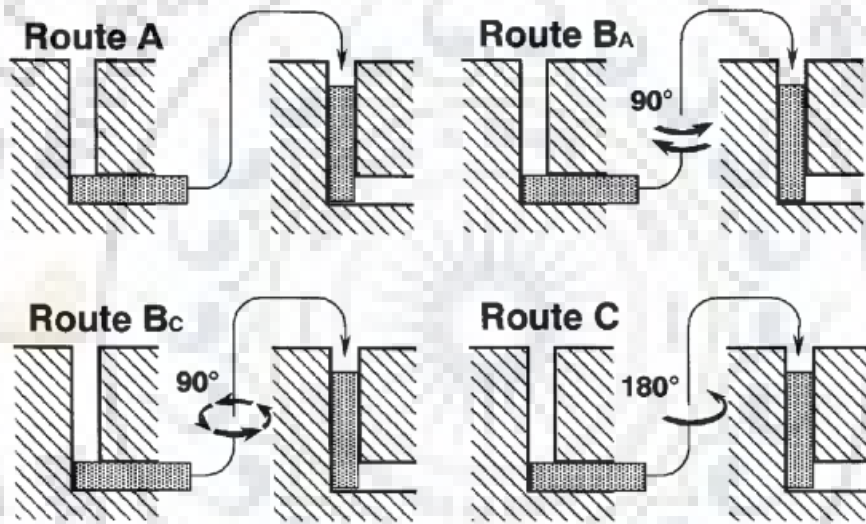
Figure 2.13: Various routes of ECAP process

Rao et al. [2.123] investigated the mechanical properties of Al 6061 alloy subjected to multidirectional cryoforging and observed the significant improvement in strength (388 MPa) and hardness (115 HV) of cryoforged Al 6061 alloy as compared to solution treated alloy (180 MPa, 50 HV) due to solid solution strengthening and grain boundary strengthening.

Sitdikov et al. [2.124] studied the effect of pass strain on the mechanical properties of 7475 Al alloy subjected to warm multidirectional forging and found the significant work softening effect at low strain while with increasing strain, mutually intersecting shear bands (MSBs) were observed. Continuous dynamic recrystallisation was responsible for grain fragmentation in sub micron meter range during warm multi axial forging as reported in their work.

Cherukuri et al. [2.125] compared the properties of AA 6061 Al Alloy at room temperature up to accumulated strain 4, processed by ECAP, MAF, and ARB. Ultrafine grain structure with submicron grain size was obtained in all three techniques. They have found that multi axial forging followed by rolling gives significant improvement of mechanical properties.

Kim et al. [2.126] studied effect of ECAP and followed by low temperature aging on the mechanical properties of 2024 Al alloy and found that Post ECAP low temperature aging treatment is quite effective for enhancing the mechanical properties of 2024 Al Alloy.

Ma et al. [2.127] investigated the effect of warm ECAP processing on anisotropic tensile strength of 2024 Al alloy and found the significant improvement in tensile strength of ECAP processed alloy in longitudinal direction as compared to transverse direction resulting from suppression of dynamic recovery in transverse direction at warm ECAP processing at 150^0C.

Alhamidi et al. [2.128] performed an experiment on Al 2024 for producing ultrafine grained material by HPT. They found that a maximum elongation of 75 % is obtained with an initial strain rate of 10^{-2} s^{-1} at 673K, which shows a high strain rate super plasticity. Super plastic deformation of HPT processed Al 2024 alloy is due to the grain boundary sliding.

Fang et al. [2.129] observed the tensile strength, elongation, static toughness and fracture mode of casting Al-63 wt% Cu and Al-3.9 wt% Cu alloys subjected to ECAP. It was seen that for both alloys, there is an improvement in tensile and fracture strength with increasing ECAP passes, while elongation is independent of ECAP pass. Finally, they concluded that static toughness of Al-cu alloy is enhanced with high ECAP pass.

Mallikarjana et al. [2.130] produced ultrafine grain in Aluminium alloy 2014 by ECAP and studied the mechanical properties of Al-2014. They have found that there is a significant increase in yield strength and ultimate tensile strength of the alloy with corresponding increases in elongation. The increase in strength, hardness and elongation of ECAP processed Al alloy was attributed to formation of UFG microstructure as observed in their work.

Liu et al. [2.131] investigated the evaluation of microstructures in severely deformed AA 3104 aluminium alloy processed by multiple compressions in channel die and found that multiple constrained compressions in channel die increases the flow stress markedly with strain along with the formation of large scale shear bands. At lower strain, dislocation cells and extended boundaries are observed which are transformed in to cell block structure with high angle lamellar boundaries as reported in their work.

Pao et al. [2.132] studied the Fatigue crack propagation in ultrafine grained Al–Mg alloy and observed the lower fatigue crack growth threshold for the UFG Al–7.5 Mg alloy, while higher fatigue crack growth rate for UFG Al-7.5 Mg alloy as comparison to coarse grain counterparts.

Chung et al. [2.133] investigated the mechanical properties and fatigue behavior of solid solution treated 6061 Al alloy fabricated by equal channel angular pressing (ECAP) process and observed the significant improvement in yield, tensile and high cycle fatigue strength, while drop in low cycle fatigue (L.C.F) strength was observed due to reduction in fatigue ductility after ECAP processing.

Hockauf et al. [2.134] produced ultrafine grains in age hardenable aluminium 6063 alloy by ECAP and investigated the influence of precipitates on low-cycle fatigue and crack growth behavior. They showed that newly formed, coherent precipitates in the thermally recovered condition directly contribute to more planar slip behaviour, to slip localization and to early failure during LCF loading. In addition to this, precipitate morphology also affects fatigue crack propagation, and that this is closely related to slip reversibility, even in the UFG regime.

Kumar et al. [2.135] studied the fatigue behaviour of cryorolled and room temperature rolled Al-Mg alloy 6082 and observed that cryorolled and room temperature rolled Al-alloy, examined under HCF regime, shows a significant enhancement in fatigue strength as compared to bulk Al-alloy. The improvement in fatigue life is found more in case of CR samples as compared to RTR samples for same amount of thickness reduction due to suppression of dynamic recovery at cryogenic temperature as reported in their work.

Meyer et al. [2.136] investigated the crack growth behaviour of ultrafine grained Al 6063 alloy processed by ECAP and observed the lower threshold intensity factor and faster fatigue crack growth rate near low intensity factor range for UFG alloy as compared to coarser grain counterparts.

Malekjani et al. [2.137] observed the role of shear bending on fatigue ductility of ultrafine grained aluminium 2024 alloy and found that fatigue ductility depends upon the density of amount of shear bending. High density of shear bending contributed for better fatigue ductility, resulting higher low cycle fatigue strength as reported in their work.

2.10   Problem formulation:

2.10.1 Current Literature on Bulk Ultrafine grained and Nanostructured Materials:

An extensive literature survey has been made on development of high strength Al alloys processed through severe plastic deformation (SPD) techniques. The important findings from the literature are given as below.

➢ Bulk SPD processing techniques have been found to be attractive for the development of advanced materials with significant improvement in mechanical properties.

➢ SPD techniques enhance the mechanical properties not only by grain refinement process but also causes the material to develop various crystalline defects and structural features such as Nano twins, Nano particles, non-equilibrium grain boundaries and grain boundary segregation of solute atoms.

➢ The SPD technique such as Multiaxial Forging at low temperature (77 K) utilizes the combined effect of low temperature and severe plastic strain applied to fabricate bulk UFG structure, and has not been applied in 2014 Al alloys so far.

➢ The problem of poor tensile ductility in ultrafine grained (UFG) Al alloys has been resolved by introducing nanosized precipitates in to the UFG structure, which has led to improvement in both strength and ductility.

➢ Further, rolling at low temperature (77 K) has also been effective in producing Bulk UFG structure in various metals and alloys and has been applied to a number of materials including various Al alloys. But the effect of cryorolling on Al 2014 is scarce in the literature, thus, it is needed to be explored further.

➢ The improvement in high cycle fatigue behaviour of various bulk ultrafine grained Al alloys has been observed as compared to coarser grain counterparts in high cycle fatigue regime.

➢ The improvement in low cycle fatigue in UFG Al alloys has been observed at the expense of strength through proper heat treatment.

➢ The precipitation of various phases during annealing has affected the mechanical properties such as tensile strength, high cycle fatigue, low cycle fatigue and fracture toughness of age hardenable Al alloys significantly.

➢ The improvement in fracture toughness in UFG Al is attributed to small grain size.

2.10.2 Motivation

There are several advantages of SPD techniques for developing UFG microstructure in the metals and alloys; however the quantity and volume of metals/alloys produced through these techniques are limited. For the large scale mass production, cryorolling and cryoforging could be potential techniques for producing ultrafine and nanostructures in the bulk materials. In age hardenable Al alloys, strengthening through precipitation is an efficient method, which has received significant attention for several years. Apart from this, the damage tolerance application of bulk UFG alloys needs considerable attention for the researchers and scientists. For the damage tolerance applications of bulk UFG alloy, there must be good fatigue and fracture properties. In addition, the response of material must be investigated in presence of pre-existing crack. Pre-existing crack in the material could induce the sudden fracture in the material without giving previous warning. The literature on the fatigue and fracture behaviour of UFG Al alloys is very scarce. Moreover, grain boundary strengthening as well as precipitation plays a vital role in imparting tensile strength, ductility and enhanced fracture properties to Al alloy. A thorough understanding of effect of second phase precipitates on the fatigue and fracture properties in UFG Al alloys is essential to maximize its strengthening contribution for simultaneous improvement in strength, ductility, fatigue and fracture toughness. Therefore, the present research work has been focused to develop ultrafine grained precipitation hardenable Al alloy (Al 2014 Alloy) from their bulk Al alloy by using cryorolling and cryoforging technique.

2.10.3 Objectives

The following objectives in Al 2014 alloy were formulated based on the current literature in UFG Al alloys.

➢ To produce ultrafine grained Al 2014 alloy from its bulk alloy by cryorolling and multidirectional cryo forging to study its influence on tensile and fracture properties.

➢ To investigate the effect of annealing afterwards cryorolling and multidirectional cryoforging on the tensile strength, ductility and fracture toughness of bulk UFG Al 2014 alloy.

➢ To investigate the effect of cryorolling and followed by annealing on high cycle fatigue (HCF) properties of bulk UFG Al 2014 alloy.

- To investigate the effect of cryorolling and followed by annealing on fatigue crack growth (FCG) behaviour of bulk UFG Al 2014 alloy.
- To investigate the effect of multidirectional cryoforging and followed by annealing on strain hardening behaviour, fracture toughness and macroscale fracture mechanism of bulk UFG Al 2014 alloy.
- To investigate the strengthening contributions to the yield strength from different strengthening mechanism for multidirectional cryoforged and followed by annealed Al 2014 alloy.

2.10.4 Work plan and Layout of the thesis.

Chapter 1 highlights a brief introduction to the material used in the present investigation, various SPD processes used to produce UFG materials, applications of UFG materials in various fields. The literature relevant to the present research work on ultrafine grained Al alloys is critically reviewed in **Chapter 2**. A brief description of various strengthening mechanisms in UFG/nano structured precipitation hardenable aluminium alloys is made. The mechanical properties of ultrafine grained aluminium alloys reported in the literature are summarized. A critical review of literature as to various thermo mechanical routes applied for pure metals and Al alloys is summarized in this chapter. It forms a strong basis to formulate the key objectives pertaining to the development of ultrafine grained Al alloys (Al 2014) with improved strength and ductility as compared to their commercially available bulk Al alloys.

All the related experimental techniques and procedures employed in the present work are outlined in the **Chapter 3**. The experimental procedures adopted for various thermo mechanical processing in the present work are discussed in detail. The methodology for characterizations of UFG materials such as X-ray diffraction for the phase identification, grain and surface morphology of the UFG materials by using techniques such as Field Emission Electron Microscopy (FE-SEM)/EBSD, and Transmission Electron Microscopy (TEM) are discussed. The precipitation morphology of the UFG materials was studied by TEM. The mechanical properties of the UFG materials were measured by, Fracture toughness test (K_Q & J integral), high cycle fatigue test, fatigue crack growth test, tensile test and hardness test.

In Chapter 4, Section 4.1 In this section, Microstructural evolution, precipitation sequence, and fracture toughness of cryorolled Al 2014 alloy subjected to annealing treatment are

reported. Effects of cryorolling (CR) and followed by annealing (CR+AN) on the high cycle fatigue strength of bulk UFG Al 2014 alloy were investigated and discussed in **section 4.2**. The influence of cryorolling and followed by annealing on the fatigue crack growth (FCG) behavior of bulk UFG Al 2014 alloy is discussed in section **4.3**.

Chapter 5 is subdivided into three sub sections 5.1, 5.2, and 5.3. In **section 5.1** comparative studies of mechanical properties and microstructure evolution in Al 2014 alloy subjected to multidirectional room temperature forging and multidirectional cryoforging up to cumulative strain 2.4 are reported. In **section 5.2**, multidirectional cryoforged Al 2014 alloy is post annealed in the temperature range from 150°C to 350°C with the interval of 50°C for the duration of 1 hour to investigate its influence on strain hardening behavior, macroscopic fracture mechanisms, and fracture toughness. Strengthening contributions to the yield strength from different strengthening mechanism have been evaluated in **Section 5.3.** The overall conclusions and the scope of future work are given in **Chapter 6**.

References

[2.1] R. Z. Valiev, A. V. Korznikov, R. R. Mulyukov. "Structure and properties of ultrafine-grained materials produced by severe plastic deformation." 1993, Materials Science and Engineering: A, Vol. 168(2), 141-148.

[2.2] R. Z. Valiev, I. V. Alexandrov. "Nanostructured materials from severe plastic deformation." 1999, Nanostructured materials, Vol. 12(1-4), 35-40.

[2.3] R. Z. Valiev, Ruslan. "Nanostructuring of metals by severe plastic deformation for advanced properties." 2004, Nature materials, Vol. 3(8), 511-516.

[2.4] R. Z. Valiev, T. G. Langdon. "Principles of equal-channel angular pressing as a processing tool for grain refinement." 2006, Progress in materials science, Vol. 51(7), 881-981.

[2.5] A. P. Zhilyaev, T. G. Langdon. "Using high-pressure torsion for metal processing: fundamentals and applications." 2008, Progress in Materials Science, Vol. 53(6), 893-979.

[2.6] A. K Padap, G. P. Chaudhari, S. K. Nath, V. Pancholi. "Ultrafine-grained steel fabricated using warm multiaxial forging: Microstructure and mechanical properties." 2009, Materials Science and Engineering: A, Vol. 527(1), 110-117.

[2.7] Y. Saito, H. Utsunomiya, N. Tsuji, T. Sakai. "Novel ultra-high straining process for bulk materials—development of the accumulative roll-bonding (ARB) process." 1999, Acta materialia, Vol. 47(2), 579-583.

[2.8] J. C. Lee, H. K. Seok, J. H. Han, Y. H. Chung. "Controlling the textures of the metal strips via the continuous confined strip shearing (C2S2) process." 2001, Materials research bulletin, Vol. 36(5), 997-1004.

[2.9] Y. Beygelzimer, V. Varyukhin, S. Synkov, D. OrloV. "Useful properties of twist extrusion." 2009, Materials Science and Engineering: A, Vol. 503(1), 14-17.

[2.10] D. H. Shin, J. J. Park, Y. S. Kim, K. T. Park. "Constrained groove pressing and its application to grain refinement of aluminum." 2002, materials Science and Engineering: A, Vol. 328(1), 98-103.

[2.11] S. Zherebtsov, E. Kudryavtsev, S. Kostjuchenko, S. Malysheva, G. Salishchev. Strength and ductility-related properties of ultrafine grained two-phase titanium alloy produced by warm multiaxial forging." 2012, Materials Science and Engineering: A, Vol. 5, 155-163

[2.12] B. J. Han, Z. Xu. "Grain refinement mechanism of Fe–32Ni alloys during multiaxial forging." 2006, Materials Science and Technology, Vol. 22(11), 1359-1363.

[2.13] J. Huang, Z. Xu. "Evolution mechanism of grain refinement based on dynamic recrystallization in multiaxially forged austenite." 2006, Materials Letters, Vol. 60(15), 1854-1858.

[2.14] R. Kapoor, A. Sarkar, R. Yogi, S. K Shekhawat, I. Samajdar, J. K. Chakravartty. "Softening of Al during multi-axial forging in a channel die." 2013, Materials Science and Engineering: A, Vol. 560, 404-412.

[2.15] W. Guo, Q. Wang, B. Ye, H Zhou. "Microstructure and mechanical properties of AZ31 magnesium alloy processed by cyclic closed-die forging." 2013, Journal of Alloys and Compounds,Vol. 558, 164-171.

[2.16] B. Ravisankar. "Equal-Channel Angular Pressing (ECAP)." 2015, Handbook of Mechanical Nanostructuring, 277-297.

[2.17] M. Furukawa, Z. Horita, M. Nemoto, T. G. Langdon. "Review: processing of metals by equal-channel angular pressing." 2001, Journal of materials science, Vol. 36(12), 2835-2843.

[2.18] Z. Horita, T. Fujinami, M. Nemoto, T. G. Langdon. "Improvement of mechanical properties for Al alloys using equal-channel angular pressing." 2001, Journal of Materials Processing Technology, Vol. 117(3), 288-292.

[2.19] K. Aoki, A. Azushima. "Development and properties of high strengthened carbon steels produced by repetitive side extrusion and heat treatment process." 2007, In Materials science forum. Trans Tech Publications. Vol. 539, 2884-2891

[2.20] A. Azushima, K. Aoki. "Mechanical properties of ultrafine grained steel produced by repetitive cold side extrusion." 2002, CIRP Annals-Manufacturing Technology,Vol. 51(1), 227-230.

[2.21] J. C. Kim, Y. Nishida, H. Arima, T. Ando. "Microstructure of Al–Si–Mg alloy processed by rotary-die equal channel angular pressing." 2003, Materials Letters,Vol. 57(11), 1689-1695.

[2.22] A. Ma, Y. Nishida, K. Suzuki, I. Shigematsu, N. Saito. "Characteristics of plastic deformation by rotary-die equal-channel angular pressing." 2005, Scripta Materialia, Vol. 52(6), 433-437.

[2.23] G. I. Raab. "Plastic flow at equal channel angular processing in parallel channels." 2005, Materials Science and Engineering: A, Vol. 410, 230-233.

[2.24] F. Djavanroodi, M. Ebrahimi. "Effect of die parameters and material properties in ECAP with parallel channels." 2010, Materials Science and Engineering: A, Vol. 527(29), 7593-7599.

[2.25] K. Michibayashi, T. Masuda. "Shearing during progressive retrogression in granitoids: abrupt grain size reduction of quartz at the plastic-brittle transition for feldspar." 1993, Journal of structural geology, Vol. 15(12), 1421-1432.

[2.26] G. J. Raab, R. Z. Valiev, T. C. Lowe, Y. T. Zhu. "Continuous processing of ultrafine grained Al by ECAP–Conform." 2004, Materials Science and Engineering: A, Vol. 382(1), 30-34.

[2.27] C. Xu, S. Schroeder, P. B. Berbon, T. G. Langdon. "Principles of ECAP–Conform as a continuous process for achieving grain refinement: Application to an aluminum alloy." 2010, Acta Materialia, Vol. 58(4), 1379-1386.

[2.28] D. V. Gunderov, A. V. Polyakov, I. P. Semenova, G. I. Raab, A. A. Churakova, E. I. Gimaltdinova, N. A. Enikeev. "Evolution of microstructure, macrotexture and

mechanical properties of commercially pure Ti during ECAP-conform processing ." 2013.

[2.29] L. Olejnik, A. Rosochowski, M. W. Richert. "Incremental ECAP of plates." 2008, In Materials Science Forum. Trans Tech Publications, Vol. 584, 108-113.

[2.30] A. Rosochowski, L. Olejnik. "Incremental equal channel angular pressing for grain refinement." 2011, In Materials Science Forum. Trans Tech Publications, Vol. 674, 19-28.

[2.31] J. C. Lee, H. K. Seok, J. H. Han, Y. H. Chung. "Controlling the textures of the metal strips via the continuous confined strip shearing (C2S2) process." 2001, Materials research bulletin, Vol. 36(5), 997-1004.

[2.32] Y. H. Jin, M. Y. Huh, Y. H. Chung. "Evolution of textures and microstructures in IF-steel sheets during continuous confined strip shearing and subsequent recrystallization annealing." 2004, Journal of materials science,Vol. 39(16-17), 5311-5314.

[2.33] S. Xu, G. Zhao, X. Ren, Y. Guan. "Numerical investigation of aluminum deformation behavior in three-dimensional continuous confined strip shearing process." 2008, Materials Science and Engineering: A,Vol. 476(1), 281-289.

[2.34] J. Blanz, A. Harvey, M. Menzin, S. Rhee. U.S. Patent No. 3,758,657. Washington, DC: U.S. Patent and Trademark Office, 1973.

[2.35] A. P. Zhilyaev, T. G. Langdon. "Using high-pressure torsion for metal processing: fundamentals and applications." 2008, Progress in Materials Science, Vol. 53(6), 893-979.

[2.36] A. P. Zhilyaev, G. V. Nurislamova, B. K. Kim, M. D. Baró, J. A. Szpunar, T. G. Langdon. "Experimental parameters influencing grain refinement and microstructural evolution during high-pressure torsion." 2003, Acta Materialia, Vol. 51(3), 753-765.

[2.37] G. Sakai, Z. Horita, T. G. Langdon. "Grain refinement and superplasticity in an aluminum alloy processed by high-pressure torsion." 2005, Materials Science and Engineering: A, Vol. 393(1), 344-351.

[2.38] K. Edalati, Z. Horita. "Continuous high-pressure torsion." 2010, Journal of materials science, Vol. 45(17), 4578-4582.

[2.39] H. Y. Um, E. Y.Yoon, D. J. Lee, C. S. Lee, L. J. Park, S. Lee, H. S. Ki. "Hollow cone high-pressure torsion: Microstructure and tensile strength by unique severe plastic deformation." 2014, Scripta Materialia,Vol. 71, 41-44.

[2.40]   Y. Beygelzimer, V. Varyukhin, S. Synkov, D. Orlov. "Useful properties of twist extrusion." 2009, Materials Science and Engineering: A, Vol. 503(1), 14-17.

[2.41]   V. Varyukhin, Y. Beygelzimer, S. Synkov, D. Orlov. "Application of twist extrusion." 2006, In Materials Science Forum. Trans Tech Publications. Vol. 503, 335-340.

[2.42]   D. Orlov, Y. Beygelzimer, S. Synkov, V. Varyukhin, N. Tsuji, Z. Horita. "Plastic flow, structure and mechanical properties in pure Al deformed by twist extrusion." 2009, Materials Science and Engineering: A, Vol. 519(1), 105-111.

[2.43]   N. B. Tork, N. Pardis, R. Ebrahimi. "Investigation on the feasibility of room temperature plastic deformation of pure magnesium by simple shear extrusion process." 2013, Materials Science and Engineering: A, Vol. 560, 34-39.

[2.44]   A. Zangiabadi, M. Kazeminezhad. "Development of a novel severe plastic deformation method for tubular materials: Tube Channel Pressing (TCP)." 2011, Materials Science and Engineering: A,Vol. 528(15), 5066-5072.

[2.45]   N. Tsuji, Y. Saito, S. H. Lee, Y. Minamino. "ARB (Accumulative Roll-Bonding) and other new techniques to produce bulk ultrafine grained materials." 2003, Advanced Engineering Materials, Vol. 5(5), 338-344.

[2.46]   X. Huang, N. Tsuji, N. Hansen, Y. Minamino. "Microstructural evolution during accumulative roll-bonding of commercial purity aluminum." 2003, Materials Science and Engineering: A, Vol. 340(1), 265-271.

[2.47]   H. W. Höppel, J. May, M. Göken. "Enhanced Strength and Ductility in Ultrafine-Grained Aluminium Produced by Accumulative Roll Bonding." 2004, Advanced Engineering Materials,Vol. 6(9), 781-784.

[2.48]   Q. Cui, K. Ohori. "Grain refinement of high purity aluminium by asymmetric rolling." 2000, Materials Science and Technology,Vol. 16(10), 1095-1101.

[2.49]   J. Jiang, Y. Ding, F. Zuo, A. Shan. "Mechanical properties and microstructures of ultrafine-grained pure aluminum by asymmetric rolling." 2009, Scripta Materialia,Vol. 60(10), 905-908.

[2.50]   S. K. Panigrahi, R. Jayaganthan, V. Chawla. "Effect of cryorolling on microstructure of Al–Mg–Si alloy." 2008, Materials Letters,Vol. 62(17), 2626-2629.

[2.51]   S. V. Zherebtsov, G. S. Dyakonov, A. A. Salem, V. I. Sokolenko, G. A. Salishchev, S. L. Semiatin. "Formation of nanostructures in commercial-purity titanium via cryorolling." 2013, Acta Materialia,Vol. 61(4), 1167-1178.

[2.52] A. Yamamoto, Y. Tsukahara, S. Fukumoto. "Textures in AZ31 magnesium alloy induced by repeated cross wavy rolling." 2007, In Materials Science Forum. Trans Tech Publications. Vol. 561, 2341-2344.

[2.53] K. C. Sekhar, B. P. Kashyap, S. Sangal. "AFM characterization of structural evolution and roughness of AISI 304 austenitic stainless steel under severe deformation by wavy rolling." 2013, In Advanced Materials Research . Trans T. Vol. 794, 230-237.

[2.54] J. Y. Huang, Y. T. Zhu, H. Jiang, T. C. Lowe. "Microstructures and dislocation configurations in nanostructured Cu processed by repetitive corrugation and straightening." 2001, Acta Materialia, Vol. 49(9), 1497-1505.

[2.55] Y. T. Zhu, T. C. Lowe, H. Jiang, J. Huang. U.S. Patent No. 6,197,129. Washington, DC: U.S. Patent and Trademark Office. 2001.

[2.56] J. Y. Huang, Y. T. Zhu, H. Jiang, T. C. Lowe. "Microstructures and dislocation configurations in nanostructured Cu processed by repetitive corrugation and straightening." 2001, Acta Materialia, Vol. 49(9), 1497-1505.

[2.57] S. C. Pandey, M. A. Joseph, M. S. Pradeep, K. Raghavendra, V. R. Ranganath, K. Venkateswarlu, v Langdon. A theoretical and experimental evaluation of repetitive corrugation and straightening: application to Al–Cu and Al–Cu–Sc alloys. M. 2012.

[2.58] C. Kobayashi, T. Sakai, A. Belyakov, H. Miura. "Ultrafine grain development in copper during multidirectional forging at 195 K." 2007, Philosophical magazine letters,Vol. 87(10), 751-766.

[2.59] P. N. Rao, D. Singh, R. Jayaganthan. "Mechanical properties and microstructural evolution of Al 6061 alloy processed by multidirectional forging at liquid nitrogen temperature." 2014, Materials & Design,Vol. 56, 97-104.

[2.60] X. Y. Yang, Z. Y. Sun, X. I. N. G. Jie, H. MIURA, T. SAKAI. "Grain size and texture changes of magnesium alloy AZ31 during multi-directional forging." 2008, Transactions of Nonferrous Metals Society of China,Vol. 18, s200-s204.

[2.61] H. Miura, G. Yu, X. Yang, T. Sakai. "Microstructure and mechanical properties of AZ61 Mg alloy prepared by multi directional forging." 2010, Transactions of Nonferrous Metals Society of China, Vol. 20(7), 1294-1298.

[2.62] L. Tang, C. Liu, Z. Chen, D. Ji, H. Xiao. "Microstructures and tensile properties of Mg–Gd–Y–Zr alloy during multidirectional forging at 773K." 2013, Materials & Design,Vol. 50, 587-596.

[2.63]   B. Han, Z. Xu. "Grain refinement under multi-axial forging in Fe–32% Ni alloy." 2008, Journal of Alloys and Compounds,Vol. 457(1), 279-285.

[2.64]   A. K. Padap, G. P. Chaudhari, V. Pancholi, S. K. Nath. "Warm multiaxial forging of AISI 1016 steel." 2010, Materials & Design, 31(8), 3816-3824.

[2.65]   M. Noda, M. Hirohashi, K. Funami. "Low temperature superplasticity and its deformation mechanism in grain refinement of Al-Mg alloy by multi-axial alternative forging." 2003, Materials Transactions, Vol. 44(11), 2288-2297.

[2.66]   S. Zherebtsov, E. Kudryavtsev, S. Kostjuchenko, S. Malysheva, G. Salishchev. "Strength and ductility-related properties of ultrafine grained two-phase titanium alloy produced by warm multiaxial forging." 2012, Materials Science and Engineering: A,Vol. 5.

[2.67]   A. Rezaee-Bazzaz, S. Ahmadian. "Modeling of mechanical behavior of ultra fine grained aluminum produced by multiple compressions in a channel die." 2012, Materials & Design, Vol. 34, 230-234.

[2.68]   A. K. Padap, G. P. Chaudhari, V. Pancholi, S. K. Nath. "Microstructural evolution and mechanical behavior of warm multi-axially forged HSLA steel." 2012, Journal of Materials Science, Vol. 47(22), 7894-7900.

[2.69]   S. K. Panigrahi, R. Jayaganthan. "Development of ultrafine grained high strength age hardenable Al 7075 alloy by cryorolling." 2011, Materials & Design, Vol. 32(6), 3150-3160.

[2.70]   N. Rangaraju, T. Raghuram, B. V. Krishna, K. P. Rao, P. Venugopal. "Effect of cryo-rolling and annealing on microstructure and properties of commercially pure aluminium." 2005, Materials Science and Engineering: A, Vol. 398(1), 246-251.

[2.71]   V. M. Segal. "Equal channel angular extrusion: from macromechanics to structure formation." 1999, Materials Science and Engineering: A, Vol. 271(1), 322-333.

[2.72]   Y. Iwahashi, Z. Horita, M. Nemoto, T. G. Langdon. "The process of grain refinement in equal-channel angular pressing." 1998, Acta materialia, 1998, Vol. 46(9), 3317-3331.

[2.73]   M. Furukawa, Z. Horita, M. Nemoto, T. G. Langdon. "Review: processing of metals by equal-channel angular pressing." 2001, Journal of materials science, Vol. 36(12), 2835-2843.

[2.74] Y. Iwahashi, Zenji Horita, Minoru Nemoto, Terence G. Langdon. "An investigation of microstructural evolution during equal-channel angular pressing." 1997, Acta materialia, Vol. 45(11), 4733-4741.

[2.75] R. Z. Valiev, T. G. Langdon. "Principles of equal-channel angular pressing as a processing tool for grain refinement." 2006, Progress in materials science, Vol. 51(7), 881-981.

[2.76] Y. Saito, H. Utsunomiya, N. Tsuji, T. Sakai. "Novel ultra-high straining process for bulk materials—development of the accumulative roll-bonding (ARB) process." 1999, Acta materialia, Vol. 47(2), 579-583.

[2.77] X. Huang, N. Tsuji, N. Hansen, Y. Minamino. "Microstructural evolution during accumulative roll-bonding of commercial purity aluminum." 2003, Materials Science and Engineering: A, Vol. 340(1), 265-271.

[2.78] S. H. Lee, Y. Saito, T. Sakai, H. Utsunomiya. "Microstructures and mechanical properties of 6061 aluminum alloy processed by accumulative roll-bonding." 2002, Materials Science and Engineering: A, Vol. 325(1), 228-235.

[2.79] M. T. Pérez-Prado, O. A. Ruano. "Grain refinement of Mg–Al–Zn alloys via accumulative roll bonding." 2004, Scripta materialia,Vol. 51(11), 1093-1097.

[2.80] W. J. Kim, J. B. Lee, W. Y. Kim, H. T. Jeong, H. G. Jeong. "Microstructure and mechanical properties of Mg–Al–Zn alloy sheets severely deformed by asymmetrical rolling." 2007, Scripta Materialia, Vol. 56(4), 309-312.

[2.81] H. Jin, D. J. Lloyd. "Evolution of texture in AA6111 aluminum alloy after asymmetric rolling with various velocity ratios between top and bottom rolls." 2007, Materials Science and Engineering: A, Vol. 465(1), 267-273.

[2.82] Q. Cui, K. Ohori. "Grain refinement of high purity aluminium by asymmetric rolling." 2000, Materials Science and Technology, Vol. 16(10), 1095-1101.

[2.83] J. Jiang, Y. Ding, F. Zuo, A. Shan. "Mechanical properties and microstructures of ultrafine-grained pure aluminum by asymmetric rolling." 2009, Scripta Materialia, Vol. 60(10), 905-908.

[2.84] M. Richert, Q. Liu, N. Hansen. "Microstructural evolution over a large strain range in aluminium deformed by cyclic-extrusion–compression." 1999, Materials Science and Engineering: A, Vol. 260(1), 275-283.

[2.85] J. Y. Huang, Y. T. Zhu, H. Jiang, T. C. Lowe. "Microstructures and dislocation configurations in nanostructured Cu processed by repetitive corrugation and straightening." 2001, Acta Materialia, Vol. 49(9), 1497-1505.

[2.86] G. E. Dieter, D. J. Bacon. 1986,Mechanical metallurgy, Vol. 3. New York: McG.

[2.87] N. Hansen. "Hall–Petch relation and boundary strengthening." Scripta Materialia, Vol. 51(8), 801-806.

[2.88] J. R. Weertman. "Hall-Petch strengthening in nanocrystalline metals." 1993, Materials Science and Engineering: A, Vol. 166(1-2), 161-167.

[2.89] ASM Hanbook Volume. 2: Properties and Selection: Nonferrous Alloys and Special-Purpose Materials. ASM international, 889-896.

[2.90] G. E. Dieter, (2005). Mechanical metallurgy, 1988, SI metric edition.

[2.91] A. J. Ardell. Precipitation hardening. 1985, Metallurgical Transactions A, Vol. 16(12), 2131-2165.

[2.92] Y. M. Wang, E. Ma. "Three strategies to achieve uniform tensile deformation in a nanostructured metal." 2004, Acta Materialia, Vol. 52(6), 1699-1709.

[2.93] S. K. Panigrahi, R. Jayaganthan. "A study on the combined treatment of cryorolling, short-annealing, and aging for the development of ultrafine-grained Al 6063 alloy with enhanced strength and ductility." 2010, Metallurgical and Materials Transactions .

[2.94] Y. H. Zhao, X. Z. Liao, Z. Jin, R. Z. Valiev, Y. T. Zhu. "Microstructures and mechanical properties of ultrafine grained 7075 Al alloy processed by ECAP and their evolutions during annealing." 2004, Acta Materialia, Vol. 52(15), 4589-4599.

[2.95] T. Hu, K. Ma, T. D. Topping, B. Saller A. Yousefiani, J. M. Schoenung, E. J. Lavernia. "Improving the tensile ductility and uniform elongation of high-strength ultrafine-grained Al alloys by lowering the grain boundary misorientation angle." 2014.

[2.96] D. Canadinc, E. Biyikli, T. Niendorf, H. J. Maier. "Experimental and numerical investigation of the role of grain boundary misorientation angle on the dislocation–grain boundary interactions." 2011, Advanced Engineering Materials, Vol. 13(4), 281-287.

[2.97] A. Rollett, F. J. Humphreys, G. S. Rohrer, M. Hatherly. "Recrystallization and related annealing phenomena. Elsevier." 2004.

[2.98] H. Gao, Y. Huang. "Geometrically necessary dislocation and size-dependent plasticity." 2003, Scripta Materialia, Vol. 48(2), 113-118.

[2.99]   J. Wang, M. Furukawa, Z.Horita, M. Nemoto, R. Z. Valiev, T. G. Langdon. "Enhanced grain growth in an Al-Mg alloy with ultrafine grain size." 1996, Materials Science and Engineering: A, Vol. 216(1-2), 41-46.

[2.100] A. Loucif, R. B. Figueiredo, T. Baudin, F. Brisset, R. Chemam, T. G. Langdon. "Ultrafine grains and the Hall–Petch relationship in an Al–Mg–Si alloy processed by high-pressure torsion." 2012, Materials Science and Engineering: A, 532, 139-145.

[2.101] M. Furukawa, Z. Horita, M. Nemoto, R. Z. Valiev, T. G. Langdon. "Microhardness measurements and the Hall-Petch relationship in an Al瑕 Mg alloy with submicrometer grain size." 1996, Acta Materialia, Vol. 44(11), 4619-4629.

[2.102] M. Geetha, A. K. Singh, R. Asokamani, A. K. Gogia. "Ti based biomaterials, the ultimate choice for orthopaedic implants–a review." 2009, Progress in materials science, Vol. 54(3), 397-425.

[2.103] M. Niinomi, M. Nakai, J. Hieda. Development of new metallic alloys for biomedical.

[2.104] Y. Estrin, M. Janecek, G. I. Raab, R. Z. Valiev, A. Zi. "Severe plastic deformation as a means of producing ultra-fine-grained net-shaped micro electro-mechanical systems parts." 2007, Metallurgical and Materials Transactions A, Vol. 38(9), 1906-1909.

[2.105] http://www.britannica.com/EBchecked/topic/369081/materials.

[2.106] Y. Estrin, A. Vinogradov. "Extreme grain refinement by severe plastic deformation: a wealth of challenging science." 2013, Acta materialia, Vol. 61(3), 782-817.

[2.107] A. Vinogradov, T. Mimaki, S. Hashimoto, R. Valiev. "On the corrosion behaviour of ultra-fine grain copper." 1999, Scripta Materialia, Vol. 41(3), 319-326.

[2.108] H. Wang, Y. Estrin, Z. Zúberová. "Bio-corrosion of a magnesium alloy with different processing histories." 2008, Materials Letters,Vol. 62(16), 2476-2479.

[2.109] B. R. Sunil, T. S. Kumar, U. Chakkingal, V. Nandakumar, M. Doble. "Friction stir processing of magnesium–nanohydroxyapatite composites with controlled in vitro degradation behavior." 2014, Materials Science and Engineering: C,Vol. 39, 315-324.

[2.110] R. Z. Valiev, I. P. Semenova, V. V. Latysh, A. V. Shcherbakov, E. B. Yakushina. "Nanostructured titanium for biomedical applications: New developments and challenges for commercialization." 2008, Nanotechnologies in Russia, 3(9), 593-601.

[2.111] Y. Estrin, C. Kasper, S. Diederichs, R. Lapovok. "Accelerated growth of preosteoblastic cells on ultrafine grained titanium." 2009, Journal of biomedical materials research Part A, Vol. 90(4), 1239-1242.

[2.112] H. Wang, Y. Estrin, H. Fu, G. Song, Z. Zuberova. "The effect of pre-processing and grain structure on the bio-corrosion and fatigue resistance of magnesium alloy AZ31." 2007, Advanced Engineering Materials,Vol. 9(11), 967.

[2.113] S. K. Panigrahi, R. Jayaganthan. "Development of ultrafine-grained Al 6063 alloy by cryorolling with the optimized initial heat treatment conditions." 2011, Materials & Design, Vol. 32(4), 2172-2180.

[2.114] N. N. Krishna, R. Tejas, K. Sivaprasad, K. Venkateswarlu. "Study on cryorolled Al–Cu alloy using X-ray diffraction line profile analysis and evaluation of strengthening mechanisms." 2013, Materials & Design, 52, 785-790.

[2.115] A. Chatterjee, G. Sharma, A. Sarkar, J. B. Singh, J. K. Chakravartty. "A study on cryogenic temperature ECAP on the microstructure and mechanical properties of Al–Mg alloy." 2012, Materials Science and Engineering: A,Vol. 556, 653-657.

[2.116] P. N. Rao, S. K. Panigrahi, R. Jayaganthan. "Effect of annealing and aging treatment on mechanical properties of ultrafine grained Al 6061 alloy." 2010, Materials Science and Technology, Vol. 26(3), 371-374.

[2.117] N. Kumar, P. N. Rao, R. Jayaganthan, H. G. Brokmeier. "Effect of cryorolling and annealing on recovery, recrystallisation, grain growth and their influence on mechanical and corrosion behaviour of 6082 Al alloy." 2015, Materials Chemistry and Physics.

[2.118] I. F. Mohamed, Y. Yonenaga, S. Lee, K. Edalati, Z. Horita. "Age hardening and thermal stability of Al–Cu alloy processed by high-pressure torsion. Materials Science and Engineering: A, Vol. 627, 111-118.

[2.119] I. Mazurina, T. Sakai, H. Miura, O. Sitdikov, R. Kaibyshev. "Effect of deformation temperature on microstructure evolution in aluminum alloy 2219 during hot ECAP." 2008, Materials Science and Engineering: A, Vol. 486(1), 662-671.

[2.120] T. Shanmugasundaram, B. S. Murty, V. S. Sarma. "Development of ultrafine grained high strength Al–Cu alloy by cryorolling." 2006, Scripta materialia, Vol. 54(12), 2013-2017.

[2.121] M. H. Goodarzy, H. Arabi, M. A. Boutorabi, S. H. Seyedein, S. H. Najafabadi. "The effects of room temperature ECAP and subsequent aging on mechanical properties of 2024 Al alloy." 2014, Journal of Alloys and Compounds,Vol. 585, 753-759.

[2.122] P. Venkatachalam, S. R. Kumar, B. Ravisankar, V. T. Paul, M. Vijayalakshmi. "Effect of processing routes on microstructure and mechanical properties of 2014 Al alloy processed by equal channel angular pressing." Transactions of Nonferrous Meta.

[2.123] P. N. Rao, D. Singh, R. Jayaganthan. "Mechanical properties and microstructural evolution of Al 6061 alloy processed by multidirectional forging at liquid nitrogen temperature." 2014, Materials & Design, 56, 97-104.

[2.124] O. Sitdikov, T. Sakai, A. Goloborodko, H. Miura, R. Kaibyshev. "Effect of pass strain on grain refinement in 7475 Al alloy during hot multidirectional forging." 2004, Materials transactions, Vol. 45(7), 2232-2238.

[2.125] B. Cherukuri, T. S. Nedkova, R. Srinivasan. "A comparison of the properties of SPD-processed AA-6061 by equal-channel angular pressing, multi-axial compressions/forgings and accumulative roll bonding." 2005, Materials Science and Engineering: A, Vol. 410, .

[2.126] W. J. Kim, C. S. Chung, D. S. Ma, S. I. Hong, H. K. Kim. "Optimization of strength and ductility of 2024 Al by equal channel angular pressing (ECAP) and post-ECAP aging." 2003, Scripta Materialia, Vol. 49(4), 333-338.

[2.127] Y. W. Ma, J. W. Choi, K. B. Yoon. "Change of anisotropic tensile strength due to amount of severe plastic deformation in aluminum 2024 alloy." 2011, Materials Science and Engineering: A, Vol. 529, 1-8.

[2.128] A. Alhamidi, Z. Horita. "Grain refinement and high strain rate superplasticity in alumunium 2024 alloy processed by high-pressure torsion." 2015, Materials Science and Engineering: A, Vol. 622, 139-145.

[2.129] D. R. Fang, Z. F. Zhang, S. D. Wu, C. X. Huang, H. Zhang, N. Q. Zhao, J. J. Li. "Effect of equal channel angular pressing on tensile properties and fracture modes of casting Al–Cu alloys." 2006, Materials Science and Engineering: A, Vol. 426(1), 305-31.

[2.130] C. Mallikarjuna, S. M. Shashidhara, U. S. Mallik. "Evaluation of grain refinement and variation in mechanical properties of equal-channel angular pressed 2014 aluminum alloy." 2009, Materials & Design, Vol. 30(5), 1638-1642.

[2.131] W. C. Liu, M. B. Chen, H. Yuan. "Evolution of microstructures in severely deformed AA 3104 aluminum alloy by multiple constrained compression." 2011, Materials Science and Engineering: A, Vol. 528(16), 5405-5410.

[2.132] P. S. Pao, H. N. Jones, S. F. Cheng, C. R. Feng. "Fatigue crack propagation in ultrafine grained Al–Mg alloy." 2005, International journal of fatigue, 27(10), 1164-1169.

[2.133] C. S. Chung, J. K. Kim, H. K. Kim, W. J. Kim. "Improvement of high-cycle fatigue life in a 6061 Al alloy produced by equal channel angular pressing." 2002, Materials Science and Engineering: A, Vol. 337(1), 39-44.

[2.134] M. Hockauf, L. W. Meyer, T. Halle, C. Kuprin, M. Hietschold, S. Schulze, L. Krüger. "Mechanical properties and microstructural changes of ultrafine-grained AA6063T6 during high-cycle fatigue." 2006, Zeitschrift für Metallkunde, Vol. 97(10), 1392-1400.

[2.135] Nikhil Kumar, Sunkulp Goel, R. Jayaganthan, Heinz-Günter Brokmeier. "Effect of Grain boundary misorientaton, Deformation Temperature and AlFeMnSi-phase on Fatigue Life of 6082 Al alloy." 2017, Materials Characterization.

[2.136] L. W. Meyer, K. Sommer, T. Halle, M. Hockauf. "Crack growth in ultrafine-grained AA6063 produced by equal-channel angular pressing." 2008, Journal of Materials Science, Vol. 43(23-24), 7426-7431.

[2.137] S. Malekjani, P. D. Hodgson, P. Cizek, T. B. Hilditch. "Strain rate effect on the cyclic deformation response of UFG Al alloys." 2012, Materials Science and Engineering: A, Vol. 548, 69-74.

EXPERIMENTAL PROCEDURE

3.1   Introduction

The experimental studies were made to investigate the effect of rolling and multiaxial forging at cryogenic temperatures on the microstructural and mechanical behaviour of Al 2014 alloy. Hardness measurements and tensile tests were carried out at room temperature for all processed conditions of the samples. The tensile samples were prepared for tensile testing of forged and rolled samples. The microstructures of the deformed samples were characterized through Optical microscopy (OM), Scanning electron microscopy (SEM)/EBSD and Transmission electron microscopy (TEM). XRD was used to identify the different phases evolved during annealing treatment.

3.2   Materials

Material used in the present study was Al 2014 alloy in T6 tempered condition, which was received from Bharat Aerospace Metals, Mumbai, India, in the rectangular plate having a cross section of 200 x 200 mm^2 and a thickness of 40 mm. The chemical composition of the Al 2014 alloy is provided in Table 3.1. The mechanical properties of as received Al 2014 alloy are listed in Table 3.2. The samples with required dimensions for different processing were subjected to a solution treatment at 505°C for 2 hours followed by water quenching. An average grain size of the alloy was found to be 120 μm. The specimen dimensions employed for different thermo mechanical processing are defined below.

- ➢ Samples for forging at cryogenic temperature and room temperature were machined in prismatic shape of 33 x 30 x 27 mm^3 from the as received plate. They were subjected to cumulative strains/number of cycles such as 1.2, 1.8, and 2.4, which correspond to 2 cycles, 3 cycles, and 4 cycles, respectively.
- ➢ Samples for rolling at cryogenic temperature were machined in the form of sheets with dimension 40 x 30 x 10 mm^3. They were deformed up to various rolling reductions of 70%, and 90% corresponding to true strains of 1.2 and 2.3 respectively.

Table 3.1: Chemical Composition of Al 2014 alloy (Weight %)

Element	Cu	Si	Mg	Mn	Fe	Ti	Zn	Ni	Rest
Composition(%)	4.5	0.77	0.44	0.71	0.20	.05	.06	.009	Al

Table 3.2: Mechanical Properties of as received Al 2014 −T6 Alloy

Properties	Values
Hardness (HV)	135 HV
Ultimate Tensile Strength (UTS)	483 MPa
Yield Strength (YS)	414 MPa
% Elongation at break	13 %

3.3 Experimental Technique

3.3.1 Experimental Set up for Multiaxial Forging (MAF)

Samples in prismatic shape having 33 x 30 x 27 mm^3 dimension were machined from the as received plate and heat treated at 505°C for 2 hours followed by water quenching at room temperature. The specimens were then subjected to multiaxial forging (MAF) at 77 K using friction screw forging machine at an approximate strain rate of 10 s^{-1}.
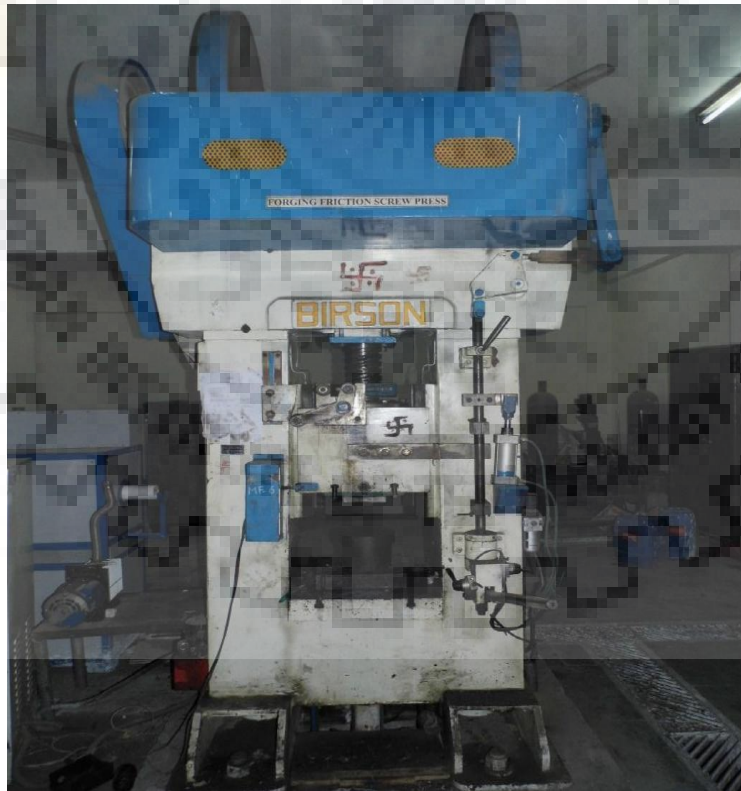
Figure 3.1: Friction screw forging machine used for Multiaxial forging

Figure 3.1 shows a schematic of friction screw forging machine used in the present work. The first forging axis was chosen parallel to the rolling direction of the as received sample following which the sample was rotated by 90° after every pass along the three axes (X, Y and Z). The sample dimension ratio of 1:1.11:1.22 was preserved constant throughout the process. MAF at cryogenic temperature was carried out by initially dipping the samples in liquid nitrogen for about 15 mins followed by soaking it for about $5 - 10$ mins after every pass in order to attain thermal equilibrium with liquid nitrogen. Figure 3.2 represents the schematic diagram of MAF for a single cycle. An axial compression of ε = - 0.20 per pass, which is calculated as equivalent true strain in one pass $(\Delta\varepsilon) = \ln\left(\frac{27}{33}\right) = -0.20$ and cumulative strain in one cycle $(\sum \Delta\varepsilon_{n=1}) = |\Delta\varepsilon_1 + \Delta\varepsilon_2 + \Delta\varepsilon_3| = -0.6$ (where 'n' is number of cycles) was applied. As MAF was successfully performed without cracking up to 4 cycles, therefore, 4 cycles were kept as the highest number of cycles in the present work. After MAF, samples for various characterizations were prepared by slicing along the plane perpendicular to the last forging axis.
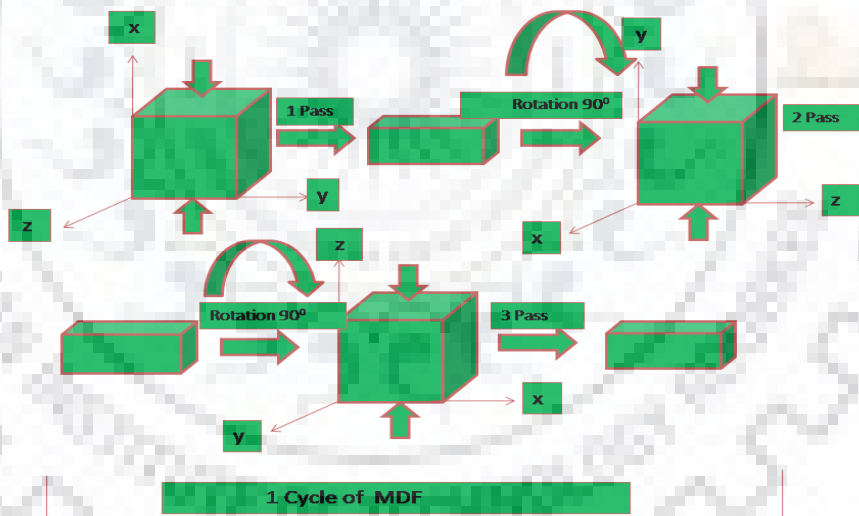
Figure 3.2: Schematic of Multiaxial forging for one cycle.

3.3.2 Experimental Set up for Rolling

Rolling at lower temperature is one of the probable procedures for producing ultrafine grains in the bulk metals and alloys as lower cold working temperatures play an active role in suppressing the dynamic recovery by accumulating a high concentration of dislocations, which then rearrange to develop ultrafine grained/nanostructures in the bulk alloys. A standard

laboratory two high rolling mill was used for rolling at cryogenic temperature (LNT) in the present work. The rolls having a diameter of 110 mm were operated at a speed of 8 rpm. Rolling was performed along rolling directions of the as received plate up to various reductions such as 70% and 90% corresponding to true strains of 1.2 and 2.3, respectively at LNT. Figure 3.3 represents the experimental set up which was used to perform rolling at LNT. The particulars of the apparatus and accessories used throughout rolling process are given below:

Figure 3.3: Experimental set up for rolling at room and cryogenic temperatures.
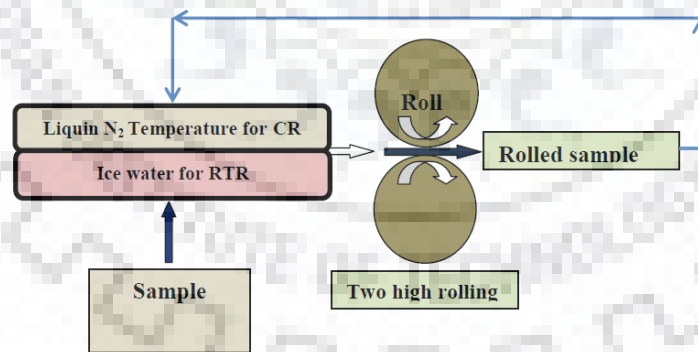
Figure 3.4: Schematic of Rolling performed at LNT and RT

The technique of rolling at LNT comprises:

➤ Samples were machined with desired dimensions of 40 x 30 x 10 mm^3 by sectioning along the plane parallel to the rolling direction. Figure 3.4 represents a complete

schematic of rolling which was performed along the rolling directions at LNT. Appropriate heat treatment was given before cryorolling.

➢ Samples were dipped in the liquid nitrogen cans for about 15 min initially in order to attain thermal equilibrium with liquid nitrogen prior to rolling. Following this, they were rolled and immediately dipped in liquid nitrogen for cryorolling after ever pass in order to retain the microstructure.

➢ The successive passes after the first rolling pass were given after an interval of 5- 10 min, and the final thickness reduction was achieved in several passes during rolling. A small reduction of 0.2 mm per pass was applied to avoid additional heat generation in the samples.

➢ True strains corresponding to various reductions after rolling were calculated using the formula given below.

$$e \; = \; \ln \frac{\text{Final thickness after rolling}}{\text{Initial thichness before rolling}} \tag{3.1}$$

3.4 Characterization Techniques

3.4.1 Optical Microscopy (OM)

OM was used to examine microstructures of the initial solution treated (ST) alloy and after forging and rolling the solution treated (ST) alloy to various cumulative strains. LEICA DMI5000 M with magnification lenses ranging from 5x to 100x and attached with a digital video camera connected to computer was used (Figure 3.5).
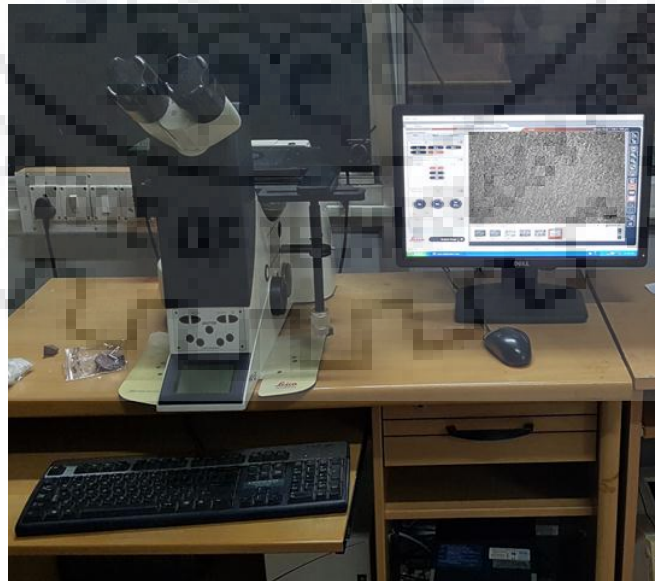
Figure 3.5: LEICA DMI5000 M- Optical microscopy used in the present work

For the preparation of samples, the selected part of the material was cut on diamond cutter. The sample was then mounted and grounded using SiC abrasive papers of different grit sizes, usually 320 to 2000 grit. Water was used to eliminate the embedding of abrasive particles in to soft aluminium alloys. These polished samples were then cloth polished using paste of magnesium oxide with water. The cloth polished samples were then dried and etched with 50 ml of Poulton's reagent mixed with 25 ml HNO3, 40 ml solution of 3 g chromic acid per 10 ml of water. After etching for 1 min, these samples were examined under Leica optical microscope under the polarized light.

3.4.2 Electron Back Scatter Diffraction (EBSD) Analysis

FEI Quanta scanning electron microscope (SEM) equipped with energy dispersive spectroscopy (EDS) and electron backscattered diffraction (EBSD) facility was used to examine the microstructural features evolved in the bulk alloy after deformation at room and cryogenic temperatures. EBSD characterization enables to investigate the misorientations development, type of grain boundary evolution, local texture, and phase recognition on the surfaces of polycrystalline metals. Further, this can be used to identify the activation of shear bands, different twinning and slip systems along with the mechanism of grain fragmentation in severely deformed specimens. Figure 3.6 shows the FE-SEM equipped with EBSD and Figure 3.7 shows a typical EBSD geometry.
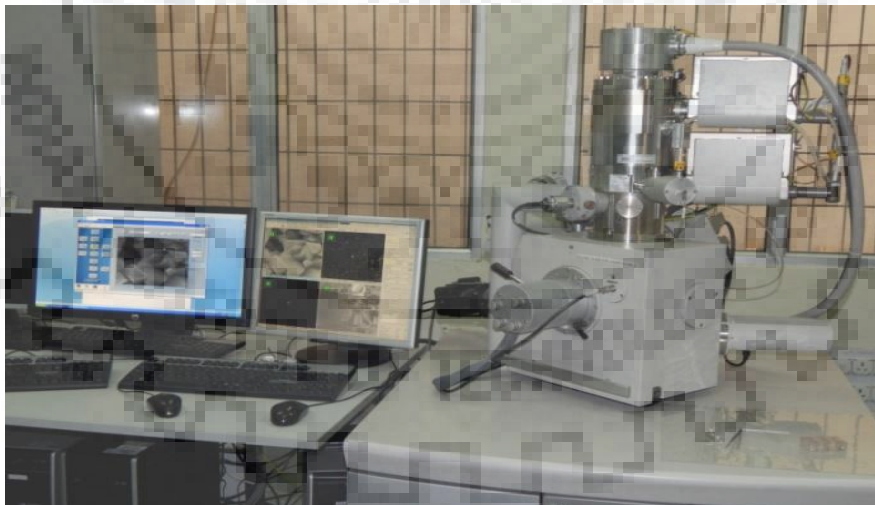
Figure 3.6: FEI Quanta 200 FEG-SEM

During EBSD measurements, the flat and mirror polished crystalline specimen is inclined at 70˚ to the horizontal and is placed in front of the EBSD detector furnished with the phosphor screen. The phosphor screen is attached to a compact lens for focusing the image onto the CCD camera which produces visible lines known as Kikuchi bands. The EBSD

pattern is examined by detecting the kikuchi pattern by applying Hough transform in SEM equipped with EBSD software. The obtained scans were further analyzed in the TSL OIM software package in order to determine overall microstructure characteristics such as misorientations distribution, grain size and in-grain misorientations. The region to be investigated in the deformed sample was cut by the help of diamond cutter. While cutting the samples, a continuous flow of cold water was ensured in order to avoid heat generation in the deformed samples which might cause changes in microstructures of the sectioned surface. The samples were then mechanically ground with emery papers having grit sizes ranging 320, 400, 600, 800, 1200, 1500 and 2000 followed by cloth polishing on a high-speed wheel using magnesium oxide suspension having mesh size as 0.024 micron along with water to obtain mirror polished surface.
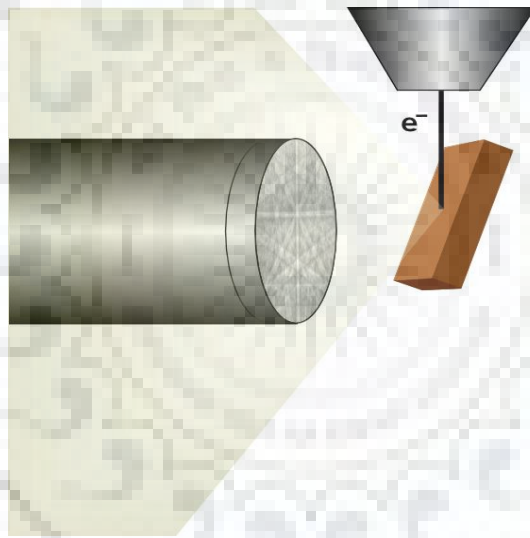
Figure 3.7: Schematic of the typical EBSD geometry

Finally, electropolishing was performed at a potential of 13 volts by making the sample as anode and stainless steel block as cathode in the circuit and maintaining a temperature of -30 °C of the electrolyte containing methanol and nitric acid in a ratio of 80:20 by volume. After 1 min of electropolishing, samples were instantly removed from the electrolyte and rinsed off with pure water followed by drying with a blower.

3.4.3 Scanning Electron Microscopy (SEM)

The fracture morphology of the Al 2014 alloy samples broken in tensile test, 3-point bend test, high cycle fatigue test, and fatigue crack growth rate test after cryorolling and cryoforging was analyzed in scanning electron microscopy (SEM).The broken samples were cleaned in ultrasonic bath before fracture studies in SEM in order to remove the contaminants from the fractured surface.

3.4.4 Transmission Electron Microscopy (TEM)

Transmission Electron Microscopy (TEM) is a technique which characterizes specimens up to very high magnification to atomic resolution transmitting a beam of electrons from thin specimens. The transmitted electrons after interacting with each other forms an image, which is focused and magnified on a fluorescent screen. TEM is widely used in various scientific fields such as physical, chemical and biological sciences due to their small De Broglie wavelength of electrons which offers them very high resolution. TEM is very useful in investigating chemical compositions, general microstructure evolution as a result of deformation, dislocation density, precipitates evolution, various defect configuration such as stacking faults, twin faults, shear bands etc. via X-ray, electron energy and diffraction pattern analysis. Therefore, the microstructural evolution that had occurred as a result of cryoforging and cryorolling and after annealing was investigated through a FEI Technai 20 TEM operated at 200 KV, which is shown in Figure 3.8(a). The different hardware components of TEM are shown in Figure 3.8(b).
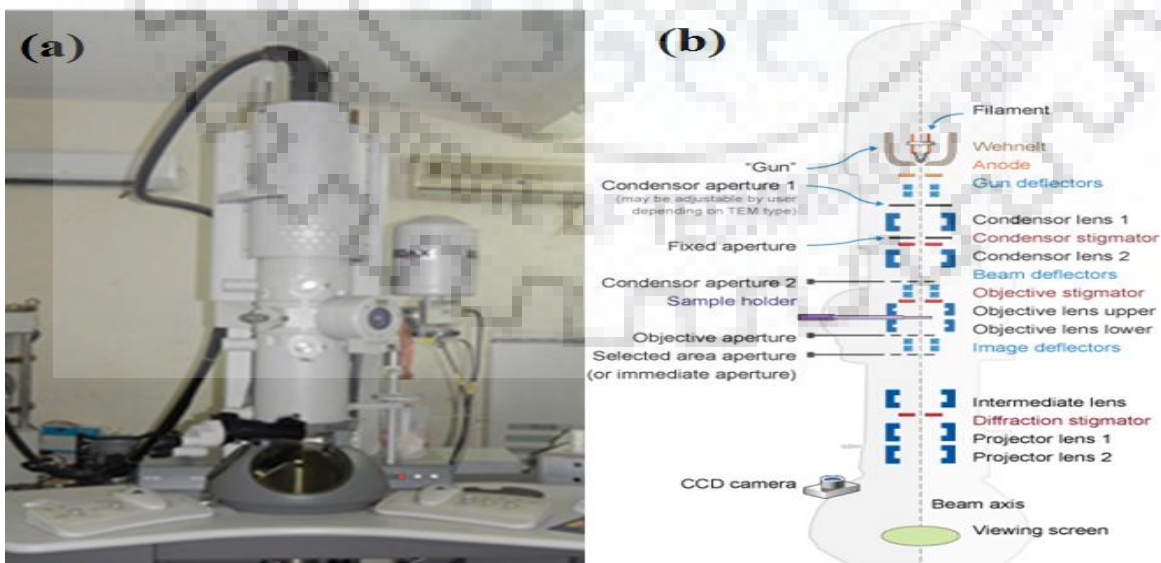
Figure 3.8: (a) Photograph of TEM Unit, **(b)** Schematic representation of TEM

The TEM samples were prepared by thinning and polishing the samples from both the sides using silicon carbide emery papers with grit sizes as 100, 220, 320, 400, 600, 800, 1200, 1500 and 2000 till thickness in the range between 80 μm to 100 μm was achieved. The thin foils of the samples were cleaned with acetone followed by punching into a disc of 3 mm diameter. The final polishing of the discs was performed via twin jet polishing in an electrolyte containing a mixture of methanol and nitric acid (75:25), maintained at a temperature of -40˚C and a potential of 20V. The electropolished samples were cleaned twice in methanol and dried.

3.4.5 X-ray Diffraction (XRD)

XRD is an analytical method used to determine the lattice parameter, crystallite size, microstrain, dislocation density, degree of crystallinity, phase identification and phase quantification of the material. XRD (Bruker AXS D8 Advance instrument) using Cu Kα radiation was used in the present work to identify the phases, to study the effect of cryoforging and cryorolling on peak broadening and peak shifting and to calculate the dislocation density of the deformed Al 2014 alloy. The XRD, Bruker AXS D8 Advance instrument is shown in Figure 3.9 (a).
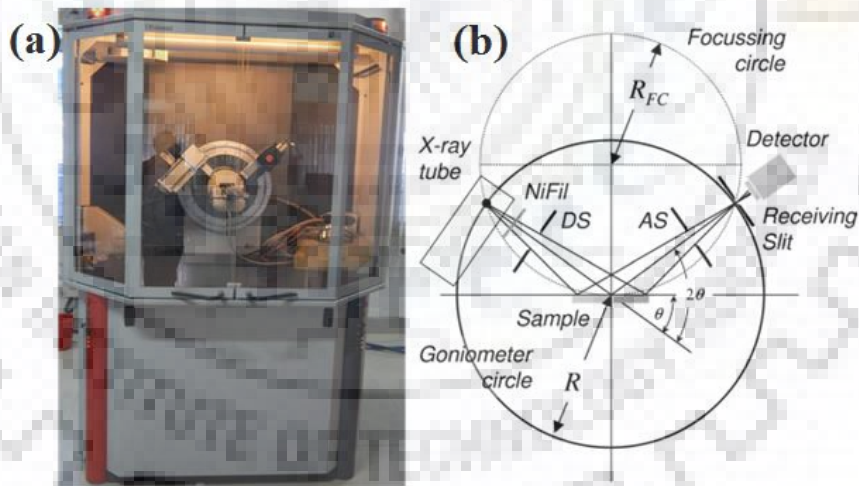
Figure 3.9: (a) XRD Unit θ/2θ (Bruker AXS D8 Advance diffractometer, **(b)** Representation of diffraction (θ/2θ) in Bragg–Brentano geometry

Figure 3.9 (b) shows the working principle of the XRD set up.The X-rays produced by the cathode ray tube are filtered, collimated and focused towards the sample which after satisfying the Bragg's Law ($n\lambda=2d \sin \theta$) during their interaction with the sample produces a constructive interference and a strong intensity of diffracted ray emerges. These diffracted X-rays are then

detected and processed by the detector. Samples are scanned through a range of 2θ angles to detect all possible directions of the lattices which undergoes diffraction. Further, PAN analytical X'Pert HighScore software was used for data analysis.

3.5   Mechanical Characterization

3.5.1   Vickers Hardness Test

Vickers hardness, FIE-Model: VM 50 PC was used for hardness measurements according to ASTM E384-11[ε1]. The hardness was measured on the plane perpendicular to the last forging axis in case of forged samples while it was measured on the rolling plane in case of rolled samples. The samples for hardness were mechanically ground with emery papers up to 1200 grit size followed by cloth polishing to make the surface scratch free. Hardness for various deformed conditions were measured by applying a load of 5 Kgf for a dwell time of 15 secs. A total of 10 readings were taken and average value was reported as a hardness measurement. The machine on which hardness was performed is shown in Figure 3.10.

Figure 3.10: Vickers hardness (FIE-Model: VM 50 PC) tester

3.5.2 Tensile testing

Tinious Olsen 25 KN machine (S-Series, H25K-S) was used to perform the tensile tests at room temperature with a cross head speed of 1 mm/minute (Figure 3.11).

Figure 3.11: Tensile testing machine

The strength and ductility of the as -received alloy and the processed alloy were evaluated from the stress – strain data. The small size substandard tensile samples having a rectangular cross section as per the ASTM E8/E8M were prepared with gauge length equal to 10 mm and 20 mm respectively for cryoforged as well as cryorolled sample using a wire cut electro discharge machining (WEDM) In order to preserve accuracy in the dimensions from the center of each condition for cryoforged samples while for cryo rolled samples, gauge length used was 20 mm. Prior to testing, samples were polished properly to provide scratch free edges, surfaces and uniform gauge length. Minimum three measurements for each condition were made and an average value of three tests was reported.

3.6 Fatigue and Fracture Toughness Testing

The fatigue and fracture toughness testing were performed on INSTRON-8802 machine. The sample after cryorolling and cryoforging was made according to ASTM 1820 and ASTM E 466-07 for fracture and fatigue test, respectively. The cryorolled samples were tested for high cycle fatigue (HCF), fatigue crack growth rate (FCGR) test and 3-point bend test while

cryoforged samples were tested for the 3-point bend test only due to the insufficient volume of material after cryoforging. For high cycle fatigue (HCF) test of samples, the thickness of sample used was 3 mm while for fatigue crack growth rate test, it was 6.5 mm, in the present work. The sample thickness used for 3-point bent test performed on cryoforged samples was 3.75 mm. The Fig. 3.12, Fig. 3.13 and Fig. 3.14 shows the sample used for high cycle fatigue (HCF), fatigue crack growth rate (FCGR) test and 3-point bend test in the present work. Fig. 3.15 shows the instron machine used for carrying out fatigue and fatigue crack growth rate test in this work.

Dimensions of compact tension (CT) sample
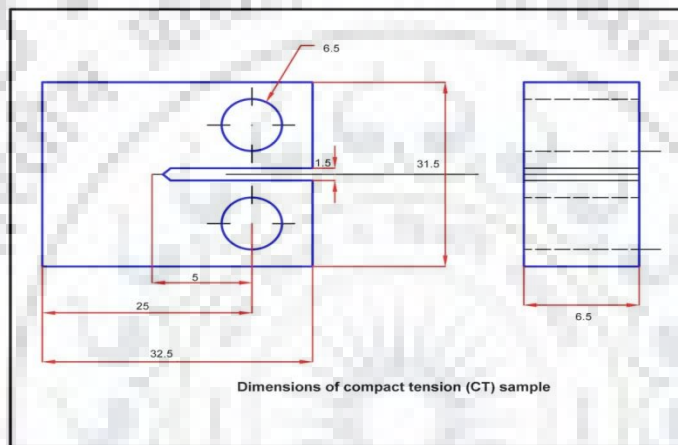
Figure 3.12: Dimensions of compact tension (CT) sample used for FCGR test
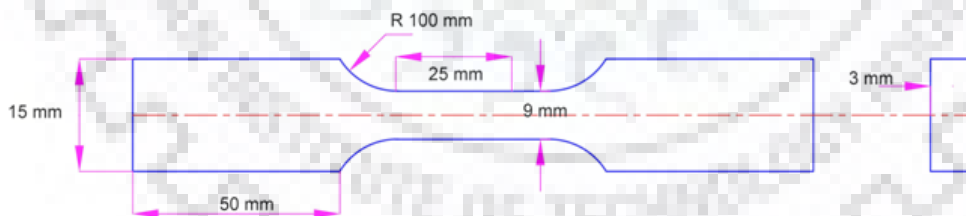
Figure 3.13: Dimensions of high cycle fatigue (HCF) test sample used

a = 3.75mm
B = 3.75mm
W= 7.50mm
S = 30.0mm
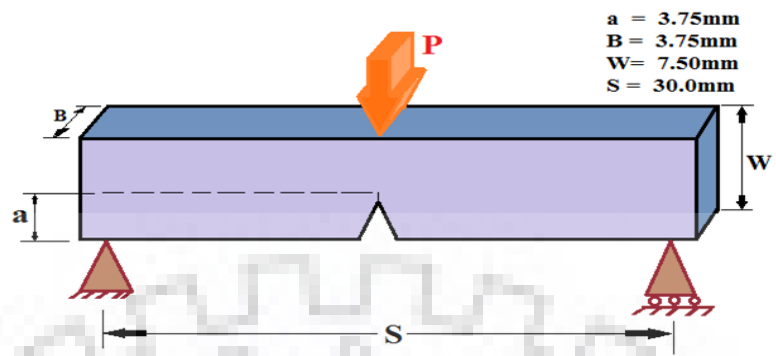
Figure 3.14: Dimensions of 3-point bent test sample used for fracture toughness test

Figure 3.15: Instron 8802 machine used for fatigue testing

<div align="right">

Chapter 4

</div>

CRYOROLLING (RESULTS & DISCUSSION)

This chapter describes the effect of cryorolling on microstructure and mechanical properties of Al 2014 alloy. The first section of this chapter discusses the effect of cryorolling and followed by annealing (in the temperature range 100°C – 350°C) on microstructural evolution, precipitation sequence, tensile properties and fracture toughness of Al 2014 alloy. In the second section, a detailed study of the high cycle fatigue behavior (HCF) of cryorolled and followed by annealed Al 2014 alloy in the temperature range from 100°C -250°C has been discussed. The fatigue crack growth (FCG) behavior of bulk UFG Al 2014 alloy after annealing treatment is discussed in third section 4.3 of this chapter.

4.1 Influence of Cryorolling and Followed by Annealing on Microstructural Evolution, Precipitation Sequence, Tensile Properties and Fracture Toughness of bulk UFG Al 2014 alloy

4.1.1 Introduction

Aluminum alloys (2xxx series) are extensively used for high strength structural applications especially in aircraft, automotive, and construction industries, owing to their high specific strength, fatigue and fracture resistance properties [4.1-4.2]. Presence of copper in the alloy improves the fracture toughness, the high temperature properties and machinability of alloys [4.3]. The 2014 aluminum alloy is one of the most popularly used alloy from 2xxx series [4.4]. It is an age hardenable alloy where strengthening is achieved through solution hardening, dispersion hardening, and precipitation hardening [4.5]. Hardening in this alloy is achieved through precipitation of Al_2Cu or $Al_2CuMgSi$ phases during aging. However, the extent of hardening achieved through these methods is moderate [4.5]. The strength of this alloy can further be increased by refining grain sizes in the range of ultrafine to nanometer regime. It has been well established that ultrafine grained material produced through SPD techniques have high strength, toughness, fatigue and fracture resistance properties, which may be utilized in aerospace, automotive and construction sectors [4.6-4.7]. In recent years, several SPD techniques such as Equal channel angular processing (ECAP), Accumulative roll bonding (ARB), Repetitive Corrugation and Straightening (RCS), High pressure torsion (HPT), have been well developed to obtain ultrafine/Bulk nanostructured material with

<div align="center">

62

</div>

improved mechanical properties [4.8-4.11]. It has been reported that UFG structure formed from SPD methods requires very large deformation at low temperature under high pressure [4.12-4.13]. This limits the use of SPD techniques where it is not possible to impose large plastic strain under high pressure. To overcome this drawback of SPD techniques, cryorolling has been well established as one of the prospective methods to realize ultrafine microstructure in bulk material [4.14]. Cryorolling requires less plastic strain and relatively low load as compare to other SPD processes to effectuate severe strain for producing bulk ultrafine/ nanostructured material. Conventional rolling at liquid nitrogen temperature reduces the mobility of dislocations by suppressing dislocation cross slips and climbs in high stalking fault energy metals (Al alloys) facilitating the formation of UFG microstructure by inducing high defect/dislocation density [4.15-4.16]. This technique has been attempted on several metals and alloys to obtain UFG microstructure with improved strength and hardness properties. Recently, an extensive research work has been conducted to develop UFG microstructure by conventional rolling at liquid nitrogen temperature with enhanced mechanical properties in heat treatable Al alloys such 6061, 6063, 7075/ non heat treatable Al alloy 5083 [4.17-4.21]. Panigrahi et al. [4.18-4.20] reported the improvement in mechanical properties as a result of ufg microstructure in 6063 and 7075 aluminum alloy processed through cryorolling treatment. Rangaraju et al. [4.15] have studied the effect of cryorolling and annealing on the microstructure and mechanical properties of pure aluminum and observed the enhanced value of tensile strength, yield strength and ductility with a grain size below than 500 nm. Shanmugasundaran et al. [4.22] produced the UFG microstructure on Aluminum alloy 2219 by cryorolling and reported the improved value of strength and ductility of this alloy by post deformation short annealing and aging treatment.

Based on past studies, it is well established that cryorolled material offers significant strength and hardness related properties. However, there are certain limitations and challenges related to use of cryorolled material owing to its limited ductility or low strain hardening ability. In addition to this, fracture toughness of cryorolled material is not well established in earlier published work. Recently, various researchers have contributed in evaluating the fracture toughness of SPD processed metals and alloys. Hohenwarter et al. [4.23] reported the fracture toughness of ultrafine grained Ni produced by high pressure torsion by J integral method, stretched zone width and COD method. They observed the improved values of strength and fracture toughness of SPD processed ultrafine grained Ni. They have also investigated the

fracture toughness of ultrafine grained iron processed by HPT process and reported the pronounced differences in fracture toughness values and fracture surface appearance when measurement were performed in three different crack orientation. Fracture behaviour of UFG iron was anisotropic as reported in their work [4.24]. Li et al. [4.25] evaluated the fracture toughness of nanostructured zirconium processed through cryorolling and observed the enhanced values of plain strain fracture toughness (K_{IC}) as compared to coarse-grained Zr as a result of formation of nano, sub-micrometer and micrometer sized grain after post annealing of cryorolled samples.

It may be mentioned that very limited literature exists on the the fracture toughness of SPD processed Al alloys. Recently, Darban et al. [4.26] have investigated the fracture toughness of Al 7075 alloy subjected to Equal channel angular pressing (ECAP) by performing fracture toughness test in Disk shaped compact test (DCT) specimen and reported the improved value of fracture toughness. The same Al alloy 7075, processed by cryorolling, was investigated for plain strain fracture toughness (K_{IC}) by Das et al. [4.27]. A significant improvement in fracture toughness of cryorolled Al alloy was reported in their work. The key issue to use UFG material processed by cryorolling or any other SPD process is due to its limited strain hardening response and formability. The UFG material shows low strain hardening response due to artifacts from processing, instability in crack nucleation/propagation, and unstable microstructure as reported in the literature [4.28]. In addition to this, UFG material is not thermally stable due to high defect density and high energy stored in the deformed state, which leads to the low formability and low strain hardening ability of UFG material fabricated by cryorolling and other SPD processes [4.29].

Post annealing treatments after cryorolling has been identified as promising method to improve tensile and fracture properties with improved ductility in metals and alloys [4.30]. Annealing is also essential to identify the temperature at which microstructure is stable and diffusion rate is very high, which leads to high superplastic properties of UFG alloy fabricated by cryorolling [4.30].

Al 2014 alloy has high strength and widely used in aerospace and automotive applications. One of the major requirements of this alloy for its applicability in these sectors is that its properties should be retained even at high temperature up to $300^{\circ}C$ without any degradation.

However, the age hardenable alloy at high temperature does not offer good properties due to coarsening of precipitates.

Most of the work related to Al 2014 alloy was focused towards the effect of various SPD processes such as ECAP, HPT, MAC (multi axial compression) on the strength, hardness, and microstructure - property correlation. Besides this, the effect of post deformation treatments such as short annealing and age hardening response of this alloy up to temperature of 200°C after these processes has been well explored. However, the effect of cryorolling and post deformation annealing up to high temperature 350°C on the precipitation sequence, tensile properties and fracture toughness of Al 2014 is scarce in the literature. Therefore, the present work is focused to study the effect of annealing on microstructural evolution, precipitation sequence, tensile properties and fracture toughness over a wide range of temperatures in cryorolled Al 2014 alloy.

4.1.2 Experimental Procedure

The Al 2014 alloy plate was procured from Bharat Aerospace Metals; Mumbai, India in T6 treated condition in the form of 40 mm thick plate. The chemical composition of the alloy has been given in Chapter 3. The rectangular samples of dimensions 40 mm x 30 mm x 10 mm were machined from the as received plate and solution treated at 505°C for 2 hours to dissolve all the second phase particles and quenched in water. The solution treated samples were subjected to cryorolling up to a true strain of 2.3 using conventional rolling machine with liquid nitrogen. To perform cryorolling, samples were dipped in to liquid nitrogen for 20 minutes initially and 10 minutes after each successive rolling pass. In order to study the influence of annealing on the microstructure evolution, tensile strength and fracture toughness, all the cryorolled samples were annealed from temperature 100°C to 350°C for the duration of 45 minutes. To investigate the mechanical behavior of solution treated, cryorolled, cryorolled followed by annealed sample, the tensile and hardness tests were performed at room temperature with the help of H25K-S Tinius Oslen tensile testing machine and Vickers hardness tester, respectively. The tensile samples were prepared by following ASTM E-8 standard and for each condition, minimum of 3 samples were tested to achieve reproducibility. To investigate the crack growth resistance of solution treated alloy, cryorolled alloy and cryorolled followed by annealed alloy, fracture toughness tests were performed using a special attachment of 3-point bend test on H25K-S Tinius Oslen tensile testing machine. The microstructural features and precipitate evolution during annealing at different temperature

were characterized by TEM and XRD studies. The TEM studies were carried out on Philips CM 12 transmission electron microscope operating at 120 volt, while XRD studies were performed using Bruker AXS D8 Advance instrument with Cu K α radiation. TEM sample was prepared by mechanically grinding the sample to 100 μm with emery papers and subsequently thinning the sample by twin jet electropolisher with a solution of 25% nitric acid and 75% methanol at a temperature of -30°C. The fractured surface of tensile as well as 3-point bend test specimen was examined by SEM.

4.1.3   Results

4.1.3.1 Microstructure

Microstructure of starting solution treated material and CR material is characterized by optical microscopy in the present work. The optical micrograph of as received material after solution treatment is shown in Fig. 4.1.1(a). The alloy exhibits elongated structure with an average grain size of 120 μm. When solution treated alloy is cryorolled up to thickness reduction of 90%, the elongated structure is further elongated in rolling direction (Fig. 4.1.1(b)) in such a way that original grain boundaries got perturbed with the evolution of dislocation cell boundaries and transformed in to ultrafine grains. However, the transformation of coarser grains in to UFG is difficult to characterize under optical microscopy; therefore, TEM studies were carried out for characterizing high strain samples.
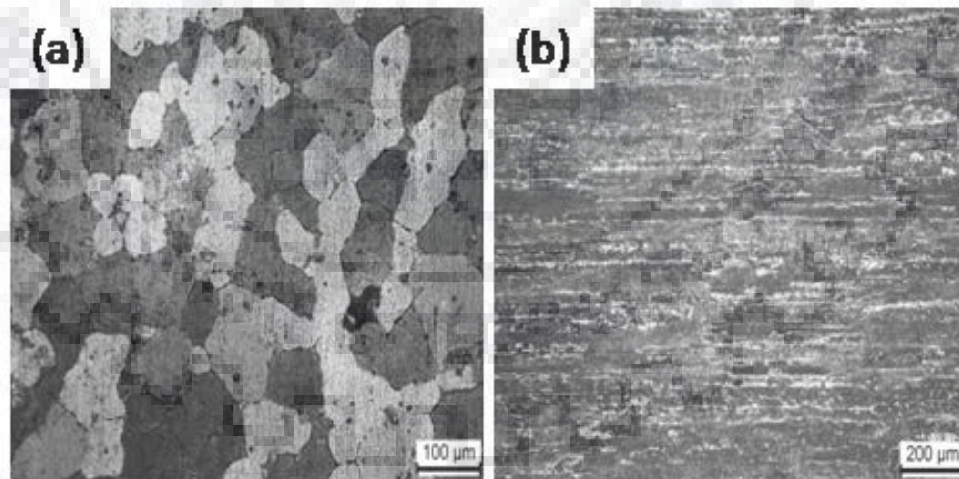
Figure 4.1.1: Optical micrograph of Al 2014 alloy: (a) Solution Treated; (b) CR

Microstructure evolution during annealing of cryorolled Al 2014 alloy has been studied through TEM in the present work. Fig. 4.1.2 (a) shows the TEM micrograph of as CR material subjected to an effective true strain of 2.3.
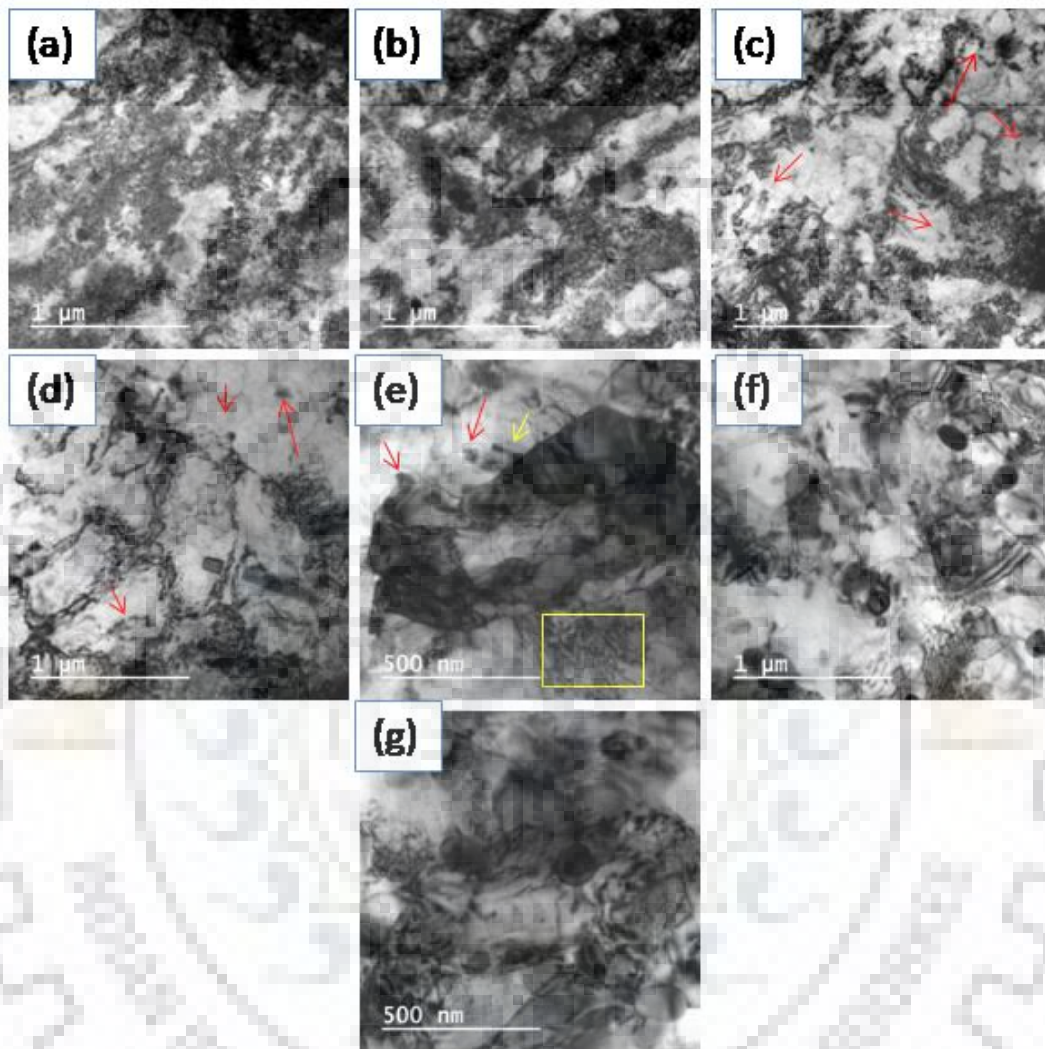
Figure 4.1.2: TEM micrographs of cryorolled Al 2014 alloy for various processed conditions:
(a) As CR; (b) CR +100°C; (c) CR +150°C; (d) CR +200°C; (e) CR +250°C;
(f) CR +300°C; (g) CR +350°C

When Al 2014 alloy is cryorolled up to a true strain of 2.3, high density of dislocations are generated inside the sample. The CR alloy in Fig. 4.1.2(a) shows the elongated dislocation cells and subgrains lying along the rolling directions. These elongated cells and subgrains are surrounded by ill defined grain boundaries as depicted by Fig. 4.1.2 (a). Some of the cells in CR samples are well within the range of nanocrystalline regime. In addition to this, dislocation tangling zone in some areas can be clearly visualized from the TEM micrograph. After

annealing at 100°C and 150°C for 45 minutes, a significant change in microstructure of as CR sample was observed. Fig. 4.1.2 (b) shows the TEM micrograph corresponding to sample annealed at 100°C. On annealing at 100°C for 45 minutes, dislocation density in cryorolled samples is slightly reduced and due to the rearrangement of dislocations, subgrains were formed as depicted from the Fig. 4.1.2 (b). However, the number of sub grains formed at this temperature was quite less. From Fig. 4.1.2 (b), it is also evident that some of the subgrains formed at this temperature are in the size range of 50-100 nm. When sample is annealed at a temperature of 150°C , dislocation density is gradually reduced in the cryorolled sample (Fig. 4.1.2 (c)). In this case, number of subgrains is prominent as compared to sample annealed at 100°C. It is due to the fact that some of the dislocations were annihilated slightly at this temperature due to recovery process and relaxation and transformation of cell boundaries in to subgrain walls. However, subgrain size is comparatively much more as compared to sample annealed at 100°C as depicted from the Fig. 4.1.2 (c). In addition to this, some of spherical precipitate particles which are marked by red arrow on Fig. 4.1.2(c) can also be observed at this annealing condition. Fig. 4.1.2 (d) shows the TEM micrograph of cryorolled Al 2014 alloy annealed at 200°C. The dislocation density is significantly reduced at this temperature as observed from TEM micrograph corresponding to this condition. The evolution of precipitation (marked by red arrow) can also be observed at this temperature as illustrated by Fig. 4.1.2 (d). To observe these particles more clearly at annealing temperature of 150°C, higher magnification TEM images are shown in Fig. 4.1.3 (a)-(c).
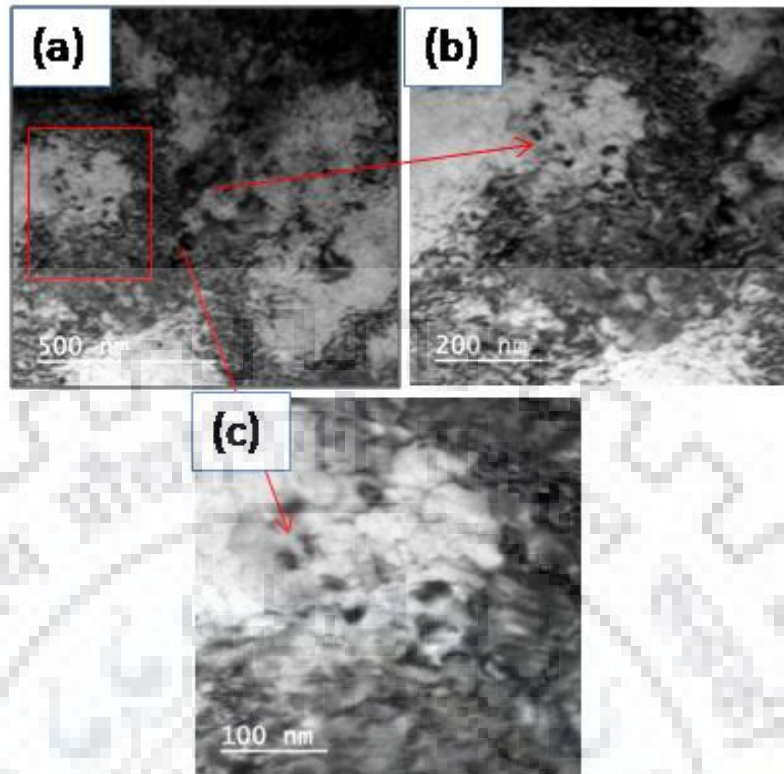
Figure 4.1.3: Higher magnification TEM micrographs of cryorolled Al 2014 alloy annealed at 150°C

.
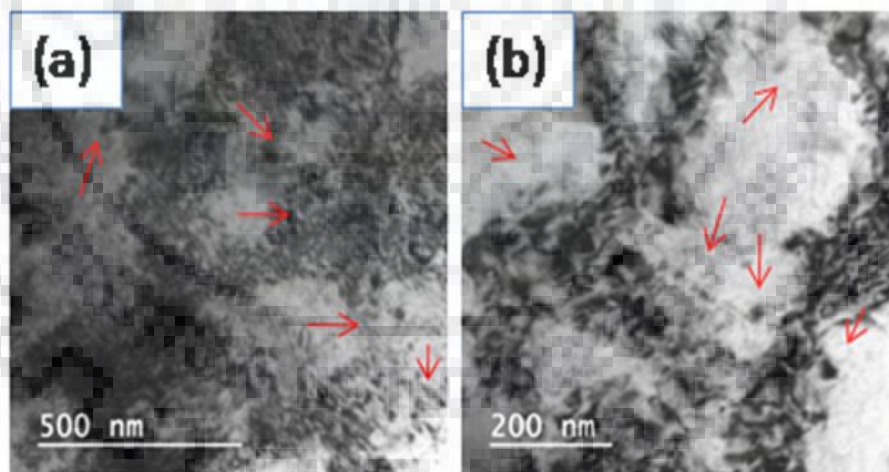
Figure 4.1.4: Higher magnification TEM micrographs of cryorolled Al 2014 alloy annealed at 200°C

Similarly, higher magnification TEM micrographs of sample annealed at 200°C are shown in Fig. 4.1.4 (a)-(b) and Fig. 4.1.5 (a)-(c). From Fig. 4.1.5(a)-(c), it is observed that some the fine grains are nucleated at the periphery of second phase particles. The heavy deformation during cryorolling leads to the formation of deformation zone, which consists of high dislocation density and fine sub grains. The deformation zones are preferable sites for recrystallisation and this phenomenon is known as particle stimulated nucleation (PSN) [4.31]. Since the large second phase particles are lumped together with fine grains along the grain boundary at annealing temperature of 200°C, the similar phenomenon of particle stimulated nucleation (PSN) is believed to occur at this temperature [4.17]
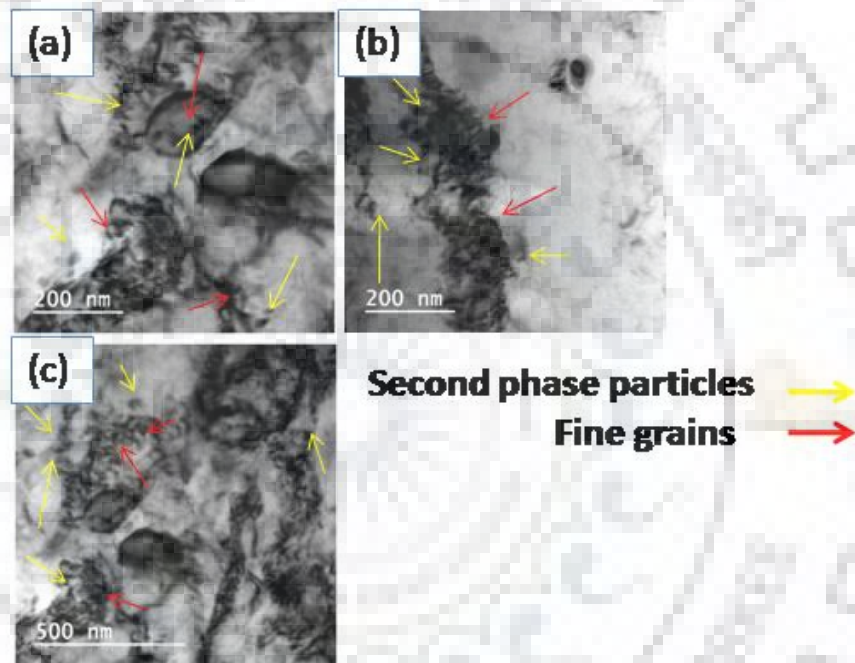
Figure 4.1.5: Higher magnification TEM micrographs of cryorolled Al 2014 alloy annealed at 200°C showing the particle stimulated nucleation (PSN)

Fig. 4.1.2(e) shows the TEM micrograph corresponding to cryorolled samples annealed at 250°C. An enormous drop in the dislocation density at this temperature is observed as compared to sample annealed at 100°C, 150°C, and 200°C with the evolution of spherical (marked by red arrows) and needle shape particles (marked by yellow arrow and square box) as depicted from Fig. 4.1.2 (e). In addition to this, the observed subgrains in this temperature are much more equiaxed and strain free as compared to sample annealed at low temperature. However, sub grain sizes in the range of 250-350 nm is observed in this temperature. High magnification TEM micrographs of the samples annealed at 250°C are shown in Fig. 4.1.6 (a)-

70

(d). It is evident that UFG microstructure is still retained at this temperature with evolution of spherical and needle, second phase precipitate particles. However, the number and volume fraction of needle second phase precipitate particles are seen more as compared to spherical particle at this temperature as illustrated from Fig. 4.1.6. Moreover, the pinning of grain boundary by these particles is also observed at this temperature as observed from TEM micrographs.
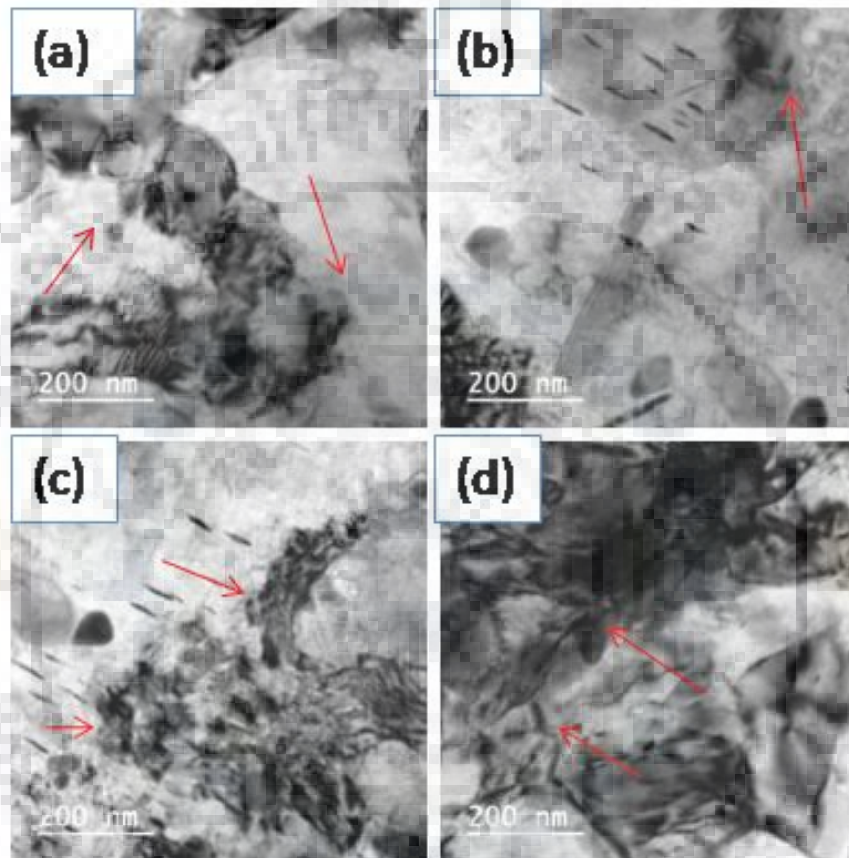
Figure 4.1.6: Higher magnification TEM micrographs of cryorolled Al 2014 alloy annealed at 250°C

Fig. 4.1.2(f) shows the TEM micrograph of cryorolled Al 2014 alloy annealed at 300°C. The dislocation density is significantly reduced and grain coarsening has become prominent at this temperature. Additional TEM images at various locations of sample corresponding to this condition are shown in Fig. 4.1.7 (a)-(d) to observe the detailed features of the annealed alloy and it reveals the formation of the duplex microstructure with the grain sizes in the range of 400 nm - 1µm at this temperature.
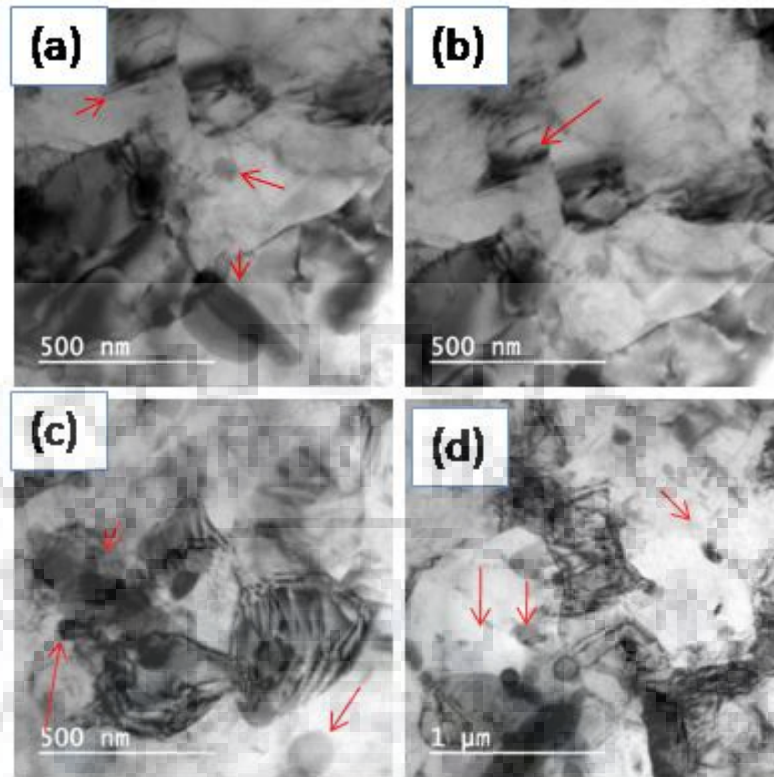
Figure 4.1.7: TEM micrographs corresponding to sample annealed at 300°C

The second phase precipitate particles with larger size as compared to sample annealed at 250°C were also observed at this annealing condition. However, the number and volume fraction of these particles, especially needle type becomes lesser as compared to sample annealed at 250°C as depicted from Fig. 4.1.2(f) and Fig. 4.1.7(a)-(d).

When cryorolled samples were further annealed at a temperature of 350°C, dislocation free equiaxed grains sizes in the range of 500 nm - 1µm were formed as seen from TEM micrographs corresponding to this condition (Fig. 4.1.2(g) and Fig. 4.1.8 (a)-(c)). The second phase particles evolved in this condition becomes much coarser than the sample annealed at previous conditions. These second phase particles interact with grain boundaries and leftover dislocations inside the grains as shown in Fig. 4.1.8 (a)-(c) correspond to sample annealed at 350°C.
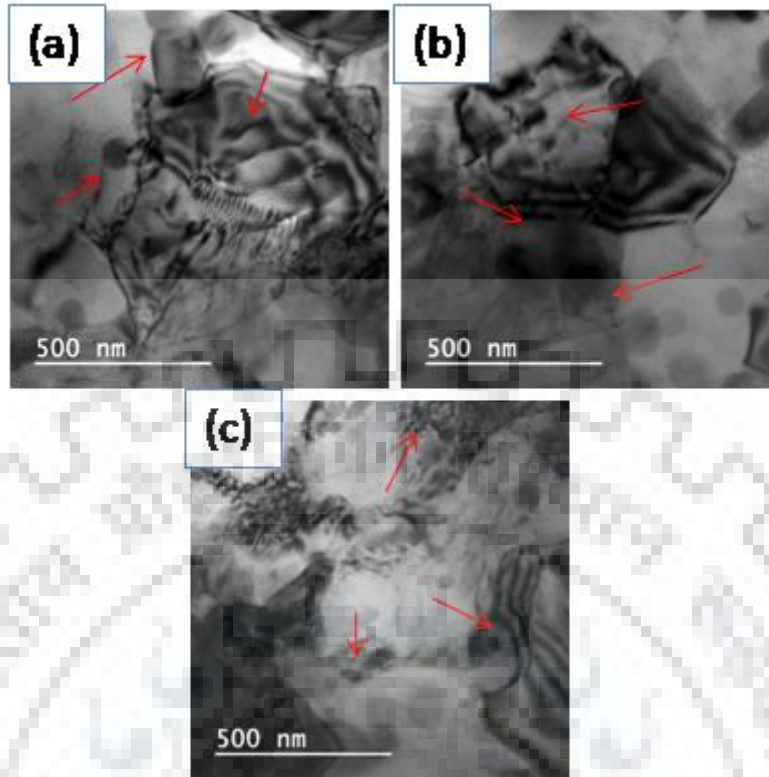
Figure 4.1.8: TEM micrograph corresponding to sample annealed at 350°C

4.1.3.2 Mechanical Properties

Hardness of cryorolled Al 2014 alloy at different annealing temperatures ranging from 100°C to 350°C is shown in Fig. 4.1.9. The hardness of starting solution treated alloy is 115 HV. When solution treated alloy was cryorolled up to a cumulative true strain of 2.3 (90% thickness reduction), the Vickers hardness has increased from 115 HV to 164 HV. To study the trend of variation of hardness with respect to annealing temperatures, as CR samples were annealed from 100°C to 350°C for the duration of 45 minutes. After annealing at 100°C for 45 minutes, the hardness of cryorolled Al 2014 has increased from 164 HV to 181 HV. When samples are annealed at 150°C for the same duration, a slight drop in hardness is observed. The hardness of cryorolled Al 2014 alloy becomes 174 HV at the annealing temperature of 150°C. Further, annealing of cryorolled samples at the temperature of 200°C, hardness has decreased marginally from 174 HV to 169 HV. When as CR samples were further annealed at a temperature of 250°C, the hardness is suddenly drops from 169 HV to 123 HV. This drop in hardness is continued up to the temperature of 350°C. The hardness drops drastically from 123 HV to 100 HV, when samples were annealed at 300°C as compared to sample annealed at

73

250°C. After annealing at a temperature of 350°C, the hardness becomes 88 HV and nearly becomes constant at further temperatures.
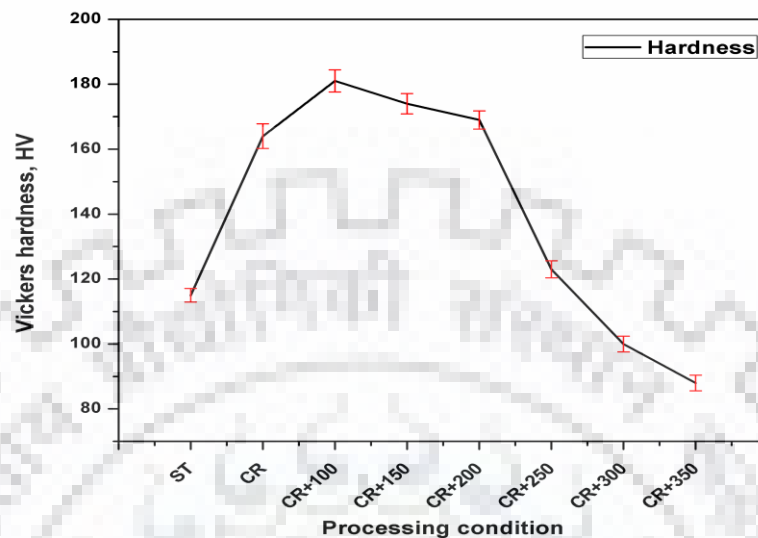
Figure 4.1.9: Variation of Hardness for cryorolled (CR) Al 2014 alloy for various processed Conditions

Variation in tensile properties of cryorolled (CR) Al 2014 alloy is shown in Fig. 4.1.10. The ultimate tensile and yield strength of as received material after solution treatment is observed as 245 MPa and 176 MPa, respectively, with 18.5% elongation. The ultimate tensile and yield strength of solution treated material after cryorolling up to 90% thickness reduction has increased from 245 MPa to 447 MPa and 176 MPa to 428 MPa, respectively. However, the ductility has reduced from 18.5% to 4.8 % as compared to solution treated alloy. When cryorolled samples are annealed at a temperature of 100°C, the UTS and yield strength have further increased to 553 MPa and 510 MPa, respectively with slight improvement in ductility (6.3%). After annealing at 150°C, the UTS and yield strength have decreased to 511 MPa and 456 MPa respectively with 7.5% elongation. At the annealing temperature of 200°C and 250°C, the significant drop in tensile and yield strength is observed as compared to cryorolled Al 2014 alloy. However, this strength is still higher than the starting solution treated alloy. The UTS and yield strength has reached from 447 MPa to 487 MPa and 428 MPa to 433 MPa, respectively with 9.5% elongation at annealing temperature of 200°C as compared to cryorolled alloy. This drop in UTS and yield strength has further continued at a temperature of 250°C. The UTS and yield strength becomes 362 MPa and 310 MPa, respectively, at annealing temperature of 250°C.
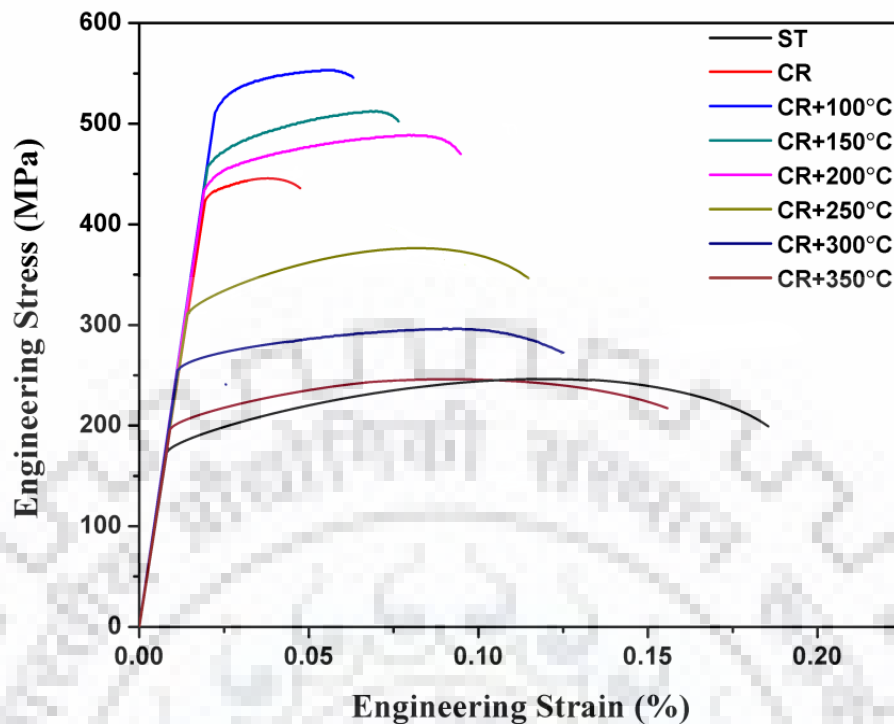
Figure 4.1.10: Stress-Strain curve for cryorolled Al 2014 alloy for various processed Conditions

Table 4.1.1: Mechanical properties of cryorolled (CR) and annealed alloy for various processed conditions

Processed Condition	Ultimate Tensile Strength (MPa)	Yield Strength (MPa)	Elongation (%)
Solution Treated	245	176	18.5
Cryorolled (CR) 90%	447	428	4.8
CR + 100°C	553	510	6.3
CR + 150°C	511	456	7.5
CR + 200°C	487	433	9.5
CR + 250°C	362	310	11.8
CR + 300°C	285	201	13
CR + 350°C	247	196	16

However, the ductility has increased from 9.5% to 11.8% as compared to sample annealed at 200°C. After annealing at 300°C, the ultimate tensile and yield strength decreases drastically from 362 MPa to 285 MPa and 310 MPa to 201 MPa with an improvement in ductility from 11.8% to 13% as compared to sample annealed at 250°C. With further annealing at a temperature of 350°C, the tensile and yield strength of cryorolled samples have decreased from 285 MPa to 247 MPa and 201 MPa to 196 MPa, respectively, as compared to sample annealed at 300°C. However, the ductility has increased from 13% to 16 % at this

75

temperature, when compared to sample annealed at 300°C. Mechanical properties of cryorolled and cryorolled followed by annealed samples are shown in Table 4.1.1.

4.1.3.3 XRD Results

Fig. 4.1.11 shows the XRD patterns of solution treated Al 2014 alloy and cryorolled samples, followed by annealing treatment at different temperatures ranging from 100°C to 350°C.
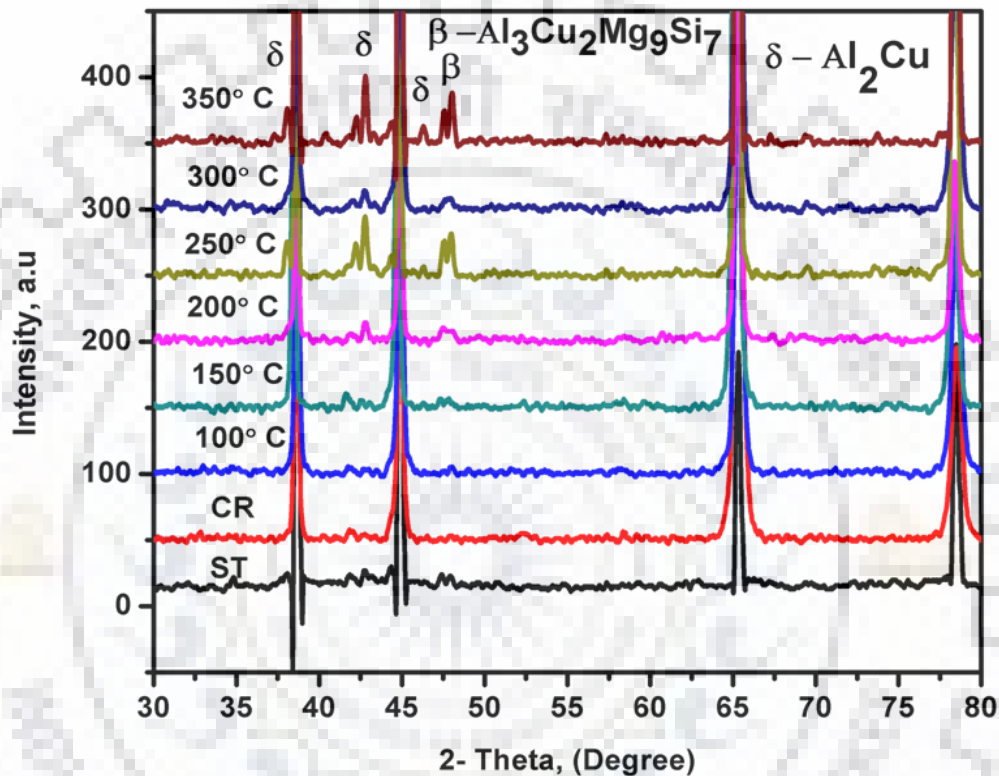
Figure 4.1.11: XRD plot for cryorolled Al 2014 alloy for various processed conditions

The solution treated sample does not show   peak pertaining to Al_2Cu and $Al_3Cu_2Mg_9Si_7$. This indicates that these phases are completely dissolved in Al matrix after solution treatment. The similar XRD pattern are observed corresponding to cryorolled samples up to thickness reduction of 90% and cryorolled followed by annealed sample up to 100°C as in case of solution treated samples. However, when the samples are annealed at a temperature of 150°C, the presence of small intensity peak of phase Al_2Cu is observed. The $Al_3Cu_2Mg_9Si_7$ phase peak is not observed in XRD pattern of sample annealed at 150°C. The XRD plot has significantly changed at annealing temperature of 200°C. The presence of peaks corresponding to phase Al_2Cu and $Al_3Cu_2Mg_9Si_7$ is observed at this temperature. These peaks

are also seen at annealing temperature of 250°C and 300°C as observed from the Fig. 4.1.11. However the intensity of these peaks increased with increasing annealing temperature.

4.1.3.4   Fracture Toughness (K_Q)

UFG materials processed by SPD techniques or any other processing route generally have exceptional mechanical and physical properties, but deformation behavior is deteriorated due to reduced strain hardening response and inability to accommodate extra storage of dislocation when the grain sizes are in the range of ultrafine to nanometer regime [4.23-4.24]. There has been a lot of efforts in past by several researchers to elaborate the various strategies for improving the tensile ductility or elongation to failure in SPD processed metals/alloys. Although ductility related issues of UFG metals are given prime importance, fracture toughness is yet to be explored for its potential   structural applications. Fracture toughness is a unique parameter through which a broader diversified view of deformation behavior of metals and alloys can be well estimated [4.24]. Fracture toughness tests usually measures the stress intensity factor at which the pre-existing crack in material grows to a critical size. This information is very important particularly when metals and alloys used for engineering/structural applications. In such applications, a reasonable amount of toughness is required, otherwise on applying load, pre-existing crack will lead to brittle fracture. Usually, tensile test does not give the information regarding the fracture toughness of the material because it involves the uniaxial deformation of material [4.32]. Fracture toughness testing involves high amount of tensile tri-axiality around the crack tip which gives more general insight in to fracture and damage tolerance of metals and alloys subjected to different stress levels. However , the fracture toughness testing in UFG materials fabricated by cryorolling and other SPD processes is very difficult due to the limited dimensions obtained after these processes. It becomes more difficult when a condition of small scale yielding near the crack tip is also imposed. In such a situation, a thickness of material must satisfy the plain strain condition as per the ASTM standards. Fracture toughness of cryorolled Al 2014 alloy is not well studied in the past. In addition to this, it is very important to study the influence of annealing for a wide range of temperature on fracture toughness of cryo rolled Al 2014 alloy. Therefore, a 3-point bend fracture toughness testing has been carried out in present work using SENB (single edge notch bending) specimen to evaluate various fracture parameters viz. Plain strain   fracture toughness (K_{IC}) (Based on ASTM standard 399), equivalent energy fracture toughness (K_{ee}) (Based on ASTM standard 992), and J integral .

77

(i) Evaluation of Plain strain fracture toughness (K_IC): Plain strain fracture toughness (K_IC) is a fracture parameter used to characterize crack in LEFM (Linear Elastic Fracture Mechanics). In LEFM approach, plastic zone near the crack tip is very small. To achieve plain strain condition near the crack tip, samples were prepared as per the ASTM standard 399 in the present work [4.33]. Typical dimensions of the cryorolled Al 2014 alloy is shown in Fig. 4.1.12.

a = 3.75mm
B = 3.75mm
W = 7.50mm
S = 30.0mm
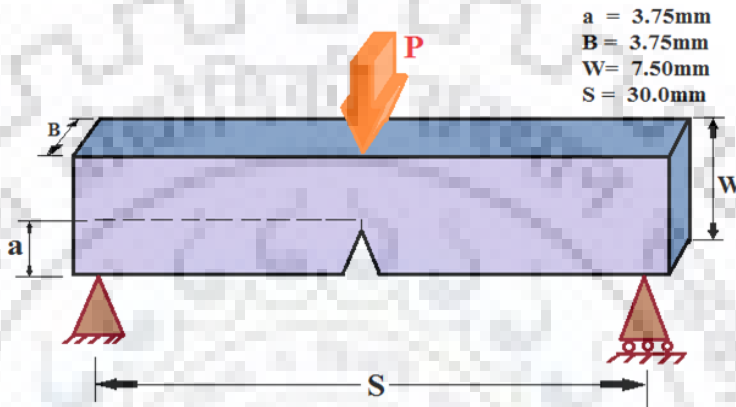
Figure 4.1.12: Specimen for 3-Point bend test

All specimens were pre-cracked by help of computer controlled wire cut EDM machine to an initial relative crack length of $a/W = 0.5$. It is very important to note that pre-cracking loads were limited to low values to keep the plastic zone near the crack tip small [4.34]. To start the test, specimens were monotonically loaded to failures to measure the load and extension. Finally, the load –extension curve is recorded. The load and extension curve test results were analyzed to determine a provisional value of fracture toughness K_IC, which is denoted by K_Q. For determining provisional value of fracture toughness K_Q, provisional load P_Q and crack length was measured. A secant line having a slope less than 5% from the original line were drawn and the point at which this 5% secant slope line intersect the load –extension curve were denoted by P_Q.

The P_Q value was used to determine corresponding K_Q value and determined by following equation as per the ASTM standard 399 [4.35 -4.36].

$$K_Q = \frac{P_Q}{B} \frac{S}{W^{3/2}} f(a/w) \tag{4.1}$$

The quantities a, B, W are shown in figure.

The value of the quantity $f(a/w)$ is determined by following equation

$$f(a/w) = \ 3\left(\frac{a}{W}\right)^{1/2} \frac{\left[1.99 - \frac{a}{W}\left(1-\frac{a}{W}\right)\left(2.15 - 3.93\frac{a}{W} + 2.7\frac{a^2}{W^2}\right)\right]}{2\left(1+2\frac{a}{W}\right)\left(1-\frac{a}{W}\right)^{3/2}} \tag{4.2}$$

The measured K_Q value from above equations is known as plain strain fracture toughness K_{IC}, if it satisfies the following two validity requirement.

i) $\frac{P_{max}}{P_Q} \leq 1.10$ and

ii) Crack length a, specimen thickness B, and unbroken ligament   (b) must satisfy following relation

$$a,\ B,\ b \ > \ 2.5 \left(\frac{K_Q}{\sigma_y}\right)^2$$

If above two conditions are not met, the measured K_Q value is known as provisional fracture toughness or apparent fracture toughness [4.33, 4.35]. In this work, it was seen that these two conditions are not fulfilled by cryorolled Al 2014 alloy because of small sample size obtained after processing. So, we have reported the apparent fracture toughness of cryorolled Al 2014 alloy in the present work.

Load –Extension curve after 3-point bend test for cryorolled Al 2014 alloy is shown in Fig. 4.1.13. A secant line is drawn whose slope is 5% less than the original line to find out provisional load P_Q. Now, P_{max} has to be calculated and this value of P_{max} and P_Q is used in equation no (4.1) for checking the validity of test [4.35]. In this work, it was observed that the equation is not satisfied for all processed conditions of cryorolled Al 2014 alloy. So, the tests for determining plain strain fracture toughness K_{IC} are invalid. P_Q value is used in equation (4.1) for determining the value of K_Q. Since the test is invalid, the obtained value of K_Q is known as provisional fracture toughness or apparent fracture toughness.
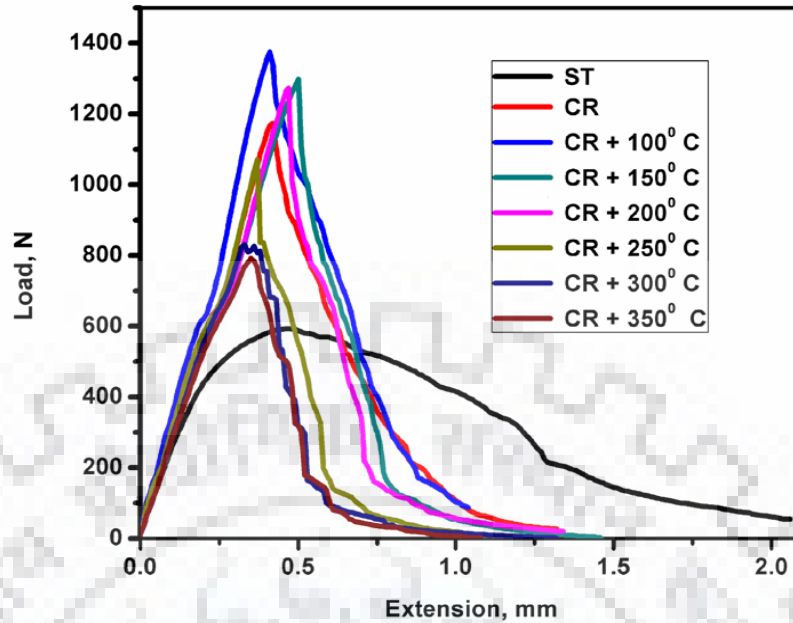
Figure 4.1.13: Load-Extension curve after 3-point bend test for cryorolled Al 2014 alloy for various processed conditions

For solution treated Al 2014 alloy, calculated apparent fracture toughness is

$$K_Q = 19.37 \text{ MPa}\sqrt{m}$$

The same procedure is used to find the apparent fracture toughness K_Q for other processed conditions of cryorolled Al 2014 alloy. The values of apparent fracture toughness are shown in Table 4.1.2 and variation is shown in Fig. 4.1.14.
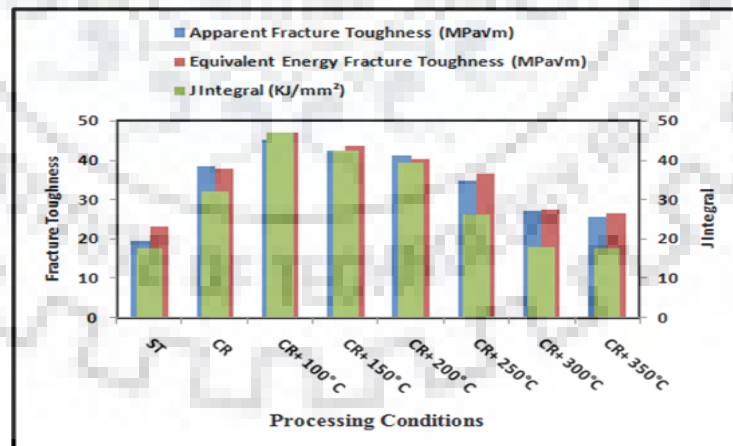
Figure 4.1.14: Variation of Fracture toughness parameters for various processing conditions

Table 4.1.2: Various Fracture parameters for Cryorolled Al 2014 Alloy for different processing Conditions

Processed Condition	Apparent Fracture toughness (MPa$\sqrt{m}$)	Equivalent Energy Fracture toughness (MPa$\sqrt{m}$)	J integral (crack propagation energy in KJ/mm²)
ST	19.37	23.06	17.77
As cryorolled	38.37	37.8	32.15
CR + 100°C	45.06	47.05	46.89
CR + 150°C	42.26	43.53	42.34
CR + 200°C	41.3	40.2	39.4
CR + 250°C	34.8	36.7	26.2
CR + 300°C	27.1	27.5	18.05
CR + 350°C	25.6	26.5	17.63

ii) Evaluation of equivalent energy fracture toughness (K$_{ee}$): Plain strain fracture toughness testing as per ASTM E399 standard requires comparatively larger sample size to achieve a plain strain condition. During the fracture toughness testing of cryorolled Al 2014 by following ASTM standard 399, it was observed that the test could not be satisfy the validity requirement and it was difficult to find out the true fracture toughness by following ASTM standard E399. A fracture parameter K$_{ee}$ known as equivalent energy fracture toughness based on ASTM standard E992 is used for comparing the fracture toughness of cryorolled Al 2014 alloy. It has been reported that fracture toughness K$_{ee}$ obtained by equivalent energy method over estimates the fracture toughness K$_{IC}$ obtained by following ASTM standard E399 for a valid test by 6% to 22%. Since the dimensions obtained after SPD processing is very limited, this method becomes handy and useful for calculating fracture toughness of SPD processed metals/alloys [4.37-4.38]. The basic procedure of this method is same as ASTM standard 399. However, an equivalent load P_E has to be determined instead of provisional load P_Q as per ASTM standard E992. In this method, area A$_L$ under load-displacement diagram up to linear part P$_L$ is determined first, then, the area A$_T$ up to maximum load is calculated. Equivalent load P$_E$ and equivalent energy fracture toughness K$_{ee}$ is found by using following equations.

$$P_E = P_L \sqrt{\frac{A_T}{A_L}} \qquad (4.3)$$

$$K_{ee} = \frac{P_E}{B} \frac{S}{W^{3/2}} f(a/w) \qquad (4.4)$$

All the variables a, w, and $f(a/w)$ in above equations are same as used in ASTM standard E 399.
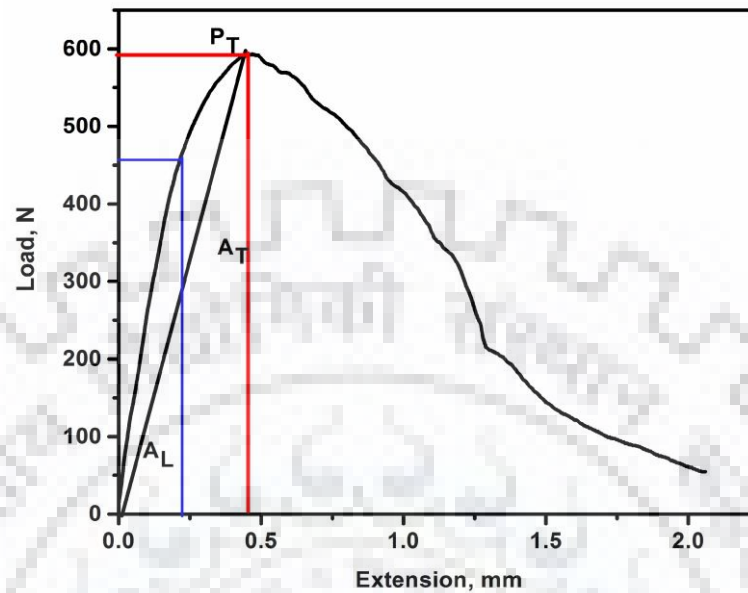
Figure 4.1.15: Measurement of Equivalent energy fracture toughness K_{ee} for Solution treated alloy

To calculate fracture toughness K_{ee} of solution treated Al 2014 alloy, from equivalent energy method, Fig. 4.1.15 is constructed as per the ASTM standard E992 as discussed earlier. Now, P_L from load displacement diagram is a linear part. The area under load- extension diagram considering linear/elastic part is calculated and this area is denoted by A_L. Finally, the area A_T under load – displacement diagram up to maximum load P_T is determined.

In the present work, A_T =141.96 mm^2

$$P_T = 591.5 \text{ N}$$

$$A_L = 69.58 \text{ mm}^2$$

$$P_L = 455 \text{ N}$$

The equivalent load P_E is calculated by above equation (4.3) and its value is found to be 729.5 N. This value of P_E is substituted in equation (4.4) to find out equivalent energy fracture toughness K_{ee}. K_{ee} for solution treated alloy is found to be 23.90 MPa$\sqrt{m}$ .The similar procedure is applied to find out K_{ee} for Al 2014 alloy subjected to other processed condition. The values of equivalent energy fracture toughness K_{ee} is shown in Table. 2 and variation is shown in Fig. 4.1.14.

iii) Evaluation of J integral: LEFM approach is valid as long as the plastic zone near the crack tip is confined to a very small region. But, the material response near the crack tip does not remain elastic in some situation. In such situations, fracture parameter calculated from LEFM approach does not give accurate results. EPFM (elastic plastic fracture mechanics) is very helpful when the plastic zone near the crack tip is wide and spread. J integral is another fracture parameter used in EPFM for characterizing the crack [4.33, 4.35]. It may be mentioned that J integral can be viewed as both an energy parameter and stress intensity parameter. Rice [4.39] have reported that for linear elastic material, J is a more general version of energy release rate G and is determined by following relation

$$J = \frac{K_I{}^2}{E} \tag{4.5}$$

The J integral in EPFM can be defined as potential energy difference between the specimens, when crack grow in a plastic material. In the simplest form, it may be mentioned that J integral for linear elastic material in LEFM approach gives the crack initiation energy, while J integral for elastic plastic material in EPFM provides the crack propagation energy [4.40].

J integral for SENB specimen in the present work is evaluated using following equation as per the ASTM standard 1820-15a [4.40-4.41].

$$J = \frac{2}{B}\frac{A}{b} \tag{4.6}$$

Where

A = area under the load vs extension curve

b = unbroken ligament (W-a)

B = Specimen thickness

For solution treated Al 2014 alloy, area under load –extension diagram up to the maximum load is determined. Specimen thickness B of SENB specimen for the present work is 3.75 mm, while unbroken ligament b is also 3.75. These values are substituted in above equation (4.6) for determining J integral. For solution treated alloy, J integral value is determined as 17.77 KJ/m^2. The similar procedure is adopted to determine the J integral for cryorolled Al 2014 alloy subjected to other processed conditions. The J integral values for various processed conditions for Al 2014 alloy is shown in Table. 2 and variation is shown in Fig. 4.1.14.

4.1.4 Discussions

4.1.4.1 Evolution of second phase/precipitates during annealing

In order to investigate the effect of cryorolling and followed by annealing on the fracture toughness of Al 2014 alloy, it is very essential to know the evolution of

phases/precipitates during the annealing treatment. There are lots of published works on precipitation in Al-Cu, Al-Cu-Mg, and Al-Cu-Si-Mg alloys but the early stage of precipitation is still debatable However, based on several studies, it is generally accepted that there are three possible precipitation sequences in these alloys, which are responsible for precipitation hardening [4.42- 4.46].

(1) α_{sss} $\rightarrow$ GPZ $\rightarrow$ θ'' $\rightarrow$ θ' $\rightarrow$ θ (Al_2Cu)

(2) α_{sss} $\rightarrow$ GPBZ $\rightarrow$ S'' $\rightarrow$ S' $\rightarrow$ S (Al_2CuMg)

(3) α_{sss} $\rightarrow$ GPZ $\rightarrow$ Q' $\rightarrow$ Q ($Al_3Cu_2Mg_9Si_7$ or $Al_4Cu_2Mg_8Si_7$)

where 'α_{sss}' is the supersaturated solid solution, GPZ is the Cu based clusters in Al matrix known as Guinier-Preston zones, θ'' and θ' are the metastable Al_2Cu phases and θ is stable Al_2Cu phase. Similarly, GPBZ is the Cu/Mg based clusters known as Guinier-Preston-Bagariastkij Zones. 'Q' is the quaternary phase and denoted by λ having a composition of AlCuMgSi [4.42- 4.46].

Recently, Dhal et al. (47) have investigated the precipitation kinetics of Al 2014 alloy and they observed the following precipitation sequence when the alloy is processed through cryorolling.

$$\alpha_{sss} \rightarrow GPZ \rightarrow \lambda' \rightarrow \theta' + \lambda' \rightarrow \theta + \lambda$$
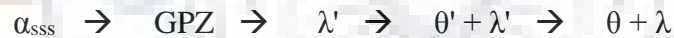
It has been reported that the precipitation sequence in the quaternary alloy (Al-Cu-Si-Mg) generally depends on the relative amount of alloying element [4.44]. If the Cu content is high (about 4% mass), the θ precipitation sequence is more likely to occur as reported in the literature [4.44]. Chakarbarti et al. [4.45] have also reported for high copper quaternary alloy that the precipitation sequence of Mg_2Si (β) phase, in addition to that of θ phase may be observed in such alloy only when Mg/Si ratio is greater than 1. However, if the ratio of Mg/Si ratio is less than 1, as in case of aluminum alloy 2014, which is predominately a quaternary alloy of Al-Cu-Si-Mg, the precipitation of Q phase (quaternary phase) or S phase (ternary phase) sequence is more likely to occur as reported in their work. However, the quantity of Si favors the presence of Q phase or S phase during precipitation process. They reported that if Si amount is very small, ternary S phase will come out of the matrix and if it is high, the presence of Q phase is observed.

In the present work, precipitate evolution in Al 2014 alloy during cryorolling and cryorolling followed by annealing has been investigated by TEM and these results are well

correlated with XRD results for all processed conditions. Fig. 4.1.2(a) shows the TEM microstructure of cryorolled Al 2014 alloy up to thickness reduction of 90%. The second phase precipitate particles are not seen in Fig. 4.1.2(a), which is a TEM micrograph of Al 2014 subjected to cryorolling up to thickness reduction 90%. The XRD pattern corresponding to this condition does not reveal any peak pertaining to the second phase precipitate particle as depicted from Fig. 4.1.11. It may be mentioned that at cryogenic temperature, these precipitate particles are not able to come out from Al matrix due to insufficient thermal energy and suppression of dislocation cross slip and climb, due to which these particles were retained in the solid solution. When samples were annealed at 100°C, the dislocation density is slightly reduced in samples; however, the second phase particles are still not seen at this temperature as observed from TEM micrograph shown in Fig. 4.1.2 (b). The XRD pattern also does not show any peak corresponding to any precipitation phase at this temperature. Besides, comparison of the hardness at this temperature with respect to solution treated and cryorolled Al 2014 alloy up to thickness reduction of 90% , reveals that hardness was maximum at this temperature. This indicates that some precipitates are evolving, which provide hardening effect at this temperature but XRD pattern and TEM micrographs were not able to recognize this phase. This hardening effect might be due to formation of GP zones, which are very fine clusters of Cu atoms in Al matrix, which can be identified only by HRTEM and DSC studies as reported in the literature [4.42-4.43]. However, Bassani et al. [4.43] have studied the DSC analysis of same alloy and found that GP zones in this alloy generally forms in the temperature range of 50°C -100°C. The TEM micrograph corresponding to sample annealed at the temperature of 150°C is shown in Fig. 4.1.2(c). The very few small spherical particles are seen at this temperature as observed from TEM micrographs shown in Fig. 4.1.2(c). To visualize these particles more clearly, higher magnification images (Fig. 4.1.3(a)-(c)) are used in the present work. The XRD pattern corresponding to sample annealed at 150°C also revealed the presence of peak of Al_2Cu phase. TEM micrographs and XRD pattern corresponding to sample annealed at $150°C$ confirms the evolution of small spherical particles of Al_2Cu phase at this temperature. However, no evidence of quaternary phase Q ($Al_3Cu_2Mg_9Si_7$ or $Al_4Cu_2Mg_8Si_7$) is observed from TEM micrographs and XRD pattern corresponding to this temperature. Various authors have reported this phase (Al_2Cu) as metastable θ' phase in Al-Cu-Si-Mg alloy [4.42, 4.46]. Since hardness at this temperature were observed to be less as compared to sample annealed

85

at a temperature of 100°C, the dissolution of GP zones might be possible with evolution of metastable θ' phase at this temperature. The standard DSC peak of this alloy as reported in literature [4.43] was studied and found that for this alloy, the dissolution of GP zones occurs at temperature ranging from 100°C -150°C. When cryorolled samples were annealed at 200°C, similar small size spherical particle (as in case of sample annealed at 150°C were also observed in this temperature (Fig. 4.1.4). The XRD pattern corresponding to sample annealed at 200°C also shows the peak pertaining to θ' phase (metastable Al_2Cu phase) as observed from Fig. 4.1.11. This indicates that the evolution of θ'phase is still continued at this temperature. At annealing temperature of 250°C, the significant change in microstructure and XRD pattern are observed. The evolution of fine needle shape precipitates can be observed from TEM micrographs (Fig. 4.1.6) corresponding to sample annealed at 250°C. In addition to this, spherical particles are also seen along with fine needle shape precipitates. However, the size of spherical particles observed in this temperature is more as compared to sample annealed at 150°C, and 200°C. The peak corresponding to these particles (spherical as well as fine needle) can also be observed from the XRD pattern (Fig. 4.1.11) corresponding to sample annealed at 250°C. The fine needle shape phase observed at this temperature is reported as λ' phase (metastable $Al_3Cu_2Mg_9Si_7$ or AlCuMgSi phase) by various researchers in the past [4.42, 4.46]. Fig. 4.1.7 shows the TEM micrographs corresponding to sample annealed at 300°C. At this temperature, small size spherical particles (θ' phase) become coarser and transformed in to stable θ phase (stable Al_2Cu). In addition to this, metastable λ' phase is also observed in the form of stable λ phase as observed from TEM micrograph corresponding to sample annealed at this temperature. It is observed that needle like metastable λ' phase is transformed in to stable rod like phase λ at this temperature. XRD pattern of sample annealed at 300°C is shown in Fig. 4.1.11. The peak corresponding to both phases θ' and λ' is observed in XRD plot at this temperature. The intensity of peaks of both phases is small as depicted from Fig. 4.1.11. This might be possible that both metastable phases have transformed in to their stable counterparts due to which intensity of these peak become less for the sample annealed at 300°C. Here, it is very important to note that both stable and metastable phases have same composition due to which peaks of both phases were observed at same angles [4.46]. The XRD pattern shown at this temperature also substantiates the formation of stable phases θ and λ at this temperature.

Fig. 4.1.8 shows the TEM micrograph corresponding to sample annealed at 350°C. It is clear that at this temperature, both stable θ and λ phases are observed as in case of sample annealed at 300°C; however, these phases become much coarser than the sample annealed previously at 300°C. In addition to this, number and volume fraction of these phases are observed to be more as compared to sample annealed at 300°C. The XRD result corresponding to sample annealed at 350°C also confirms the formation of stable θ and λ phases. The intensity of these phases θ and λ is   also observed to be more at this temperature as compared to sample annealed at 300°C, which confirms the higher volume fraction of these phases at this temperature.

Based on the above discussion, it may be mentioned that precipitation reaction in cryorolled Al 2014 alloy starts in the range of 50°C to 100°C with the formation of GP zones. These GP zones starts dissolving in the Al matrix with the evolution of metastable θ' phase in the temperature range of 100°C to 150°C. The evolution of metastable phase θ' is continued without precipitation of metastable λ' phase up to temperature 200°C. At the temperature of 250°C, fine needle structured metastable λ' phase starts evolving with the metastable θ' phase. Finally, these metastable phases θ' and λ' become coarser and transformed in to stable θ and λ phases in the temperature range of 250°C to 350°C.

The precipitation sequence in the present work is observed to be

$$\alpha_{sss} \quad \rightarrow \quad GPZ \quad \rightarrow \quad \theta' \quad \rightarrow \quad \theta' + \lambda' \quad \rightarrow \quad \theta + \lambda$$

It is quite different from the precipitation sequence reported by Dhal et al. [4.47] for the same alloy for the same range of annealing temperature. Dhal et al. [4.47] observed the nucleation of λ' phase after the GP zones. However, the nucleation of θ' phase is observed in the present work after the formation of GP zones. This might be due to the slight variation of composition of alloying element in Al 2014 alloy used in this work due to which θ' phase is nucleated first after the GP zone.

4.1.4.2 Influence of Cryorolling and Cryorolling followed by annealing on Mechanical properties:

In the present work, effect of annealing on the mechanical properties is investigated by performing tensile test and Vickers hardness test. The tensile strength, yield strength and hardness of solution treated Al 2014 are found to be 245 MPa, 176 MPa, and 115 HV, respectively, with 18.5% ductility. When solution treated alloy was cryorolled up to thickness reduction of 90%, the mechanical properties have significantly improved (Tensile strength

447 MPa, yield strength 428 MPa and hardness 164 HV) with reduction of ductility from 18.5% to 4.8%. The cryorolled samples shows high strengthening effect due to the grain size reduction well below than 1μm, the accumulation of high dislocation density by suppressing mobility of dislocation by cross slip and climb at liquid nitrogen temperature , and solid solution strengthening as observed from TEM micrograph corresponding to sample cryorolled up to thickness reduction 90%. Similar results were reported by Rao et al. [4.17] during cryorolling of Al 6061 alloy. The ductility of cryorolled sample is reduced as compared to solution treated sample because of reduced strain hardening ability of cryorolled Al 2014 alloy at cryogenic temperature. When cryorolled samples were annealed at 100°C, the tensile strength, yield strength and percentage elongation was significantly improved from 447 MPa to 553 MPa, 428 MPa to 510 MPa and 4.8 % to 6.3 %, respectively. As discussed earlier that, the TEM micrograph and XRD pattern do not reveal any information corresponding to this condition, except that dislocation density was slightly reduced at this temperature. However, the observed strength and ductility was more as compared to cryorolled sample. The observed high strength corresponding to sample annealed at 100°C might be more due to formation of GP zones at this temperature. These GP zones are the clusters of Cu atom in Al matrix which cannot be observed by normal TEM and XRD studies. To visualize these zones, high resolution TEM studies are required. However, the presence of these zones can also be observed through DSC studies. In the past, various researchers have performed   DSC studies on this alloy. Based on their studies, it was observed that GP zones in this alloy generally forms in the temperature range of 50°C – 100°C [4.43-4.45]. So, it may be inferred that strength corresponding to this temperature is increased due to formation of GP zones. It has been reported that these GP zones are clusters of few Cu atoms in Al matrix and forms coherent precipitates [4.44]. The clustering produces a local strain and due to which hardness of GP zones is observed to be more as compared to other precipitation sequences of this alloy. In addition to this, ductility at this temperature was observed more as compared to cryorolled samples. It is due to the fact that dislocation density gets reduced slightly at this temperature due to dynamic recovery resulting increased ductility.

When samples were annealed at 150°C, the tensile strength, and yield strength decreased from 553 MPa and 510 MPa to 511 MPa and 456 MPa, respectively, as compared to sample annealed at 100°C. However, the strength is still more than the as CR sample as well as solution treated sample. In addition to this, hardness drops from 181 HV to 174 HV with

improvement in ductility from 6.3% to 7.5% as compared to sample annealed at 100°C. The ductility is improved because at this temperature softening effect due to dynamic recovery is more as compared to sample annealed at 100°C. TEM micrograph corresponding to this condition also confirms it. The dislocation density has reduced due to dynamic recovery as compared to sample annealed previously as depicted from Fig. 4.1.2(c). Based on the discussion section 4.1.4.1, GP zones starts dissolving in the Al matrix with the formation of metastable phase θ' at this temperature. This phase is semi coherent with Al matrix as reported in literature [4.42]. It has been reported in various published work that presence of precipitates (coherent or semicoherent) in matrix offers resistance to the motion of dislocation, which results in strengthening effect [4.44]. When precipitates are fully coherent (GP zones) and semicoherent (θ" and θ' phase) with matrix, there exists a strong lattice misfit strain between precipitated particle and matrix interface as reported in the literature [4.47]. This misfit strain is responsible for obstructing the dislocation motion strongly by these coherent and semi coherent phases, which cause the strengthening effect at this temperature. However, the strength observed is comparatively lesser than the sample annealed at temperature 100°C. This is due to the fact that at 100°C, fully coherent precipitates (GP zones) are formed as discussed earlier. These GP zones have lesser activation hill as compared to θ' phase due to low surface energy and strain energy associated with it as reported in literature [4.48]. Since, the activation hill required for formation of GP zones is low with low surface energy and low strain energy, the size of critical nuclei is less and homogeneous nucleation is favored [4.48]. These GP zones (clusters of Cu atom atoms in Al matrix) are homogeneously distributed in Al matrix and provide much more strengthening effect as compared to θ' phase.

At the annealing temperature of 200°C, the tensile strength and yield strength have decreased from 511 MPa and 456 MPa to 487 MPa to 433 MPa, respectively, as compared to sample annealed at 150°C. However, the ductility (9.5%) at this temperature was observed to be more as compared to sample annealed previously at 150°C (7.5%). The TEM micrograph corresponding to this condition is shown in Fig. 4.1.2(d). The precipitation sequence at this temperature is also discussed in section 4.1.4.1. At this temperature, it is seen that metastable phase θ' is nucleated and number and volume fraction of this phase is more as compared to sample annealed at previous temperature (150°C). However, the strength observed at this temperature is less as compared to sample annealed at 150°C. It is due to the fact that during

annealing at this temperature, strengthening effect due to precipitation hardening and softening effect due to dynamic recovery are competing, which results in a compromise between strength and ductility at this temperature. TEM images corresponding to this temperature show that the dislocation density is significantly reduced at this temperature, however, precipitation of θ' phase is still continued. This suggests a slight reduction in strength with marginal improvement of ductility from 7.5% to 9.5% at this temperature as compared to sample annealed at 150°C.

When cryorolled Al 2014 alloy was annealed at 250°C, the tensile strength, yield strength and hardness suddenly drops from 487 MPa, 433 MPa, and 169 HV to 362 MPa, 310 MPa, and 123 HV, respectively, with improvement in ductility from 9.5% to 11% as compared to sample annealed at 200°C. In present work, at this temperature, both metastable phases θ' and λ' phases have evolved from the matrix as observed from precipitation sequence discussed in section 4.1.4.1. However, the number and volume fraction of metastable λ' phase was observed more as compared to metastable θ' phase as depicted from TEM micrograph corresponding to this condition. It is also observed that hardening in this alloy is primarily achieved due to formation of GP zones and metatstable phase θ'. When cryorolled samples were annealed at this temperature, two possibilities exist. The softening may occur due to dynamic recovery while other is softening due to recrystallisation effect. The decrease in strength and hardness, while rise in ductility is mainly due to formation of dislocation free equiaxed grains due to recrystallisation effect at this temperature. It may be mentioned that softening effect due to recrystallisation effect is much more dominating as compared to softening effect due to recovery effect at this temperature. In addition to this, number and volume fraction of the hardening phase θ' was also observed less as compared to λ' phase as depicted from TEM micrograph, due to which significant reduction in strength and hardness was observed at this temperature.

When samples were annealed further at a temperature of 300°C, the tensile and yield strength drops from 362 MPa and 310 MPa to 285 MPa and 201 MPa, respectively, as compared to sample annealed at 250°C with improvement in ductility from 11.8% to 13%. It is due to the transformation of metastable θ' and λ' phases in to coarser stable θ and λ phases at this temperature as discussed earlier. These phases were incoherent with the matrix and do not contribute in strengthening during annealing. The increase in ductility is observed due to formation of dislocation free equiaxed grains due to recrystallization effect at this temperature.

90

With further annealing at a temperature of 350°C, the tensile strength, yield strength, and ductility are found to be 247 MPa , 196 MPa, and 16%. The decrease in strength and rise in elongation as compared to sample annealed previously is observed, due to the coarsening of stable precipitates θ and λ and formation of equiaxed grains, which are almost free from dislocation at this temperature. From TEM micrograph (Fig. 4.1.2(g)), it is clear that grain size is larger at this temperature as compared to sample annealed previously, which means recrystallisation reaction is fast at this temperature.

4.1.4.3 Fracture surface morphology after tensile testing:

Fracture surface after tensile testing of cryorolled Al 2014 alloy was examined by SEM. Fig. 4.1.16(a) shows the fracture surface of solution treated sample after tensile testing. The void length and void width is more for the solution treated sample as compared to other processed conditions. In addition to this, most of the voids in solution treated samples have larger size with respect to sample processed for various conditions. The length to width ratio (L/W) for voids in solution treated sample is also more as observed from fractograph corresponding to solution treated sample. It has been reported that size of voids during plastic deformation controls the fracture mode [4.49]. Since the void parameters like void length, void width, void length to width ratio is more for solution treated sample, and it predominately fails through ductile manner [4.49]. When solution treated samples were cryorolled up to thickness reduction of 90%, the fracture surface consists of majority of brittle steps marked by rectangular box as depicted from Fig. 4.1.16(b). However, other fracture parameter s like void length, void width, ratio of length of void to width ratio (L/W) is slightly low for cryorolled sample as observed from Fig. 4.1.16(b). This substantiates that cryorolled sample has lower ductility than the solution treated sample. Along with brittle facets, some finer dimples can be observed from the figure corresponding to cryorolled sample (Fig. 4.1.16(b)). It is due to the fact that various nucleation sites are active in cryorolled sample due to formation of ultrafine grain and these adjacent microvoids coalesces together before they grow to a larger size as reported in literature [4.49]. In the past, various researchers have reported that fine dimples/microvoids in fracture surface generally do not contribute to ductility [4.50].
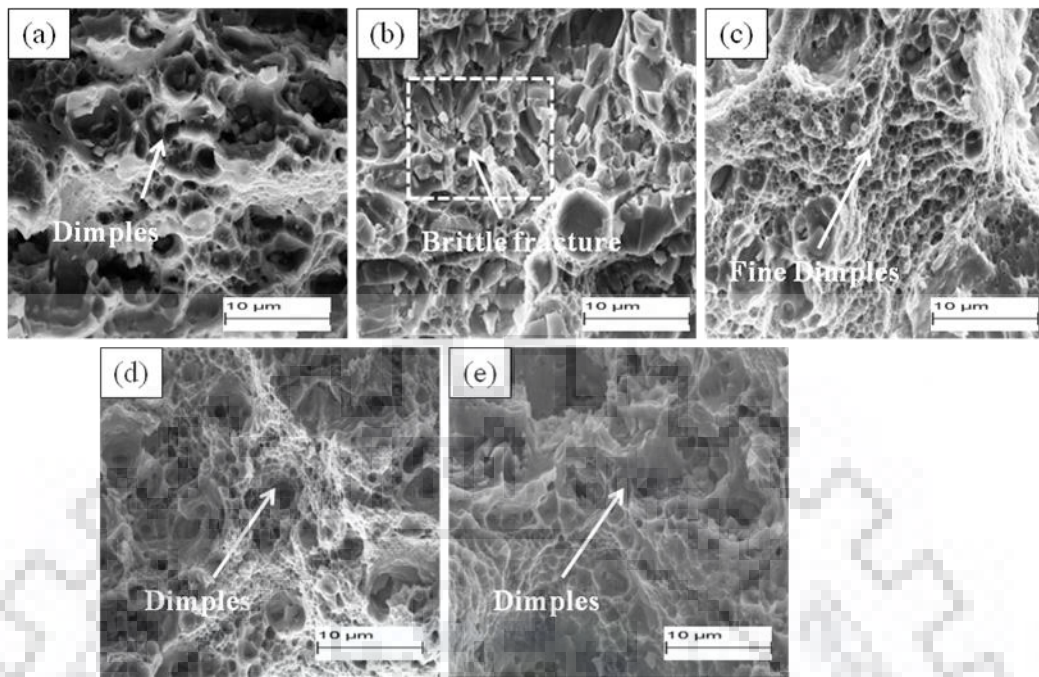
Figure 4.1.16: Fractographs of cryorolled Al 2014 alloy after tensile testing for various processed conditions : (a) Solution treated (ST) ; (b) As cryorolled (CR) ; (c) CR +100°C; (d) CR +250°C ; (e) CR +350°C

It may be mentioned that fine grains/ fine dimples facilitates in propagation of crack as reported in literature [4.51]. Once the crack is initiated in such type of systems, it moves rapidly due to which ductility is lost. This is the main reason due to which ductility of cryorolled sample was observed less as compared to solution treated alloy.

Fig. 4.1.16(c) shows the fractographs corresponding to sample annealed at 100°C. On comparing the SEM photographs for cryorolled samples and sample annealed at 100°C, it is observed that number of brittle facets has decreased in sample annealed at 100°C as compared to cryorolled sample. In addition, fracture surface of sample annealed at 100°C is entirely perturbed with numerous fine dimples/voids. However, length to width (L/W) ratio for voids in sample annealed at 100°C is less with respect to cryorolled sample. Instead of deeper dimples, shallow dimples are observed at these conditions. It has been reported that dimples can be very deep, conical shape or quite shallow depending upon the microstructure and plasticity of the material [4.49]. The formation of shallow dimples in the present case may be due to the joining of microvoid due to the shear along slip bands as reported in literature [4.49]. In addition to this, bigger dimples/voids were homogeneously distributed in the entire surface with fine dimples at this condition. Void coalescence zone consists of bigger dimples as well as fine dimples. The number and volume fraction of dimples were also observed more

92

at this temperature as compared to cryorolled sample. As we have seen previously that GP zones in this alloy were formed at 100°C. These GP zones are coherent with the matrix and homogeneously nucleated within the grain. It has been reported that microvoids nucleates at the region of localized strain discontinuity associated with small second phase particles, inclusions, grain boundaries and dislocation pile ups [4.49]. In the present work, it might be possible that fine dimples might have nucleated between the interface of GP zones and Al matrix, while large dimples were observed due to inclusion, which has larger size than the second phase particles present in Al 2014 Alloy as reported in literature [4.49]. Recently, Li et al. have reported that interface between fine precipitates (Here GP zones) and matrix provides strength to the material [4.48]. In the present work, fine dimples were nucleated at the interface of GP zones and Al matrix as discussed earlier, the strength corresponding to this condition is observed to be more as compared to cryorolled sample. The ductility corresponding to this condition was observed slightly more as compared to cryorolled samples due to the homogeneous distribution of larger as well as fine dimples in fracture surface. In such a situation, crack path does not remain straight and possibility of crack branching is more due to which crack propagation is slow and ductility is improved.

Fig. 4.1.16(d) shows the SEM micrograph corresponding to sample annealed at 250°C. At this temperature, fracture surface entirely perturbed with large number of coarser dimples. However, finer dimples were still observed, the number and volume fraction of finer dimple was observed less as compared to sample annealed previously. At this temperature, both metastable phases θ' and λ' were nucleated as discussed earlier in the section. Finer dimples were nucleated at the interface of λ' and θ' with the matrix. Since the number and volume fraction of θ' phase was observed less due to transformation of meta stable θ' phase in to stable θ phase, the number of finer dimples were observed less as compared to sample annealed at previously. In addition to this, softening effect due to recrystallisation is also continued due to which significant amount of plastic deformation takes place at this temperature. Since the hardening contribution for λ' phase was less as compared to θ' as discussed earlier, the interface between λ' phase and matrix was weak, resulting lesser strength as compared to sample annealed previously. However, the observed ductility is more as compared to sample annealed previously due to formation of dislocation free equiaxed grain and large number of coarser dimples which does not help in crack propagation resulting improved ductility of the alloy at this temperature.

93

Fig. 4.1.16 (e) shows the fracture surface corresponding to sample annealed at 350°C. At this temperature, it is observed that void coalescence zone consist of majority of larger number of bigger dimples. It has been reported that size of dimples on the fracture surface is governed by number and distribution of microvoids that are nucleated [4.50]. In addition to this, when fracture surface consists of larger dimples, the nucleation cites are few due to which microvoid grow to a large size before coalescence of microvoids. At this temperature (350°C), coarser stable precipitates are formed and the microvoids are nucleated on these second phase particles. Since the size of these precipitates is large as compared to metastable precipitate, the dimples size is observed to be more as compared to sample annealed previously. In the present work, void size and void length to width ratio observed is large for sample annealed at both temperatures (300°C and 350°C), due to which material resistance to failure has decreased resulting drop in strength and increase in ductility. The similar observations were made by Krishna et al. [4.50] during cryorolling of Al 8090 alloy.

4.1.4.4 Fracture surface morphology after 3-Point Bend Test

Fig. 4.1.17(a) shows the fracture surface morphology of solution treated sample after 3-point bend test. Fracture surface of solution treated sample consists of well developed dimples over entire surface as depicted from Fig. 4.1.17 (a). However, these dimples are elongated and conical. It is also observed from this figure that one axis of these dimples is larger than other axis. This is the characteristic of ductile tearing fracture as reported in literature [4.51]. It has been reported that dimples shape and size are governed by the state of stress within the material as microvoid form and coalesces [4.51]. In the present work, 3-point bend test is performed in Mode-1 loading in which applied loading is perpendicular to crack propagation direction. This results in a high amount of triaxiality near the crack tip, leading to the ductile tearing fracture. Fig. 4.1.17 (b) shows the fracture surface morphology of as cryorolled sample. Fracture surface consists of the fine as well as coarser elongated dimples as depicted from Fig. 4.1.17 (b). The number of fine dimples was observed to be more as compared to coarser dimples. This is due to the formation of UFG microstructure in alloy after cryorolling as discussed in previous sections. All fracture parameters such as K_Q, K_{ee}, and J integral corresponding to this condition are observed to be more as compared to solution treated sample. It may be because of the strengthening effect after cryorolling due to formation of dislocation cells, dislocation tangles and sub grains. In addition to this, the resistance to the crack growth has increased due to formation of heavily deformed microstructure in the

94

sample, resulting higher fracture toughness after cryorolling. The similar observations were made by Das et al. during the cryorolling of Al 7075 alloy [4.27].
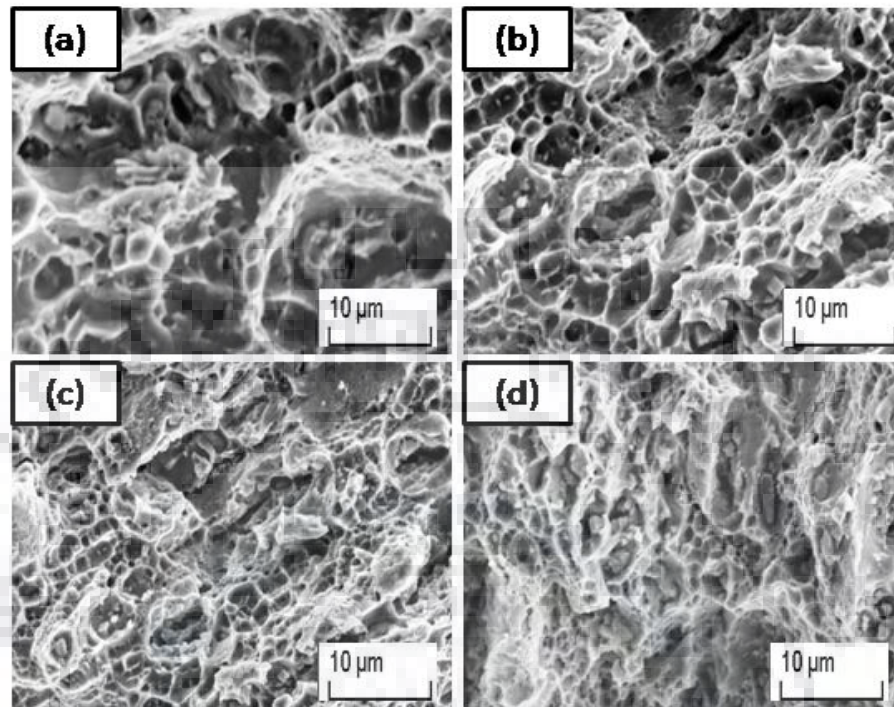
Figure 4.1.17: Fractographs of cryorolled Al 2014 alloy after 3-point bend test for various processed conditions (a) Solution treated (ST); (b) As cryorolled (CR); (c) CR +100°C; (d) CR +150°C

The SEM photograph of sample annealed at 100°C is shown in Fig 4.1.17. (c). The SEM photograph corresponding to this condition clearly reveals that fracture surface consists of majority of finer elongated dimples. The crack propagation path is transgranular, which is very narrow as compared to solution treated sample and cryorolled sample. As discussed in section 4.1.4.1 that this processed condition favours the formation of GP zones, which are homogeneously distributed in the matrix. It has been reported that large amount of fine precipitates in the matrix provides strength [4.47]. It may be possible that finer dimples may nucleate in the interface of matrix and GP zones, and these GP zones are homogeneously distributed inside the grain as discussed earlier, resulting higher strength and provide more resistance to crack growth. In addition to this, the crack initiation in such system is difficult, resulting higher fracture toughness observed at this condition.

The Fig. 4.1.17(d) shows the SEM micrograph corresponding to sample annealed at 150°C after 3-point bend test. From this figure, it is evident that fracture mode is

95

transgranular as in case of sample annealed previously. However, the number of finer dimples observed is less as compared to sample annealed at 100°C. As discussed previously that this temperature favours the dissolution of GP zone with evolution of few spherical shape metastable precipitate θ'. Due to the dissolution of GP zones, finer dimples were observed less at this temperature. The fracture toughness of aluminum alloys is influenced by many factors such as crystal structure, coarse impurity particle of intermetallic phases, precipitate free zone, and precipitate located on grain and at grain boundaries [4.48]. Li et al. [4.48] have reported that if the matrix and grain boundaries have a big strength difference, the fracture toughness will decrease due to ease of initiation of crack at the interface. At this temperature, few spherical metastable particles were observed as discussed earlier. The interface between these particle and matrix is slightly brittle as compared to GP zone and matrix. This interface might be the crack initiation and propagation source due to which a low value of fracture toughness is observed as compared to sample annealed previously. However, fracture toughness is observed to be still more as compared to solution treated and cryorolled sample due to the formation of dislocation substructure and metastable precipitates.

Fig. 4.1.18(a) shows the fracture surface morphology of sample annealed at 200°C after 3- point bend test. Fracture surface corresponding to this condition was observed to be approximately same as sample annealed at 150°C. However, the fine dimpled features was more as compared to sample annealed at 150°C. This might be due to the complete dissolution of GP zones and formation of larger number of metastable precipitates θ' with respect to sample annealed at 150°C. Fracture mode was still observed as transgranular tearing fracture. In the present work, the fracture toughness observed at this temperature was less as compared to sample annealed previously due to two reasons. Firstly, Crack initiation has become easy due to recovery effect and formation of equiaxed grain corresponding to this condition as reported in literature [4.48]. Secondly, some of the second phase particles may nucleate at the grain boundaries due to particle stimulated nucleation as reported in literature [4.31] and become the crack initiating source resulting decrease in fracture toughness parameters at this condition.The Fig. 4.1.18 (b) shows the fracture surface morphology of sample annealed at 250°C. The fracture surface appearance after 3-point bend test was observed nearly same as sample annealed at 200°C. This is due to the formation of metastable λ' phase at this temperature as observed from TEM and XRD studies. The fracture toughness parameters at this temperature were observed less as compared to sample annealed previously

due to the precipitation of metastable λ' phase. It shows a less hardening effect as compared to θ' phase which facilitates crack initiation resulting lowered value of fracture toughness.
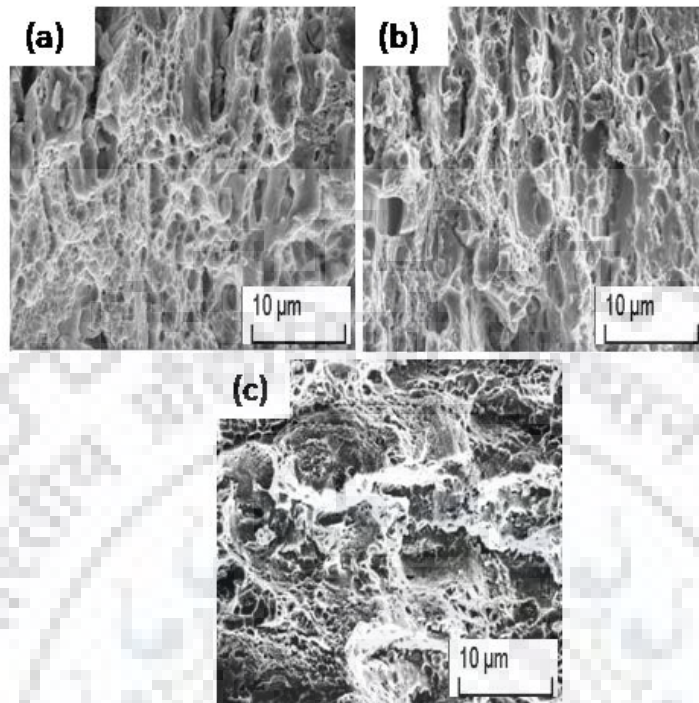
Figure 4.1.18: Fractographs of cryorolled Al 2014 alloy after 3-point bend test for various processed conditions (a) CR +200°C; (b) CR +250°C; (c) CR +350°C

It has been reported that fracture toughness in fiber textured alloy is good as compared to alloy having highly recrystallized structure or equi axed grains morphology [4.48]. Based on this fact, it may be mentioned that combined recovery and recrystallisation have facilitated the grain coarsening resulting reduced fracture toughness at this temperature.

Fig. 4.1.18 (c) shows the fracture surface morphology of sample annealed at 350°C. The significant change in fracture surface is observed at this condition. The number of dimpled features becomes less as compared to sample annealed previously. In some of the zone, brittle facets are also observed as depicted from Fig. 4.1.18 (c). From this micrograph, it is evident that crack has propagated rapidly leaving the brittle facets/cleavage facets. This might be due to evolution of coarser stable precipitates θ and λ which are brittle in nature. Once the crack is initiated on these particles, it moves rapidly resulting lower fracture toughness parameters corresponding to this sample condition. The similar fracture surface was observed for the sample annealed at 300°C due to formation of stable precipitates, which are coarser and brittle and help in crack propagation.

4.1.5 Conclusions

The influence of cryorolling and cryorolling followed by annealing on precipitate evolution, tensile properties and fracture toughness of Al 2014 alloy have been studied and following conclusions were made on the basis of experimental findings of the present work.

- The cryorolling is effective to improve the mechanical properties such as tensile strength (245 MPa-447 MPa) and yield strength (176 MPa-428 MPa) of Al 2014 alloy as compared to starting solution treated alloy due to formation of UFG microstructure, dislocation tangled zones, and dislocation substructure. However, the drop in % elongation (18.5%-4.8%) is observed due to lack of strain hardening ability of cryorolled Al 2014 alloy as compared to solution treated alloy.

- Annealing at 100°C for 45 minutes results in improvement of strength (UTS 447 MPa-553 MPa) and slight improvement of ductility (4.8%-6.3%) as compared to cryorolled Al 2014 alloy due to formation of GP zones and recovery effect at this temperature. With further annealing from 100°C -200°C, the slight drop in strength was observed due to the dissolution of GP zone and formation of metastable precipitate Al_2Cu. This drop in strength was drastic in the temperature ranging from 200°C -350°C due to formation of metastable phase $Al_3Cu_2Mg_9Si$ followed by stable coarser precipitates Al_2Cu and $Al_3Cu_2Mg_9Si$. However, the ductility is improved with increasing annealing temperature due to dynamic recovery (which results softening) and recrystallisation resulting formation of dislocation free equiaxed grain.

- The trend of variation of typical fracture parameters K_Q, K_{ee}, J integral with annealing temperature was observed to be same as tensile properties i.e fracture toughness parameters of cryorolled Al 2014 alloy was observed to be more as compared to solution treated alloy. After annealing in the range of 100°C -350°C, fracture toughness parameters were observed to be more at 100°C due to formation of coherent GP zones while annealing after 100°C -350°C, the drop in fracture toughness parameters were observed due to combined phenomenon of precipitation, softening due to dynamic recovery and recrystallisation.

- The fracture surface morphology after tensile test revealed the typical ductile fracture with coarser dimples for solution treated alloy. After cryorolling up to thickness reduction of 90%, fracture surface consists of majority of fine dimples due to formation of UFG microstructure. After annealing from temperature ranging from 100°C -350°C, the bimodal dimpled features were observed in fracture surface. The failure mechanism of solution treated and cryorolled alloy after 3-point bend test was observed as ductile tearing fracture. However, with

98

increasing annealing temperature up to 250°C, the failure mechanism was transgranular ductile tearing fracture and transforms in to transgranular brittle fracture in the temperature range of 250°C -350°C.

4.2 Influence of Cryorolling and followed by annealing on High Cycle Fatigue behavior of Ultrafine Grained Al 2014 alloy

4.2.1 Introduction

In the past few years, the improved mechanical properties of ultrafine grain material produced by severe plastic deformation (SPD) techniques as compared to bulk materials have been well reported in the literature (4.52- 4.54). The ultrafine grain (UFG) Al alloy processed by severe plastic deformation (SPD) methods shows a very good combination of tensile strength, yield strength, hardness and toughness, which enables these material suitable for light weight structural applications in automotive and aerospace engineering [4.53-4.54]. However, in addition to the primary properties of these ultrafine grain (UFG) alloys such as tensile strength and hardness, its fatigue behavior is very essential for the structural components experiencing dynamic loads during service conditions. Therefore, the fatigue test can provide the comprehensive and diversified deformation behavior of material under cyclic loading as compared to monotonic loading [4.54].

The Wohler's popular work on fatigue has shown that if the uniaxial stress is far below a static strength of the material, no damage would occur to the material or structure. However, if the same load is applied cyclically/repeatedly many times, it will lead to a complete fracture of the material [4.55]. The fatigue failure is now indentified as one of the major problems of structure, machineries, bridges and pressure vessels where they experience cyclic loading. Therefore, ultrafine grain (UFG) material processed by severe plastic deformation (SPD) methods ought to be tested for fatigue life under cyclic loading. Unfortunately, fatigue studies of ultrafine grain (UFG) material fabricated by severe plastic deformation (SPD) methods is difficult due to complex testing procedure under cyclic loading as well as the requirement of larger sized specimens for conducting fatigue test to meet ASTM standards. In the recent years, the effect of cyclic loading on bulk ultrafine grain (UFG) alloy fabricated by severe plastic deformation (SPD) methods has been reported. Meyer et al. [4.56] have investigated the crack growth behavior of equal channel angular pressing (ECAP) processed AA6063 under cyclic loading for the coarse grain structure, bimodal structure, and monomodal

ultrafine grained (UFG) structure and reported that ultrafine grain (UFG) structure have faster crack growth rate and lower fatigue threshold value as compared to coarse grain structure under low cycle fatigue regime. Khatib et al. [4.57] compared the high cycle fatigue performance of high pressure torsion (HPT) processed Cu with the coarse grain (CG) Cu using miniaturized specimen under symmetrical loading. They observed that at higher stress amplitude (180 MPa) and up to the 10^7 loading cycle, fatigue strength of HPT processed Cu is more as compared to coarse grain (CG) Cu due to nanocrystalline microstructure. However, at lower stress amplitude and above 10^7 loading cycle, fatigue resistance of HPT processed Cu is decreased as compared to coarse grain (CG) Cu due to grain coarsening/cyclic softening in this regime. Vinogradov [4.58] has reported a detailed review on fatigue crack initiation and fatigue crack growth behavior of ultrafine grain (UFG) material produced by severe plastic deformation (SPD) methods and shown that fatigue strength of ultrafine grain (UFG) materials with planar slip follows the Hall-Petch relationship in the same way as the yield strength of coarser grain material.

$$\sigma_f = \sigma_{0f} + k_f\, d^{-1/2} \tag{4.7}$$

Where σ_{0f} and k_f are the material properties and σ_f is the fatigue strength. $\sigma_{0f} =$ friction stress representing the overall resistance of the crystal lattice to dislocation movement, $k =$ the locking parameter which measures the relative hardening contribution of the grain boundaries. However, fatigue strength of FCC materials with high stacking fault energy showing wavy slip does not have any effect on grain size due to formation of cell structure. Cavaliere et al [4.59] have made the extensive review on the fatigue properties of ultrafine grain (UFG) and nanocrystalline materials and concluded that high cycle fatigue strength of ultrafine grain (UFG) materials generally depends upon crack initiation phase while low cycle fatigue strength of materials is dependent on crack propagation phase. In their study, it was revealed that low cycle fatigue resistance in the region of intermediate to high plastic strain amplitude has decreased for ultrafine grain (UFG) material while high cycle fatigue resistance in the region of intermediate to low plastic strain amplitude has increased with the reduction in grain size [4.59]. The similar results were reported by Landgraf [4.60] and Morrow [4.61] and it was shown that high cycle fatigue strength of the material depends upon elastic strength of the material; while low cycle fatigue of the material is governed by fatigue ductility. Based on

their study, it can be shown that total strain range is sum of elastic and plastic strain range and is expressed by the following relationship [4.59-4.60].

$$\frac{\Delta\varepsilon_t}{2} = \frac{\Delta\varepsilon_{el}}{2} + \frac{\Delta\varepsilon_{pl}}{2} \qquad (4.8)$$

$$\frac{\Delta\varepsilon_t}{2} = \frac{\sigma_f'}{E}(2N_f)^b + \varepsilon_f'(2N_f)^c \qquad (4.9)$$

Where $\Delta\varepsilon_t$, $\Delta\varepsilon_{el}$ and $\Delta\varepsilon_{pl}$ are total, elastic, and the plastic strain ranges, σ_f' is the fatigue strength coefficient, $2N_f$ is the number of cycles to failure, ε_f' is the fatigue ductility coefficient, 'b' is fatigue strength exponent and 'c' is fatigue ductility exponent. However the above equation (4.8) and (4.9) are much more useful for low cycle fatigue as compared to high cycle fatigue.

An et al. [4.62] have studied the cyclic deformation response of ultrafine-grained (UFG) Cu and nanocrystalline (NC) Cu-Al processed by ECAP by implementing high cycle fatigue (HCF) and low cycle fatigue (LCF)) tests. They revealed that high cycle fatigue and low cycle fatigue performance of metals and alloys are influenced prominently by stacking fault energy (SFE) in ultrafine grain (UFG) and nanocrystalline (NC) Cu/Cu-Al alloys. The improved high cycle fatigue and low cycle fatigue life were observed for nanocrystalline (NC) Cu-Al with decreasing stacking fault energy (SFE) resulting simultaneous increase in monotonic strength, ductility as well as decreased cyclic softening behavior as reported in their work. For years, researchers have proposed that fatigue strength of metals and alloys can be enhanced by improving the tensile strength. However, this strategy for improving fatigue strength of metals and alloys has found to be imperfect as reported in literature [4.63]. Recently, Liu et al. [4.63] have proposed the new strategy for improving the high cycle fatigue strength of Cu-15 at.% Al alloy having moderate grain size. They reported that significant amount of damage reduction can contribute and supplement to the strengthening methods for remarkable improvement in high cycle fatigue strength of Cu-15 at. % Al alloy resulting from microstructural optimization, which facilitates the reduced initial damage due to severe plastic deformation (SPD) processing. The recrystallized ultrafine grain (UFG) microstructure produced by cold rolling and annealing has been identified as optimized microstructure, which prevents the local strain concentration/damage and helps in raising the high cycle fatigue strength as reported in their work. It may be mentioned that fatigue behavior of ultrafine grain material (UFG) ought

to be explored further for providing general pathway so that these materials can be used for long term high strength structural applications.

Most of the earlier work on high cycle fatigue (HCF) and low cycle fatigue (LCF) properties has focused to achieve the improved fatigue resistance in ultrafine grain (UFG) single phase metals produced by equal channel angular pressing (ECAP) especially in Cu, Ni, Ti, pure Al [4.64-4.68] and non heat treatable Al-Mg alloy [4.69]. However, very limited information is available on fatigue performance of age hardenable Al alloys fabricated by SPD techniques. In the last two decades, various severe plastic deformation (SPD) techniques such as equal channel angular pressing (ECAP) [4.70-4.71], high pressure torsion (HPT) [4.72], accumulative roll bonding (ARB) [4.73], cyclic-extrusion-compression (CEC) [4.74] and repetitive corrugation and straightening (RCS) [4.75] have been developed to refine grain size of material from sub micron meter to nanometer range. However, ultrafine grain (UFG) material produced by severe plastic deformation (SPD) processes is in limited quantity due to restriction of sample dimensions obtained after these processes [4.19]. In addition to this, scaling of these processes is also quite complex. It has been reported that 46% of Al alloys in the form of continuous sheets and plates are used extensively in aerospace, construction and automotive industries [4.76]. Therefore, cryorolling has emerged as a promising route for producing ultrafine grain (UFG) microstructure in metals and alloys. Another advantage of producing ultrafine grain (UFG) microstructure through cryorolling over severe plastic deformation (SPD) methods is due to the difference in grain fragmentation process and nature of grain boundary character. In cryorolling, grain fragmentation is facilitated through suppression of dynamic recovery at cryogenic temperature; while simultaneous occurrence of dynamic recovery and recrystallisation contributes to the grain refinement in severe plastic deformation (SPD) methods [4.77]. The deformation behaviour of various bulk ultrafine grain (UFG) Al 6061 [4.78], Al 6063 [4.79], Al 7075 [4.18] and Al 5083 [4.21] alloy under monotonic loading has been well studied in the past. However, the influence of cyclic loading on the fatigue performance of bulk ultrafine grain (UFG) Al alloys fabricated by cryorolling is limited in the literature. Al 2xxx series are extensively used in high strength structural applications and aircraft structural parts [4.2]. Al 2014 alloy is one of most popularly used element of 2xxx series in light weight structural applications [4.1]. Strengthening in this alloy is achieved through age hardening process [4.30]. In addition to this, short term and long term annealing treatment may be used to improve the mechanical properties of this alloy. Usually,

severe plastic deformation (SPD) processed or cryorolled material has unstable microstructure due to the presence of irregular grain boundaries and high dislocation density [4.47]. Such type of microstructure is not suitable for high strength and high speed applications where the minimum toughness and formability are required [4.30,4.47]. Also, the cyclic hardening and cyclic softening behaviour during fluctuating load largely depends upon the nature/amount of solutes in solid solution and shape, size and morphology of second phase particles. It has been reported that solute atoms and precipitate particles emerge out from the matrix during annealing treatment and obstruct the motion of dislocation by suppressing recovery, recrystallisation and grain growth [4.80-4.81]. The age hardenable Al 2014 alloy contains Cu, Si, Mg, and Mn as major alloying elements. The various phases/precipitates evolved during post CR annealing of this alloy are GP zones, metastable θ' phase (Al_2Cu) and metastable λ' phase (AlCuMgSi) and have been published in the our earlier work [4.82]. The shape, size, and morphology of these precipitates greatly affect the fatigue resistance of this alloy, which has not been reported so far. Therefore, the present work was focused to investigate the effect of grain refinement and precipitates/second phase particles on high cycle fatigue resistance of bulk ultrafine grain (UFG) Aluminum 2014 alloy processed through cryorolling and followed by annealing in the temperature range from 100°C to 250°C for the duration of 45 minutes. The detailed microstructural characterizations of the processed Al alloy through SEM and TEM were made to substantiate fatigue behaviour of the alloy.

4.2.2 Experimental

The 2014-T6 Aluminum alloy was purchased from Bharat Aerospace Metals Private Limited Mumbai, India in the form of 40 mm thick plate. The elemental composition of the alloy has been described in earlier section and Chapter 3. The as received 2014 Al plate was machined in to prismatic samples of dimensions 80 mm x 60 mm x 12 mm and solutionised at 505°C for 2 hours to remove any dislocation present previously and quenched in water at room temperature. These samples were cryorolled (CR) up to a thickness reduction of 75%. The cryorolling of solution treated (ST) samples were performed by immersing the solution treated (ST) samples in to liquid nitrogen (-196°C) for 20 minutes before first pass and 10 minutes after each successive rolling pass. The cryorolled (CR) samples were subjected to annealing (CR+AN) for 45 minutes for four different temperatures of 100°C, 150°C, 200°C, and 250°C. The various samples naming with their corresponding processing condition has been shown in Table 4.2.1. The mechanical behavior of solution treated (ST), cryorolled (CR),

cryorolled followed by annealed (CR+AN) samples was investigated by performing tensile test and hardness test through H25K-S Tinius Oslen tensile testing machine and Vickers hardness tester, respectively. The tensile tests were performed at a constant crosshead speed and at a strain rate of 5×10^{-4} S^{-1} and the samples were prepared as per ASTM E-8 sub size standard. To investigate the fatigue resistance of solution treated (ST), cryorolled (CR), cryorolled followed by annealed (CR+AN) alloy, fatigue tests were performed on 50 kN load cell INSTRON 88 servo hydraulic axial fatigue testing machine at a stress controlled mode. The samples for high cycle fatigue test were prepared by following ASTM E466-07 standard. The fatigue tests were conducted in axially loaded specimens under constant stress amplitude. The stress ratio R is taken as 0.1 while frequency of the test is maintained at 20 Hz with sinusoidal waveform for all the processed conditions. The microstructural characteristics of solution treated (ST), cryorolled (CR), and cryorolled followed by annealed (CR+AN) samples before fatigue tests and after fatigue tests were characterized by TEM. The details of TEM sample preparation has been explained in Chapter 3 and our earlier published work (83). The fracture surface morphology of fatigued samples for all processed conditions after fatigue test was examined by FE SEM Quanta 200. All TEM and SEM studies were carried out for the samples tested at constant stress amplitude of 110 MPa in the present work. The experimental flow diagram in the present work is shown in Fig. 4.2.1.

Table 4.2.1: Abbreviations for various sample conditions in the present work

Sample name	Processing conditions
ST	As received Al 2014 alloy solution treated at 505°C for 2 hours and water quenched
CR	ST alloy cryorolled up to thickness reduction 75%
CRF	Cryorolled alloy after fatigue test
$CR + AN_{100-250}$	Cryorolled followed by annealed at various temperatures starting from 100°C to 250°C with the interval of 50°C for the duration of 45 minutes
$CR+ANF_{100-250}$	Cryorolled followed by annealed at various temperature starting from 100°C to 250°C with the interval of 50°C after high cycle fatigue testing
$CR+AN_{100}$	Cryorolled followed by annealed at 100°C
$CR+AN_{150}$	Cryorolled followed by annealed at 150°C
$CR+AN_{200}$	Cryorolled followed by annealed at 200°C
$CR+AN_{250}$	Cryorolled followed by annealed at 250°C
$CR+ANF_{100}$	Cryorolled followed by annealed alloy at 100°C after fatigue testing
$CR+ANF_{150}$	Cryorolled followed by annealed alloy at 150°C after fatigue testing
$CR+ANF_{200}$	Cryorolled followed by annealed alloy at 200°C after fatigue testing
$CR+ANF_{250}$	Cryorolled followed by annealed alloy at 250°C after fatigue testing
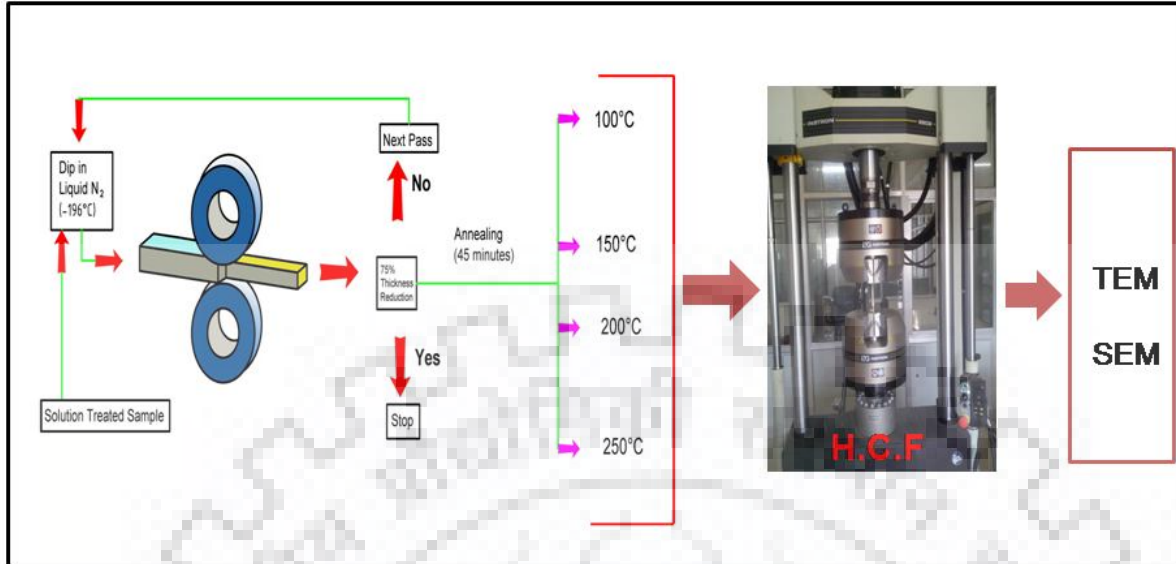
Figure 4.2.1: Experimental flow diagram for fatigue testing

4.2.3 Results

4.2.3.1 Microstructure

Microstructural features of solution treated (ST) and cryorolled (CR) samples were observed by using optical microscopy in this work. The optical micrograph of solution treated Al 2014 alloy has been shown in Fig. 4.2.2(a).
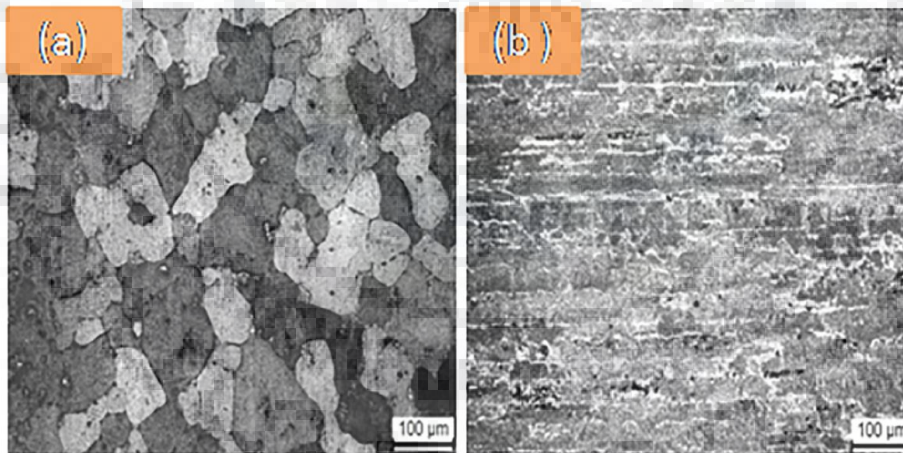
Figure 4.2.2: Optical micrograph of Al 2014 alloy: (a) Solution Treated; (b) CR 75%

It is clear from this figure that initial microstructure of solution treated (ST) Al 2014 alloy shows mixed type of grains, some of the grains are equiaxed larger size , some are slightly elongated and some smaller grains, whose grain size is approximately 50 μm are nucleated in the vicinity of elongated grain. The grain size in the starting material varies in the

range of 50 – 120 μm. Fig. 4.2.2(b) shows the optical microstructure of CR Al 2014 alloy. On cryorolling (CR) up to thickness reduction of 75%, these grains are elongated in the rolling direction as evident from the Fig. 1(b). The well defined grain boundaries of solution treated (ST) samples were transformed in to ill-defined grain boundaries after cryorolling. These boundaries are known as dislocation cell boundaries, which subsequently transformed in to ultrafine grains. However, ultrafine grains in cryorolled (CR) samples are characterised through TEM studies due to limitation of optical microscopy.

The TEM microstructure of cryorolled (CR) alloy before fatigue testing is shown in Fig. 4.2.3(a) and Fig. 4.2.4(a)-(b). The microstructure of cryorolled (CR) sample before fatigue testing exhibits highly deformed microstructure with ill defined grain boundaries. The entire microstructure is perturbed with diffused and irregular grain boundaries along with dislocation tangling zone and dense dislocation walls (DDWs).
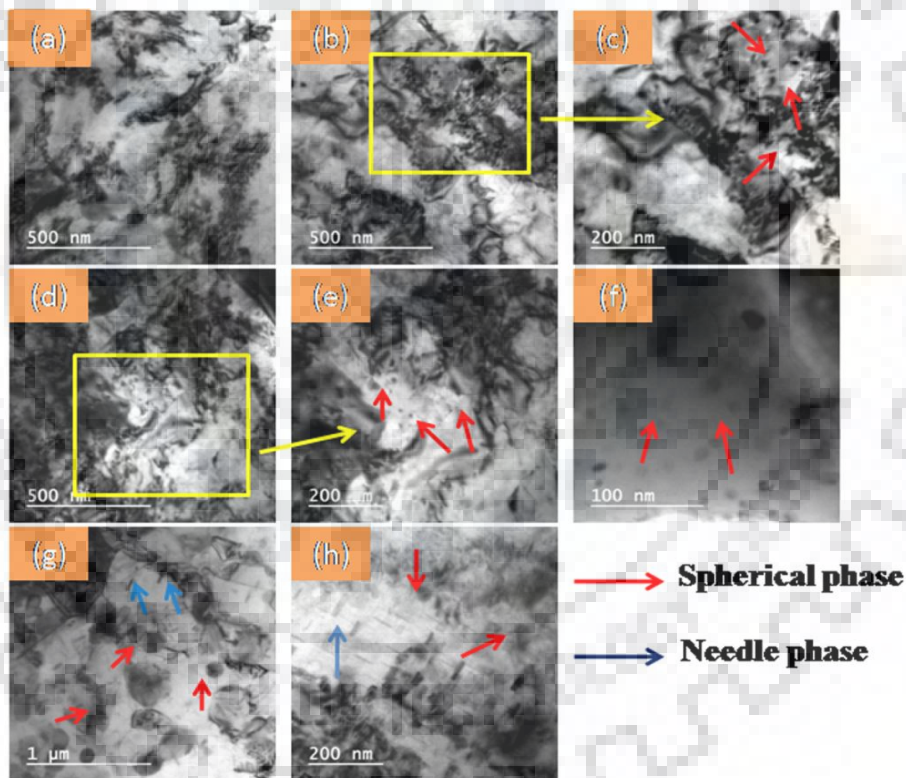
Figure 4.2.3: TEM micrographs of Al 2014 alloy for various processing conditions ; (a) CR Al 2014 alloy (b) CR+AN$_{100}$ Al 2014 alloy (c) CR+AN$_{100}$ Al 2014 alloy at higher magnification (d) CR+AN$_{150}$ Al 2014 alloy (e) CR+AN$_{150}$ Al 2014 alloy at higher magnification (f) CR+AN$_{150}$ Al 2014 alloy at higher magnification (g) CR+AN$_{250}$ Al 2014 alloy (h) CR+AN$_{250}$ Al 2014 alloy at higher magnification

The selected area electron diffraction (SAED) pattern corresponding to cryorolled (CR) condition is shown in Fig. 4.2.4(a) as inset reveals the elongated spots which substantiate the highly deformed microstructure with ill defined grain boundaries due to presence of ultrafine grains. Fig. 4.2.4(c)-(d) depicts the TEM microstructure of cryorolled (CR) Al 2014 sample after fatigue testing (CRF). Comparison of the microstructure of CR and cryorolling followed by fatigue tested alloy (CRF), has shown no significant change in the microstructure as depicted from Fig. 4.2.3 (a) and Fig. 4.2.4(a)-(d). However, a slight change in arrangement of dislocations can be noticed in fatigue tested sample as observed from Fig. 4.2.4(c) and Fig. 4.2.4(d). The dislocations in the fatigued sample are arranged in the form of banded structure along with dislocation tangled and DDWs (Fig. 4.2.4(c)).
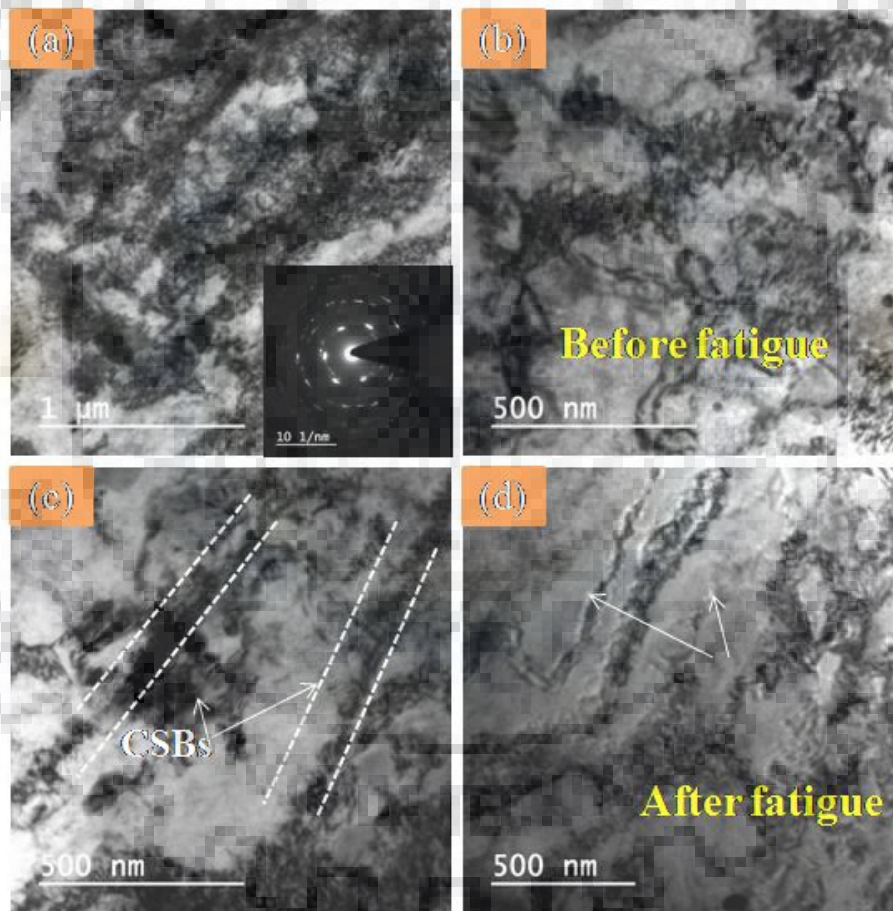
Figure 4.2.4: TEM micrographs of CR Al 2014 alloy before and after fatigue test (a) CR Al 2014 before fatigue test; (b) CR Al 2014 at different sample location before fatigue test; (c) CRF Al 2014 alloy; (d) CRF Al 2014 alloy at different sample location

TEM micrographs of same sample at different location are shown in Fig. 4.2.4(d). These bands are also observed in these locations, but dislocation density is slightly less as compared to Fig. 4.2.4(a)-(b). The similar results were reported by Malekjani et al [4.77] during low cycle fatigue testing of Al 2024 alloy.

The TEM micrograph corresponding to sample annealed at 100°C (i.e. CR+AN$_{100}$) before fatigue testing is shown in Fig. 4.2.3(b)-(c), and Fig. 4.2.5(a)-(b). Fig. 4.2.3(c) and Fig. 4.2.5(b) are the higher magnification TEM micrographs at this annealed condition. It depicts that after annealing of cryorolled (CR) samples at 100°C, a slight reduction in the dislocation density is observed due to the rearrangement of dislocations in to subgrains. It also shows the evolution of very few fine spherical phase (marked by arrow) as observed from higher magnification TEM micrographs.
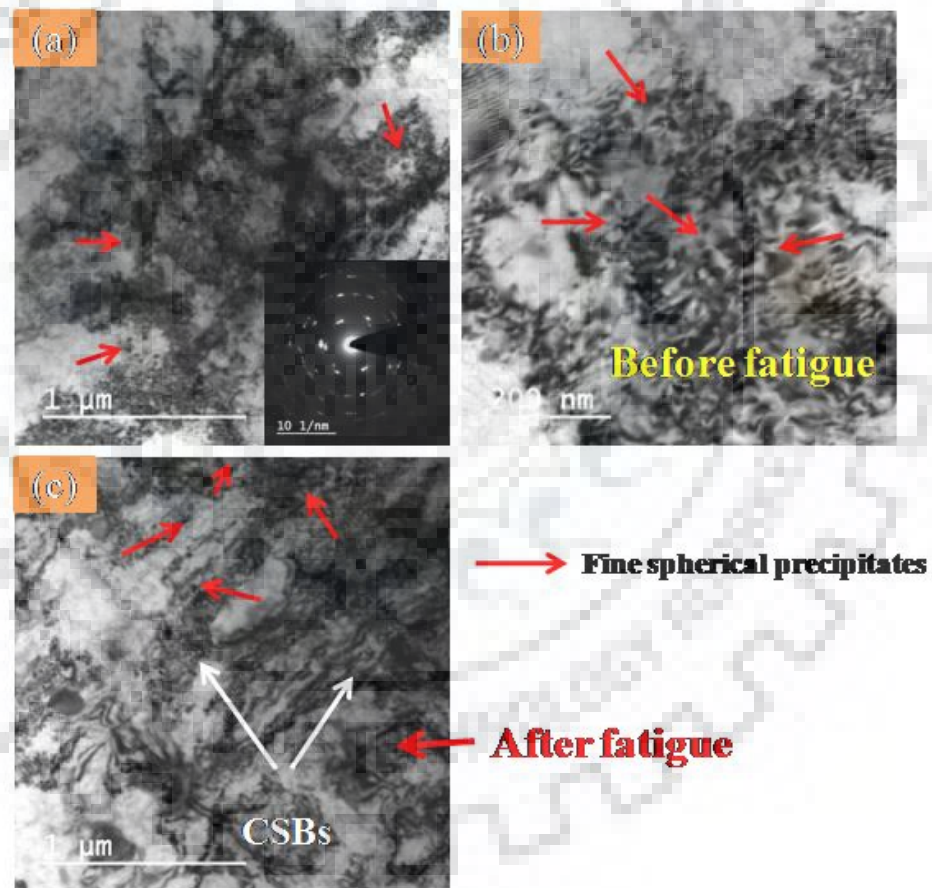
Figure 4.2.5: TEM micrographs of cryorolled followed by annealing of Al 2014 alloy at 100°C before and after fatigue test (a) CR+AN$_{100}$ Al 2014 alloy; (b) CR+AN$_{100}$ Al 2014 alloy at different sample location; (c) CR+ANF$_{100}$ Al 2014 alloy

The SAED pattern corresponding to this sample condition (shown as inset in Fig. 4.2.5(a)) is quite similar as observed for cryorolled (CR) sample (Fig. 4.2.4(a)). However, rings are slightly continuous as compared to cryorolled (CR) sample. The TEM micrograph of the sample annealed at 100°C after fatigue testing (CR+ANF$_{100}$) is shown in Fig. 4.2.5(c). The dislocation density is very high as compared to sample processed at previous annealed condition as evident from this figure. The banded structure of dislocation (marked by white arrow) is also observed for annealed alloy at this temperature after fatigue testing. However, the densities of these bands are quite high as compared to cryorolled followed by fatigue tested (CRF) samples. It indicates that cyclic deformation increases the dislocation density in the fatigue tested (CR+ANF$_{100}$) sample as compared to recovery effect at this temperature for annealed sample i.e (CR+AN$_{100}$) sample. A few fine spherical phase (marked by red arrow) is also observed after fatigue testing at this processed condition.

Fig. 4.2.3(d)-(f) and Fig. 4.2.6(a)-(b) shows TEM micrographs of cryorolled sample annealed at 150°C (i.e. CR+AN$_{150}$ sample condition). Fig. 4.2.3(e)-(f) and Fig. 4.2 6(b) are the higher magnification micrographs corresponding to this condition.
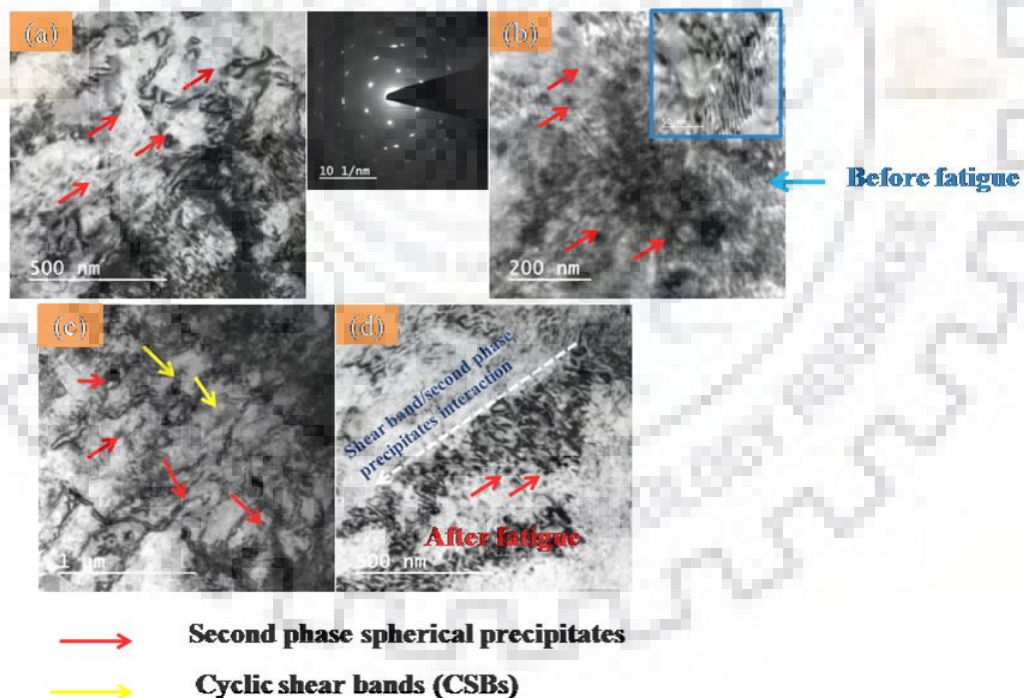
Figure 4.2.6: TEM micrographs of cryorolled followed by annealing of Al 2014 alloy at 150°C before and after fatigue test, (a) CR+AN$_{150}$ Al 2014 alloy; (b) CR+AN$_{150}$ Al 2014 alloy at higher magnification   (c) CR+ANF$_{150}$ Al 2014 alloy;   (d) CR+ANF$_{150}$ Al 2014 alloy at different sample location

On annealing at 150°C, dislocations in the sample are gradually reduced through annihilation process and transformed in to sub grain walls without noticeable change in the microstructure. However, the numbers of sub grains are more as compared to cryorolled followed by annealed at 100°C (CR+AN$_{100}$) sample. It may be mentioned that some of the ill defined grain boundaries are recovered, relaxed and rearranged in to sub grains at this process condition. In addition to this, some of the fine spherical precipitates (marked by arrow) are also observed during annealing of cryorolled (CR) alloy at 150°C as depicted from these figures. Moreover, these precipitates size were also slightly larger than the sample processed at 100°C. The SAED pattern corresponding to Fig. 4.2.6 (a) at this sample condition is shown. The rings become much more continuous as compared to sample annealed previously. Moreover, the some elongated along with broader spots were observed on the SAED pattern of Fig. 4.2.6 (a) resulting from recovery associated at this temperature. The TEM microstructure for fatigue tested alloy at this annealed condition (CR+ANF$_{150}$) sample is shown in Fig. 4.2.6(c)-(d). The microstructure of annealed sample (without fatigue testing) (CR+AN$_{150}$) sample and fatigue tested sample at this annealing condition (CR+ANF$_{150}$) sample do not show any significant changes in precipitates/sub grain size. However, the fatigue induced slip bands (marked by yellow arrow in Fig. 4.2.6(c) and marked by straight line in Fig. 4.2.6(d) oriented at 45^{0} along the rolling direction are prominent in fatigue tested sample (CR+ANF$_{150}$). The spherical precipitates evolved at this temperature also observed for fatigue tested (CR+ANF$_{150}$) sample. The TEM micrograph of cryorolled (CR) sample after annealing at 200°C (CR+AN$_{200}$) is shown in Fig. 4.2.7(a)-(b).The significant decrease in the dislocation density is observed at this process condition. The spherical precipitates observed at this annealing condition are also seen at this condition. In addition to this, sub grains formed at this condition are slightly bigger than the sample annealed at 150°C i.e (CR+AN$_{150}$) sample condition. However, the grain sizes are still within the ultrafine regime. The volume fraction of spherical precipitates are more for (CR+AN$_{200}$) sample with respect to (CR+AN$_{150}$) sample as noticed from Fig. 4.2.7(a)-(b). However, these second phase precipitates became slightly coarser as compared to sample annealed at 100°C and 150°C. The SAED pattern (shown as inset in Fig. 4.2.7(a)) in this sample condition are mostly continuous rings suggesting large number of subgrains resulting from recovery and recrystallisation process at this condition.
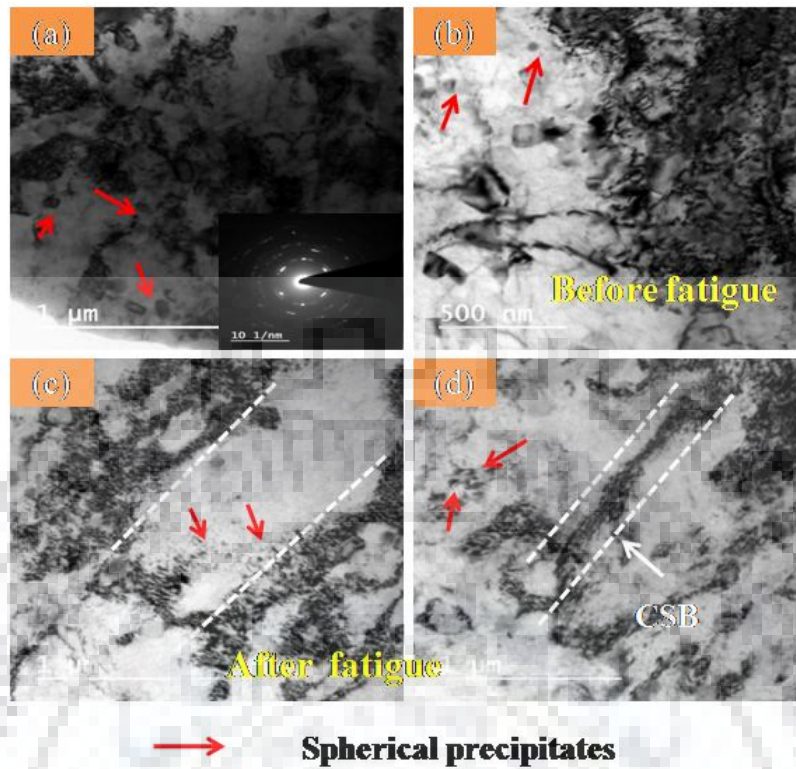
Figure 4.2.7: TEM micrographs of cryorolled followed by annealing of Al 2014 alloy at 200°C before and after fatigue test , (a) CR+AN$_{200}$ Al 2014 alloy ; (b) CR+AN$_{200}$ Al 2014 alloy at different sample location ; (c) CR+ANF$_{200}$ Al 2014 alloy ; (d) CR+ANF$_{200}$ Al 2014 alloy at different sample location

The TEM micrograph of the sample annealed at 200°C after fatigue testing (CR+ANF$_{200}$) is shown in Fig. 4.2.7(c)-(d) at various sample locations. The cyclic hardening and softening have induced the shear bands (marked by dotted straight lines) in the fatigue tested sample (CR+ANF$_{200}$) at this annealing condition as observed from TEM micrographs (Fig. 4.2.7(c)-(d)). Since these shear bands are developed during fatigue loading, it can be referred as fatigue induced cyclic slip bands (CSBs) as reported in the literature [4.84]. The small spherical precipitate particles pinning the boundaries of shear bands are seen from Fig. 4.2.7(c)-(d). The fatigue induced cyclic shear bands are less for fatigue tested (CR+ANF$_{200}$) sample as compared to (CR+ANF$_{150}$) sample.

111
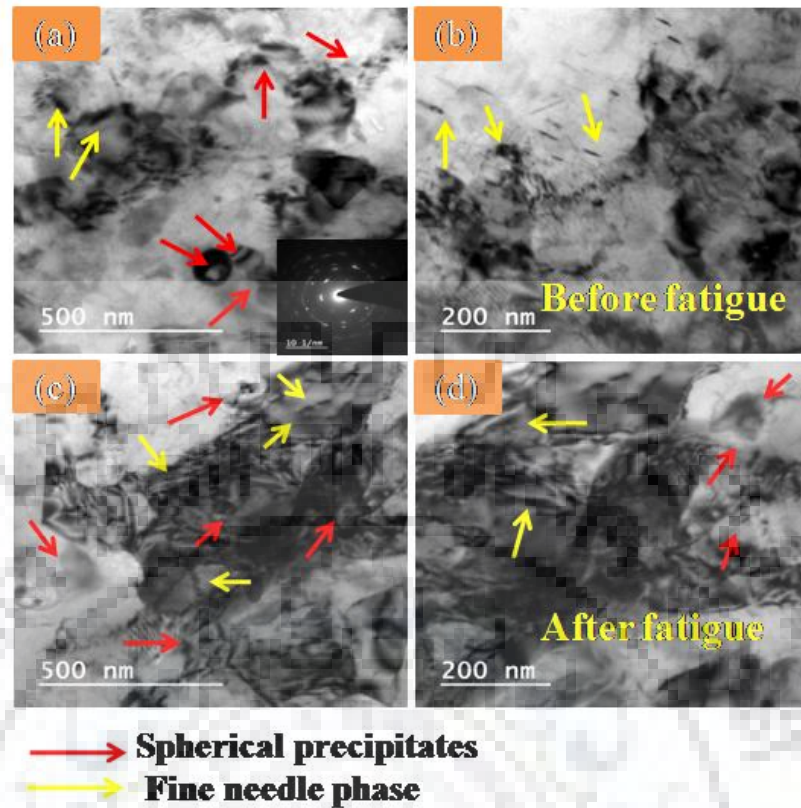
Figure 4.2.8: TEM micrographs of cryorolled followed by annealing of Al 2014 alloy at 250°C before and after fatigue test , (a) CR+AN$_{250}$ Al 2014 alloy ; (b) CR+AN$_{250}$ Al 2014 alloy at different sample location ; (c) CR+ANF$_{250}$ Al 2014 alloy ; (d) CR+ANF$_{250}$ Al 2014 alloy at different sample location

Fig. 4.2.3(g)-(h), and Fig. 4.2.8(a)-(b) shows the TEM micrograph of cryorolled (CR) sample annealed at 250°C before fatigue testing (CR+AN$_{250}$ sample condition). A considerable decrease in the dislocation density is observed from these figures. In addition to this, subgrains formed at this temperature becomes more equiaxed and relaxed (strain free) as compared to sample annealed at 200°C i.e (CR+AN$_{200}$) sample. A large number of fine needle precipitate (marked with yellow arrow) particle along with few second phase spherical precipitate (shown with red arrow) are observed from the TEM micrograph. The SAED pattern corresponding to this condition is shown as inset in Fig. 4.2.8(a). The continuous spotty rings which are slightly wider are observed as compared to the sample annealed previously suggesting that recrystallisation is dominating over recovery at this sample condition. The TEM microstructure for sample annealed at 250°C after fatigue testing (CR+ANF$_{250}$) is shown in Fig. 4.2.8(c)-(d). The increase in dislocation density after fatigue testing can clearly be visualized from the microstructure. The most of the second phase

112

particles (needle and spherical) evolved at this temperature are trapped inside the high dense dislocation structure as evident from this figure. The pinning effect of these second phase particles on the grain boundaries is also observed. The slip bands induced due to fatigue loading are not clearly seen at this process condition.

4.2.3.2 High Cycle Fatigue

The conventional S-N test approach devised by Wohler has been used to determine the stress- life (S-N) curve in the present work. To produce S-N curve, a range in fatigue life for each load level/stress amplitude has been estimated for a specified value of R ratio $\left(\frac{\sigma_{min}}{\sigma_{max}}\right)$. R ratio has been taken as 0.1 for all experiments in the present work. The stress amplitude (σ_a) for each processed condition was varied from 60 MPa to 170 MPa depending upon the ultimate tensile strength (UTS) of each condition in this work. To plot S-N curve, specimen in each condition is tested first at high stress amplitude where failure is expected in very short cycles. The stress amplitudes in each processed condition for each succeeding specimen was decreased till one to two specimens successfully passed the specified number of cycles without failure. The maximum stress at which run out obtained for a specified number of cycles is taken as fatigue limit. For non ferrous alloys such as Al alloy, Mg, Cu alloy, fatigue limit is not well defined. Therefore, fatigue strength based on 10^6 cycles has been used to estimate high cycle fatigue strength of the solution treated (ST), cryorolled (CR), cryorolled and followed by annealed samples in the temperature range from 100°C to 250°C i.e. CR+AN$_{100-250}$ samples of Al 2014.

Based on the experimental data, the S-N curve for Al 2014 alloy for various processed condition is plotted in Fig. 4.2.9. The curve has been drawn between stress amplitude (σ_a) and number of cycles to failure in linear S and log N scale as shown in Fig. 4.2.9.
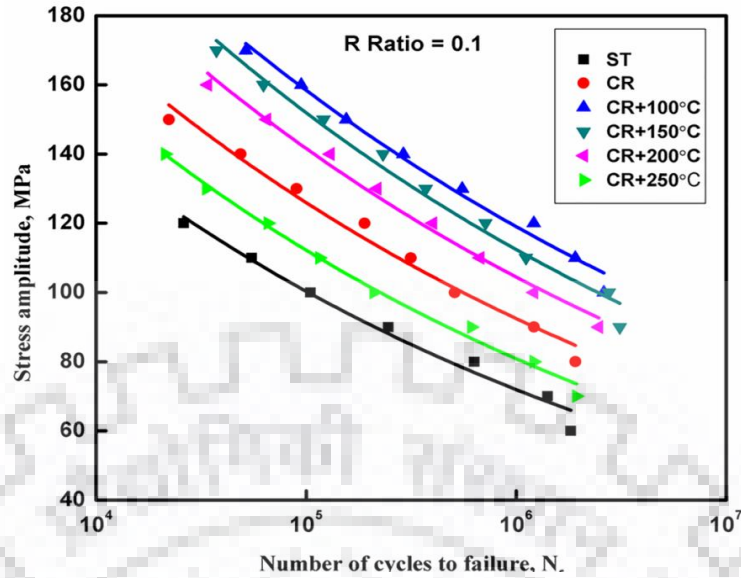
Figure 4.2.9:   S-N curve for Al 2014 alloy for various processing conditions

From the S-N curve, it is clear that fatigue strength of solution treated (ST) Al 2014 alloy is 72 MPa. After cryorolling, fatigue strength has increased from 72 MPa to 93 MPa. The fatigue strength of CR+AN$_{100}$ sample is found to be 121 MPa as depicted from Fig. 4.2.9. A slight reduction in the fatigue strength of CR+AN$_{150}$ (121 MPa-113 MPa) is observed as compared to CR+AN$_{100}$ sample. With further annealing from 150°C -200°C, the fatigue strength has gradually decreased and becomes 113 MPa and 106 MPa, respectively. The fatigue strength has decreased drastically when cryorolled (CR) samples were annealed at 250°C as compared to CR and CR+AN$_{100}$ samples and becomes 83 MPa.

Basquin has modeled the S-N curve for high cycle fatigue regime, where the nominal strain is elastic expressed by the following equation [4.81]

$$\sigma_a = \frac{\Delta\varepsilon}{2} E = \sigma_f'\left(2N_f\right)^b \qquad (4.10)$$

Where σ_a =   alternating stress amplitude, $\frac{\Delta\varepsilon}{2}$ = elastic strain amplitude, $2N_f$ = number of load reversals to failure, Where σ_f' = fatigue strength coefficient, b = fatigue strength exponent. It can be observed from Basquin's equation (4) that fatigue life is strongly dependent on fatigue strength coefficient (σ_f') elastic strain amplitude $\left(\frac{\Delta\varepsilon_{el}}{2}\right)$ and fatigue strength exponent (b) in high cycle fatigue regime. Lesser the elastic strain amplitude $\left(\frac{\Delta\varepsilon_{el}}{2}\right)$ and fatigue strength exponent (b), more will be the fatigue life. The higher values of fatigue strength coefficient (σ_f') correspond to high cycle fatigue strength of metal/alloys.

114

In the present work, the elastic strain amplitude has been calculated for solution treated (ST), cryorolled (CR), and cryorolled followed by annealed (CR+AN) alloy for various stress amplitudes to observe its effect on high cycle fatigue region. The elastic strain amplitude has been calculated by using equations (4.10) and variation of elastic strain amplitude with respect to various processing condition is shown in Fig. 4.2.10 and Fig. 4.2.11. It is observed (Fig. 4.2.10) that elastic strain amplitude for solution treated (ST), cryorolled (CR), and cryorolled followed by annealed alloy (CR+AN$_{100-250}$) alloy increases with increasing stress amplitude while at a particular stress amplitude, elastic strain amplitude is minimum for sample annealed at 100°C (CR+AN$_{100}$) as seen from Fig. 4.2.11.
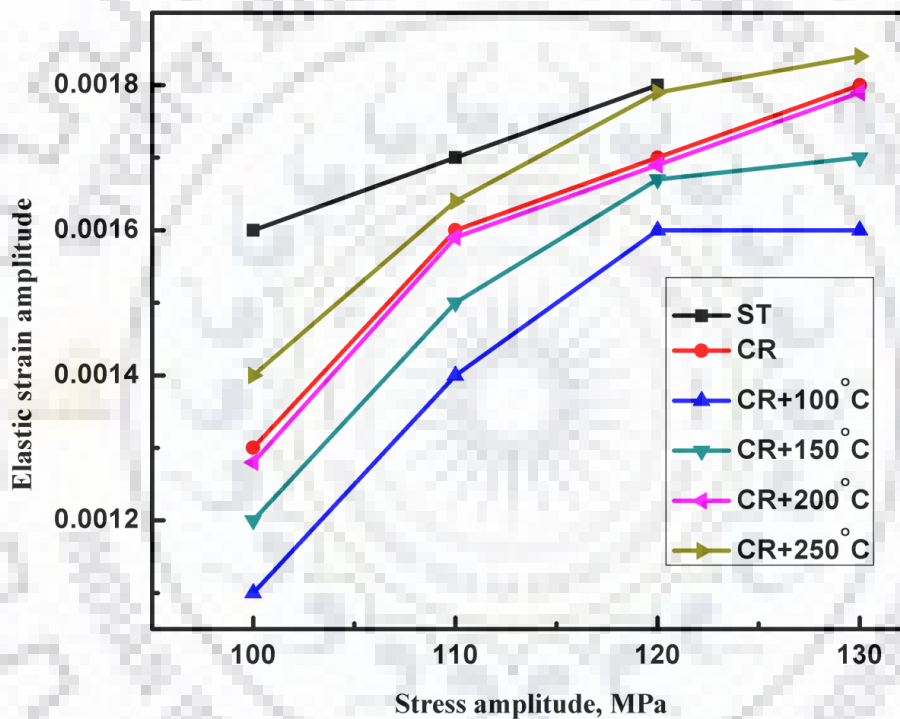
Figure 4.2.10: Variation of elastic strain amplitude with respect to various stress amplitudes for different processing conditions
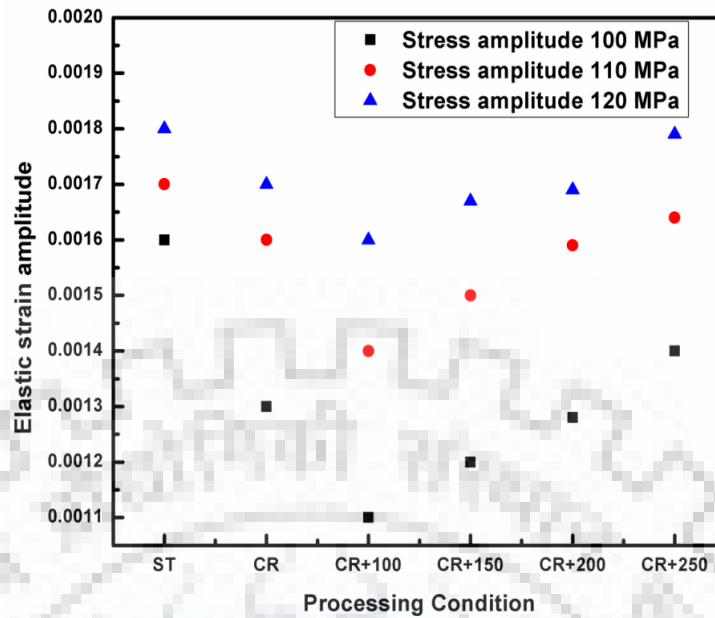
Figure 4.2.11: Variation of elastic strain amplitude in Al 2014 alloy with respect to various processing conditions for constant stress amplitudes (100 MPa, 110 MPa, 120 MPa)

To calculate fatigue strength coefficient (σ_f') and fatigue strength exponent (b), statistical techniques (ANNOVA) has been used to fit the nonlinear power S-N curve. The S-N curve for each processed condition is modelled by using analysis of variance (ANNOVA). The various high cycle fatigue properties such as high cycle fatigue strength, fatigue strength coefficient (σ_f') and fatigue strength exponent (b) are listed in Table. 4.2.2. It is observed that fatigue strength coefficient and fatigue strength exponent is maximum and minimum for sample annealed at 150°C (CR+AN$_{150}$) and $100°$C (CR+AN$_{100}$) respectively in this work.

Table 4.2.2: List of high cycle fatigue properties for various processing conditions

Sample condition	High cycle fatigue strength $\sigma_{f,}$ (MPa)	Fatigue strength coefficient (σ_f')	Fatigue strength exponent (b)
ST	72	586.13	-0.1445
CR	93	649.55	-0.1346
CR + AN$_{100}$	121	720.50	-0.1241
CR + AN$_{150}$	113	750.50	-0.1308
CR + AN$_{200}$	106	710.75	-0.1321
CR + AN$_{250}$	83	637.82	-0.1423

116

4.2.4   Discussions

4.2.4.1 Effect of deformation on precipitation behavior of Al 2014 alloy

The detailed investigations on the evolution of precipitate phases during cryorolling and followed by annealing up to temperature range 100°C to 350°C have been discussed in section 4.1. Fig. 4.2.3(a) shows the TEM micrograph of Al 2014 alloy after cryorolling. The microstructure of cryorolled (CR) sample consisting of ill defined grain boundaries with majority of dislocation tangling zones as depicted from this figure. It can be observed from the microstructure of cryorolled (CR) sample that precipitates were not observed when solution treated (ST) sample were deformed at cryogenic temperature. It is due to the fact that, in solution treated (ST) Al 2014, the solutes are completely dissolved in the Al matrix but when solution treated (ST) alloy is cryorolled (CR), the solute atoms are still retained in the matrix. It might be possible that at cryogenic temperature, a solute atom does not have sufficient thermal energy for atomic migration to occur due to which precipitation reaction not takes place. Fig. 4.2.3 (b)-(c) is TEM micrograph of cryorolled sample after annealing at 100°C. The ill defined grain boundaries of cryorolled (CR) sample has been relaxed and transformed in to well defined dislocation free sub grains. Fig. 4.2.3 (c) is the higher magnification micrographs of (CR+AN$_{100}$) sample to observe features more clearly. The large number of fine metastable spherical θ' phase can be seen in the grain interior as observed from these figures. This phase has been reported as Al$_2$Cu phase in previous section 4.1. The reason for nucleation of fine spherical phase within the grain interior at the low annealing temperature of 100°C can be explained on the basis of classical nucleation theory, which suggests that nucleation of metastable θ' phase (Al$_2$Cu) at the grain boundaries is not easy due to the slow diffusion rate of Cu atoms at low annealing temperature.

Fig. 4.2.3 (d)-(f) are the low and higher magnification TEM micrograph of cryorolled (CR) sample subjected to annealing at 150°C (CR+AN$_{150}$ sample). The large number of metastable spherical precipitates (θ' phase) can be seen along the grain boundary while few of these spherical precipitates are located within the grain interior. It is due to the fact that with increasing annealing temperature, diffusion rate for migration of Cu atom from center of grain to grain boundaries increases. In addition to this, size of metastable spherical phase θ' increases slightly as observed from higher magnification TEM micrographs (Fig. 4.2.3(d)-(f)) corresponding to this sample condition. It is due to the fact that the grain boundaries are favourable nucleation sites for the precipitation due to its high energy state and system can

easily relaxed to a low energy state (85). Moreover, the grain boundaries have more random structure and it can easily accommodate strain.

The Fig. 4.2.3 (g)-(h) shows the low and high magnification TEM micrographs of cryorolled sample annealed at 250°C. The dislocation density is significantly reduced at this annealing condition as observed from these figures. The coarser spherical precipitates are seen with few fine needle type metastable λ' phase. This phase has been reported as AlCuMgSi in earlier section 4.1. The most of the precipitates (spherical and needle type) evolved from the matrix as discussed earlier due to thermal energy. With increasing annealing temperature from 100°C to 250°C, the size of spherical precipitate increases continuously. The strain energy for precipitating spherical phase in Al matrix increases with increasing size of precipitate as reported in literature [4.85]. This excess strain energy can only be stored in the higher energy configurations such as grain boundaries (GBs), triple junctions due to which with increasing annealing conditions, precipitates are located near the grain boundaries as observed in the present work.

Yang et al. [4.86] have investigated the precipitation behaviour of Al-4Mg-.3Cu processed through high pressure torsion (HPT) followed by in situ heating in STEM. They observed the evolution of various kinds of precipitates in HPT processed Al-4Mg-.3Cu alloy. At low strain, most of the precipitates are located in grain interior while at high strain, majority of precipitates are distributed along the grain boundaries (GBs) as reported in their work. However, precipitates were not observed when solution treated (ST) Al 2014 alloy is cryorolled to the desired thickness reduction in the present work. It is believed that processing at cryogenic temperature suppresses the rate of precipitation kinetics due to which precipitation does not take place when Al 2014 alloy is deformed through cryorolling.

When cryorolled (CR) samples were annealed from 100°C to 250°C, most of the precipitates are located within the grain interior at low temperature of 100^0C due to low diffusion rate. However, with increasing annealing temperature from 150°C to 250°C, diffusion rate increases due to which most of the precipitates are located/ nucleated along the grain boundaries (GBs).

4.2.4.2 Effect of deformation and post deformation annealing on high cycle fatigue properties

The effect of cryorolling and afterwards annealing on high cycle fatigue strength has been investigated up to annealing temperature of 250°C in the present work. The TEM microstructure of cryorolled sample after fatigue testing (CRF sample) is shown in Fig. 4.2.4 (c)-(d). The microstructure of cryorolled followed by fatigue tested sample i.e CRF sample primarily consists of fatigue induced slip bands. The fatigue crack nuclei initiates as an invisible microcrack in these fatigue induced slip bands. These bands are known as cyclic slip bands (CSBs) and formed due to localized cyclic plastic deformation [4.84-4.87-4.88]. Sangid [4.90] has proposed mechanism for the formation of slip bands during cyclic loading and reported that these bands as a persistent slip bands (PSBs) in FCC material/alloy. It is a process of repetitive forward and reverse loading. The defects are generated in the form of dislocations which multiply and accumulate within the material during cyclic loading resulting in enhanced dislocation density as reported in the literature [4.89-4.90-4.91]. High dislocation density during cyclic loading further increases total energy of the system and to minimize total energy of system, dislocation are arranged in to unique structure known as slip bands. It may be mentioned that slip bands are the zone where the high strain is localised during fatigue loading. The fatigue life basically consists of two important phases until the failure has occurred: (i) crack initiation phase (ii) crack propagation phase. The crack initiation phase further depends on three important things during cyclic loading: (i) cyclic slip/cyclic slip bands (ii) nucleation of micro cracks (iii)micro crack growth and all these three things depend on the stress concentration of micro cracks. In order to understand the mechanism of initiation of fatigue crack, it is very essential to understand the dislocation mechanics in cyclic loading. Seeger [4.92] and Friedel [4.93] have reported that during cyclic loading, strain localisation takes place in the form of slip bands, which are precursor for fatigue crack initiation. Sangid [4.90] reported that large number of dislocations are generated during cyclic loading and slip process begins at first stage. This slip process is continued until dislocations are blocked by nearby obstacle, grain boundaries or second phase particles/ precipitates. On further applying the load, local stress causes the nucleation of another dislocation or blocked dislocation to pass their obstacle by various processes such as climb, kink, jog or shearing. This whole process is repeated in same path due to its low energy configuration during the whole course of cyclic loading. This path may be planar or wavy depending upon the stacking fault energy of metals.

Low stacking fault energy metals favours the planar path while high stacking fault metals favours the wavy path. The dislocation moving in same path during cyclic loading leads to the formation of slip band (cyclic slip bands) or persistant slip bands. The plastic deformation due to the cyclic loading generates positive and negative dislocations due to forward and reverse loading. Hence, it may be mentioned that the defects are multiplied, accumulated and annihilated in slip bands, which exhibit strain hardening leading to the formation of low energy configuration either ladder structure or parallel slip band structure. The dislocation pile up occurs at the grain boundaries due to increase in dislocation density, which leads to stress concentration. This activates slip in neighbouring grain. With the increase in accumulated strain, it is localised in to very small regime of slip bands resulting initiation of fatigue micro crack.

In cryorolled (CR) sample, grains are well within the ultrafine regime having sizes in the range of 100 nm- 300 nm. It has been reported that fine grains lead to reduced flaw size and due to which it is very difficult to impose a stress concentration near micro crack tip resulting higher crack initiation period in cryorolled (CR) sample [4.59]. Therefore, the cryorolled (CR) sample has shown higher fatigue life in the present work as compared to ST sample having coarser grains. However, the increment in fatigue strength (72 MPa – 93 MPa) of cryorolled (CR) sample is observed to be only 29% as compared to solution treated (ST) alloy in the present work. It has been reported that dislocation slip mode has significant effect on the material properties during the plastic deformation [4.94]. Recently, Zhang et al. [4.94] have studied the influence of dislocation slip mode on high cycle fatigue (HCF) performance of ultrafine- grained (UFG) Cu and Cu-Zn alloy subjected to equal-channel angular pressing (ECAP). The marginal improvement in fatigue strength (80 MPa-100 MPa) of ECAP processed UFG Cu was observed in their work. However, the addition of Zn (11%) in to Cu has significantly raises the high cycle strength from 80 MPa to 180 MPa as reported in their work. Their findings suggest that the significant improvement in high cycle fatigue strength can be achieved in metals and alloys having planar slip mode with low stacking fault energy (SFE) as compared to wavy slip materials having high stacking fault energy. The similar phenomenon might occur due to wavy slip nature of Al 2014 alloy, which favours the dynamic recovery and intense strain localisation during high cycle fatigue testing due to which marginal improvement in high cycle fatigue strength of cryorolled (CR) material was observed as compared to solution treated (ST) alloy.

The TEM micrograph for cryorolled sample annealed at 100°C after fatigue testing (CR+ANF$_{100}$) is shown in Fig. 4.2.5(c). The density of cyclic slip bands (CSBs) is increased as compared to cryorolled (CR) sample as evident from this figure. Very fine spherical precipitates (θ' phase) can also be observed along with these CSBs. These fine spherical precipitates have pinned the grain boundary and cyclic slip bands (CSBs) during cyclic loading as depicted from Fig. 4.2.5 (c). The dispersoids and precipitates exert a Zener drag force 'Z' on grain boundary and this force can be expressed by following expression [4.76].

$$Z = k \left(\frac{f}{r} \right) \tag{4.11}$$

Where k = coherency constant, λ = interfacial energy of grain boundary being passed, f = volume fraction of dispersoid/second phase precipitates, r = average radius of dispersoid/second phase precipitates. It is clear from the above equation (4.11) that drag force required for grain boundary migration is directly proportional to f, while inversely proportional to 'r'. For (CR+ANF$_{100}$) sample, the average radius of spherical precipitates (metastable/semicoherent θ' phase) is very small due to which Zener pinning force is very high at grain boundary at this condition. In addition to this, some of these particles were dispersed in CSBs and obstruct the dislocation motion and micro crack growth resulting improved fatigue strength at this process condition as compared to solution treated (ST) and cryorolled (CR) alloy. Moreover, the crack initiation phase is delayed in such a system due to coherency associated with fine second phase metastable precipitates. The TEM micrograph corresponding sample annealed at 150°C after fatigue testing (CR+ANF$_{150}$) is shown in Fig. 4.2.6 (c) – (d). The dislocation density is slightly improved as compared to (CR+AN$_{150}$) sample as observed from this figure. The numerous CSBs along with metastable spherical precipitates (θ' phase) can be seen in fatigue tested (CR+ANF$_{150}$) sample due to cyclic plastic deformation and cyclic strain localization in these zones. The size of these precipitates is slightly larger than the sample annealed at 100°C. The various reports of past researchers have suggested that precipitate loses its strengthening effect with increase in size [4.30,4.89]. The Zener pinning force for cryorolled followed by annealed sample at 150°C after fatigue testing (CR+ANF$_{150}$) is less as compared to sample annealed at 100°C (CR+ANF$_{100}$) due to which fatigue micro crack initiation is relatively easy in sample annealed in 150°C resulting lesser fatigue strength of cryorolled sample, as compared cryorolled sample annealed at 100°C. However, the observed fatigue strength of sample annealed at 150°C is still more than solution treated (ST) and cryorolled (CR) due to precipitation hardening effect of

121

metastable spherical precipitates (θ' phase), which delay the micro crack growth period by obstructing its propagation during cyclic loading.

The TEM micrograph of cryorolled followed by annealed at 200°C after fatigue testing (CR+ANF$_{200}$) is shown in Fig. 4.2.7(c)-(d). The cyclic strain localization has developed cyclic slip bands in the sample as observed from these figures. The spherical precipitates (θ' metastable phase) are still seen in this condition. However, their size has increased significantly as compared to sample annealed at previous conditions due to recrystallisation process. The Zener pinning force has reduced considerably as compared to sample annealed at 100°C and 150°C due to increase in size of second phase metastable precipitate. This promotes faster recrystallisation process and higher misfit between dislocation and secondary phase particles as noticed from equation (4.11). It has been reported that stress concentration effect strongly depends upon size of dispersoids/second phase particles in the matrix and with increasing size of second phase particles, the ease of building stress concentration in microcrack nucleated due to cyclic slip will increase resulting reduced fatigue life. Therefore, the fatigue strength of cryorolled sample annealed at 200°C (CR+ANF$_{200}$) is less as compared to sample annealed at 100°C (CR+ANF$_{100}$) and 200°C (CR+ANF$_{150}$) sample. However, annealed sample at 200°C has showed higher fatigue strength as compared to solution treated (ST) and cryorolled (CR) Samples. It is due to the evolution of semicoherent metastable phase θ' which is slightly coarser as compared to (CR+ANF$_{100}$) and (CR+ANF$_{150}$) sample but still semi coherent with matrix and shows hardening effect when compared with solution treated (ST) and cryorolled (CR) samples. These semi coherent metastable precipitates θ' obstruct the dislocation motion during cyclic slip process and some of these particles get aligned along CSBs as observed from Fig. 4.2.7(d) and promotes zig-zag micro crack growth resulting reduced microcrack growth and increases the crack propagation period. Therefore, fatigue life of cryorolled followed by annealed sample at 200°C is noticed higher with respect to cryorolled (CR) and solution treated (ST) sample.

The TEM micrograph corresponding to cryorolled sample annealed at 250°C after fatigue testing (CR+ANF$_{250}$) is shown in Fig. 4.2.8(c)-(d). In this condition, the significant drop in the dislocation density is realized in comparison to previous annealed samples after fatigue test. Also, metastable fine needle (λ' phase) as well as few coarser stable θ phase are observed. The strengthening effect of needle phase (λ' phase) is less as compared to metastable spherical θ' phase and it is transformed in to stable θ phase (Al$_2$Cu) and become

122

coarser. Moreover, dislocation free recrystallized grain and these second phase particles are also observed from Fig. 4.2.8(c)-(d). The fine needle precipitates and coarser spherical stable phase pinning the grain boundary can also be observed from TEM micrographs but the Zener pinning force is not too much effective to suppress the recrystallisation reaction and the dislocation pile up. The grain size has increased in the range of 300 nm – 500 nm as compared to all other sample conditions, however, still well within the ultrafine region. The fatigue strength of sample annealed at 250°C (CR+ANF$_{250}$) is seen less with respect to sample annealed at 100°C (CR+ANF$_{100}$), 150°C (CR+ANF$_{150}$), and 200°C (CR+ANF$_{200}$). The second phase precipitates particle controls the fatigue strength of sample annealed at 250°C. In this case, size of spherical precipitates has increased significantly and few of these spherical coarser precipitates (θ phase) and fine needle phase particle are distributed in cyclic slip bands (CSBs) as observed from Fig. 4.2.8 (c)-(d). The spherical particle becomes coarser, brittle and therefore microcrack nucleation as well as growth is very easy due to ease of imposing stress concentration near microcrack. In addition to this, the alloy major hardening phase is metastable θ' phase (Al$_2$Cu) as observed from tensile and hardness results in section 4.1. The strengthening effect of fine needle meta stable λ' phase is less as compared to metastable θ' phase (Al$_2$Cu). So, these fine needle precipitates are unable to accumulate cyclic slip and dislocation pile up during cyclic strain localization due to which fatigue strength is observed to be less for sample annealed at 250°C (CR+ANF$_{250}$) as compared to all other annealing condition. It may be mentioned that micro crack growth during crack initiation phase has increased due to precipitation of fine needle and coarser stable spherical phase resulting reduced fatigue strength of cryorolled sample annealed at 250°C (CR+ANF$_{250}$).

The observed fatigue strength of sample annealed at 250°C (CR+ANF$_{250}$) is found to be more than solution treated (ST) alloy. It is due to fact that grain boundary strengthening has much more effect on increasing the high cycle fatigue strength of sample annealed at 250^{0}C (CR+ANF$_{250}$) as compared to solution treated (ST) alloy. The microcrack nucleation is sluggish due to reduced grain size of annealed sample at 250°C (CR+ANF$_{250}$) as compared to solution treated (ST) alloy. In addition to this, the stress concentration is not easy to build near the microcrack due to reduced crack size caused by cyclic plastic localization in cryorolled sample annealed at 250°C after fatigue testing. Hence, the microcrack nucleation as well as its growth is difficult in this condition due to which fatigue strength of annealed sample at 250°C is found to be higher than solution treated (ST) sample.

4.2.4.3 Fracture surface morphology after fatigue testing

Fracture surface of solution treated (ST), cryorolled (CR), and cryorolled and followed by annealed alloy after fatigue testing i.e CR+ANF$_{100-250}$ alloy has been examined by FE SEM. The fracture surface topography of solution treated (ST) sample after fatigue testing is shown in Fig. 4.2.12 (a)-(c).
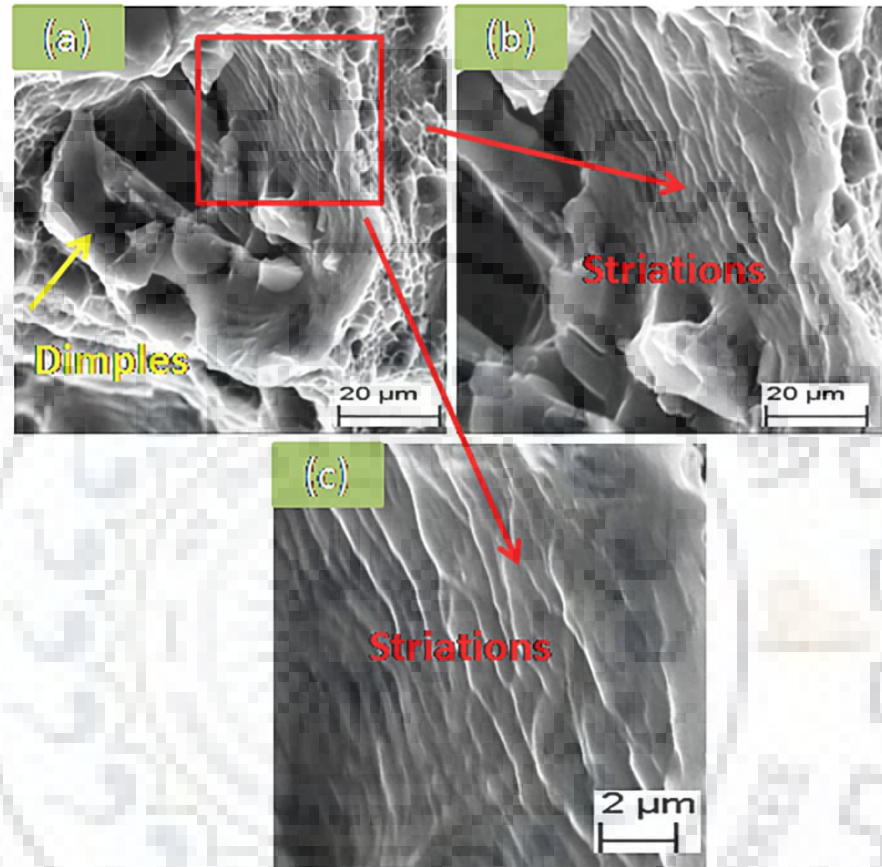
Figure 4.2.12: Fractographs corresponding to ST Al 2014 alloy after fatigue testing

The fatigue failure in solution treated (ST) samples primarily occurs through ductile manner as depicted from Fig. 4.2.12(a). The larger dimples which are marked by yellow arrows can be seen in fractographs of solution treated (ST) alloy. In addition to this, fatigue striations which are shown in rectangular box can also be observed in fractographs of solution treated (ST) alloy as shown in Fig.4.2.12(a)-(c). The striation width is approximately 1µm as observed from Fig. 4.2.12(c), which is the fractograph taken at higher magnification. Fatigue striations represent the growth of fatigue crack during cycle loading. Various models have been proposed by various researchers for fatigue crack growth under cyclic slip process [4.53]. Based on these models, it may be proposed that fatigue striations are result of continuous blunting and resharpening of crack tip during loading and unloading phase in one load cycle of

fatigue load. These striations are very tiny and closely spaced ridges as observed from the fracture surface of solution treated (ST) alloy after fatigue test in Fig. 4.2.12(b)-(c). The mechanism of formation of striations in cyclic loading is shown in Fig. 4.2.13.
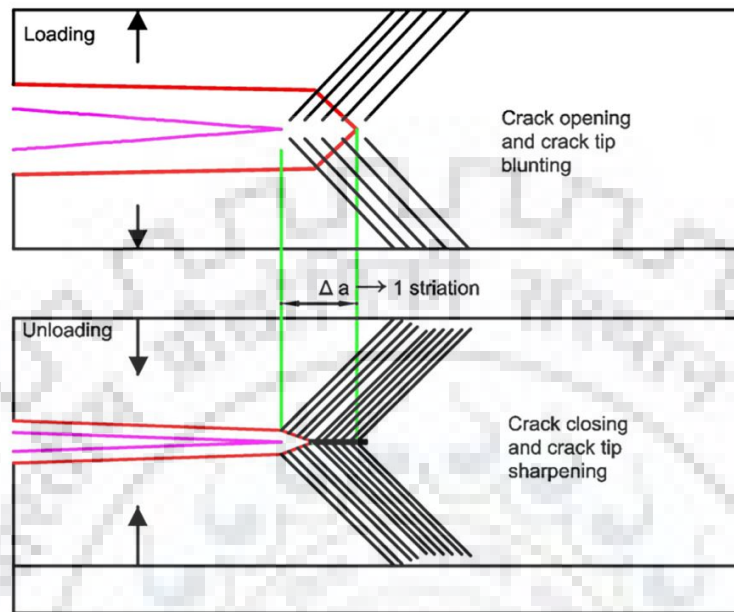
Figure 4.2.13: Mechanism showing the formation of striations in cyclic loading

Striation represents the position of crack tip at a point of time in fracture surface. Larger the distance between the striations, the fatigue crack growth in one load cycle will be more as reported in literature [4.89].

Fig. 4.2.14(a)-(c) shows the fractographs of cryorolled sample after fatigue test. The cryorolled alloy shows fine dimples (marked by arrow) as observed from fractographs. The dimple size has decreased as compared to solution treated (ST) sample due to grain refinement in cryorolled sample as discussed in our earlier published work [4.83]. Fatigue crack propagation area is difficult to observe at low magnification fractograph (Fig. 4.2.14(a)). Therefore, high magnification fractographs (Fig. 4.2.14(b)-(c)) were taken to observe crack growth features in cryo rolled sample. Relatively, fine gentle steps (rectangular box region) as compared to solution treated (ST) alloy can be seen in Fig. 4.2.14(c). The similar features are also observed by Chao et al. [4.95] during fatigue crack growth of age hardenable Al 7075. This might be due to presence of inclusion, second phase particles in Al 2014 alloy due to which clear striations are not observed as reported in their work. However, these features may be referred as striations because the fatigue crack propagation definitely occurs through these gentle steps as observed from Fig. 4.2.14(c). The width of these

striations is less than 1 µm and on quantitatively measuring, the width of the striations comes out to be 0.2 µm as observed from Fig. 4.2.14(c).
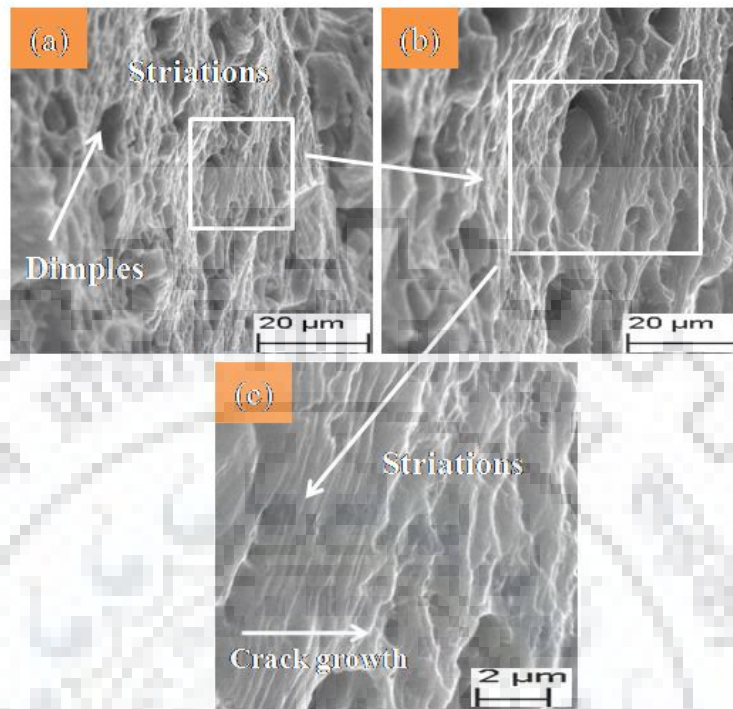
Figure 4.2.14: Fractographs corresponding to CR Al 2014 alloy after fatigue testing

This is far less than solution treated (ST) sample. It may be mentioned that cryorolled sample has relatively low fatigue crack growth rate as compared to solution treated (ST) alloy due to which it showed higher fatigue strength in the present work with respect to ST alloy. Das et al. [4.96] have compared the striation width for bulk and cryorolled Al 7075 for different thickness reduction and compared the fatigue crack growth mechanism for coarser grain and fine grain Al 7075. Based on their studies and past studies of Vinogradov [4.58], the Fig. 4.2.15 has been drawn to explain the crack growth mechanism in bulk alloy and fine grain alloy which depicts the transition of transgranular crack path for bulk ultrafine grain (UFG) alloy from intergranular crack path as in case of coarser grain material. It may be mentioned that in coarser grain (ST alloy), fatigue strength is controlled by resistance of grains without effect of grain boundaries while in case of cryorolled (CR) alloy, the fatigue resistance is dominated by interaction of grain boundaries and propagating micro crack. It might be possible that interaction of grain boundaries and propagating crack might have enhanced the width of plastic zone near crack tip resulting retardation in crack growth in cryorolled Al 2014 alloy.
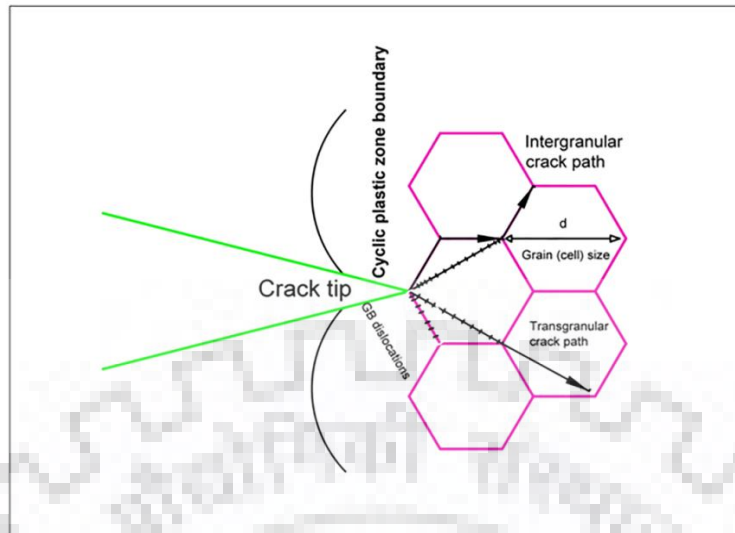
Figure 4.2.15: Influence of grain boundaries (GBs) on fracture mode of coarser as well as fine grain metals

The fractographs corresponding to cryorolled sample annealed at 100°C after fatigue testing (CR+ANF$_{100}$) is shown in Fig. 4.2.16(a)-(c). The fine dimples (marked by white arrow) are seen in fracture surface of fatigue tested sample at this annealing condition (CR+ANF$_{100}$) as observed from the Fig. 4.2.16 (a). This might be due to the nucleation of microvoid at second phase particle such as very fine spherical semi coherent precipitates θ' at this process condition as discussed in section 4.1. The fatigue micro crack growth region (rectangular box) is shown in Fig. 4.2.16(b)-(c). These are the higher magnification fractographs of Fig. 4.2.16(a) to observe fatigue crack growth region more clearly. Fatigue striations can be seen in the area marked by rectangular box in Fig. 4.2.16(b)-(c). The striations formed in this case are very fine and even not visible in low magnification. The higher magnification fractograph depicts much clear visibility of theses striations marking as observed from Fig. 4.2.16(c). The striation width is approximately 0.13 μm as noticed from Fig. 4.2.16(c). The observed striation width is less as compared to solution treated (ST) and cryorolled (CR) sample as discussed earlier. The micro crack growth rate for cryorolled sample annealed at this condition (CR+ANF$_{100}$) has been reduced as compared to solution treated (ST) and cryorolled (CR) sample. There might be two possible mechanisms for crack retardation in this process condition as reported in literature (4.96] : (i) The interaction between the propagating crack and very fine spherical precipitate obstructs the crack movement resulting reduced fatigue crack growth and striation width. The grain boundaries (GBs) may also act as a topological obstacle to the propagating crack when crack moves one

127

step while by passing the fine precipitates during crack precipitate interaction at GBs (ii) The propagating crack might slide the grain boundary in PFZs (precipitate free zones) due to which voids are created.
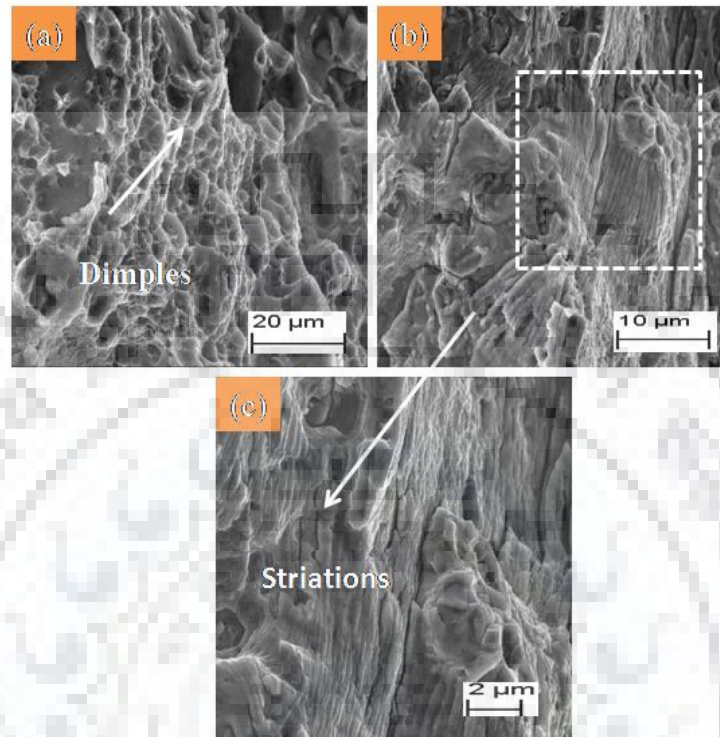
Figure 4.2.16: Fractographs corresponding to CR+ANF$_{100}$ Al 2014 alloy

These voids further leaves the wedges at the triple junctions resulting enhanced plastic zone near crack tip. It may be mentioned that enhanced plastic zone retard the crack growth by blunting the crack tip. Similar observations were reported by Das et al. (96) during high cycle fatigue of Al 7075 after cryorolling.

The fractographs corresponding to sample annealed at 150°C after fatigue testing (CR+ANF$_{150}$) is shown in Fig. 4.2.17(a)-(c). The fractographs shows large number primary dimples marked by arrow as shown in Fig. 4.2.17(a). The shape and structure of these dimples are same as observed for samples annealed at 100°C. However, the size of these dimples is slightly larger than the sample annealed previously. It might be due to the activation of comparatively lesser number of nucleation sites and microvoids caused by recovery process for annealed sample at 150°C after fatigue testing (CR+ANF$_{150}$) which leads to increase in the size of microvoid/second phase precipitate resulting increased dimple size.

This observation can also be confirmed from Fig. 4.2.17(a) and Fig. 4.2.16(a) that the number and volume fraction of microvoids has been decreased for sample annealed for 150°C with

respect to sample annealed at 100°C. Fig. 4.2.17(b) and Fig. 4.2.17(c) are the higher magnification fractographs of rectangular zone in Fig. 4.2.17(a). Fatigue crack growth zone can clearly be visualized through these fractographs.
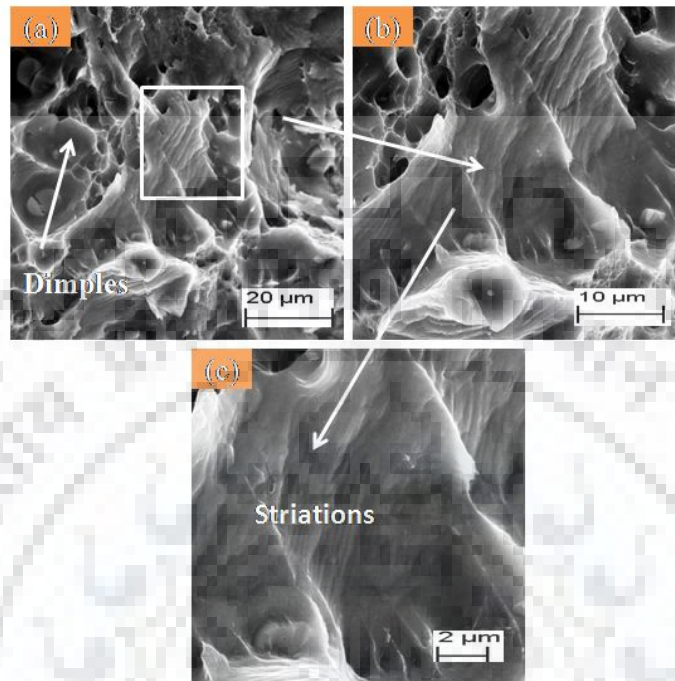
Figure 4.2.17: Fractographs corresponding to CR+ANF$_{150}$ Al 2014 alloy

The fine striation markings are observed in Fig. 4.2.17(b) and Fig. 4.2.17(c). On comparing the striation gap for solution treated (ST), cryorolled (CR), and cryorolled followed by annealed sample at 100°C after fatigue testing (CR+ANF$_{100}$) , it is observed that striation gap for sample annealed at 150°C (CR+ANF$_{150}$) is less than solution treated (ST) and cryorolled (CR) sample while it is slightly larger than sample annealed at 100°C (CR+ANF$_{100}$) samples. The striation width for fatigue tested (CR+ANF$_{150}$) sample is observed to be 0.16 μm as observed from Fig. 4.2.17(c). The slight enhancement in striation width accelerates fatigue crack growth for annealed sample at 150°C (CR+ANF$_{150}$) with respect to sample annealed at 100°C (CR+ANF$_{100}$) resulting slight decrease in fatigue limit for this process condition. Meyer et al. (56) investigated the crack growth characteristics for Al 6063 alloy processed through ECAP and reported that crack tip plasticity has a significant role in blunting the propagating crack. It may be mentioned that after annealing at 150°C, size of spherical precipitates slightly increases and these precipitates loses its hardening effect with increasing annealing temperature as discussed earlier. The stress concentration around these precipitates is easy to build as discussed in earlier sections 4.2.4.2. When crack tip

interact with these precipitates, the size of plastic zone in the vicinity of crack tip is reduced due to ease of building of stress concentration around crack tip as compared to sample annealed at 100°C (CR+ANF$_{100}$), which leads to sharpening of crack tip. This is another reason for reduced fatigue strength of sample annealed at 150°C with respect to sample annealed at 100°C.

The fractographs corresponding to cryorolled followed by annealed sample at 200°C after fatigue testing (CR+ANF$_{200}$) is shown in Fig. 4.2.18(a)-(d).
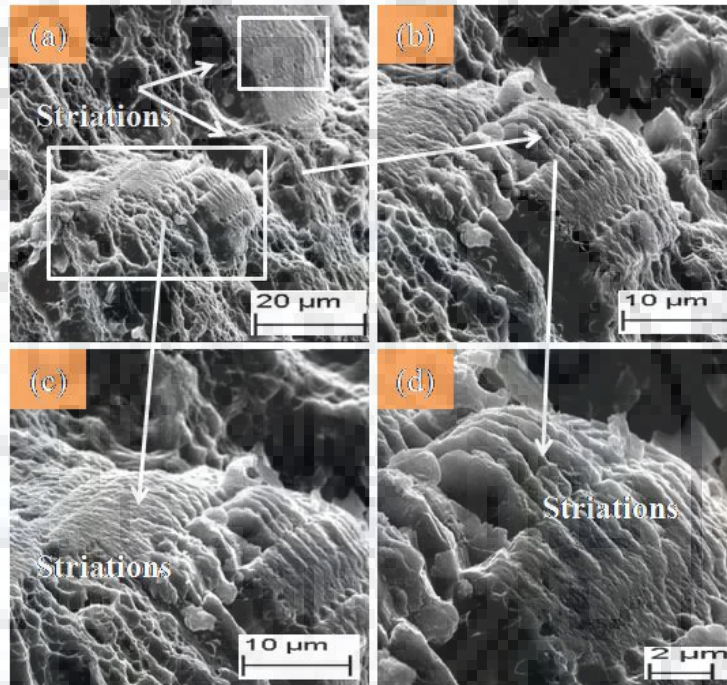
Figure 4.2.18: Fractographs corresponding to CR+ANF$_{200}$ Al 2014 alloy

The mixed mode transgranular fracture is dominated in fracture surface of fatigue tested sample as observed from Fig. 4.2.18 (a)-(d). Fracture surface is perturbed with few coarser as well fine dimples along with cyclic cleavage steps in fatigue crack growth regime. The dimples are shallow and slightly elongated for fatigue tested (CR+ANF$_{200}$) sample with respect to previous conditions. The rectangular box has been shown to highlight the fatigue crack growth region in Fig. 4.2.18(a). Fatigue crack growth zones contain fine striations in wavy, corrugated, and cyclic cleavage surface as observed from higher magnification fractographs (Fig. 4.2.18(b)-(d)). The striation width is hard to measure because fatigue striations were not well developed. This process condition favours the evolution of large number of spherical metastable precipitates (θ' phase). The size of spherical precipitates is comparatively larger than the sample annealed previously. However, they are still

130

semicoherent but due to slight coarsening, their hardening effect is less in comparison to previous annealed samples. In addition to this, due to the large size of these precipitates, multiple number of high concentration points exists. In such a situation, two possibilities exist (i) microcrack due to cyclic loading may initiate at these high stress concentration point and coagulate together resulting rapid crack propagation, leaving behind the cyclic cleavage fatigue crack growth surface (ii) Malikjani et al [4.77] have reported that fatigue crack growth rate strongly depends upon the coherency of precipitates. The presence of shearable and coherent precipitates favours the planar reversible slip and zig-zag crack growth resulting reduced fatigue crack growth while with decreasing coherency of precipitates in the microstructure diminish the reversibility of slip and crack tortuosity, leading to improved fatigue crack growth rate as reported in their work. The similar trendmay happen in the present case, the coherency of spherical metastable phase θ' is decreasing with increasing annealing temperature from 100°C to 250°C resulting decreased crack tip tortusity, which further leads to decreased fatigue life for sample annealed at 200°C with respect sample annealed at 100°C and 150°C.

Fig. 4.2.19(a)-(e) shows the fractographs of cryorolled sample annealed at 250°C after fatigue testing (CR+ANF$_{250}$ sample condition). The fracture mode of annealed sample at 250°C after fatigue testing (CR+ANF$_{250}$) is quite similar to fatigue tested sample at 200°C (CR+ANF$_{200}$). The number and volume fraction of coarser dimples are more for sample annealed at 250°C with respect to sample annealed previously. This might be due to the combined recovery and recrystalization process at this process condition. The fatigue crack growth zone is shown by rectangular box in Fig. 4.2.19(b). To observe more clearly, higher magnification photographs of fatigue crack growth zone are shown in Fig. 4.2.19(c)-(e). From Fig. 4.2.19 (c)-(e), it is clear that fatigue striations were formed leaving the flat facets behind in the fatigue crack growth zone. Fatigue striations formed here also are not well developed as observed in cryorolled followed by annealed sample at 200°C. Such striations can be termed as brittle striations as reported in literature [4.55]. This might be due to the formation of stable coarser spherical precipitate (θ phase) and nucleation of fine needle metastable λ' phase as discussed in section 4.1. The crack may initiate such coarser, stable and brittle precipitates and coagulate together with rapid propagation of crack resulting reduced fatigue strength as compared to cryorolled (CR), cryorolled followed by annealed sample at 100°C, 150°C, and 200°C . However, the observed fatigue strength is still more than ST sample because of

precipitation of metastable needle (λ' phase) which suppresses the micro crack growth during crack initiation phase.
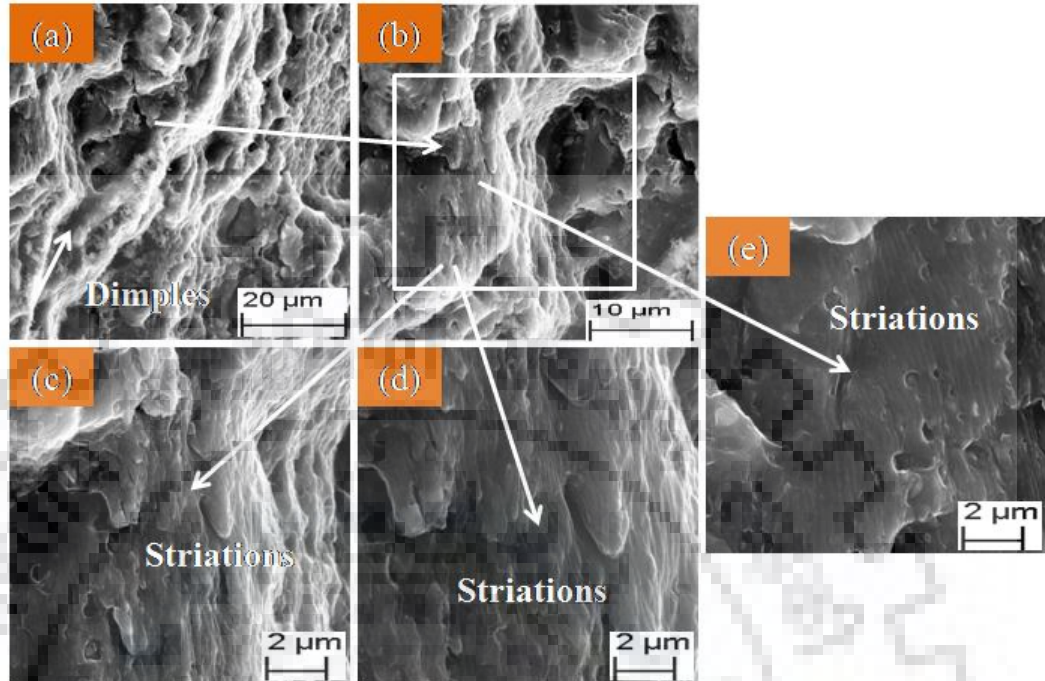
Figure 4.2.19: Fractographs corresponding to CR+ANF$_{250}$ Al 2014 alloy

4.2.5 Conclusions

The high cycle fatigue strength of Al 2014 alloy subjected to cryorolling and annealing has been discussed in detail in the present investigation and the major findings of the work can be summarised in following points.

- The significant improvement in high cycle fatigue strength (72 MPa-93 MPa) of cryorolled (CR) Al 2014 alloy was observed as compared to ST Al 2014 alloy. The improvement in high cycle fatigue strength of cryorolled (CR) alloy is attributed to the formation of ultrafine grains in cryorolled (CR) sample, which suppresses the microcrack nucleation and microcrack growth due to presence of large number of grain boundaries.

- Annealing at 100°C for 45 minutes results an improvement of fatigue strength (σ_f - 93 MPa-121 MPa) as compared to cryorolled Al 2014 alloy due to formation of metastable spherical precipitate phase θ' (Al$_2$Cu). Further annealing from 100°C -200°C, the slight drop in fatigue strength was observed due to gradual coarsening of metastable precipitate θ' phase. This drop in fatigue strength was drastic in the temperature ranging from 200°C -250°C due to formation of metastable phase Al$_3$Cu$_2$Mg$_9$Si (λ' phase) along with stable coarser precipitates Al$_2$Cu (θ phase).

- The influence of cryorolling on fatigue limit is attributed to presence of ultrafine grains which increases the crack initiation phase by reducing the stress concentration near crack tip and thereby ultimate raise the fatigue strength of cryorolled (CR) alloy. On the other hand, influence of cryorolling and followed by annealing is attributed to combined recovery and recrystallisation process, which enhance the plastic zone size near crack tip due to crack tip/precipitate interaction, resulting enhanced fatigue crack growth resistance at low temperature annealing.

4.3 Effect of Cryorolling and followed by annealing on Fatigue Crack Growth Behaviour of Ultrafine Grained Al 2014 alloy

4.3.1 Introduction

Ultrafine grained (UFG) materials produced through severe plastic deformation (SPD) methods have been thoroughly studied in the past few years[4.97]. The significant improvement in the mechanical properties achieved in UFG material fabricated by SPD methods have attracted much attention for commercializing these materials for high strength applications such as automotive, aerospace and structural sectors[4.6,4.98,4.99] . However, for the widespread use of UFG materials, the damage tolerance properties such as fracture toughness, fatigue resistance, and fatigue crack growth behavior ought to be addressed critically for ensuring damage safe design of mechanical components subjected to cyclic loading [4.52] . The understanding of the fatigue properties of UFG meals/alloys is very essential because the repeated load induced by fatigue loading could induce the complete failure of mechanical components during service conditions without providing previous warning [4.100]. A large body of work has been performed on the UFG materials having grain size in the range of 100 nm to 1 μm and numerous investigations have shown that monotonic strength properties have been significantly improved after grain size reduction is well below than 1 μm. The basic reason behind the improvement of montonic strength properties of UFG metals/alloy might be due to the enhancement of local plastic deformation energy, which is the energy required for the movement of the dislocations inside the grain[4.101]. With more energy required for the movement of the dislocations, yield strength of the metal and alloys will be more as reported in literature [4.101]. The dependence of monotonic strength properties on the grain size has also been expressed mathematically as per the famous Hall-Petch relationship as per the following equation..

$$\sigma_y = \sigma_o + k.D^{-1/2} \qquad\qquad (4.12)$$

Where σ_y is the yield stress, σ_o is the lattice friction stress, k is the Hall-Petch constant and D is the grain size. Based on this, it may be mentioned that montonic strength properties such as tensile strength, yield strength and ductility related issues of UFG metals/alloy has been significantly explored in various earlier publications of several researchers [4.88,4.102,4.103]. However, the effect of grain size on the cyclic plasticity, fatigue life, and fatigue crack propagation behavior of UFG metal/alloy is still vague and reported in very few literatures.

Hanlon et al. [4.100] reported that high cycle fatigue resistance of the metals/alloys increases after the grain size reduction in the range of 100 nm - 1μm at the expense of fatigue crack growth rate (FCGR). The detailed study and extensive review was made by Cavaliere [4.104] on the fatigue behavior of ultrafine grained (UFG) and nanocrystalline material (NC) and revealed that high cycle fatigue strength (HCF) of nanocrystalline material improved with decreasing grain size, while the susceptibility of crack initiation decreases on refining the grains well below than 1μm. The same author [4.104] revealed that low cycle fatigue strength of UFG materials fabricated by SPD processing deteriorates when grain sizes is in the range of 100 nm- 1 μm. The similar findings were reported by Hoppel et al. during the strain controlled test of various UFG metals and alloys i.e Cu, Al, Al 6061 and α brass[4.54,4.105]. They observed the shorter fatigue strength of bulk UFG metals and alloys in low cycle fatigue (LCF) regime of intermediate to high plastic strain amplitudes. On the other hand, the improved high cycle fatigue strength of bulk UFG metals/ alloys is observed in intermediate to low plastic strain amplitudes during stress controlled mode as reported in literature [4.54,4.105] . The comparison between the fatigue life of UFG metals and coarser grain metals and alloys can be well explained by total strain fatigue life diagram as reported in review paper of Mughrabi [4.52]. The following equations are very helpful for understanding the total strain fatigue life diagram as mentioned in literature [4.52]

$$\frac{\Delta\varepsilon_t}{2} = \frac{\Delta\varepsilon_{el}}{2} + \frac{\Delta\varepsilon_{pl}}{2} \qquad\qquad (4.13)$$

$$\frac{\Delta\varepsilon_t}{2} = \frac{\sigma_f'}{E}\left(2N_f\right)^b + \varepsilon_f'\left(2N_f\right)^c \qquad\qquad (4.14)$$

In above equations (4.13) and (4.14), $\Delta\varepsilon_t$, $\Delta\varepsilon_{el}$ and $\Delta\varepsilon_{pl}$ are the total, the elastic, and the plastic strain ranges respectively, while σ_f' is known as fatigue strength coefficient, $2N_f$ is the number of load reversals/cycles before failure, ε_f' and b are called fatigue ductility coefficient

134

and strength exponent , while 'c' is the fatigue ductility exponent as discussed in section 4.2. On comparing the first term of equation (4.13) and equation (4.14), the equation for the high cycle fatigue (HCF) regime is obtained which is known as Basquin law and expressed as per following equation.

$$\sigma_a = \frac{\Delta \varepsilon}{2} E = \sigma_f'(2N_f)^b \qquad (4.15)$$

For the low cycle fatigue (LCF) regime the well known Coffin-Manson relationship is used which is obtained by comparing second term of equation (4.13) and equation (4.14) and can be expressed by following equation.

$$\frac{\Delta \varepsilon_{pl}}{2} = \varepsilon_f'(2N_f)^c \qquad (4.16)$$

The total strain fatigue life diagram is shown in Fig. 4.3.1 as proposed in literature [4.5].

Total strain life diagram for UFG and coarser grain material
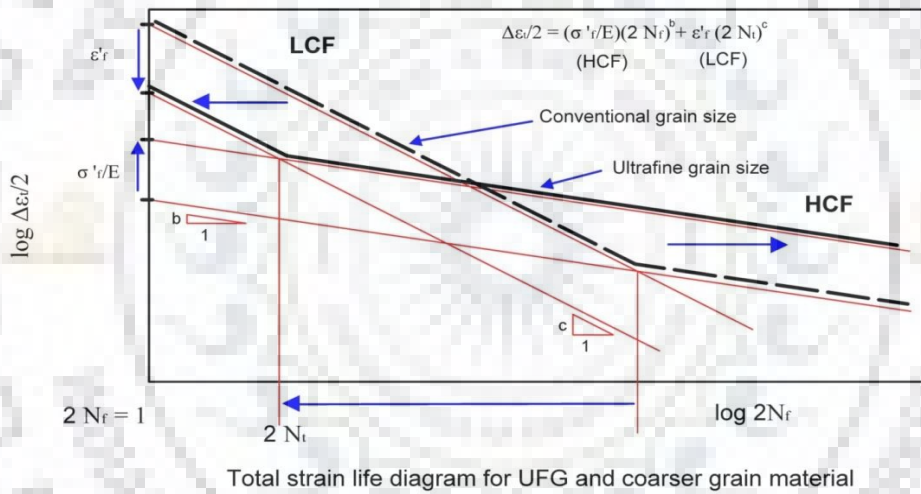
Figure 4.3.1: Total strain fatigue life diagram

From the graphical representation of log-log plot between the total strain amplitude $\frac{\Delta \varepsilon_t}{2}$ and load reversal to failure, i.e 2 N_f shows that for the coarser grain (CG) metals/alloys, the low cycle fatigue (LCF) strength is significantly high due to improvement of fatigue ductility coefficient ε_f' while for UFG metals/alloys, LCF strength is less as compared to coarser grain (CG) counterparts due to lack of ductility. Based on this discussion, it may be mentioned that HCF strength depends upon the fatigue strength coefficient σ_f' which in turn is controlled by yield strength of the material, while low cycle fatigue (LCF) strength depends upon the fatigue ductility coefficient ε_f'. From the microscopic point of view, fatigue life of a component can be divided in to crack initiation phase as well as crack growth phase. In crack

135

initiation phase, microcrack is too small to be visible while during crack growth phase, crack grows significantly up to the final failure. However, the crack initiation phase and crack growth phases must be investigated separately because the various factors have a great influence on the crack initiation phase while little or no influence on the crack growth phase. It is reported that fatigue lives of metals and alloys largely depends upon the growth life of fatigue crack due to which crack propagation behavior of UFG material must be investigated [4.106]. Patlan et al. [4.69] studied the fatigue crack growth behavior of bulk UFG 5056 Al-Mg alloy processed by equal channel angular pressing (ECAP). The fatigue crack growth (FCG) behavior of ECAP processed Al-Mg alloy was observed to be more at small stress intensity factor ranges ΔK as compared to its coarser grain counterpart. The serrated crack profile and zig-zag crack growth was found to be primary mechanism associated with coarser grain (CG) alloy, resulting reduced fatigue crack growth in CG alloy as described in their work. Chung et al. [4.107] investigated the fatigue crack growth (FCG) behavior of Al 6061 alloy processed by equal channel angular pressing (ECAP) and compared the Fatigue crack growth (FCG) behavior of bulk UFG Al 6061 alloy with its coarser grain counterparts. The ECAP processed alloy was observed to have a lower fatigue threshold and faster crack growth (FCG) rate as compared to unECAPed alloy in their work [4.107]. It was reported in their study that crack path tortuosity has a significant role in blunting the crack propagation path of unECAPed alloy resulting reduced fatigue crack growth rate (FCGR) of unECAPed Al 6061 alloy. Recently, Meyer et al.[4.56] studied the crack growth behavior of 2 pass and 8-pass ECAP processed Al 6063 alloy and compared its fatigue crack growth behavior with its coarser grain (CG) counterparts. The coarser grain (CG) alloy was observed to have a higher fatigue threshold and lower crack growth rate as reported in their work while for UFG alloy, lower fatigue threshold along with faster crack growth rate was measured. This is attributed to the higher crack path deflection and larger crack driving force for the crack propagation in coarser grain (CG) alloy as compared to bulk UFG alloy as noticed from their work [56]. Although, the fatigue crack growth (FCG) behavior of UFG metals/alloys has been investigated in past, few report as discussed earlier, the generalized statement about the fatigue crack propagation behavior of UFG metals/alloys can not be made since some literature has also reported opposing trends during fatigue crack growth rate (FCGR) testing. Collini et al. [4.108] compared the fatigue crack growth resistance of ECAP processed ultrafine grained (UFG) Cu with coarser grain (CG) and found that fatigue crack growth resistance of UFG Cu

was higher as compared to coarser grain (CG) especially at high stress intensity factor ranges ΔK. Similar studies were found by Das et al. [4.96] during the fatigue crack growth rate (FCGR) testing of bulk UFG Al 7075 alloy processed through cryorolling (CR). The diffused crack branching mechanism was the preliminary reason for the enhanced fatigue crack growth resistance of bulk UFG alloy as reported in their work.

Based on the above discussions, it can be seen that majority of the earlier published work of various researchers related to high cycle fatigue (HCF), low cycle fatigue (LCF) and fatigue crack growth (FCG) behavior has been performed on the ECAP processed Ti, Ni, Cu , pure Al and Al-Mg alloys . However, the fatigue studies especially fatigue crack growth (FCGR) behavior of the bulk UFG precipitation hardenable Al alloys deformed through other SPD methods are scarce in literature. Effect of precipitation on the montonic strength properties of bulk UFG Al 6061, Al 6063, and Al 7075 has been well reported in earlier published work of various researchers [4.111-4.112,4.80] . However, the influence of post deformation annealing on the fatigue and fracture behavior of bulk UFG Al 2xxx series alloys especially Al 2014 alloy developed by cryorolling (CR) has not been studied in detail. Recently, the effect of precipitation on the high cycle fatigue (HCF) behavior of cryorolled (CR) Al 2014 alloy has been investigated and found that fine spherical phase θ' (Al$_2$Cu) has a significant effect on improving its fatigue life [4.113]. However, the crack growth studies for the cryorolled (CR) as well as post annealed cryorolled (CR) Al 2014 are scarce in the literature. Therefore, the present work is envisaged to investigate the effect of cryorolling and post deformation annealing in the temperature ranging from 100°C to 250°C on fatigue crack growth rate FCGR (da/dn) of bulk UFG Al 2014 alloy. The detail microstructural features were characterised by the FESEM and TEM for substantiating the fatigue crack propagation behavior of deformed Al 2014 alloy.

4.3.2   Experimental

For the present investigation, Al 2014 alloy is used. The chemical composition of the alloy has been given in Chapter 3. The as received plate of Al 2014 alloy having a thickness of 40 mm is machined in to rectangular samples of dimensions 80 mm x 60 mm x 20 mm and solution treated at 505°C for 120 minutes. These samples were deformed through cryorolling (CR) up to a true strain of 1.2, in order to produce UFG microstructure in the starting solutionised Al 2014 alloy. The procedure of cryorolling (CR) has been explained in our earlier published work [4.82] and earlier section 4.1 and 4.2 . These deformed samples were

annealed from 100°C to 250°C with an interval of 50°C for the time duration of 1 hour. The mechanical properties such as tensile strength (TS), yield strength (YS) and % elongation of solution treated (ST), cryorolled (CR) and annealed alloy (CR+AN) is determined by performing tensile test in H25K-S Tinius Oslen tensile testing machine with a strain rate of 5 x 10^{-4} S^{-1} and a constant crosshead speed. Fatigue crack growth rate (FCGR) tests were performed on solution treated (ST), cryorolled (CR) and annealed (CR+AN) by following ASTM 647-08 standard using the compact tension (CT) specimen. The dimensions of the compact tension (CT) sample used in the present work are shown in Fig. 4.3.2. Fatigue crack growth rate, da/dN (FCGR) test usually involves the notched specimen which is subjected to cyclic loading and acceptably precracked in fatigue. The FCGR (da/dN) is expressed as a function of stress intensity factor range ΔK and is defined as material resistance to the stable crack extension under fatigue loading. The R ratio $\left(\frac{\sigma_{min}}{\sigma_{max}}\right)$ for all processed condition during FCGR tests in this work were maintained at 0.1.
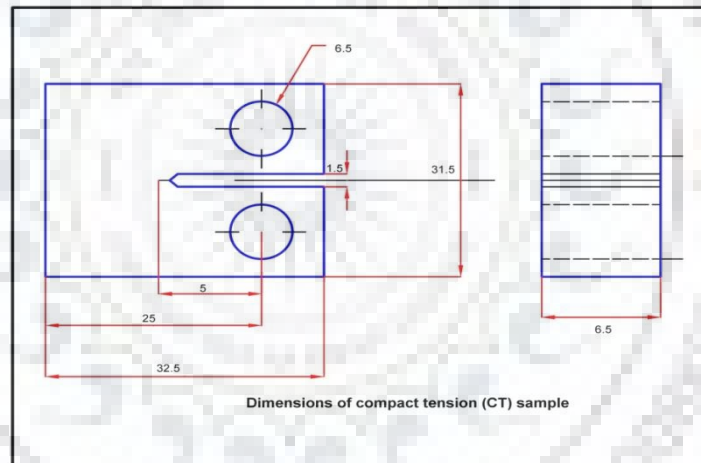
Figure 4.3.2: Dimensions of compact tension (CT) sample used in present work

Clevis loading fixtures were used for the CT specimen subjected to tensile-tensile fatigue as described in literature [4.19]. The FCGR test is started by conducting fatigue pre cracking up to .10 B, h, or 1 mm, whichever is greater and growing the precrack in such a way that final K_{max} during pre cracking could not exceed the initial K_{max} under existing loading condition, frequency 20 Hz, stress ratio R = 0.1, initial and final crack size 15 mm and 25 mm, respectively. For determining the crack growth rate, Constant Force Amplitude Test procedure is used in accordance with ASTM 647-08 standard. During the Constant Force Amplitude Test, each sample of ST, CR, CR+AN alloys were tested at a constant force range (ΔP) under

given loading condition . ΔK increasing values were used for finding out da/dN values i.e crack growth rate and unknowns 'C' and 'm' values in Paris equation $\left(\frac{da}{dN} = C\Delta K^m\right)$.

The microstructural features of ST, CR, CR+AN alloy were characterized by optical, TEM, and EBSD. The details of TEM sample preparation has been explained in our earlier published work [4.83] and earlier sections 4.1 and 4.2. EBSD sample was prepared by mechanical polishing with the help of fine cloth and followed by elecropolishing using an etchant having a composition of 80% methanol and 20% nitric acid at a 13 V for 60 sec. The step size of .05 μm was used for all the processed sample in the present study during EBSD scans. The fracture surface morphology of FCGR tested samples for all processed conditions was examined by FE SEM Quanta 200.

4.3.3 Results

4.3.3.1 Optical Microstructure

The optical microscopy has been used for characterizing the microstructural features of solution treated (ST) and cryorolled (CR) Al 2014 alloy in this work. Fig. 4.3.3(a) corresponds to the optical microstructure of the starting solution treated (ST) alloy.
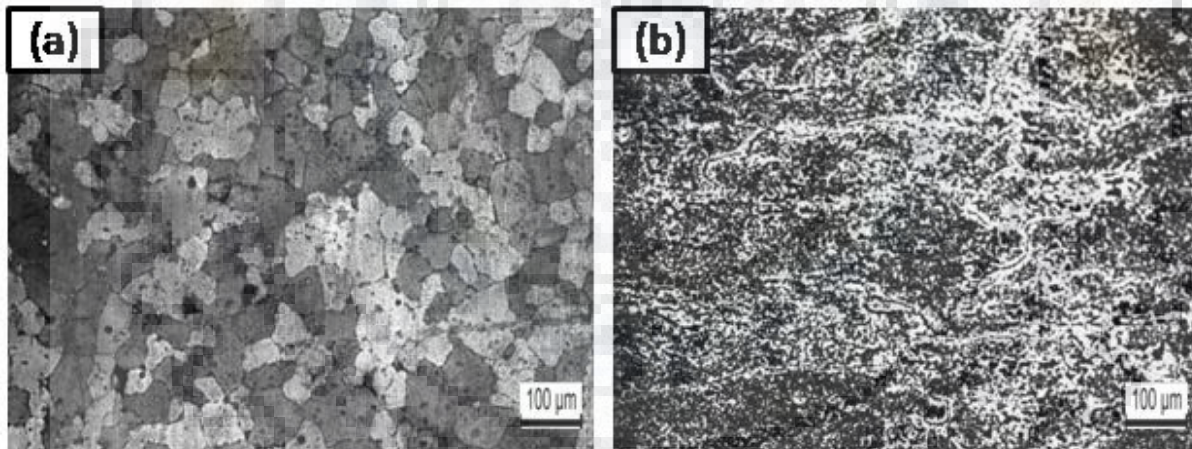
Figure 4.3.3: Optical micrographs of (a) ST alloy; (b) cryorolled (CR) alloy

The slightly equiaxed microstructure having a grain size in the range of 50 μm – 200 μm can be visualised from this figure. When solution treated Al 2014 alloy is cryorolled (CR) up to true strain of 1.3, the coarser grains in the solution treated (ST) alloy are transformed in to elongated sub structure, which are severely deformed having a low aspect ratio as observed from Fig. 4.3.3(b). Usually optical microscopic studies in severely deformed alloy does not provide the information regarding dislocation sub structure formed along with the quantification of high angle and low angle grain boundaries during the deformation.

Therefore, microstructural features of high strain samples/ deformed samples were characterized by the help of TEM and EBSD in this work.

4.3.3.2 EBSD Studies

The microstructural evolution in Al 2014 alloy after cryorolling (CR) and followed by annealing (CR+AN) in the temperature range from 100°C to 250°C has been investigated by performing EBSD studies on corresponding samples in the present work. The inverse pole figure (IPF) map superimposed with grain rotation (GR) angles is shown in Fig. 4.3.4. Fig. 4.3.4(a) shows the inverse pole figure (IPF) map of cryorolled (CR) sample.
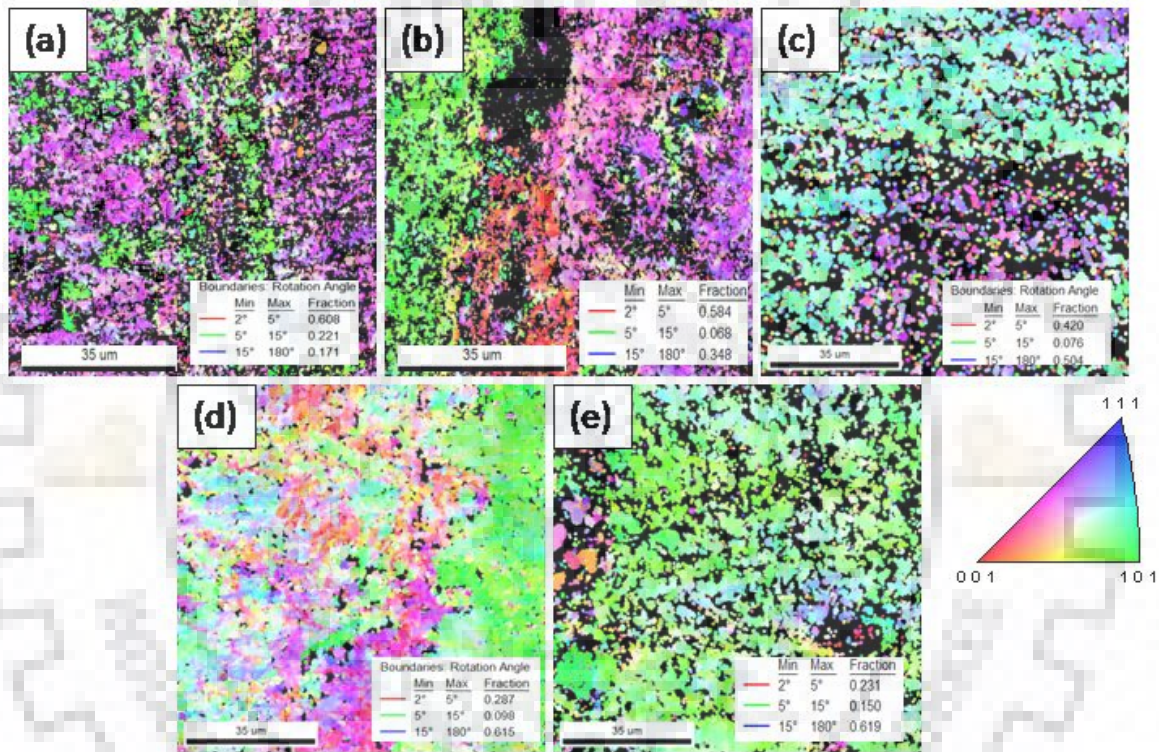
Figure 4.3.4: The inverse pole figure (IPF) map superimposed with grain rotation (GR) angle for various processed condition, (a) CR Al 2014 alloy; (b) CR Al 2014 annealed at 100°C; (c) CR Al 2014 annealed at 150°C   ;   (d) CR Al 2014 annealed at 200°C ; (e) CR Al 2014 annealed at 250°C

Severe deformation imposed by cryorolling (CR) can be visualized as observed from this figure. In addition, severely deformed along with elongated substructures which are having a low aspect ratio along the rolling direction can be observed for the cryorolled (CR) sample as noticed from Fig. 4.3.4(a). The grain rotation (GR) angle superimposed on this Fig. 4.3.4(a) can be divided in two three parts: (i) 2 - 5° (misorientations, dislocations, and very low angle grain boundaries)   (ii) 5- 15° (low angle grain boundaries) (iii) > 15°C (high angle

140

grain boundaries). The high fraction of misorientation, very low angle grain boundaries and dislocations were observed for cryorolled (CR) sample as observed from this figure. When cryorolled (CR) sample is annealed at 100°C, a slight decrease in the volume fraction of dislocations, and very low angle grain boundaries and slight increase in fraction of high angle grain boundaries were observed. On annealing at 150°C, 200°C, and 250°C, the fraction of dislocations and very low angle grain boundaries are slightly decreased at 150°C, while this drop was significant at the annealing temperature of 200°C and 250°C as observed from grain rotation (GR) angle map superimposed on IPF map corresponding to these sample conditions (Fig. 4.3.4(c)-(e)), respectively. However, the number of fraction of high angle grain boundaries (>15⁰) for these annealing conditions 150°C, 200°C and 250°C significantly increases with increasing annealing temperature and observed to be maximum for 250°C.
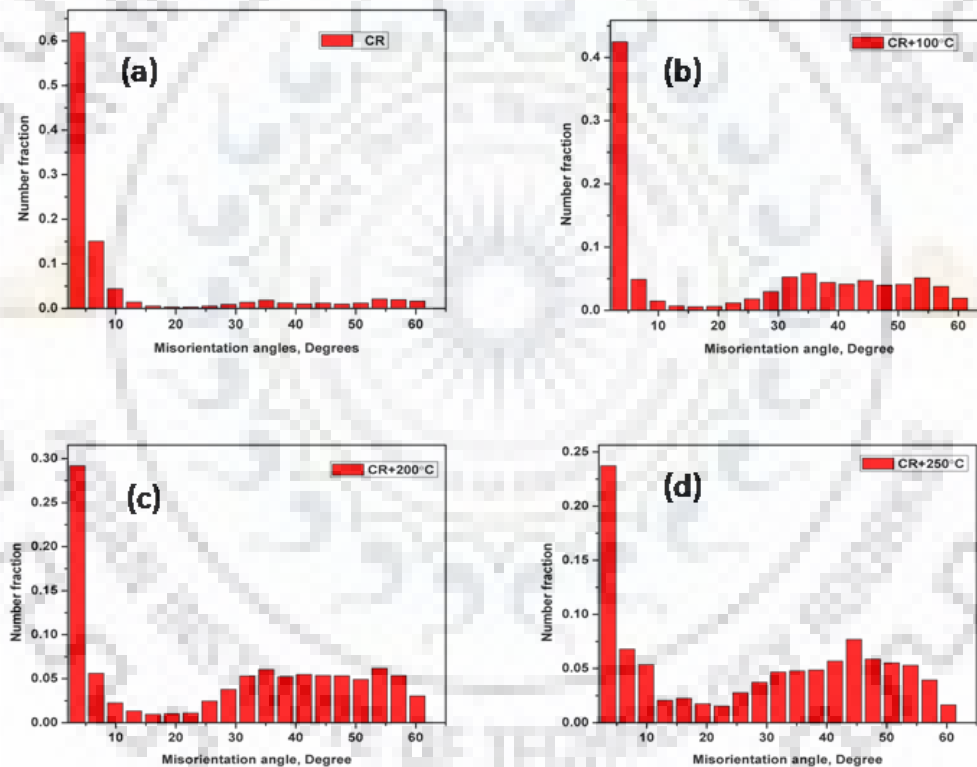
Figure 4.3.5: Grain boundary misorientation distribution histograms for , (a) CR Al 2014 alloy; (b) CR Al 2014 annealed at 100°C; (c) CR Al 2014 annealed at 200°C ; (d) CR Al 2014 annealed at 250°C

The histogram showing boundary misorientation distribution (number fraction with respect to misorientation angle) for cryorolled (CR) and annealed alloy (CR+AN) at 100°C to 250°C is shown in Fig. 4.3.5 (a)-(d). It confirms the similar trend as ascribed by grain rotation (GR) angle map superimposed in IPF map in previous (Fig. 4.3.4(a)-(e)).

The partition of IPF map (PIPF) is also shown in Fig. 4.3.6(a)-(d) for cryorolled followed by annealed (CR+AN) alloy at temperatures 100°C, 150°C, 200°C and 250°C. The grain orientation spread (GOS) < 1° is taken for evaluating the number fraction of recovered grains as discussed in the literature [4.114]. Fig. 5(a) shows the PIPF map for cryorolled sample annealed at 100°C. It is evident from this figure that numbers of recovered grains are very few in this process condition. However, with increasing annealing temperature from 150°C to 250°C , the fraction of recovered grains have increased as depicted from Fig. 4.3.6(b)-(d) corresponding to theses sample condition.

Figure 4.3.6: The partition of IPF map (PIPF) map for, (a) CR Al 2014 annealed at 100^0 C; (b) CR Al 2014 annealed at 150°C; (c) CR Al 2014 annealed at 200°C; (d) CR Al 2014 annealed at 250°C

4.3.3.3 TEM Studies

TEM studies were performed to investigate the microstructural changes during the cryorolling (CR) and followed by annealing (CR+AN) in the temperature ranging from 100°C to 250°C and the microstructural features are shown in Fig. 4.3.7(a)-(f). The cryorolled (CR) sample consists of diffused, irregular and ill defined grain boundaries as observed from Fig. 4.3.7(a). Dislocation tangling zone, DDW's (Dense dislocation walls) along with fine dislocation cells are also seen for cryorolled (CR) sample as depicted from Fig. 4.3.7(a). At an annealing of 100°C, some of dislocations are annihilated and transformed in to subgrains as noticed from Fig. 4.3.7(b), However, the number of subgrains formed at this annealing condition (100°C) are very less which substantiates that recovery effect at this temperature is not so prominent. A very few fine spherical precipitates (which are marked by red arrow) were

also observed corresponding to this sample condition as seen from TEM micrograph at this condition (Fig. 4.3.7(b)). When sample is annealed at 150°C, a noticeable change in the microstructure is observed (Fig. 4.3.7(c)). In this case, diffused ill defined grain boundaries formed due to heavy deformation are relaxed significantly with reduced dislocation density. Some of ill defined grain boundaries rearranges and transformed in to equiaxed subgrains, whose size is slightly bigger than previous annealed condition. Along with equiaxed subgrain, a fine spherical phase is still observed which is slightly coarser than sample annealed at 100°C.
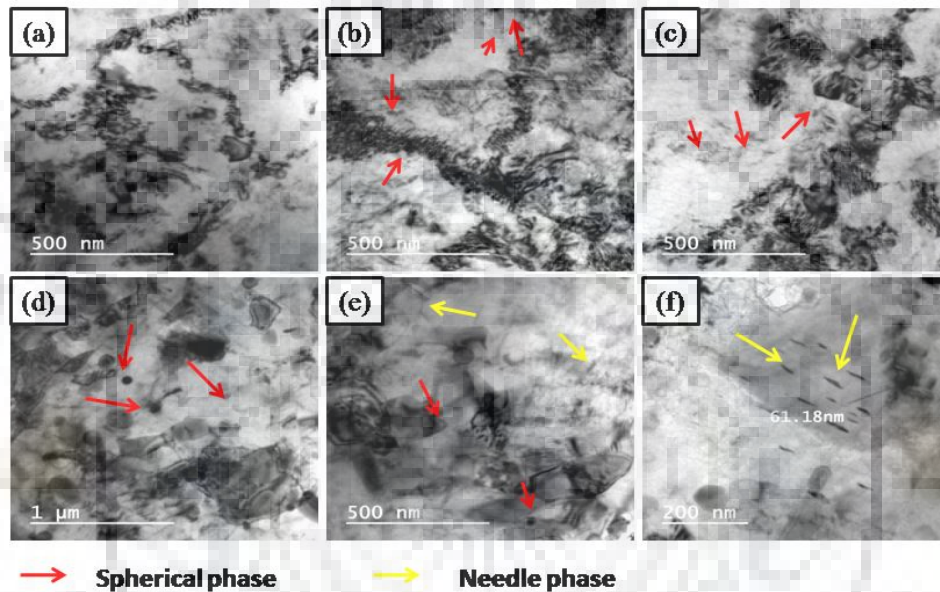
Figure 4.3.7: TEM micrographs for various processed condition, (a) CR Al 2014 alloy; (b) CR Al 2014 annealed at 100°C; (c) CR Al 2014 annealed at 150°C ; (d) CR Al 2014 annealed at 200°C ; (e) CR Al 2014 annealed at 250°C; (f) CR Al 2014 annealed at 250°C at higher magnification

The substantial decrease in the dislocation density is observed when sample is annealed at 200°C (Fig. 4.3.7(d)). In addition, subgrain size has slightly increased at this condition as compared to previous annealed condition samples. Fine spherical phase is still seen at this sample condition (200°C) as before, however the size of this phase has increased slightly as compared to sample annealed at 100°C, and 150°C. It can be inferred that recovery effect at this sample condition (200°C) is accelerated due to which subgrain size as well as fine spherical size has increased along with reduced dislocation density. The recovery effect is further accelerated along with the sign of recrystallisation process when samples are annealed at 250°C as depicted from Fig. 4.3.7(e). Combination of equiaxed subgrain and recrystallised grain along with reduced dislocation content can be observed from the Fig. 4.3.7(e), which is

143

the TEM micrographs corresponding to sample annealed at 250°C. In addition, the significant change in the precipitation behavior was also noticed at this condition. Along with spherical phase (marked by red arrows), a fine needle phase (marked with yellow arrows) is also observed as noticed from Fig. 4.3.7(e). The spherical phase becomes significantly coarser at this condition while needle phase was very fine as seen from TEM micrographs corresponding to this sample condition. For better visualization of needle phase and spherical phase, high magnification TEM micrograph is also shown in Fig. 4.3.7(f) corresponding to sample annealed at 250°C.

4.3.3.4 Mechanical Properties

The mechanical properties (UTS, YS, % elongation and hardness) of cryorolled (CR) and annealed alloy (CR+AN) in the temperature range 100°C to 250°C are discussed in earlier section 4.1.
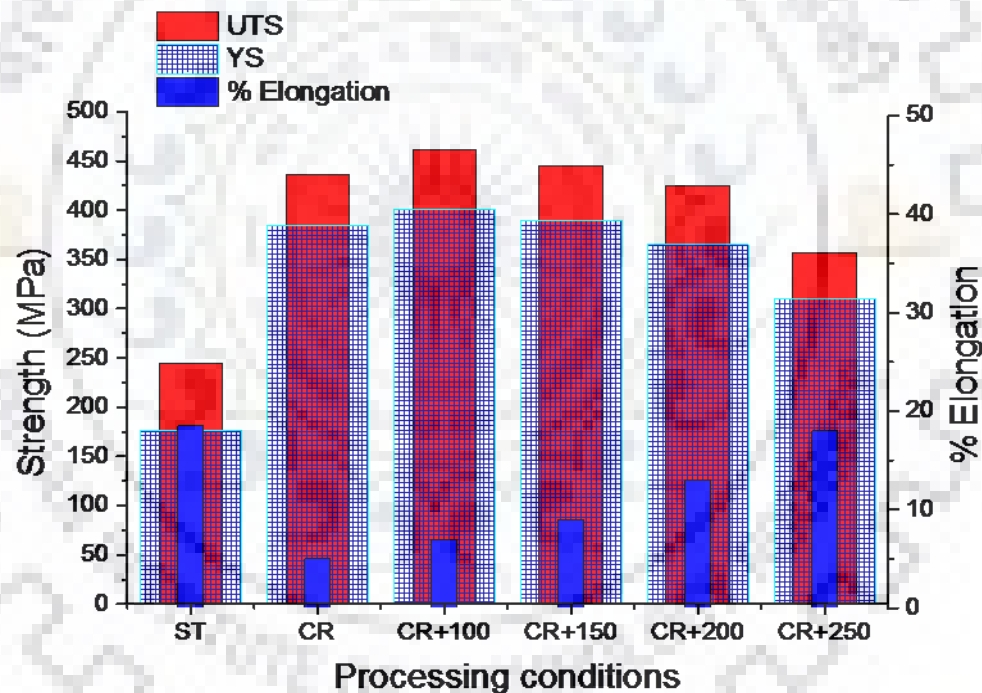
Figure 4.3.8: Variation of Tensile strength, Yield strength, and % Elongation with respect to various processing conditions

The variation in mechanical properties is shown in Fig. 4.3.8. It is observed from Fig. 4.3.8 that significant improvement in tensile, yield strength and hardness of Al 2014 alloy after grain size reduction as compared to solution treated (ST) alloy. On annealing of cryorolled (CR) alloy in the temperature range of 100°C to 250°C, the tensile, yield strength and hardness have increased up to 100°C while from 150°C - 200°C, the slight decrease in these

properties was observed. However, on annealing at 200°C – 250°C, the significant decrease in strength and hardness was noticed.

The total % elongation of solution treated (ST) alloy was observed to be 18.5 %, which is reduced to 4 % due to cryorolling (CR) while upon annealing in the temperature range 100°C – 250°C, the % elongation of cryorolled (CR) alloy rises significantly and becomes 18% at 250°C as noticed from Fig. 4.3.8.

4.3.3.5 Fatigue crack growth rate (FCGR) test results

Fatigue life until failure can be divided in to two parts i) crack initiation period ii) crack propagation period. First phase is associated with crack nucleation and while second phase is concerned with macrocrack growth. It is very important to identify the conditions at which the crack growth takes place before unstable failure. For example, in a pressure vessel, these fatigue cracks may give rise to explosion. Therefore, it is essential to monitor the fatigue crack growth by periodic inspections.

Fatigue crack growth test has been conducted on solution treated (ST), cryorolled (CR) and cryorolled followed by annealed (CR+AN) alloy in the temperature range 100°C -250°C to find out its crack growth resistance in this work. Usually, fatigue crack growth test results cover the range of ΔK (stress intensity factor range) and fatigue crack growth rate (FCGR). In these experiments, fatigue crack growth rate (da/dN) is plotted with respect to ΔK (stress intensity factor range) on log-log plot. The following expression is used to model the different region I, II, III of fatigue crack growth curve as shown in Fig. 4.3.9 as reported in literature [4.115].

$$\frac{da}{dN} = f_R(\Delta K) \tag{4.17}$$

Region I, II, and III are the threshold ΔK region, the Paris ΔK region, the stable tearing crack growth region, respectively, as described in literature. The threshold value of stress intensity factor in regime I is denoted by ΔK_{th} and concerned with minimum value of stress intensity factor below which macro crack can not be initiated in to the material.

145
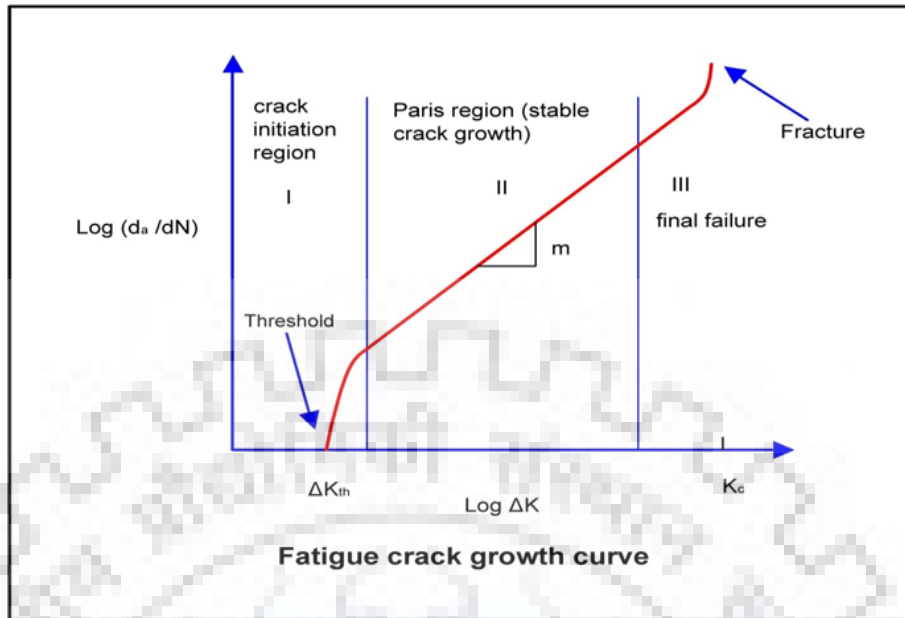
Figure 4.3.9: Schematic showing the three stages of fatigue crack growth curve

The region II is stable crack propagation region and can be modelled by following equation as described in literatures [4.34]

$$\frac{da}{dN} = C(\Delta K)^m \qquad (4.18)$$

Where C and m are material constants and can be obtained by linear regression of the equation

$$log\left(\frac{da}{dN}\right) = log(C) + mlog(K) \qquad (4.19)$$

Where m is the slope of Paris regime and $log(C)$ is intercept on y axis.

The crack growth rate in Stable tearing crack growth region III is too high resulting very less crack growth life due to which engineering significant of this region is limited.

On the basis of above discussion, stage II Paris crack growth region has been investigated for all the processed condition (ST, CR, CR+AN$_{100-250}$) and values of constant C and m has been evaluated and listed in Table. 4.3.1. The fatigue crack growth rate curves for various processed conditions are shown in Fig. 4.3.10.

From the analysis of fatigue crack growth rate curves following points can be highlighted.

(i)   For a given applied stress intensity factor (ΔK) range, fatigue crack growth resistance of bulk UFG Al 2014 alloy has decreased resulting faster crack growth rate especially at low stress intensity factor range ΔK as compared to coarser grain counterpart (ST alloy).

146

(ii)   The significant improvement in fatigue crack growth resistance is observed on annealing of cryorolled (CR) alloy up to temperature range 100°C – 200°C and observed to maximum at 100°C, while decrease in fatigue crack growth resistance is observed at the annealing temperature of 250°C as compared to CR, and sample annealed at 100°C, 150°C, 200°C.

(iii)   The values of threshold intensity factor (ΔK_{th}) increases after cryorolling (CR) as compared to solution treated (ST) alloy.

(iv)   On annealing in the temperature range of 100°C - 250°C, the threshold intensity factor (ΔK_{th}) further increases and observed to be maximum at 100°C as compared to solution treated (ST) and cryorolled (CR) alloy.

Table 4.3.1: List of fatigue crack growth properties for various processed condition

Sample condition	m	C	ΔK_{th} *(MPa$\sqrt{m}$)*
ST	3.2	4×10^{-9}	5.8
CR	6.2	9×10^{-18}	7.17
CR + 100°C	3.5	3×10^{-7}	12.2
CR + 150°C	4.1	4×10^{-15}	8.43
CR + 200°C	5.3	8×10^{-9}	7.44
CR + 250°C	6.9	6×10^{-14}	6.35
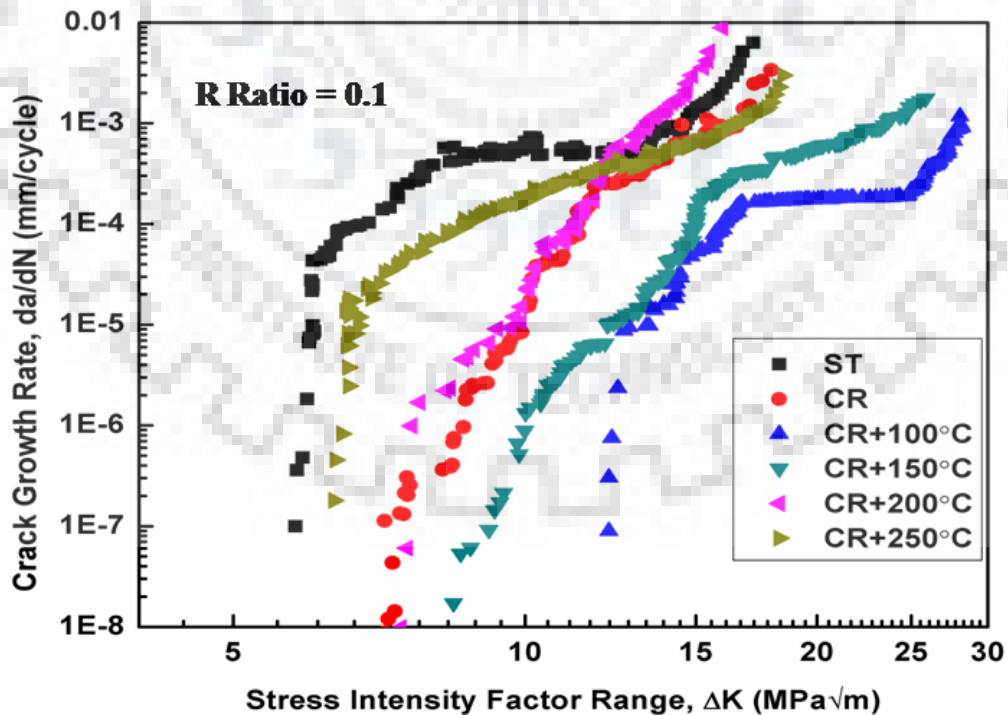
Figure 4.3.10: Fatigue crack growth curves for various processed conditions

4.3.4   Discussions

4.3.4.1   Factors affecting the crack growth rate near low intensity factor range:

In the present investigation, the fatigue crack growth test results for ST, CR, and CR+ AN alloys shows two important findings: (i) Fatigue crack growth resistance of bulk UFG Al 2014 alloy developed by cryorolling (CR) has lower fatigue crack growth resistance and higher crack stress intensity factor ΔK_{th} as compared to solution treated (ST) alloy (ii) on annealing, the fatigue crack growth resistance and crack stress intensity factor ΔK_{th} has improved as compared to ST as well as cryorolled (CR) alloy and these values are observed to be maximum for cryorolled followed by annealed alloy at 100°C.

Crack stress intensity factor is characterized by threshold stress intensity factor ΔK_{th} by estimating fatigue crack growth rate as 10^{-7} mm/cycle in this work . A value of threshold stress intensity factor ΔK^{th} is listed in Table 4.3.1. Constant C and m (Paris constant) for stage II regime for all processed condition is evaluated as described in previous section and shown in Fig. 4.3.11 and Table 4.3.1.
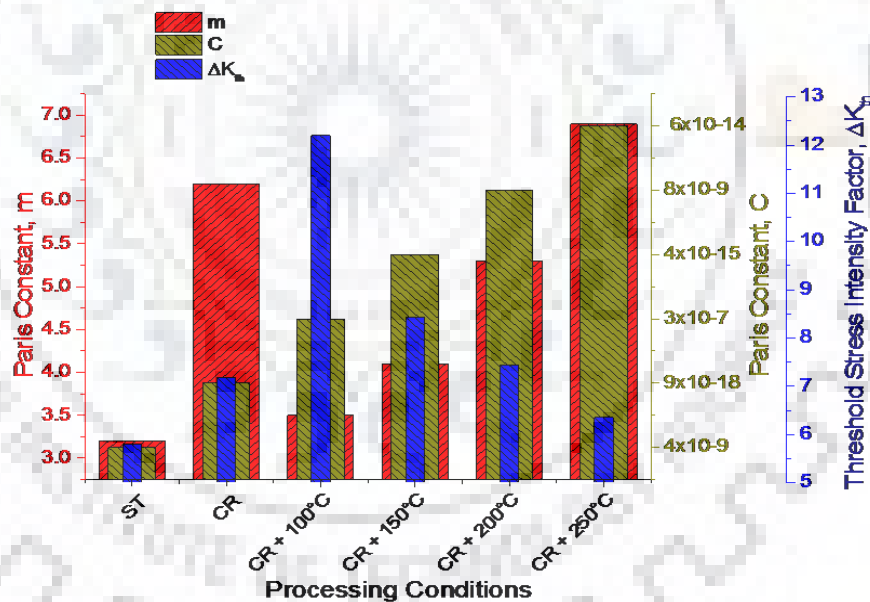
Figure 4.3.11: Variation of Paris constant m, C and threshold intensity factor for various processing conditions

Fig. 4.3.10 shows the plot between the crack growth rate (da/dN) and stress intensity factor range ΔK for various processed condition in this work. Solution treated (ST) coarser grain alloy shows lower fatigue crack growth rate (FCGR) and lower threshold stress intensity factor ΔK_{th} as compared to cryorolled (CR) alloy, especially in low and mid intensity factor range ΔK as evident from the Fig. 4.3.10 and Fig. 4.3.11. The observed value of Paris constant

m (Fig. 4.3.11) for ST alloy also confirms the same as it is lower for ST alloy as compared to cryorolled (CR). It means that fatigue crack propagation rate in bulk UFG Al 2014 alloy in low stress intensity factor ranges is higher as compared to coarser grain ST alloy. The similar findings were observed in various earlier published literatures on fatigue crack growth behavior of bulk UFG[4.69,4.116-4.117]. Recently, Yin et al. [4.118] studied the effect of grain size on fatigue crack growth behavior of 2524 Al alloy and revealed that fatigue crack growth resistance deteriorates after grain size reduction well below 1μm. Crack closure effect is observed to be higher for coarser grain alloy as compared to bulk UFG alloy in their study. Similar findings were reported by Meyer et al. [4.56] during the fatigue crack growth rate testing of unECAPed and ECAPed Al 6061 alloy and observed the less tortuous crack path for bulk UFG alloy resulting lesser crack driving force and higher fatigue crack growth rate for bulk UFG Al 6061 alloy. The similar trend is observed in the present work during fatigue crack growth rate testing of ST and cryorolled (CR) Al 2014 alloy. The fractured compact tension (CT) samples after FCGR testing for various conditions are shown in Fig. 4.3.12 (a)-(e).
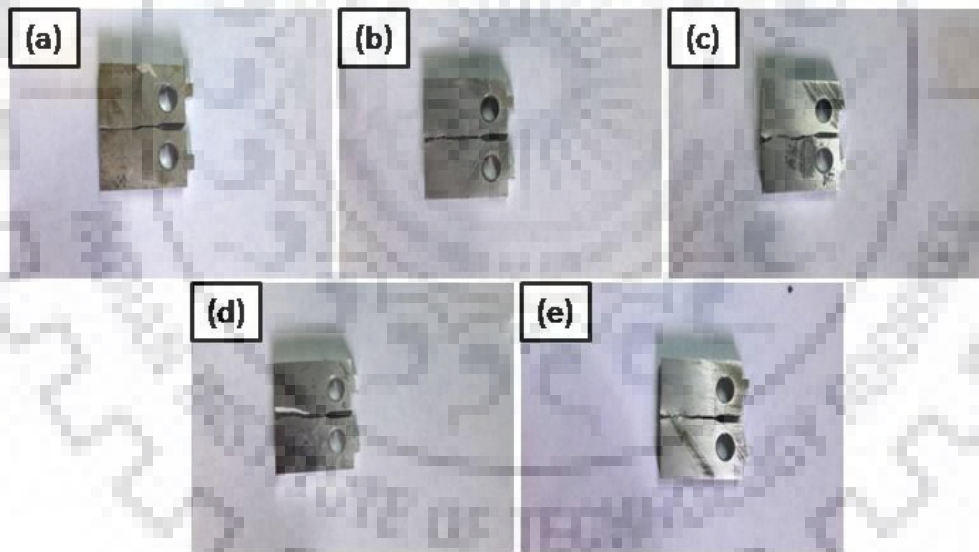
Figure 4.3.12: Fractured compact tension (CT) sample showing the profile of fracture path for (a) ST Al 2014 alloy ; (b) CR Al 2014 alloy; (c) CR Al 2014 annealed at 100°C; (d) CR Al 2014 annealed at 150°C ; (e) CR Al 2014 annealed at 250°C

Fig. 4.3.12(a)-(b) are the fractured compact tension (CT) sample for solution treated (ST) and cryorolled (CR) Al 2014 alloy. These figures also confirms that fracture surface profile of

cryorolled sample (CR) is slightly flat while for ST alloy it is slightly curved. It confirms that during the fracture process, less tortuous path is available for cryorolled (CR) sample as compared to ST alloy due to which fatigue crack propagation is fast in cryorolled (CR) alloy. However, it is very important to understand the growth mechanism of fatigue crack microscopically for ST as well as cryorolled (CR) alloy. Now, it is well established that growth behavior of small fatigue crack is strongly microstructure sensitive as reported in literature [4.106]. Goto et al. [4.106] and Vinogradove [4.58] reported that crack behaviour in near threshold slow crack growth regime is strongly microstructure sensitive while at the intermediate regime, it is microstructure insensitive. It is reported that growth behavior of small fatigue crack closely depends upon the cyclic plastic zone (CPZ), which can be expressed by the following equation as described in the literature [4.106]

$$r_{rp} = \frac{1}{2\sqrt{2\Pi}} \left(\frac{\Delta K_{eff}}{2\sigma_0}\right)^2 \qquad (4.20)$$

Where r_{rp} = radius of cyclic plastic zone near crack tip, ΔK_{eff} = Effective stress intensity factor range which is equal to $U\Delta K$. Here, U is crack opening ratio and ΔK is stress intensity factor range and σ_0 = Yield stress.

Above model devised by the Goto et al. [4.106] predicts the growth of small crack well near low intensity factor range for the coarser grain (CG) ST alloy as well as ultrafine grained (UFG) cryorolled (CR) Al 2014 alloy. From the equation (4.20), it is obvious that for the ST Al 2014 alloy, yield stress (YS) is very less due to which radius r_{rp} of cyclic plastic zone is very high. It is reported that roughness induced crack closure depends upon size of RPZ near crack tip. When RPZ is greater than grain size, crack path follows intergranular crack path and provides roughness induced crack closure [4.106]. The similar thing might occur for the coarser grain (CG) solution treated alloy because size of reversible cyclic plastic zone (RPZ) is much larger than the grain size. In addition, large number of neighbouring grains provides sufficient plasticity to the material, resulting roughness induced crack closure for ST alloy in low stress intensity factor range. This can be confirmed from the fractograph (Fig. 4.3.13(a)) corresponding to ST alloy near low intensity factor range. From Fig. 4.3.13(a), it is clear that for solution treated (ST) alloy, roughness induced crack closure is prominent due to larger width of cyclic plastic zone resulting significant crack tip plasticity. This mechanism is shown in Fig. 4.3.14 (a)-(c), where it is seen that large number of grains are well within the cyclic plastic zone which imparts intergranular crack path in coarser grain ST alloy (Fig. 4.3.14(c)).

On the other hand, yield stress for cryorolled (CR) alloy is more due to which radius r_{rp} of cyclic plastic zone for CR alloy is very less. In this case, size of reversible plastic zone (RPZ) is less than the grain size (Fig. 4.3.14(a)) of the material due to which crack may propagate along straight growth path as reported in the literature [4.14]. Fractograph corresponding to cryorolled (CR) alloy near low intensity factor range confirms the same trend as observed from the Fig. 4.3.13(b).
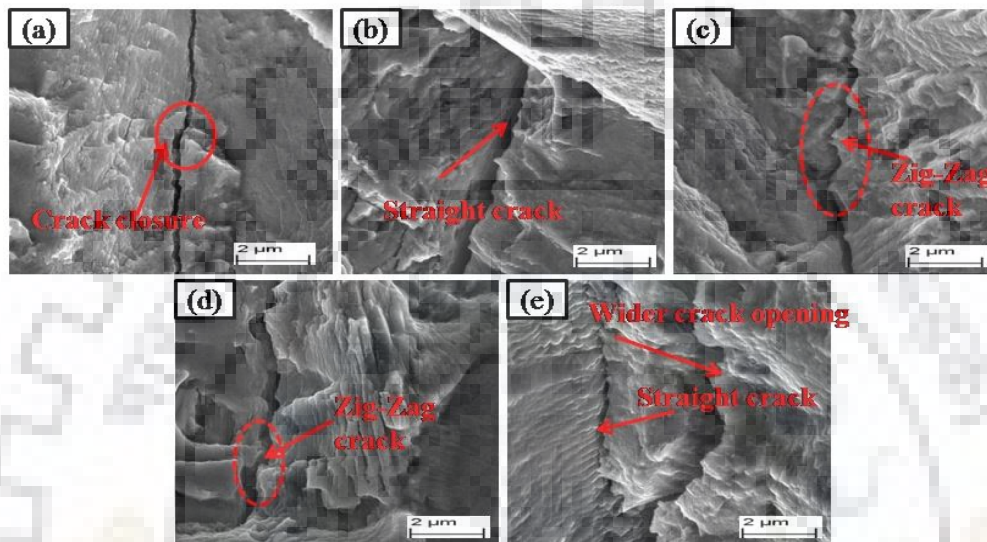
Figure 4.3.13:   Fractographs showing the crack profile near low intensity factor range for (a) ST Al 2014 alloy ; (b) CR Al 2014 alloy; (c) CR Al 2014 annealed at 100°C; (d) CR Al 2014 annealed at 150°C ;   (e) CR Al 2014 annealed at 250°C

The mechanism showing the formation of cyclic plastic zone for fine grain material near low intensity factor range is shown in Fig. 4.3.14(a). From this figure, it is evident that for fine grained material, cyclic plastic zone near crack tip is lesser than the grain size which provides less tortuous path for crack growth and reduces the crack tip plasticity, resulting straight crack growth path and faster crack growth rate near low intensity factor range.

The crack growth behaviour of cryorolled followed by annealed alloy in the temperature range 100°C -250°C is entirely different as compared to cryorolled (CR) alloy in the present investigation. The value of observed Paris constant 'm' is minimum for cryorolled followed by annealed alloy at 100°C as observed from Table. 4.3.1 and Fig. 4.3.10, while threshold intensity factor ΔK_{th} is maximum for the same condition.
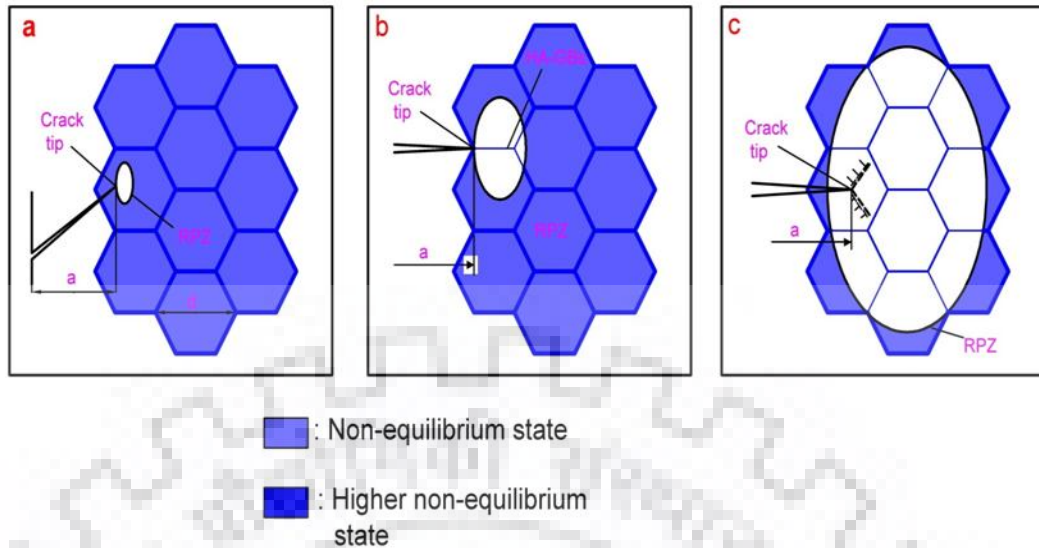
Figure 4.3.14: Mechanism showing the relationship between cyclic reversible plastic zone (RPZ) and grain size when (a) RPZ is less than grain size; (b) RPZ is slightly greater than the grain size ; (c) RPZ is significantly greater than grain size

On further annealing in the temperatures 150°C, 200°C, and 250°C, the slight increase in the 'm' value while significant drop in the threshold intensity factor ΔK_{th} (Fig. 4.3.11 and Table. 4.3.1) is observed substantiating that at low intensity factor range, sample annealed at 100°C has higher fatigue crack growth resistance and threshold intensity factor ΔK_{th} which deteriorates   when sample was   annealed in the temperatures 150°C, 200°C, and 250°C. Fractographs corresponding to sample annealed in the temperature range 100°C -250°C near low intensity factor is shown in Fig. 4.3.13(c)-(e). From these fractographs, it is evident that roughness induced crack path, serrated crack profile is present for cryorolled sample annealed at 100°C (Fig. 4.3.13(c)). However, this feature is decreasing gradually when sample were annealed in the temperatures 150°C, 200°C, and crack path becomes almost straight at 250°C as observed from Fig. 4.3.13(d)-(e). From these observations, it is clear that fatigue crack propagation for annealed alloy at 100°C is slow due to which it shows higher crack growth resistance near low stress intensity factor range. On the other hand, on annealing in the temperatures 150°C, 200°C, and 250°C, fatigue crack propagation increases gradually, causing decrease of fatigue crack growth resistance but it is still more than cryorolled (CR) alloy. It is reported that crack growth rate of precipitation hardenable alloy is strongly affected by presence of shearable and non shearable precipitates [4.77]. It was observed that cryorolled followed by annealed alloy at 100°C shows higher fatigue crack growth resistance not only in low intensity factor range but also at higher intensity factor range. The presence of spherical

152

precipitates as well as needle might be the possible reason for this. In this study, detailed TEM investigation was not carried out, In our earlier published work [4.82] and from section 4.1, various kind of precipitates were observed during post deformation annealing in the temperature range 100°C - 250°C. The observed precipitation sequence in this temperature range has been identified as
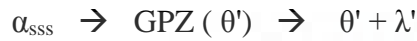
$$\alpha_{sss} \; \rightarrow \; GPZ\,(\,\theta') \; \rightarrow \; \theta' + \lambda'$$

Where α_{sss} is the supersaturated solid solution, θ' is fine semicoherent spherical phase (Al_2Cu) and λ' is fine semicoherent needle phase (AlCuMgSi). θ' phase is observed in the temperatures range 100°C - 200°C, while along with θ' phase, λ' phase is observed at annealing temperature of 250°C in this study. In addition, with increasing annealing temperature from 100°C - 250°C, this phase become slightly coarser and loses the coherency with the matrix as described in our earlier published work and present work [4.82].

Malekjani et al. [4.77] reported that mechanical properties of material are greatly affected by the shape, size and distribution of precipitates. When the precipitates are coherent with the matrix, the dislocations are not cut by the fine particles and forms loops around these fine coherent phases at the interface and prevents cyclic strain localization and stress concentration resulting increase in crack initiation period. The similar mechanism might occur in the present case for the sample annealed at 100°C. The fine semicoherent spherical phase θ' (Al_2Cu) evolved at this temperature (100°C) forms loop and facilitates resistance to strain localization and stress concentration due to which threshold stress intensity factor ΔK_{th} is observed to be maximum as compared to all other sample conditions in this work. In addition, these fine semicoherent spherical precipitates θ' (Al_2Cu) obstructs the fatigue crack growth and provides significant plasticity to the crack tip resulting enhanced fatigue crack growth resistance for the sample annealed at 100°C. The another reason for improved fatigue crack growth resistance on this sample condition (100°C) might be due to the presence of planar reversible slip caused by fine semicoherent spherical phase θ' (Al_2Cu), which promotes significant zigzag crack growth along with higher crack tip deflection as reported in literature [4.77]. To confirm this, EDAX of crack path for sample annealed at 100°C and 250°C was carried out in this work and shown in Fig. 4.3.15(a)-(b). From these figures, it is evident that fine spherical phase Al_2Cu is responsible for significant crack tip deflection and zig zag crack growth due to which fatigue crack growth resistance is significantly improved for this sample condition (100°C) as compared to other conditions. Upon annealing at 250°C, the spherical phase Al_2Cu and

153

needle phase AlCuMgSi are observed (Fig. 4.3.15(b) which provides straight growth path during fatigue crack propagation due to coarsening of spherical Al_2Cu phase. With increasing annealing temperature from 100°C to 200°C, the spherical phase becomes coarser gradually and loses coherency with the matrix. In addition, these coarser precipitates facilitates ease in stress concentration resulting gradual decrease in crack initiation period, which further reduces the threshold stress intensity factor ΔK_{th} gradually as compared to sample annealed at 100°C. However, the observed threshold stress intensity factor ΔK_{th} is still more than ST and cryorolled (CR) alloy because these precipitates are becoming coarser with increasing annealing temperature as compared to sample annealed at 100°C.
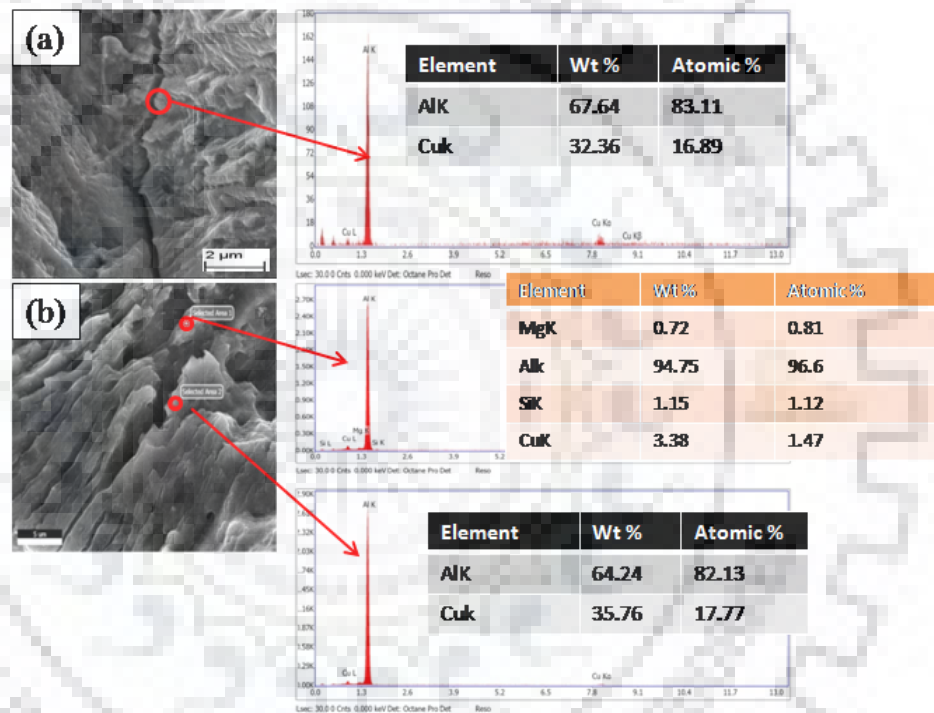
Figure 4.3.15: EDAX of crack profile near low intensity factor range for (a) CR Al 2014 annealed at 100°C;   (b) CR Al 2014 annealed at 250°C

However, they are still very fine and impart significant obstruction to dislocation motion due to which observed threshold stress intensity factor ΔK_{th} is still more than ST and cryorolled (CR) alloy where precipitates were not evolved. The fatigue crack growth resistance in the temperature range from 100°C -200°C gradually decreases as compared to sample annealed at 100°C while still more than cryorolled (CR) alloy as observed from the Fig. 4.3.10. With increasing annealing temperature from 100°C -200°C, the observed drop in fatigue crack growth resistance as compared to sample annealed at 100°C might be due to the presence of coarser nonshearable precipitates, which does not favour planar reversible slip

resulting less crack tip deflection and less crack path tortousity as reported in the literature. The SEM photograph (Fig.4.3.13(d)-(e)) corresponding to sample annealed at 150°C and 250°C also confirms the less crack path tortousity and crack tip deflection as compared to sample annealed at 100°C.

The threshold stress intensity factor ΔK_{th} and fatigue crack growth resistance of sample annealed at 250°C is observed to be less than cryorolled (CR) alloy in this work. This is due to the fact that in this sample condition along with spherical phase θ' (Al_2Cu), fine needle phase λ' (AlCuMgSi) is also observed as seen from TEM micrographs. The spherical phase becomes significantly coarser while needle phase is still very fine. Apart from this recovery, recrystallisation also takes place at this temperature as seen from TEM and EBSD studies in this work. The coarser spherical phase provides more number of stress concentration points due to which threshold stress intensity factor ΔK_{th} observed to be less as compared to cryorolled (CR) sample. In addition, crack can penetrate along this spherical and needle phase precipitates easily in straight line manner as discussed earlier resulting faster crack growth rate as compared to other conditions in this work.

4.3.4.2 Factors affecting the crack growth rate at high stress intensity factor range :

To investigate the crack growth behaviour of solution treated (ST), cryorolled (CR) and cryorolled followed by annealed alloy in high stress intensity factor range, detailed fractographic studies were made in present investigation after FCGR (fatigue crack growth rate) testing.

 Fig. 4.3.16 shows the fracture surface of ST (solution treated) alloy after fatigue crack growth rate testing. Fig. 4.3.16 (a)-(e) shows the low and higher magnification fractographs of ST alloy after FCGR test. Crack initiation and crack growth region (rectangular yellow box) can easily be visualised from the low magnification fractograph (Fig. 4.3.16(a)) corresponding to solution treated (ST) alloy. To observe crack growth region more clearly, the higher magnification fractographs are shown in Fig. 4.3.16 (b)-(e). The crack growth occurs due to formation of striations as observed from these fractographs at this condition. In addition, striation with wider gap (approximately 3μm) was observed as noticed from higher magnification fractograph (Fig. 4.3.16 (e)) corresponding to this condition. It is reported that striations represent the crack growth during cyclic loading [4.113]. Wider the striation gap, faster is the crack growth during cyclic loading [4.113]. For the solution treated (ST) alloy,

155

striation gap is more substantiating the faster crack growth in high stress intensity factor range during fatigue crack growth testing.
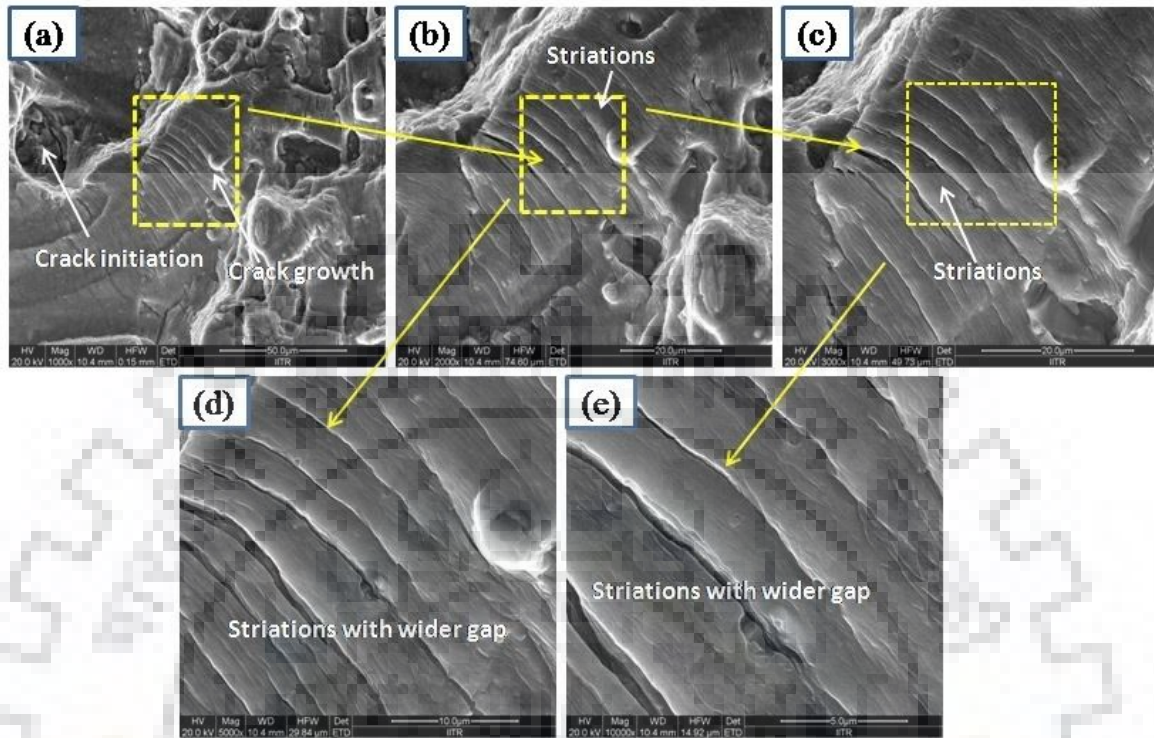
Figure 4.3.16: Low and high magnification fractographs of solution treated (ST) Al 2014 at higher stress intensity factor range

Fig. 4.3.17(a)-(d) shows the low and higher magnification fractographs corresponding to cryorolled (CR) sample after fatigue crack growth rate testing. Fine striations were observed for cryorolled (CR) sample after fatigue crack growth rate testing as observed from higher magnification fractographs (Fig. 4.3.17(b)-(d)) corresponding to this sample condition. Striation width is approximately 0.20µm as observed from higher magnification fractograph (Fig. 4.3.17(d) of cryorolled (CR) sample, which substantiate that fatigue crack growth resistance of cryorolled (CR) has significantly improved as compared to solution treated (ST) alloy in high stress intensity factor range. The similar findings were observed by Das et al. [4.96] during fatigue crack growth rate testing of cryorolled Al 7075 in high stress intensity factor range.
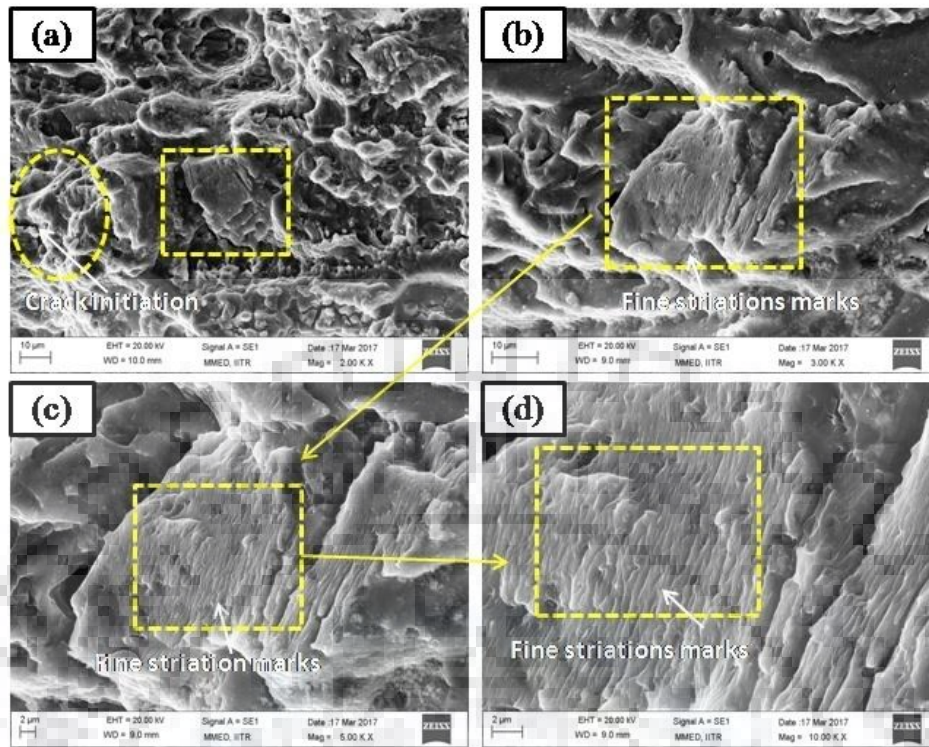
Figure 4.3.17: Low and high magnification fractographs of CR Al 2014 at higher stress intensity factor range
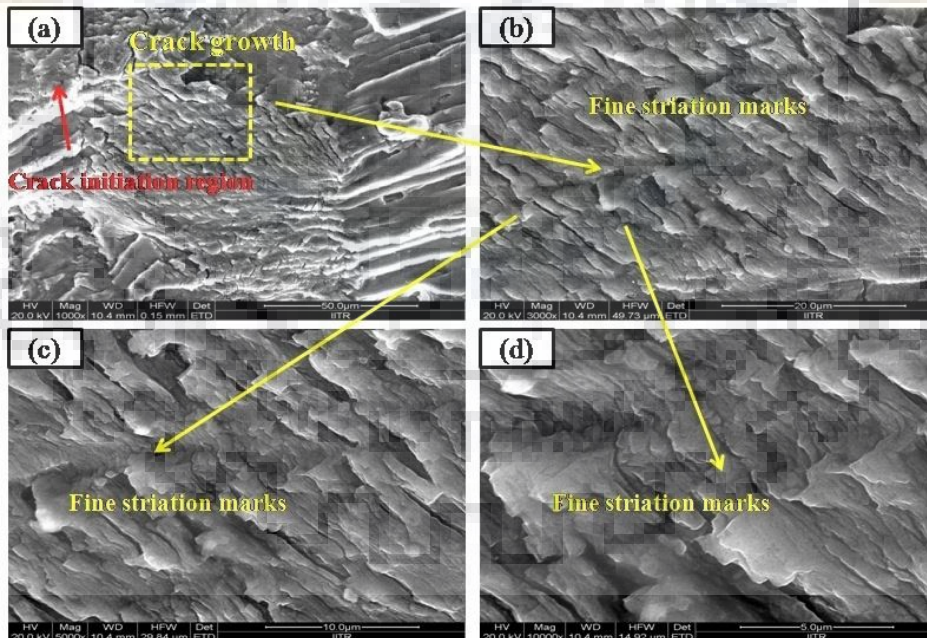
Figure 4.3.18: Low and high magnification fractographs CR Al 2014 annealed at 100°C at higher stress intensity factor range

157

Fractographs corresponding to sample annealed at 100°C is shown in Fig. 4.3.18(a)-(d). Very fine interrupted striations are seen from higher magnification fractographs (Fig. 4.3.18(b)-(d)) corresponding to this sample conditions. Interrupted striation might be due to the presence of fine spherical semicoherent phase θ', which obstructs the crack propagation during fatigue crack growth testing. In addition, the striation gap is nearly 0.12 μm corresponding to this sample condition, which is less than cryorolled (CR) sample due to which fatigue crack growth resistance of cryorolled followed by annealed alloy at 100°C is significantly improved as compared to previous conditions.

Fig. 4.3.19 (a)-(d) shows the low and higher magnification fractographs of cryorolled sample annealed at 150°C after fatigue crack growth rate testing.
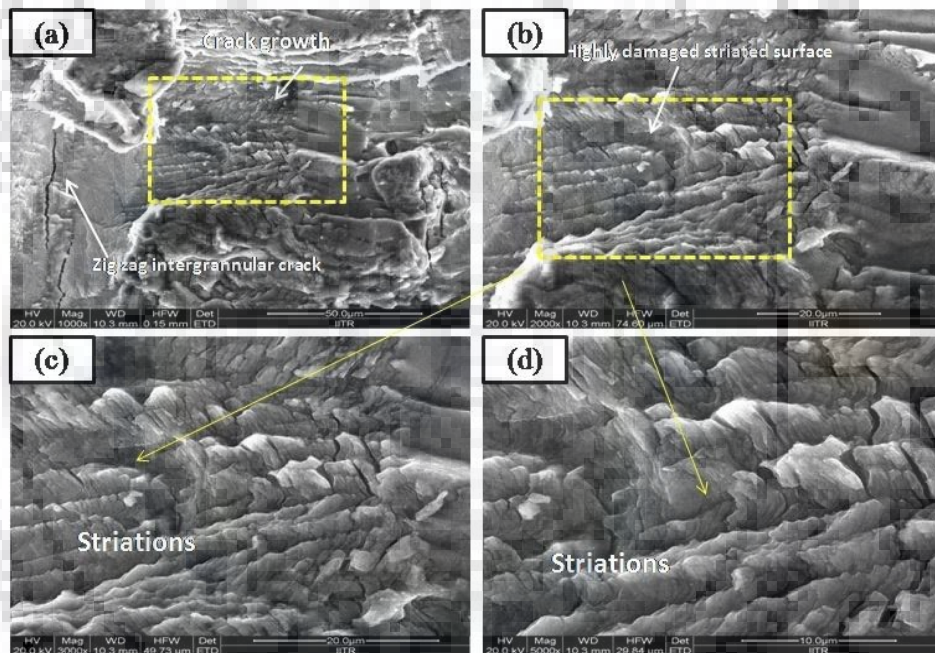
Figure 4.3.19: Low and high magnification fractographs CR Al 2014 annealed at 150°C at higher stress intensity factor range

The fracture surface in this condition is almost similar as in case of sample annealed at 150°C. Fine interrupted striations are also observed in this sample condition. However, striation gap is slightly larger than sample annealed at 100°C. The striation gap is almost 0.14 μm as observed from higher magnification fractographs (Fig. 4.3.19 (b)-(d)) corresponding to this sample condition, which means that fatigue crack growth resistance has slightly decreased as compared to sample annealed at 100°C. However, fatigue crack growth resistance for sample annealed at 150°C is still more than ST and CR sample in high stress intensity factor

range because striation gap for this condition is less than solution treated and cryorolled (CR) sample.

Low and high magnification fractographs for sample annealed at 200°C and 250°C is shown in Fig. 4.3.20(a)-(d) and Fig. 4.3.21(a)-(e), respectively. From these fractographs, it is evident that striation width increases with increasing annealing temperature and observed to be maximum (approximately 3µm) for sample annealed at 250°C, while for observed striation width for sample annealed at 200°C is 2 µm. This indicates that fatigue crack growth resistance in high stress intensity factor range at annealing temperatures of 200°C and 250°C has significantly decreased and observed to be minimum for sample annealed at 250°C.
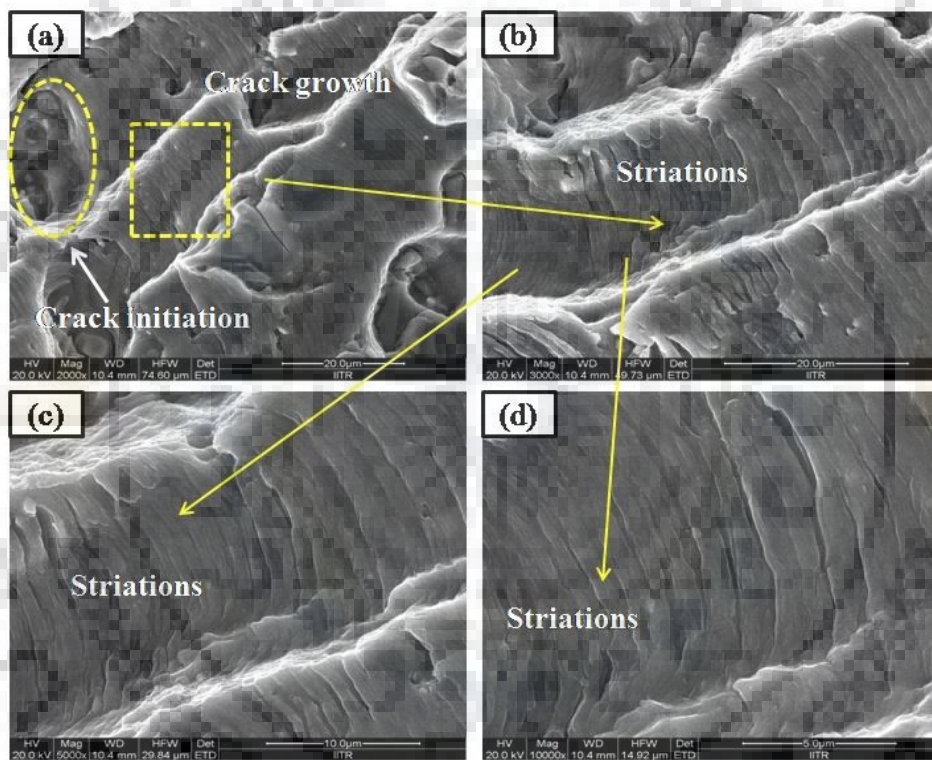
Figure 4.3.20: Low and high magnification fractographs of CR Al 2014 annealed at 200°C at higher stress intensity factor range
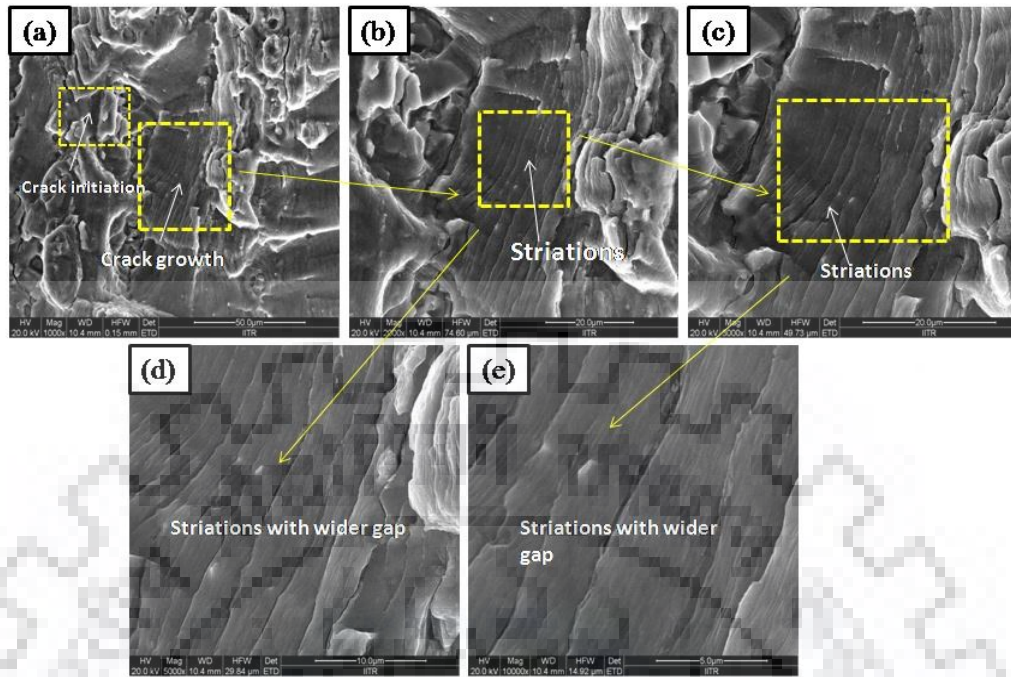
Figure 4.3.21: Low and high magnification fractographs of CR Al 2014 annealed at 250°C at higher stress intensity factor range

4.3.5 Conclusions

The fatigue crack growth behaviour of cryorolled and followed by annealed Al 2014 alloy has been studied in detail in the present work and following conclusions are made.

- The cryorolled (CR) Al 2014 alloy shows faster crack growth rate and lower fatigue crack growth resistance in low stress intensity factor range when compared to coarser grain (CG) solution treated (ST) alloy due to absence of roughness induced crack closure mechanism, which provides less tortuous crack path during cyclic loading.

- The improvement in threshold stress intensity factor ΔK_{th} (5.8 $MPa\sqrt{m}$-7.17 $MPa\sqrt{m}$) of cryorolled (CR) Al 2014 alloy was noticed with respect to coarser grain solution treated (ST) Al 2014 alloy. The improvement in threshold stress intensity factor ΔK_{th} of cryorolled (CR) alloy is due to the formation of UFG microstructure after cryorolling.

- On annealing in the temperature range 100°C - 250°C, the significant improvement in fatigue crack growth resistance of cryorolled alloy near low stress intensity factor range is observed at 100°C due to evolution of fine semi coherent spherical phase θ'(Al₂Cu), which act as an obstacle to crack movement and provides the significant plasticity to crack tip by enhancing the size of plastic zone near crack tip.

160

- At high stress intensity factor range, the fatigue crack growth resistance of cryorolled (CR) alloy is observed to be more than coarser grain solution treated (ST) due to formation of very fine striation as compared to solution treated (ST) alloy.

- Fatigue crack growth behavior of annealed alloy in the temperature range 100°C - 250°C at higher stress intensity factor range was observed be same as it was in low intensity factor range. On annealing in the temperature range 100°C - 250°C, the fatigue crack growth resistance of annealed alloy is improved up to 200°C as compared to solution treated (ST) and cryorolled (CR) alloy due to formation of very fine interrupted striations. However, beyond this temperature, striation width increases as compared to cryorolled (CR) sample, resulting decrease in fatigue crack growth resistance as compared to cryorolled (CR) alloy.

References

[4.1]   M. Gavgali, B. Aksakal, "Effects of various homogenisation treatments on the hot workability of ingot aluminium alloy AA2014", 1998, *Mater.Sci. Eng.A,* Vol 254(1), pp. 189-199

[4.2]   E. A. Starke, J. T. Staley, "Application of modern aluminum alloys to aircraft." 1996, Prog. Aerosp Sci, Vol 32(2), pp. 131-172

[4.3]   Y. S. D. Shenglong, "A Glimpse at the Development and Application of Aluminum Alloys in Aviation Industry ", 2005, Mater Rev, Vol 2, pp. 22 -27

[4.4]   J. Mao, S. B. Kang, J. O. Park. "Grain refinement, thermal stability and tensile properties of 2024 aluminum alloy after equal-channel angular pressing.*"* 2005, J Mater Process Tech,Vol *159(3),* pp. *314-320*

[4.5]   S. K. Varma, D. Salas, E. Corral, E. Esquivel, K. K. Chawla, R. Mahaptra, "Microstructural development during aging of 2014 aluminum alloy composite." 1999, J Mater Sci, Vol 34(8), pp. 1855-1863

[4.6]   Y. Estrin, A. Vinogradov, "Extreme grain refinement by severe plastic deformation: a wealth of challenging science." 2013, Acta Mater, Vol 61(3), pp. 782-817

[4.7]   R. B. Figueiredo, T. G. Langdon. "Using severe plastic deformation for the processing of advanced engineering materials." 2009, Mater trans, Vol 50 (7), pp. 1613-1619

[4.8]   V. M. Segal, "Severe plastic deformation: simple shear versus pure shear", Mater. Sci. Eng. A*,* 2002, Vol 338 (1), pp. 331-344

[4.9]   Y. Saito, H. Utsunomiya, N. Tsuji, T. Sakai, "Novel Ultra-High Straining Process for Bulk Materials -Development of the Accumulative Roll-Bonding (ARB) Process", 1999, Acta Mater, Vol 47, pp. 579-583

[4.10]   A. P. Zhilyaev, T. G. Langdon, "Using high-pressure torsion for metal processing: fundamentals and applications." 2008, Prog Mater Sci, Vol 53(6), pp. 893-979

[4.11]   J. Y. Huang, Y. T. Zhu, H. Jiang, T. C. Lowe, "Microstructures and dislocation configurations in nanostructured Cu processed by repetitive corrugation and straightening." 2001, Acta Mater, Vol 49 (9), pp. 1497-1505

[4.12]   R. Z. Valiev, I. V. Alexandrov, R. K. Islamgaliev, "Processing and properties of nanostructured materials prepared by severe plastic deformation." 1998, Nanostructured materials. Springer Netherlands, Vol 26, pp. 121-142

[4.13]   S. K. Panigrahi, R. Jayaganthan, Vivek Pancholi, "Effect of plastic deformation conditions on microstructural characteristics and mechanical properties of Al 6063 alloy." 2009, Mater. Des., Vol. 30(6), pp. 1894-1901

[4.14]   S. K. Panigrahi, R. Jayaganthan,   V. Chawla. "Effect of cryorolling on microstructure of Al–Mg–Si alloy", 2008, Mater Lett, Vol 62 (17), pp. 2626-2629

[4.15]   N. Rangaraju, T. Raghuram, B.V. Krishna, K.P. Rao, P. Venugopal, "Effect of Cryo-rolling and Annealing on Microstructure and Properties of Commercially Pure Aluminium", 2005, Mater. Sci. Eng. A, Vol 398, pp. 246-251

[4.16]   Y. Wang, M. Chen, F. Zhou, E. Ma, "High Tensile Ductility in a Nanostructured Metal", 2002, Nature, Vol 419, pp. 912-915.

[4.17]   P. N. Rao, D. Singh, R. Jayaganthan, "Effect of annealing on microstructure and mechanical properties of Al 6061 alloy processed by cryorolling", 2013, Mater.Sci.Tech , Vol 29(1), pp. 76-82

[4.18]   S. K. Panigrahi, R. Jayaganthan, "Development of ultrafine grained Al–Mg–Si alloy with enhanced strength and ductility", 2009, J Alloy Compd, Vol 470(1), pp. 285-288

[4.19]   S. K. Panigrahi, R. Jayaganthan, "A comparative study on mechanical properties of Al 7075 alloy processed by rolling at cryogenic temperature and room temperature." 2008, Mater Sci Forum, Vol 584, pp. 734-740

[4.20]   S. K. Panigrahi, R. Jayaganthan, "Development of ultrafine grained high strength age hardenable Al 7075 alloy by cryorolling", 2011,   Mater Des, Vol 32(6), pp. 3150-3160

[4.21]   D. Singh, P. N. Rao, R. Jayaganthan, "Microstructures and impact toughness behavior of Al 5083 alloy processed by cryorolling and afterwards annealing." 2013, Int J Min Metall Mater, Vol 20(8), pp. 759-769

[4.22] T. Shanmugasundaram , B.S. Murty , V.S. Sarma, "Development of ultrafine grained high strength Al–Cu alloy by cryorolling", 2006, Scripta Mater , Vol 54, pp. 2013-2017

[4.23] A. Hohenwarter, R. Pippan, "Fracture Toughness Evaluation of Ultrafine-Grained Nickel", 2011, Scripta Mater,Vol 64, pp. 982-985

[4.24] A. Hohenwarter, R. Pippan, "Anisotropic fracture behavior of ultrafine-grained iron", 2010, Mater Sci Eng: A, Vol 527(10), pp. 2649-2656

[4.25] M. Li, D. Guo, T. Ma, G. Zhang, Y. Shi, X. Zhang, "High fracture toughness in a hierarchical nanostructured zirconium", 2014, Mater Sci Eng. A, Vol 606, pp. 330-333

[4.26] H. Darban, B. Mohammadi, F. Djavanroodi, "Effect of equal channel angular pressing on fracture toughness of Al-7075." 2016, Eng Fail Anal, Vol 65, pp. 1-10

[4.27] P. Das, R. Jayaganthan, T. Chowdhury, I. Singh, "Improvement of Fracture Toughness (K1c) of 7075 Al Alloy by Cryorolling Process", 2011, Mater Sci Forum,Vol 683, pp. 81-94

[4.28] C. C. Koch, Optimization of strength and ductility in nanocrystalline and ultrafine grained metals, 2003, Scripta Mater, Vol 49(7), pp. 657-662

[4.29] S. K. Panigrahi, R. Jayaganthan, "Effect of Annealing on Thermal Stability, Precipitate Evolution, and Mechanical Properties of Cryorolled Al 7075 Alloy", 2011, Metall Mater Transac A,Vol 42 (10), pp. 3208-3217

[4.30] A. Dhal, S. K. Panigrahi, M. S. Shunmugam, "Influence of annealing on stain hardening behaviour and fracture properties of a cryorolled Al 2014 alloy", 2015, Mater Sci Eng. A, Vol 645, pp. 383-392

[4.31] A. Rollett, F.J. Humphreys, G.S. Rohrer, M. Hatherly, Recrystallization and Related Annealing Phenomena, Elsevier, Pergamon, 2004

[4.32] A. Hohenwarter, R. Pippan, "An Overview on the Fracture Behavior of Metals Processed by High Pressure Torsion". 2010, Mater Sci Forum,Vol 667, pp. 671-676

[4.33] W. F. Brown, Review of developments in plane strain fracture toughness testing ,1970, ASTM International, Vol. 463

[4.34] T. L. Anderson, T. L. Anderson, Fracture mechanics: fundamentals and applications, CRC press (2005)

[4.35] D.Broek, Elementary engineering fracture mechanics, Springer Science & Business Media (2012)

[4.36] F. I. Baratta, L. M. Barker. "Comparisons of fracture toughness measurements by the short rod and ASTM standard method of test for plane-strain fracture toughness of metallic materials (E 399-78), 1980, J Test Eval, Vol 8(3), pp. 97-102

163

[4.37] E. B. Tochaee, H. R. M. Hosseini, S. M. S. Reihani, "On the fracture toughness behavior of in-situ Al-Ti composites produced via mechanical alloying and hot extrusion", 2016, J Alloy Compd, Vol 681, pp. 12-21

[4.38] ASTM. E992, Standard Practice for Determination of a Fracture Toughness of Steels Using Equivalent Energy Methodology, in, 1984.

[4.39] J. R. Rice, "A path independent integral and the approximate analysis of strain concentration by notches and cracks". 1968, J Appl Mech, Vol 35 (2), pp. 379-386

[4.40] E. E. Gdoutos, Fracture mechanics: an introduction, Springer Science & Business Media, Vol 123 (2006)

[4.41] G. H. B. Donato, C. Ruggieri, "Estimation procedures for J and CTOD fracture parameters using three-point bend specimens." International Pipeline Conference. American Society of Mechanical Engineers, (2006)

[4.42] C. P. Harper, "Effect of alumina particle additions on the aging kinetics of 2014-aluminum matrix composites", 1991, Met Trans A, pp.466-471

[4.43] P. Bassani, E. Gariboldi, G. Vimercati, "Calorimetric analyses on aged Al–4.4 Cu–0.5 Mg–0.9 Si–0.8 Mn alloy (AA2014 grade)." 2007, J Ther Analy Calor, Vol 87(1), pp. 247-253

[4.44] S. Abis, M. Massazza, P. Mengucci, G. Riontino, "Early ageing mechanisms in a high-copper AlCuMg alloy", 2001, Script Mater, Vol 45(6), pp. 685-691

[4.45] D. J. Chakrabarti, D. E. Laughlin, "Phase relations and precipitation in Al–Mg–Si alloys with Cu additions." 2004, Prog MaterSci, Vol 49(3) , pp. 389-410

[4.46] I. Dutta, C. P. Harper, G. Dutta, "Role of Al_2O_3 particulate reinforcements on precipitation in 2014 Al-matrix composites", 1994, Metall Mater Trans A, Vol 25 (8), pp. 1591-1602

[4.47] A. Dhal, S. K. Panigrahi, M. S. Shunmugam, "Precipitation phenomena, thermal stability and grain growth kinetics in an ultra-fine grained Al 2014 alloy after annealing treatment", 2015, J Alloy Compd, Vol 649 , pp. 229-238

[4.48] B. Li, X. Wang, H. Chen, J. Hu, C. Huang, G. Gou, "Influence of heat treatment on the strength and fracture toughness of 7N01 aluminum alloy", 2016, J Alloy Compd, Vol 678, pp. 160-166

[4.49] K.S.Krishna, "Mechanical behavior and void coalescence analysis of cryorolled AA8090 alloy." 2016, J of Advanced Manufac Tech, Vol 25, pp. 1-7.

[4.50] G. E. Dieter, Mechanical metallurgy (2015).

[4.51] Handbook ASM, Fractography, Materials Park (2nd printing), 12, 1987: 2217

[4.52] H. Mughrabi, H. W. Höppel, Cyclic deformation and fatigue properties of very fine-grained metals and alloys, 2010, Int. J. Fatigue, Vol. 32, pp. 1413-1427.

[4.53] A. Y. Vinogradov, V. V. Stolyarov, S. Hashimoto, R. Z. Valiev, Cyclic behavior of ultrafine-grain titanium produced by severe plastic deformation, 2001, Mater. Sci. Eng; A, Vol 318, pp. 163-173

[4.54] H.W. Höppel, M. Kautz, C. Xu, M. Murashkin, T. G. Langdon, R. Z. Valiev, H. Mughrabi, An overview: fatigue behaviour of ultrafine-grained metals and alloys, 2006, Int. J. Fatigue, Vol 28, pp. 1001-1010.

[4.55] J. Schijve, Fatigue of structures and materials , Dordrecht: Kluwer Academic (2001)

[4.56] L. W. Meyer, K. Sommer, T. Halle, M. Hockauf, Crack growth in ultrafine-grained AA6063 produced by equal-channel angular pressing, 2003, J. Mater. Sci.,Vol.43, pp. 7426-7431.

[4.57] G. Khatibi, J. Horky, B. Weiss, M. J. Zehetbauer, High cycle fatigue behaviour of copper deformed by high pressure torsion, 2010, Int. J. Fatigue , Vol 32, pp. 269-278.

[4.58] A. Vinogradov, Fatigue limit and crack growth in ultra-fine grain metals produced by severe plastic deformation, 2007, J. Mater. Sci., Vol. 42, pp. 1797-1808.

[4.59] P. Cavaliere, Fatigue properties and crack behavior of ultra-fine and nanocrystalline pure metals, 2009, Int. J. Fatigue, Vol 31, pp. 1476-1489.

[4.60] R. W. Landgraf, The resistance of metals to cyclic deformation, In Achievement of High Fatigue Resistance in Metals and Alloys , (1970), Vol 25, pp1822-1826

[4.61] J. Morrow, Cyclic plastic strain energy and fatigue of metals, In Internal friction, damping, and cyclic plasticity, 1965,

[4.62] X. H. An, S. D. Wu, Z.G. Wang, Z. F. Zhang, Enhanced cyclic deformation responses of ultrafine-grained Cu and nanocrystalline Cu–Al alloys. 2014, Acta Mater, Vol. 74, pp. 200-214.

[4.63] R. Liu, Y. Tian, Z. Zhang, X. An, P. Zhang, Z. Zhang, Exceptional high fatigue strength in Cu-15at.% Al alloy with moderate grain size, 2016, Sci. Rep., Vol 6 , pp. 335-339

[4.64] H. Mughrabi , H. W. Höppel, Cyclic deformation and fatigue properties of ultrafine grain size materials: current status and some criteria for improvement of the fatigue resistance, 2000, In MRS Proceedings Cambridge University Press, Vol. 634, B2-1

[4.65] A. Vinogradov, Y. Kaneko, K. Kitagawa, S. Hashimoto, R. Valiev, On the cyclic response of ultrafine-grained copper, 1998, Mater. Sci. Forum, Vol 269, pp. 987-992.

[4.66]   E.Thiele, C. Holste, R. Klemm, Influence of size effect on microstructural changes in cyclically deformed polycrystalline nickel, 2002, Zeitschrift fuer Metallkunde., Vol 93, pp.730-736.

[4.67]   C. Holste, Cyclic plasticity of nickel, from single crystals to submicrocrystalline polycrystals, 2004, Philos. Mag. , Vol 84, pp. 299-315.

[4.68]   H. W. Höppel, J. May, M. Göken, Fatigue behavior of UFG Al: influence of the ECAP route and the magnesium content. 2008, In Proceedings of 6th International Conference on Low Cycle Fatigue (LCF6), DVM, Berlin,   Vol 21, pp. 325-332

[4.69]   V. Patlan, A. Vinogradov, K. Higashi, K. Kitagawa, Overview of fatigue properties of fine grain 5056 Al-Mg alloy processed by equal-channel angular pressing, 2001, Mater. Sci. Eng;A , Vol 300, pp. 171-182.

[4.70]   V. M. Segal, Severe plastic deformation: simple shear versus pure shear, 2002, Mater. Sci. Eng; A, Vol 338, pp. 331-344.

[4.71]   R. Z. Valiev, T. G. Langdon, Principles of equal-channel angular pressing as a processing tool for grain refinement, 2006, Prog. Mater Sci , Vol 51, pp. 881-981

[4.72]   A. P. Zhilyaev, T. G. Langdon, Using high-pressure torsion for metal processing: fundamentals and applications, 2008, Prog. Mater Sci , Vol 53, pp. 893-979.

[4.73]   Y. Saito, H. Utsunomiya, N. Tsuji, T. Sakai, Novel Ultra-High Straining Process for Bulk Materials -Development of the Accumulative Roll-Bonding (ARB) Process, 1999, Acta Mater, Vol 47, pp. 579-583.

[4.74]   M. Richert, Q. Liu, N. Hansen, Micro structural Evolution Over a Large Strain Range in Aluminium Deformed by Cyclic-Extrusion–Compression, 1999, Mater. Sci. Eng., A, Vol. 260 , pp. 275-283.

[4.75]   J.Y. Huang, Y.T. Zhu, H. Jiang, T.C. Lowe, Microstructures and Dislocation Configurations in Nanostructured Cu Processed by Repetitive Corrugation and Straightening, 2001, Acta Mater, Vol. 49, pp. 1497-1505.

[4.76]   S. K. Panigrahi, R. Jayaganthan, Effect of annealing on precipitation, microstructural stability, and mechanical properties of cryorolled Al 6063 alloy, 2010, J. Mater Sci, Vol 45, pp. 5624-5636.

[4.77]   S. Malekjani, P. D. Hodgson, P. Cizek, I. Sabirov, T. B. Hilditch, Cyclic deformation response of UFG 2024 Al alloy, 2011, Int. J . Fatigue, Vol 33, pp. 700-709.

[4.78]   P. N. Rao, R. Jayaganthan, Effects of warm rolling and ageing after cryogenic rolling on mechanical properties and microstructure of Al 6061 alloy, 2012, Mater Des, Vol. 39, pp. 226-233.

[4.79]   S. K. Panigrahi, R. Jayaganthan, A study on the mechanical properties of cryorolled Al–Mg–Si allo , 2008, Mater Sci Eng: A; Vol 480, pp. 299-305.

[4.80] S. K. Panigrahi, R. Jayaganthan, Effect of ageing on microstructure and mechanical properties of bulk, cryorolled, and room temperature rolled Al 7075 alloy, 2011, J Alloys Compd, Vol 509, pp. 9609-9616.

[4.81] N. Kumar, S. Goel, R. Jayaganthan, H.G. Brokmeier, Effect of Grain boundary misorientaton, Deformation Temperature and AlFeMnSi-phase on Fatigue Life of 6082 Al alloy, 2017, Mater Charact, Vol 21, pp. 235-247

[4.82] A. Joshi, Yogesha K. K., N. Kumar, R. Jayaganthan, Influence of Annealing on Microstructural Evolution, Precipitation Sequence, and Fracture Toughness of Cryorolled Al–Cu–Si Alloy,2016, Metall Micstr Analysis, Vol 35, pp. 1-17.

[4.83] A. Joshi, N. Kumar, K. K. Yogesha, R. Jayaganthan, S. K. Nath, Mechanical Properties and Microstructural Evolution in Al 2014 Alloy Processed Through Multidirectional Cryoforging., 2016, J Mater Eng Perform, Vol 41, pp. 1-15.

[4.84] J. Schijve, Fatigue of structures and materials in the 20th century and the state of the art, 2003, Int J Fatigue, Vol 25, pp. 679-702.

[4.85] G. E. Dieter, D. J. Bacon, Mechanical Metallurgy, 1986. New York: McGraw-Hill, Vol 3

[4.86] X. Yang, K. Li, X. An, S. Ni, W. Wei, Y. Du, M. Song, Influence of deformation microstructure on the precipitation behaviors of an Al-4Mg-0.3 Cu alloy, 2017, J Alloys Compd, Vol 695, pp. 2238-2245.

[4.87] Y. Estrin, A. Vinogradov, Fatigue behaviour of light alloys with ultrafine grain structure produced by severe plastic deformation: An overview, 2010, Int J Fatigue, Vol 32, pp. 898-907.

[4.88] D. Singh, P. N. Rao, R. Jayaganthan, "Effect of deformation temperature on mechanical properties of ultrafine grained Al–Mg alloys processed by rolling." 2013, Mater Des, Vol 50, pp. 646-655.

[4.89] S. K. Panigrahi, R. Jayaganthan. "A study on the combined treatment of cryorolling, short-annealing, and aging for the development of ultrafine-grained Al 6063 alloy with enhanced strength and ductility" 2010, Metall Mater Trans A,Vol 41, pp. 2675-2690.

[4.90] M. D. Sangid, The physics of fatigue crack initiation, 2013, Int J Fatigue,Vol 57, pp. 58-72.

[4.91] J. Polák, On the role of point defects in fatigue crack initiation, 1987, Mater Sci Eng, Vol 92, pp. 71-80.

[4.92] A. Seeger, J. Diehl, S. Mader, H. Rebstock, Work-hardening and work-softening of face-centred cubic metal crystals, 1957, Philos Mag, Vol 15, pp. 323-350.

[4.93] J. Friedel, P. Feltham, A discussion on work-hardening and fatigue in metals, 1957, P Roy Soc Lond A Mat, Vol 242 , pp. 145-159.

[4.94] Z. J. Zhang, X. H. An, P. Zhang, M. X. Yang, G. Yang, S. D. Wu, F. Z. Zhang, Effects of dislocation slip mode on high-cycle fatigue behaviors of ultrafine-grained Cu–Zn alloy processed by equal-channel angular pressing, 2013, Scripta Mater, Vol 68, pp. 389-392

[4.95] X. Chao, S. L Yang, Analysis on Fatigue Crack Propagation and Fractography of A7075 Aluminum Alloy, 2012, Appl Mech Mater, Vol 21, pp. 390-394

[4.96] P. Das, R. Jayaganthan, T. Chowdhury, I. V. Singh, Fatigue behaviour and crack growth rate of cryorolled Al 7075 alloy, 2011, Mater Sci Eng: A, Vol 528, pp.7124-7132

[4.97] A. Azushima, R. Kopp, A. Korhonen, D.Y. Yang, F. Micari, G.D. Lahoti, P. Groche, J. Yanagimoto, N. Tsuji, A. Rosochowski, A. Yanagida, Severe plastic deformation (SPD) processes for metals, 2008, CIRP Ann. - Manuf. Technol , Vol 57, pp. 716–735

[4.98] I. Sabirov, M.Y. Murashkin, R.Z. Valiev, Nanostructured aluminium alloys produced by severe plastic deformation: New horizons in development, 2013, Mater. Sci. Eng. A. Vol 560, pp. 1–24

[4.99] R.Z. Valiev, A. V Korrznikov, R.R. Mulyakov, Structure and properties of ultrafine-grained materials produced by severe plastic deformation, 1993, Mater. Sci. Engg A. Vol 168, pp. 141–148.

[4.100] T. Hanlon, E.D. Tabachnikova, S. Suresh, Fatigue behavior of nanocrystalline metals and alloys,2005,Int. J. Fatigue. Vol 27, pp. 1147–1158.

[4.101] L. Collini, Fatigue crack growth in ECAPed commercially pure UFG copper, 2010, Procedia Eng. Vol 2, pp. 2065–2074.

[4.102] R. Vafaei, M.R. Toroghinejad, R. Pippan, Evaluation of mechanical behavior of nano-rained 2024 Al alloy during high pressure torsion (HPT) process at various temperatures, 2012,Mater. Sci. Eng. A, Vol 536, pp. 73–81.

[4.103] M. Weiss, A.S. Taylor, P.D. Hodgson, N. Stanford, Strength and biaxial formability of cryo-rolled 2024 aluminium subject to concurrent recovery and precipitation, 2013, Acta Mater, Vol. 61, pp. 5278–5289

[4.104] P. Cavaliere, Fatigue properties and crack behavior of ultra-fine and nanocrystalline pure metals, 2009, Int. J. Fatigue. Vol 31, pp. 1476–1489..

[4.105] H.W. Höppel, Z.M. Zhou, H. Mughrabi, R.Z. Valiev, Microstructural study of the parameters governing coarsening and cyclic softening in fatigued ultrafine-grained copper, 2002, Philos. Mag. A, Vol 82 , pp. 1781–1794.

[4.106] M. Goto, S.Z.Z. Han, K. Euh, J.-H. Kang, S. Kim, N. Kawagoishi, Formation of a high-cycle fatigue fracture surface and a crack growth mechanism of ultrafine-grained copper with different stages of microstructural evolution, 2010, Acta Mater, Vol 58, pp. 6294–6305

[4.107] C.S. Chung, J.K. Kim, H.K. Kim, W.J. Kim, Improvement of high-cycle fatigue life in a 6061 Al alloy produced by equal channel angular pressing, Mater. Sci. Eng. A, Vol 337, pp. 39–44.

[4.108] U.C. Structures, L. Collini, Fatigue Crack Resistance of, (2006).

[4.109] R. Jayaganthan, S.K. Panigrahi, Effect of Cryorolling Strain on Precipitation Kinetics of Al 7075 Alloy, 2008, Mater. Sci. Forum., Vol. 584–586, pp. 911–916.

[4.110] S.K. Panigrahi, D. Devanand, R. Jayaganthan, Effect of Ageing on Strength and Ductility of Ultrafine Grained Al 6061 Alloy, 2009, Mater. Sci. Forum, Vol 35, pp. 633–634, pp. 303–309

[4.111] S.K. Panigrahi, D. Devanand, R. Jayaganthan, A comparative study on mechanical properties of ultrafine-grained Al 6061 and Al 6063 alloys processed by cryorolling, 2008, Trans. Indian Inst. Met., Vol 61, pp. 159–163.

[4.112] S.K. Panigrahi, R. Jayaganthan, Effect of annealing on precipitation, microstructural stability, and mechanical properties of cryorolled Al 6063 alloy, 2010, J. Mater. Sci. 45, Vol 5624–5636.

[4.113] A. Joshi, K.K. Yogesha, R. Jayaganthan, Influence of cryorolling and followed by annealing on high cycle fatigue behavior of ultrafine grained Al 2014 alloy, 2017, Mater. Charact, Vol 127, pp. 253–271

[4.114] N. Kumar, S. Goel, R. Jayaganthan, H.G. Brokmeier, Effect of grain boundary misorientaton, deformation temperature and AlFeMnSi-phase on fatigue life of 6082 Al alloy, 2017, Mater. Charact, Vol 124, pp. 229–240.

[4.115] J. Schijve, G. Campoli, A. Monaco, Fatigue of structures and secondary bending in structural elements, 2009, International Journal of Fatigue, Vol 31(7), pp.1111-1123.

[4.116] T. Leitner, A. Hohenwarter, R. Pippan, Revisiting fatigue crack growth in various grain size regimes of Ni, 2015, Mater. Sci. Eng. A, Vol 646, pp. 294–305.

[4.117] H.-K. Kim, Y.I. Lee, C.-S. Chung, Fatigue properties of a fine-grained magnesium alloy produced by equal channel angular pressing, 2005, Scr. Mater, Vol. 52, pp. 473–477.

[4.118] D. Yin, H. Liu, Y. Chen, D. Yi, B. Wang, B. Wang, F. Shen, S. Fu, C. Tang, S. Pan, Effect of grain size on fatigue-crack growth in 2524 aluminium alloy, 2016, Int. J. Fatigue, Vol 84, pp. 9–16.

MULTIAXIAL FORGING (RESULTS & DISCUSSION)

The effect of multiaxial forging and followed by annealing in the temperature range from 150°C to 350°C on microstructure evolution, tensile properties, fracture toughness, fracture mechanisms and strengthening mechanisms of bulk UFG Al 2014 alloy is discussed in this chapter. The first section of this chapter deals with the comparative study of microstructure evolution, tensile properties and fracture toughness of MDFed (multidirectional forged) Al 2014 alloy at room temperature and cryogenic temperature (-196°C). In the second section, a detailed study of the influence of multidirectional cryoforging and followed by annealing treatment in the temperature range from 150°C to 350°C on the strain hardening behavior, fracture toughness and fracture mechanism of bulk UFG Al 2014 alloy is discussed. The strengthening contributions through various strengthening mechanisms (solid solution strengthening, grain boundary strengthening and dislocation strengthening) to yield strength of MDCFed (multidirectional cryoforged) and followed by annealed Al 2014 alloy is discussed in the third section of this chapter. The observed mechanical properties are correlated with microstructural evolution investigated by optical, TEM, FeSEM and XRD studies.

5.1 Comparative study of Microstructural Evolution, Tensile Properties and Fracture Toughness of Al 2014 alloy processed through Multidirectional Room Temperature and Cryoforging

5.1.1 Introduction

.   In recent years, producing the ultrafine grained material (UFG) through the various severe plastic deformation techniques is growing enormously for achieving significant improvement in mechanical and physical properties hitherto unachieved in their bulk materials [5.1-5.2]. Various investigations have shown that UFG materials processed through SPD methods exhibit superior strength, ductility, toughness, fatigue and fracture resistance compared to the bulk materials [5.3]. Several SPD method such as Equal-channel Angular Pressing (ECAP) [5.4-5.6], High Pressure Torsion (HPT) [5.7], Accumulative Roll Bonding (ARB) [5.8], Cyclic Extrusion compression (CEC) [5.9], Repetitive Corrugation and straightening (RCS) [5.10-5.11] have been well developed for obtaining UFG microstructure

with a grain size less than 1µm in the bulk materials. All these methods are very prominent and effective for producing high defect/dislocation density in the sample, which subsequently undergo rearrangement to form ultrafine grains or nanocrystalline structure [5.4-5.11]. The major limitation of these methods is the requirement of sophisticated and expensive dies, low productivity, and small sample size, which cannot be used for industrial applications [5.12]. Multidirectional forging (MDF) is relatively a simple method for producing ultrafine or nanocrystalline structure, which can impose a large plastic strain in the sample without need of any specialized tools and equipments and have a potential to use relatively large samples that can be used for structural and industrial application [5.12- 5.13]. Multidirectional forging involves repeated compression of a work piece, with a change in axis of applied load through 90° [5.14]. Magnesium and its alloys are successfully processed by MDF to improve its mechanical properties [5.15].

Sitidikov et al. [5.13] studied the effect of plastic strain on grain refinement in 7475 Al alloy during hot multidirectional forging. They observed that at higher plastic strain of 0.7 and above true strain 3.5, ultrafine grains of size 7.5 µm are formed, while at a plastic strain of 0.4 and above true strain 0.6, coarse grains are formed. Xia et al. [5.16] studied mechanical properties and microstructure evolution in AZ61Mg alloy subjected to multidirectional forging at room temperature and observed the enhancement in tensile strength, yield strength, and elongation to failure with an average grain size of 14 µm. Yang et al. [5.17] reported enhancement in strength with moderate ductility with reduction in grain size from 22.3 µm to below 1 µm in multidirectional forging of AZ31 magnesium alloy at room temperature. Sakai et al. [5.18] reported the development of micro shear bands with high angle grain boundaries in the evolution of ultrafine grain in ferritic stainless steel processed by multiaxial forging at room temperature.

Although multidirectional forging is simple, cost effective and highly productive SPD technique for industrial application, a very less attention has been given to the processing of aluminum alloys by this processing route at cryogenic temperature. Most of the research activities for aluminum alloys are focused on structure –property correlation by ECAP, ARB and HPT at room temperature [5.19-5.20]. Bazzaz et al. [5.19] reported the mechanical behaviour of AA1100 aluminum processed by channel die multiaxial compression at room temperature with improved hardness and yield strength due to formation of ultrafine grains in the range of 80-200 nm. Kapoor et al. [5.20] observed the softening of Al during

171

multidirectional forging in channel die at room temperature. Xu et al. [5.22] compared the micro structural homogeneity of Al-4 % Cu alloy with two different processing methods such as multiaxial compression and high pressure torsion. HPT produces better microstructural homogeneity and grain refinement with improved hardness as reported in their work.

Cryo deformation is one of the potential methods to realize nanostructure in coarse grain counterparts [5. 23-5.26]. Processing at cryogenic temperature suppresses dislocation cross slips and climb in high stacking fault metals, facilitating formation of ultra fine structure by inducing high density of dislocation as compared to room temperature deformation [5.26-5.27]. Shanmugasundaram et al. [5. 28] have developed the ultrafine grain microstructure in Al-Cu alloy by cryorolling and reported that cryorolling followed by short annealing and aging treatment is an effective way for improving the strength and ductility of this alloy. Panigrahi and Jayaganthan [5.29] investigated the effect of deformation temperature on mechanical properties and microstructure of Al 6063 alloy and observed the enhancement in tensile and yield strength of cryodeformed Al 6063 alloy as compared to room temperature deformed Al 6063 alloy. Sarma et al. [5.30] studied the effect of cryorolling and annealing on the mechanical properties and microstructure of Cu-Zn and Cu-Al alloy and observed the enhancement in tensile strength of both alloys with an average grain size ranging from 0.6 to 1.2 μm. The deformation at cryogenic temperature leads to suppression of dynamic recovery, which in turn provides the increased nucleation cites during annealing and facilitating the formation of ultrafine grains in metals and alloys [5.31]. The stacking fault energy plays a significant role in improving the mechanical properties of materials subjected to cryodeformation. Recent studies of Sarma et al. [5.32] have shown that in metal with very high and very low SFEs, strength difference between cryo and room temperature deformed sample is less than 10%. The deformation mechanism changes with SFEs and temperature as reported in their work. Material with high SFEs deforms by dislocation slip while low SFEs material deforms by twinning during deformation at both RT and cryo temperature [5. 32]. Aluminum Alloy AA 2014 is an Al-Cu-Si based age hardenable alloy, which is used in aerospace industry as aircraft fitting vessels, military vehicles, bridges and weapons manufacturing. This alloy exhibits high specific strength, good fracture toughness, fatigue resistance and excellent machinability [5.33]. To improve mechanical properties of this alloy further, grain size can be refined to submicronmeter to nanometer range by applying severe plastic deformation techniques [5.34-5.37]. Studies on severe plastic deformation techniques

on Al 2014 alloy at liquid nitrogen temperature are scarce and especially grain refinement of Al 2014 alloy by multi directional forging at liquid nitrogen temperature has not been reported so far. Therefore, the present work is focused to achieve ultrafine grain structure in Al 2014 alloy through multidirectional forging at cryogenic temperature and to study the effect of multidirectional forging on mechanical properties and micro structural evolution in this alloy. Mechanical behaviour of MDFed Al 2014 alloy was studied through tensile, hardness and 3 Point Bend Test. Microstructural characteristics of the deformed Al alloy are investigated through optical microscopy, SEM, and TEM.

5.1.2 Experimental Procedure

Al 2014 alloy was procured from Bharat Aerospace Metals; Mumbai, India in T6 treated condition in the form of 40 mm thick plate. Chemical composition of alloy is listed in Chapter 3. Prismatic shape samples of dimension 33 mm x 30 mm x 27 mm were cut from the as received plate and solution treated at 505°C for 2 hours and quenched in water. Solutionised samples were subjected to multidirectional forging at cryogenic temperature as well as room temperature, using friction screw forging machine at a strain rate of 10 s^{-1}. First compression axis was parallel to rolling direction of starting sample. Repeated axial compression of $\epsilon = -0.2$ was applied in each pass to accumulate redundant plastic strain in sample at cryogenic temperature. To carry out MDF at cryogenic temperature, samples were dipped in liquid nitrogen for 20 minutes prior to each successive compression. Temperature during the cryogenic deformation was maintained at liquid nitrogen temperature (-196°C). After every pressing samples were rotated through 90^0 to maintain initial dimension ratio of 1:1.11:1.22 constant throughout the processing [5.38]. To investigate the mechanical behaviour of Al 2014 alloy at room temperature, MDF was also carried for same number of cycles by dipping samples in water instead of using liquid nitrogen for each successive pressing. Schematic of MDF procedure for one cycle is shown in chapter 3 and shown in Fig.5.1.1. In the present work, a cumulative true strain of $\sum \varepsilon_i = 0.6$ was applied in each cycle. MDF was performed on Al 2014 alloy to the cumulative true strain of 1.2 (2 cycles), 1.8 (3 cycles) and 2.4 (4 cycles) without developing crack on the sample. After MDF, mechanical and metallographic analysis was carried out on a section parallel to last compression axis. Mechanical properties of MDFed Al 2014 alloy were studied by conducting tensile and hardness test at room temperature. Tensile test was conducted at room temperature on H25K-S Tinius Oslen tensile testing machine operated at constant crosshead speed with initial strain

173

rate of 5 x 10^{-4} s^{-1} to evaluate the strength and ductility of cryo forged Al 2014 alloy for different processing conditions.
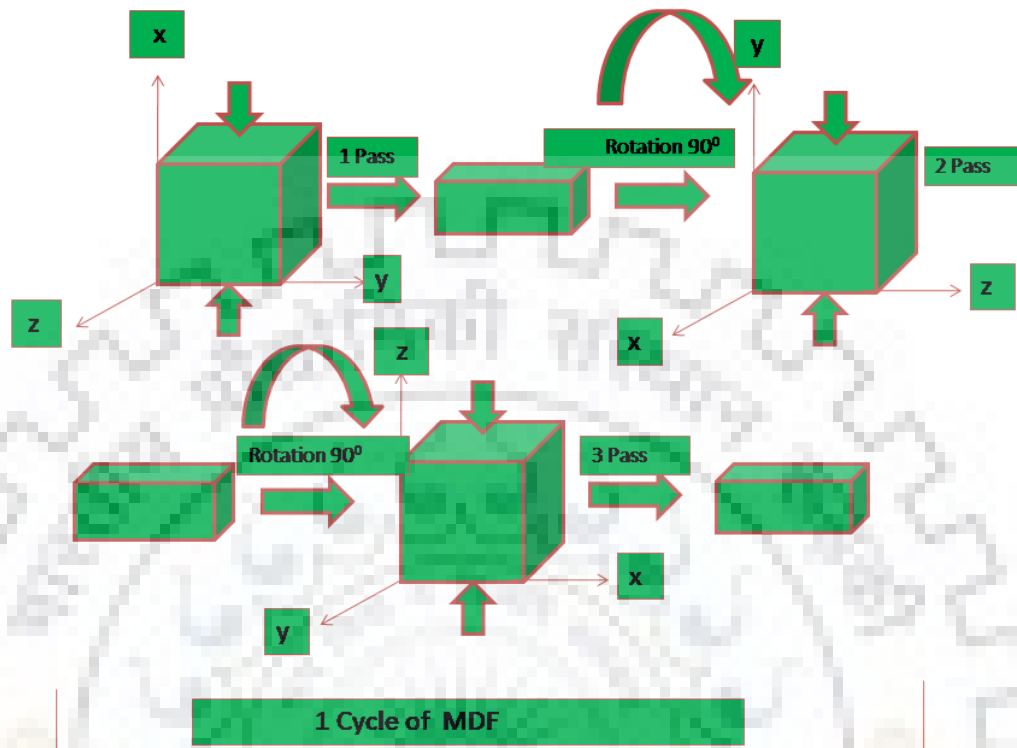
Figure 5.1.1: Schematic of MDF for one cycle

Sample were prepared as per ASTM E-8 sub size specification along the highest dimension side with a gauge length of 10 mm. Hardness is measured by FEI-VM 50 PC Vickers hardness testing machine at room temperature using a load of 5 kg with 15 seconds dwell time. Optical microscopy was carried out on Leica DMI 5000 under polarised light with Poultens reagent. TEM studies are performed by Philips CM 12 transmission electron microscope operating at 120 volt. TEM sample were prepared by mechanical grinding the sample to 100 μm with emery papers and thinning the sample by twin jet electropolisher with a solution of 25% nitric acid and 75 % methanol at a temperature of -30°C. Fractured surface of tensile specimen is examined by SEM.

5.1.3 Results and Discussion

5.1.3.1 Microstructure

Optical micrograph of starting solution treated material is shown in Fig. 5.1.2 (a). Solution treated material shows equiaxed grain sizes in range of 100 μm – 200 μm . Fig.

5.1.2(b)-(d) and Fig. 5.1.3(a)-(c) shows the optical micrograph of MDFed Al 2014 alloy processed at room temperature and cryogenic temperature respectively.
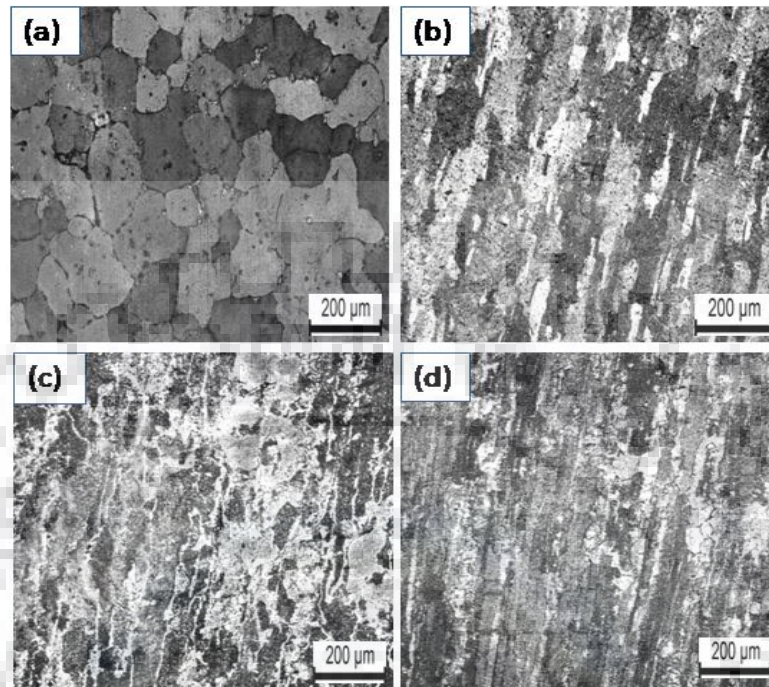
Figure 5.1.2: Optical Micrographs of MDFed Al 2014 Alloy at room temperature for various processing conditions : (a) Solution Treated ; (b) 2 cycles ; (c) 3 cycles ; (d) 4 cycles
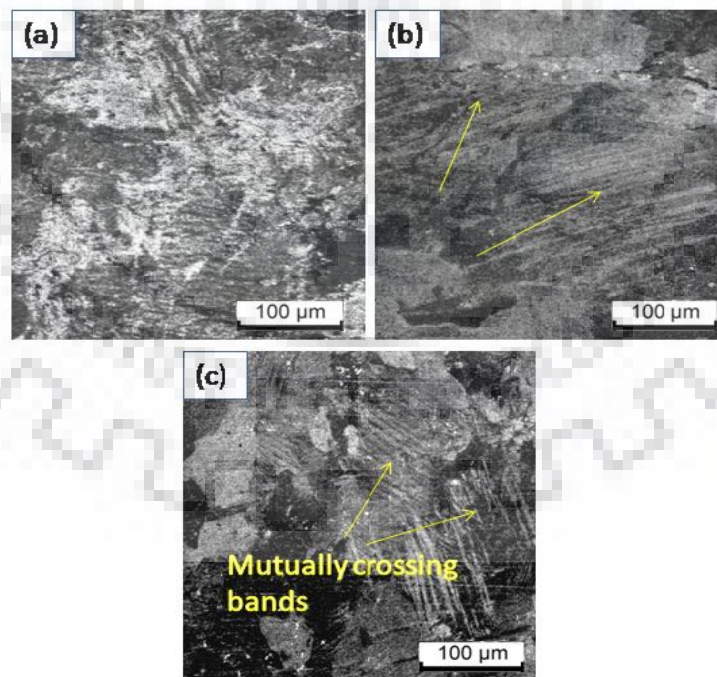
Figure 5.1.3: Optical Micrographs of MDFed Al 2014 Alloy at cryogenic Temperature for various processing conditions: (a) 2 cycles; (b) 3 cycles; (c) 4 cycles

175

These micrographs clearly show the formation of ultrafine microstructure in deformed material through Multidirectional forging at room temperature and cryogenic temperature. Grain fragmentation can be clearly seen in Fig. 5.1.2(b)-(d) which is a typical microstructure of room temperature forged samples with increasing number of cycles. However, the deformation is severe in cryoforged samples as compared to room temperature forged samples as depicted by the micrographs of cryo forged samples corresponding to Fig.5.1.3(a)-(c). Cryo forged samples show severely fragmented grains as compared to room temperature forged samples. The deformed microstructure at both temperatures shows ill defined grain boundaries with increasing number of cycles as seen from Fig. 5.1.2(b)-(d) and Fig. 5.1.3(a)-(c). It has been reported that multiaxial forging leads to formation of deformation bands in sample with increasing strain steps [5.38,5.40]. The deformation bands are not seen in room temperature forged samples, while in cryo forged samples, it is observed for all the processed conditions of samples. At lower strain of 1.2 and 1.8, these deformation bands are directed along one direction, but at higher strain of 2.4, they are mutually intersecting to each other for the cryoforged samples. Due to intersection of these slip bands, intense severe deformation takes place at localized place resulting in severe fragmentation of grains in the cryo forged samples. However, the intensity of deformation bands in cryo forged samples is not so much as observed by Rao et al [5. 38] in multidirectional forging of Al 6061 alloy. This may be due to the limited deformability of Al 2014 alloy in multidirectional forging. In the present work, it was seen that Al 2014 alloy was successively forged to 4 cycles, up to cumulative true strain of 2.4. After 4 cycles, cracks were developed in the samples in both temperatures. On the other hand, Rao et al [5. 38] were able to deform Al 6061 alloy up to cumulative true strain of 5.4 (9 cycles).

Fig. 5.1.4(a) shows the TEM micrograph of MDFed Al 2014 alloy at cryogenic temperature, subjected to cumulative true strain of 1.2 (2 cycles). When sample is subjected to multidirectional forging at liquid nitrogen temperature, large number of dislocations are generated, which leads to formation of ultrafine grain structure. At small strain of 1.2, dislocation get assembled in the form of tangles and cell boundaries. Dislocation tangles can be seen as dashed circle ,while cell boundaries are indicated by triangles in TEM micrograph of sample subjected to MDF up to cumulative strain 1.2 (2 cycles). The SAD pattern shown in Fig. 5.1.4 (a) as inset clearly reveals the presence of low angle boundaries (lesser

176

misorientation of diffraction spots) at lower strain. These boundaries are incidental dislocation boundaries (IDB) as reported in the literature [5. 39] and they are formed during the plastic deformation at low strain due to random trapping of dislocations.
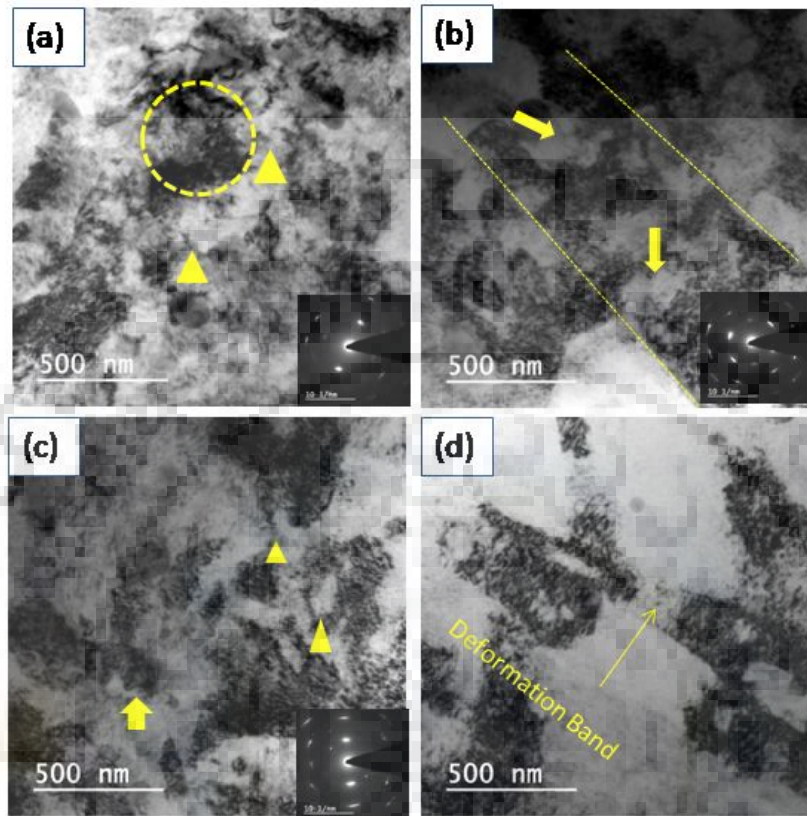
Figure 5.1.4: TEM micrograph of Al 2014 Alloy after MDF treatment at cryogenic temperature for various processing conditions: (a) 2 cycles; (b) 3 cycles; (c) 4 cycles; (d) 4 cycles with different area of sample

Fig. 5.1.4(b) shows the TEM micrograph corresponding to MDF up to 3 Cycles. Deformation band or cell band structure was observed at cumulative strain of 1.8, which is indicated by the area between the dotted straight lines in Fig.5.1.4 (b). It has been reported that at higher strain, dislocations get arranged in the form of cell band structure [5. 31,5.39]. Boundaries of cell bands are thick and known as dense dislocation walls (DDW) [5.39]. Past studies of Kuhlmann et al. [5.39] and Rollett et al. [5. 31] have reported that these dense dislocation walls (DDW) as geometrical necessary boundaries (GNB), which are formed by the dislocations generated during non uniform plastic deformation at high strain. Inside the deformation band, highly deformed microstructure consisting of dislocation cells (marked with arrows) having a size in the range of 300 nm-400 nm was observed, which was aligned in the direction of deformation band. Various studies on GNB suggest the formation of high

177

angle boundaries at larger strain, which leads to heavily deformed microstructure in sample [5.
31, 5.39] .The SAED micrograph shown in Fig. 5.1.4(b) as inset reveals the presence of high
angle boundaries (higher misorientation of diffraction spots which results ring pattern). TEM
micrograph corresponding to 4 cycles (cumulative strain 2.4) is shown in Fig. 5.1. 4(c), which
reveals the deformation of grain in to the form of dislocation cells (marked as triangle) and
dislocation tangles (marked as arrow). TEM micrograph of same sample for different area is
shown in Fig.5.1.4(d). It indicates the formation of deformation bands (marked as arrow)
having a thickness in the range of 200-300 nm, which are aligned in the plane of maximum
shear stress.
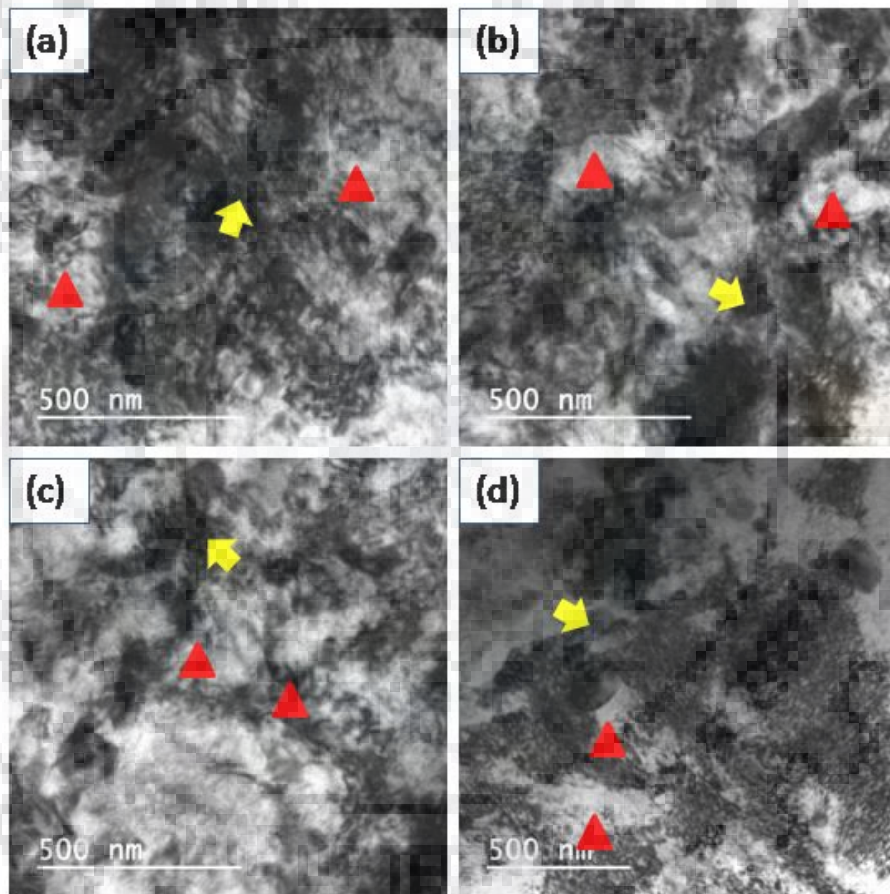
Figure 5.1.5: TEM micrograph of cryoforged Al 2014 Alloy after 4 cycles at various
locations

Fig. 5.1.5(a-d) is TEM micrograph of Cryo forged samples after 4 cycles at various locations.
Dislocation cells (marked by triangles), dense dislocation walls and dislocation tangling zone
(marked by arrows) can be identified clearly in these micrographs. Dislocation cell sizes in the
range of 100 nm-400 nm can be observed from Fig. 5.1.4 (c) to Fig. 5.1.5(a-d), which are
TEM micrographs corresponding to 4 cycle cryo forged samples at various locations. Average

cell size has been estimated from such TEM images corresponding to 4 cycles cryoforged samples at various locations. Average cell size is found to be 286 nm (Fig.5.1.6) based on statistical measurements.
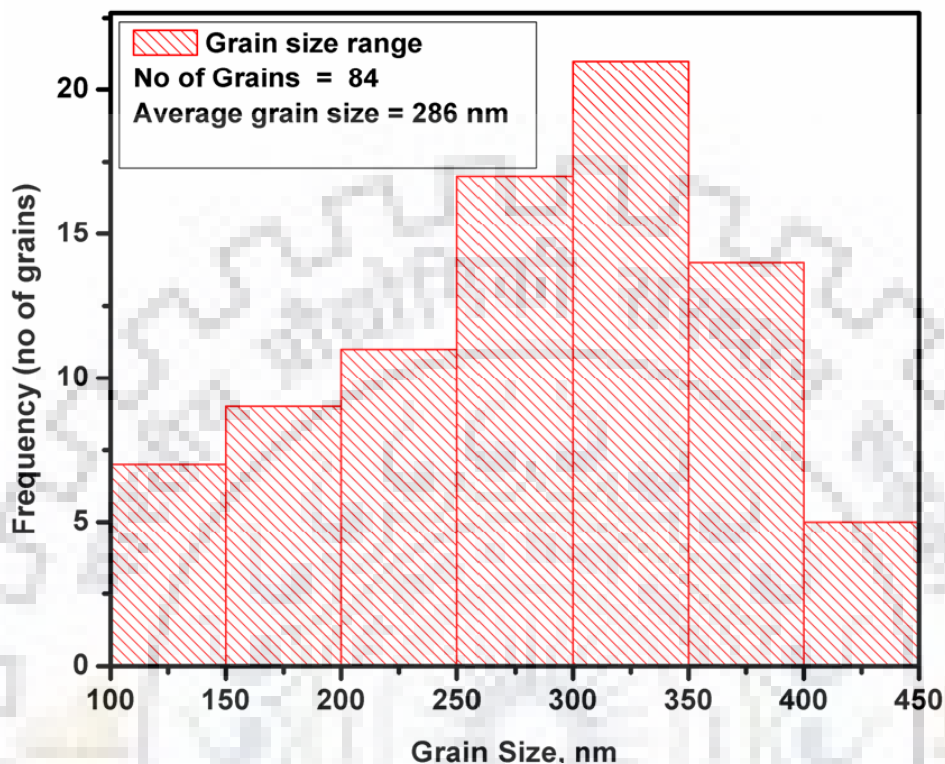
Figure 5.1.6: Histogram showing the dislocation cell size range estimated from 84 dislocation cells

With increasing applied strain from 1.2 to 2.4, dislocation density increases significantly with transformation of low angle grain boundaries to high angle grain boundaries. SAD micrograph of MDFed 4 cycles sample shown as inset in Fig. 5.1.4(c) clearly reveals the formations of high angle boundaries (ring pattern due to higher misorientation or elongated spots). Similar observations are observed by Kobayashi et al. [5. 40] during multiaxial forging of copper at 195 K. It has been reported that formation of low angle boundaries provide the dislocation strengthening while high angle boundaries impart the grain boundary strengthening [5. 20, 5.38]. TEM micrographs corresponding to MDFed Al 2014 alloy at room temperature for various processing condition is shown in Fig. 5.1.7(a)-(d). The room temperature forged sample after 2 cycles (Fig.5.1. 7 (a)) shows the formation of dislocation tangled zone (marked by arrows) in TEM micrograph.
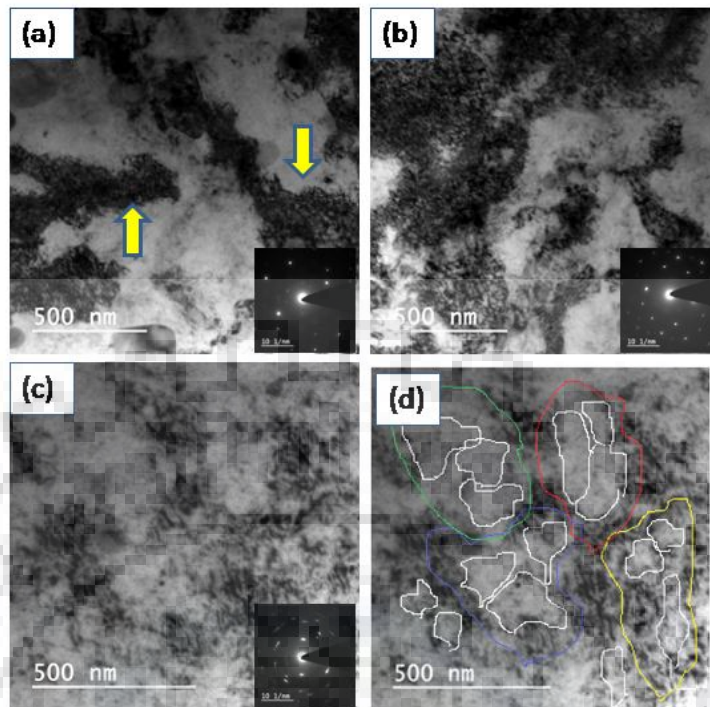
Figure 5.1.7: TEM micrograph of Al 2014 Alloy after MDF treatment at Room temperature for various processing condition: (a) 2 cycles; (b) 3 cycles; (c) 4 cycles; (d) 4 cycles

The associated SAED pattern clearly reveals the negligible misorientation after 2 cycles of MDF at room temperature. With increase in cumulative true strain up to 1.8 (after 3 cycles), dislocation density increases in the material as shown in Fig. 5.1.7(b). On comparing the microstructure with cryo forged samples, it was observed that deformation bands are not seen after 3 cycles of multidirectional forging at room temperature. The SAED pattern after 3 cycles MDF at room temperature (Fig. 5.1.7 (b)) clearly reveals the increase in misorientation as compared to 2 cycles MDFed Al 2014 alloy (Fig. 5.1.7(a)) at room temperature. TEM micrograph corresponding to room temperature forged Al 2014 alloy after 4 cycles is shown in Fig. 5.1.7(c). To understand microstructure development during MDF, four grains are shown in micrograph of 4 cycles MDFed sample (Fig. 5.1.7(d)) marked by red, blue, yellow and green colours. Inside each grain, dislocation free approximately equiaxed structure is identified which is marked with white colour. The area marked with white colour reveals the formation of ultrafine grains. The dislocation density is higher along the grain boundaries as depicted from Fig. 5.1.7(c). It is clear from Fig. 5.1.7(c) that grain boundaries are poorly delineated and due to recovery process at room temperature, dislocations are absorbed by grain boundaries partially. The SAED pattern corresponding to 4 cycles MDFed sample in the

inset (Fig. 5.1.7(c)) clearly reveals the ring pattern, suggesting higher misorientation due to the formation of ultrafine grains. The cryoforged samples reveal higher dislocation density as compared to room temperature forged samples. In addition to this, dislocation tangles zones are dominating in cryoforged samples. Grain boundaries are in metastable state due to presence of high dislocation density around the grain in cryoforged samples. On the other hand, at room temperature, cross slips and climb of dislocation are easier, which promotes dynamic recovery resulting in relaxed grain boundaries with reduced dislocation tangled zone.

5.1.3.2 Mechanical Properties

Hardness of room Temperature forged and cryo forged Al 2014 alloy with different number of cycles is shown in Fig. 5.1.8
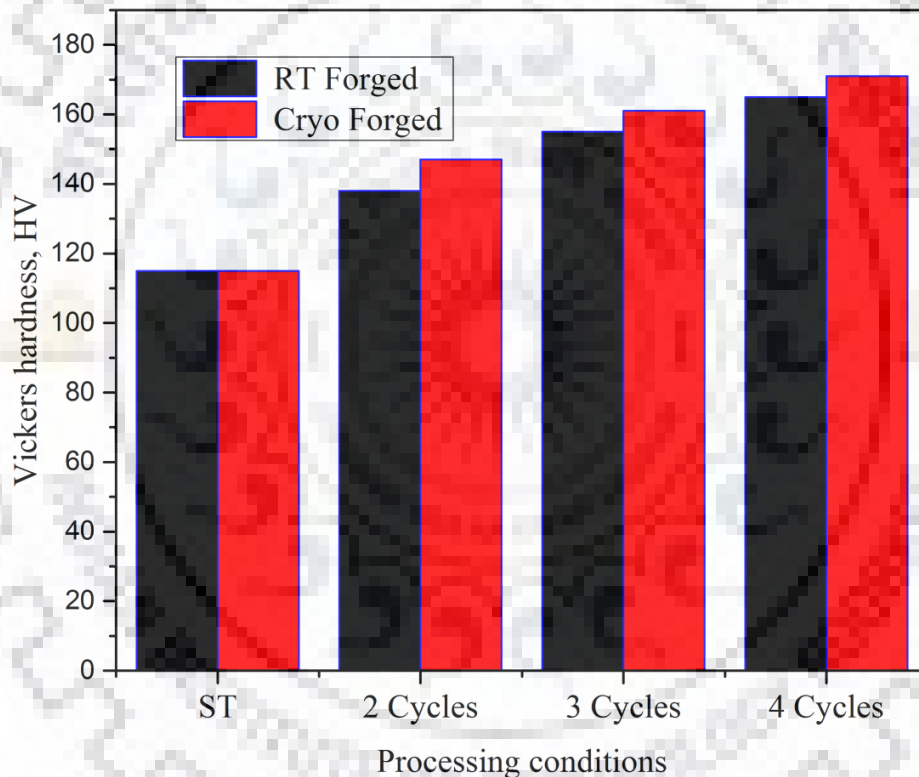
Figure 5.1.8: Variation in Hardness for room temperature forged and cryo forged Al 2014 Alloy with various processing conditions

It is observed that hardness of cryoforged material is more as compared to room temperature forged material for all processed condition. It is due to the suppression of dislocation annihilation in multidirectional forging at liquid nitrogen temperature. Hardness of the starting solution treated Al 2014 alloy was 115 HV. MDF performed at a cumulative strain of 1.2 (2 cycles) leads to increase in hardness of the alloy from 115 HV to 138 HV and 147 HV for room and cryogenic temperatures forged, respectively. At the cumulative strain of 1.8 (3

181

cycles), hardness value for room temperature forged and cryo forged sample has increased to 155 HV and 161 HV, respectively. With increase in cumulative strain up to 2.4 (4 cycles), hardness of room temperature forged material reaches to 165 HV, whereas hardness of cryo forged material becomes 171 HV. At lower strain, the increase in hardness is more for both conditions, room temperature forged alloy and cryo forged alloy, which thereafter show an increment with slow pace. This is due to the fact that at lower strain, work hardening effect is more than that of higher strain. In this study, it was observed that room temperature forged material shows 60.1% increase in hardness, whereas cryo forged material shows 66.01% increase in hardness after cumulative true strain of 2.4 as compared to solution treated alloy.

Variation in tensile properties of cryoforged and room temperature forged Al 2014 alloy is shown in Fig. 5.1.9 (a) and Fig. 5.1.9 (b) respectively. UTS and yield strength of solution treated alloy are observed as 245 MPa and 176 MPa, respectively with 18% elongation. Ultimate tensile and yield strength have subsequently increased to 436 MPa and 385 MPa, respectively upon MDF at room temperature at a cumulative strain of 2.4 (4 cycles). However, the ductility of room temperature MDFed alloy has reduced to 4% at a cumulative true strain of 2.4. For cryo forged alloy, UTS and yield strength have increased to 470 MPa and 396 MPa, respectively with 6% elongation at a cumulative true strain of 2.4 (4 cycles). These observations are similar to the observations made by Chatterjee et al. [5.41]. Increment in strength and hardness of cryo forged material with respect to room temperature forged material is due to the fact that MDF at liquid nitrogen temperature leads to suppression of dynamic recovery by reducing dislocation cross slip and climb as compared to room temperature forging. This generates high amount of dislocation density in cryo forged samples than the room temperature forged materials. Apart from enhancement in strength and hardness, cryo forged sample shows increased ductility (6% elongation to failure at a cumulative strain of 2.4) as compared to room temperature forged (4% elongation at cumulative strain 2.4) samples. Similar observations are made by Krishna et al. [5. 42] and Wang et al. [5. 27] on cryo rolling of Al-Cu alloy and pure copper, respectively.
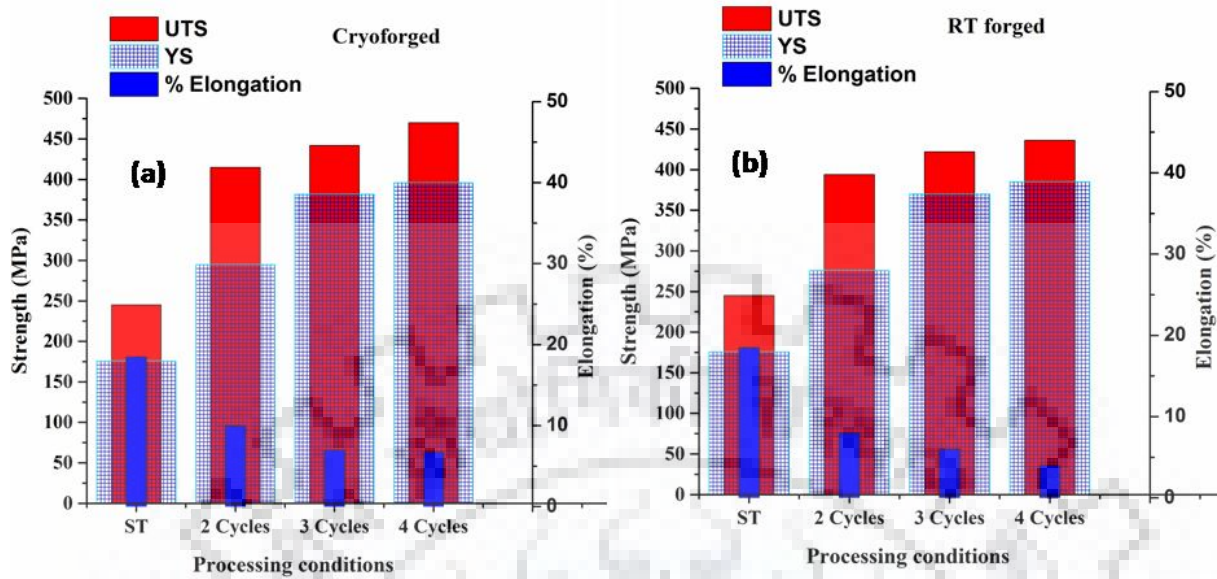
Figure 5.1.9: (a), (b), Variation in UTS, Yield Strength and % Elongation for cryo and room temperature forged Al 2014 alloy With Various processing Condition

Table 5.1.1: Mechanical properties of RT forged and Cryoforged Al 2014 alloy

Processing Condition	Hardness (HV)	Yield Strength (MPa)	UTS (MPa)	Elongation (%)
ST	115	176	245	18.5
ST + 2 Cycle RTF	138	276	394	8
ST + 3 Cycle RTF	155	370	422	6
ST + 4 Cycle RTF	165	385	436	4
ST + 2 Cycle CF	147	295	415	10
ST + 3 Cycle CF	161	382	442	7
ST + 4 Cycle CF	171	396	470	6

They observed the simultaneous strengthening and toughening due to presence of nanocrystalline/ultrafine grains, which reduce the size of nucleating flaws and enhance the resistance to crack propagation, leading to high tensile ductility [5.27, 5.42]. Mechanical Properties of RT forged and cryo forged samples are summarized in Table. 5.1.1. It is observed that Multi directional cryo forging can be used for enhancing strength and ductility of Al 2014 alloy. Strength and ductility of this alloy can further be increased by precipitation hardening mechanism.

5.1.3.3 Fractographs after Tensile Testing

Fractured surface of tensile samples of cryo forged as well as room temperature forged Al 2014 alloy was examined by SEM. Fig. 5.1.10(a) and Fig. 5.1.10(b)-(d) shows the fractographs of solution treated and cryoforged samples, respectively, after tensile test. Fig. 5.1.10(a) shows the fractograph of Solution Treated sample of Al 2014 alloy. Large size equiaxed dimples can be seen in dotted circular area on fractured surface of solutionised samples, which is a typical characteristic of ductile fracture. Ductile fracture generally occurs due to the coalescence of microvoids. The number and distribution of microvoids that nucleated in the surface control size of the dimples [5.43].
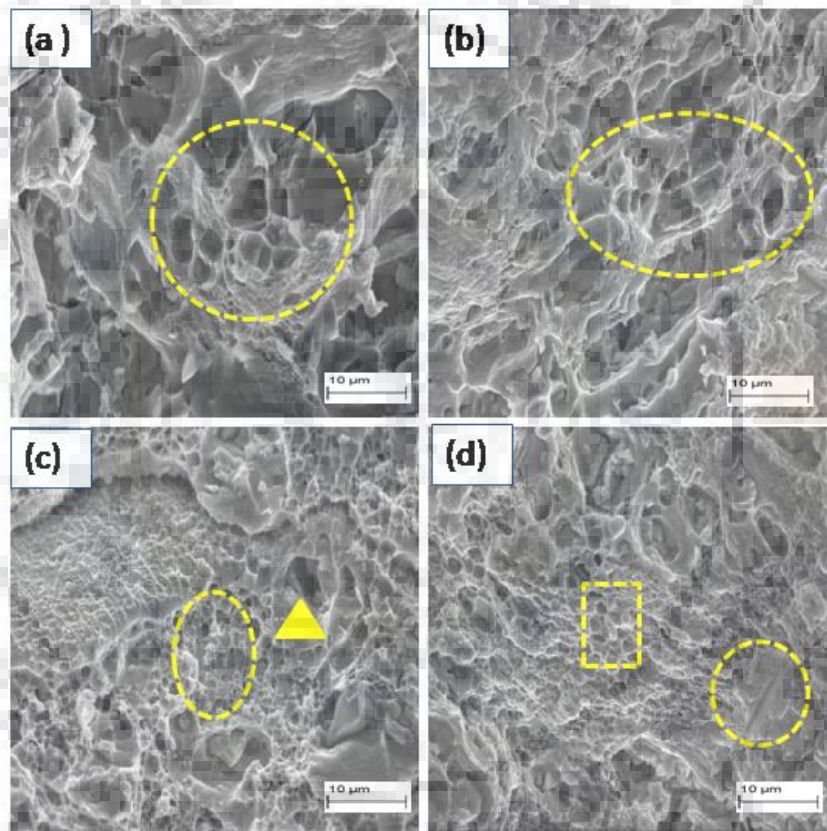
Figure 5.1.10: Fractographs of Cryo Forged Al 2014 Alloy after Tensile Test for various Processing Conditions : (a) Solution Treated ; (b) 2 cycles; (c) 3 Cycles; (d) 4 cycles

In solution treated alloy, nucleation sites are few and widely spaced, which grow to a large size before coalescing, resulting dimpled rupture. Fig. 5.1.10(b) shows fractograph corresponding to 2 cycles cryogenically forged Al 2014 alloy after tensile test. Fine dimples were observed in 2 cycles forged sample. It is due to the activation of numerous sites on fractured surface resulting from grain refinement. These sites are source for adjacent

184

microvoids to coalesce and avoid microvoids to grow to a larger size [5.43]. Similar observation was made by Fuloria et al. [5. 12] in MDFed zircalay-4. With increasing strain up to 1.8 (after 3 cycles), dual dimple size (small as well as large size dimples) were observed on the fractured surface. Dual dimpled featured can be seen in fractograph (Fig. 5.10 (c)) of 3 cycles cryoforged sample, in which large dimples are indicated by triangle while dotted oval shape area is used to show fine dimpled feature. It has been reported that material containing a dual distribution of particle size or presence of second phase particles, inclusion at grain boundary promotes a dual dimple size in fractured surface [5.44]. Large size dimples observed in fractured surface after 3 cycles may be due to the inclusions, which have larger size than the second phase particles present in Al 2014 Alloy. These inclusions have lower bond energy with the matrix. Fracture is initiated by debonding and void growth takes place at matrix - inclusion interface, which is possibly a cause of large size dimples. After a large strain, debonding may takes place at small size second phase particles with presence of small size dimples. Similar features were observed by Toda et al [5.44] during fracture of wrought Aluminum alloy. After 4 cycles (cumulative strain 2.4), fracture surface consist of very fine dimples (shown as rectangular area in Fig. 5.1.10 (d) with river marking (shown as dotted circle in Fig. 5.1.10 d), which is attributed as a Mixed mode fracture.

Fracture surface of room temperature forged samples after tensile test is shown in Fig. 5.1.11(a)-(c). Fig. 5.1.11(a) shows the fractograph of room temperature forged sample corresponding to 2 cycles. It shows the bigger dimples (shown by oval shape zone) as well as fine dimples (marked with arrow) while in case of cryo forged samples, the fracture surface after 2 cycles consist of larger dimples as compare to 2 cycles room temperature MDFed sample. With increase in cumulative true strain up to 1.8 (3 cycles), fractograph of RT forged samples shows few big size dimples with a brittle facets (shown by rectangular area in Fig.5.1. 11 (b). At a cumulative true strain of 2.4 (4 cycles), fracture surface of RT forged samples is entirely perturbed with cleavage or brittle facets (marked as rectangular area in Fig. 5.1.11(c) as compared to cryo forged samples. The Dual dimpled features in fracture surface of cryo forged samples observed in the present work substantiate the increased ductility of cryo forged samples as compared to room temperature forged samples. On the other hand, fracture surface of room temperature forged samples has shown a cleavage steps with increasing number of cycles leading to its reduced ductility.
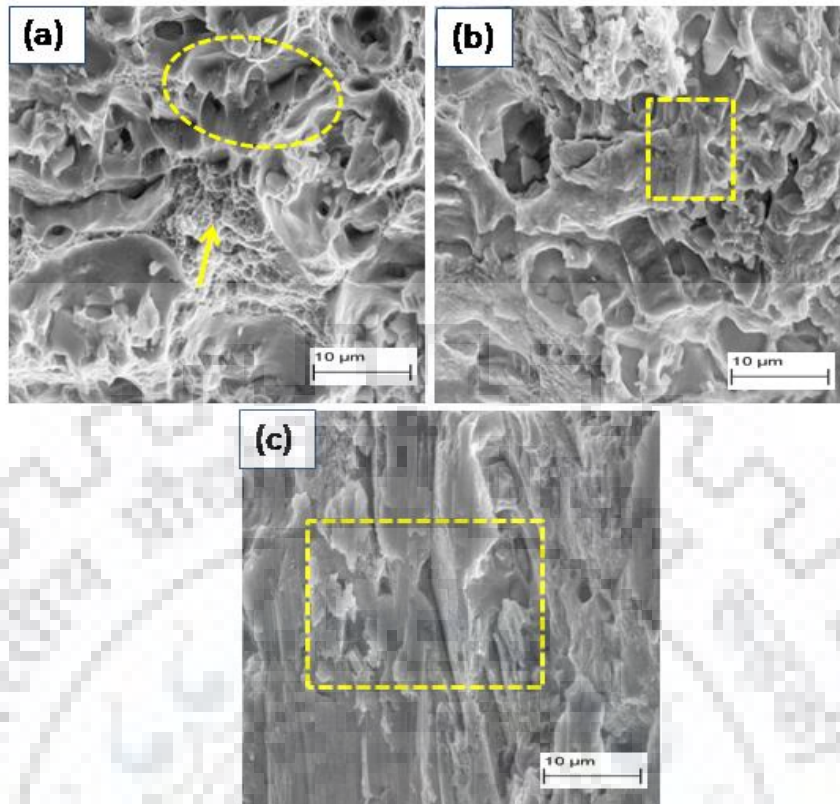
Figure 5.1.11: Fractographs of Room Temperature Forged Al 2014 Alloy after Tensile Test for various Processing Conditions : (a) 2 cycles ; (b) 3 Cycles; (c) 4 cycles

5.1.3.4 Fracture Toughness (K_Q)

SPD techniques generally lead to the increase in strength and hardness but deformation behavior is deteriorated due to decrease in ductility. Fracture toughness is a unique parameter which provides more general insight in to deformation and fracture behavior of material [5.45]. Unfortunately, fracture toughness testing is difficult in severely deformed materials due to small dimensions obtained during SPD processing to meet ASTM standards. There are very limited information on valid, plane strain fracture toughness (K_{IC}) of ultrafine grained materials due to restricted sample dimensions. In this work, cryoforged Al 2014 alloy showed a better tensile strength, yield strength and hardness as compared to room temperature forged Al 2014 alloy. Al 2014 alloy is widely used in structural and aerospace applications and to use this UFG Al alloy, it should exhibit high fracture toughness and good fatigue resistance. Sample dimensions obtained after cryoforging as well room temperature forging were not sufficient to conduct valid fracture toughness test in present work. However, based on past work of MacMaster et al [5. 46] for Al 6061 and Al 6069, fracture toughness for MDFed Al 2014 alloy has been measured by using 3 point bend test. Specimens for

186

conducting 3 point bend test were prepared by following ASTM E399-05 standard [5.47]. All Specimens were precracked by help of computer controlled wire cut EDM machine for a crack length (a = 3.75) to the width (W = 7.5) ratio of 0.5 as per ASTM standard. 3-point bend specimen thickness B is taken as 3.75 mm while unbroken ligament b (W-a = b) is taken as 3.75 mm for both room temperatures forged and cryo forged samples. The dimensions of 3 Point Bend Specimen in this work has been discussed in Chapter 3 and Chapter 4. Minimum thickness for achieving plane strain conditions and valid K_{IC} measurement is given by following equation [5.47].

$$B = 2.5 \left(K_{IC} / \sigma_0 \right)^2 \tag{5.1}$$

Where σ_0 is the 0.2 percent offset yield strength.

For determining linear elastic plane strain fracture toughness, tangent is drawn on a load – extension curve. Next, a secant line is drawn, which is having a slope 5 % less than the tangent. Point of intersection of secant line with the curve will give the value of P_s. Finally, a horizontal line at a load equal to 80 % is drawn and the distance x_1 along this line from the tangent to the actual curve is measured. If this distance exceed one fourth of the corresponding distance at P_S, the material is ductile and valid K_{IC} cannot be obtained for the material. However, if the material is brittle, the load P_s is designated as P_Q and substituted in the following equation for determining conditional value of fracture toughness for 3 point bend specimen [5.47].

$$K_Q = \frac{P_Q}{B} \frac{S}{W^{3/2}} \left[2.9 \left(\frac{a}{W} \right)^{\frac{1}{2}} - 4.6 \left(\frac{a}{W} \right)^{\frac{3}{2}} + 21.8 \left(\frac{a}{W} \right)^{\frac{5}{2}} - 37.6. \left(\frac{a}{W} \right)^{\frac{7}{2}} + 38.7 \left(\frac{a}{W} \right)^{\frac{9}{2}} \right] \tag{5.2}$$

Where a = crack length (for the present work crack length a = 3.75 mm)

The validity of test is checked by the equation $B = 2.5 \left(K_Q / \sigma_0 \right)^2$ \tag{5.3}

If B is less than the both thickness and crack length of specimen, then K_Q is known as plane strain fracture toughness K_{IC} [5.47].

Load – Extension curve for RT forged and Cryo forged Al 2014 alloy for various processing conditions is shown in Fig. 5.1.12 (a) and Fig. 5.1.12(b) respectively.

From Fig. 5.1.12 (a)-(b) for solution treated Al 2014 Alloy; maximum load at which preexisting crack grows to a critical size comes out to be 756 N. This limiting load is

designated as P_Q and substituted in equation (5.2) for determining the conditional value of fracture toughness K_Q. On Substituting the values of a, W, B, and P_Q in equation (5.2)

$$K_Q = 23.93 \text{ MPa}\sqrt{m}$$

For checking the validity of test, equation (5.3) is used.

Specimen thickness from the equation (5.2) can be obtained by substituting the values of K_Q and σ_0, which is B = 45.15 mm.

Since theoretical value of B is greater than thickness and crack length of specimen, the test is invalid. The conditional value of fracture toughness K_Q is known as apparent fracture toughness. The same procedure can be followed to calculate apparent value of fracture toughness for room temperature forged as well as cryo forged samples corresponding to each number of cycles. Fracture toughness values for each condition are shown in the Table. 5.1.2
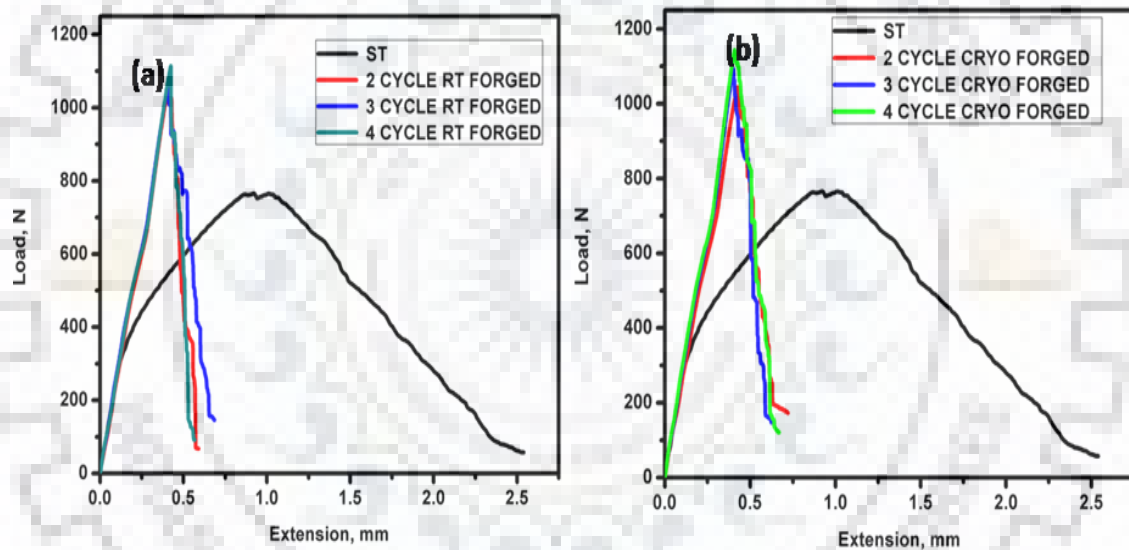
Figure 5.1.12: Load vs Extension curve for various processing conditions (a) RT forged Al 2014 alloy; (b) Cryoforged Al 2014 alloy

Table 5.1.2: Apparent Fracture Toughness values For RT Forged and Cryo Forged Al 2014 Alloy for various processing conditions

Processing Condition	RT Forged K_Q (MPa$\sqrt{m}$)	Cryo Forged K_Q (MPa$\sqrt{m}$)
Solution Treated	23.93	23.93
2 Cycle Forged	30.12	30.47
3 Cycle Forged	35	35.93
4 Cycle Forged	36.96	37.7

188

Variation of K_Q with different processed condition at both temperatures is shown in Fig. 5.1.13. It is observed that apparent fracture toughness K_Q has improved for Al 2014 alloy processed by multidirectional forging at both room temperature as well as cryo temperature. However, cryoforged samples show slightly better improvement of K_Q values as compared to room temperature forged samples. These observations are similar to observations made by Das et al. [5.48] for the cryorolled Al 7075 alloy.

The apparent Fracture Toughness (K_Q) of the processed alloy is calculated using Linear Elastic Fracture Mechanics (LEFM) in the present work. The fracture toughness of ultrafine grain material (ufg) is not studied in detail in the literature so far. Ovid'ko et al. [5.21] have studied the effect of grain size on crack blunting of nanocrystalline /ultrafine grain material. The emitted dislocations from crack tip are hindered by nearest grain boundaries if the grain size is small as reported in their work. These dislocations further repel the subsequent emitted dislocation from crack tip, and induce insignificant crack blunting in UFG material. Hence, the crack propagation is facilitated in UFG material due to which they exhibit relatively lower fracture toughness compared to its bulk counterparts. Also, opposing reports of improved fracture toughness of severely deformed material has also been reported in the literature [5.34-5.36, 5. 48). In the present work, fracture toughness of the processed Al alloy has improved due to grain refinement. It may be mentioned that fracture toughness depends upon crack initiation and crack propagation.
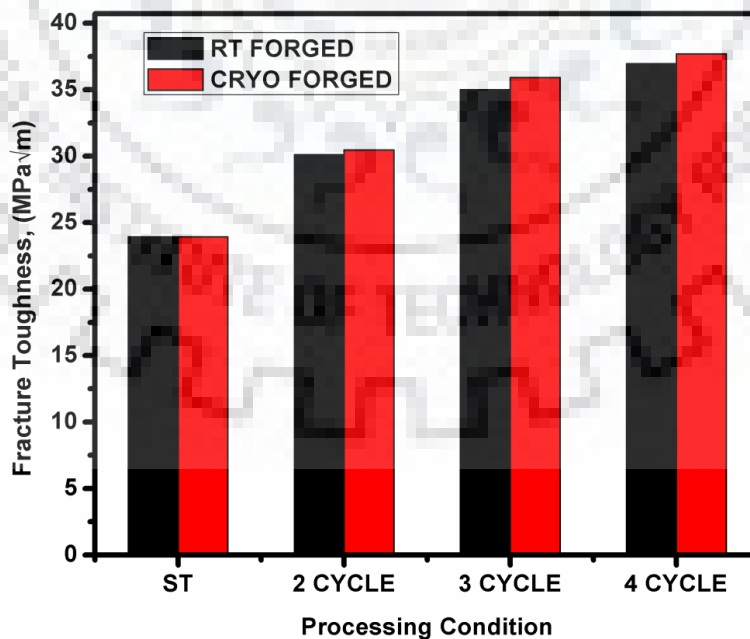
Figure 5.1.13: Variation of Apparent Fracture Toughness for RT Forged and Cryoforged Al 2014 Alloy with various processing conditions

The fracture toughness (K_{IC}) could be improved if the crack initiation is delayed. It is well known that K_{IC} is plane strain fracture toughness, which characterizes the crack in LEFM. On the other hand, if the crack propagation is made slow, fracture toughness (J_{IC}) could improve again. J_{IC} is fracture toughness parameter in EPFM approach. In this work, apparent fracture toughness (K_Q) has been calculated by using LEFM approach. It is not possible to calculate K_{IC} for a small size MDFed specimen. The improvement in K_Q for MDFed Al 2014 alloy was observed due to delayed crack initiation. However, once the crack is initiated, it moves rapidly leading to cleavage fracture as shown in fractographs (Fig. 5.1.14 and Fig. 5.1.15). It is also clear from TEM micrographs that the strengthening due to dislocation tangles and dislocation cell structure could delay the crack initiation, thereby improving the fracture strength of MDFed Al 2014 alloy.

5.1.3.5 Fractographs after 3-Point Bend Test

Fracture surface of MDFed Al 2014 alloy after 3 point bend test was characterized by SEM. Fig. 5.1.14 shows the fracture surface of Al 2014 alloy subjected to multidirectional forging at liquid nitrogen temperature for various processing conditions after 3 point bend test. Fracture surface shows elongated dimples for solution treated alloy, which is a characteristic of ductile tearing fracture [5. 49-5.50]. These elongated dimples are seen in the area indicated by dotted circle in Fig. 5.1.14(a). Tearing fracture occurs because cryo forged samples are tested in crack opening mode- I loading, in which loading is perpendicular to the direction of movement of crack mouth [5. 49]. Fig. 5.1.14 (b) shows the fractograph of 2 cycles MDFed alloy after 3 point bend test.
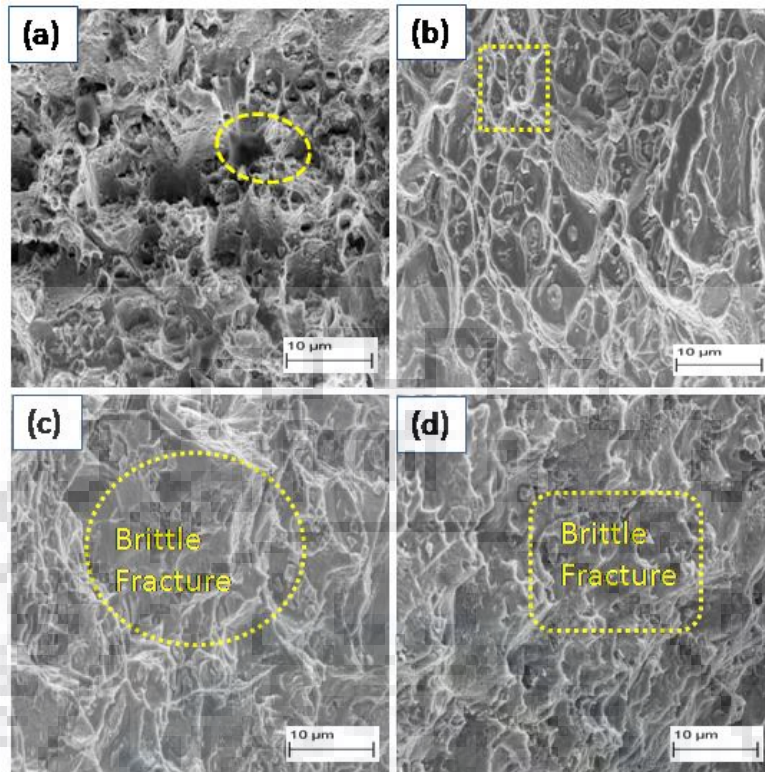
Figure 5.1.14: Fractographs of Cryo Forged Al 2014 Alloy after 3 Point Bend Test for various Processing Condition : (a) Solution Treated; (b) 2 cycles; (c) 3 Cycles ; (d) 4 cycles

Fractograph corresponding to 2 cycles MDFed alloy reveals presence of shallow elongated dimples, which can be seen in area indicated by dashed rectangle in Fig. 5.1.14(b). Also, with shallow dimples, network of cleavage steps, known as river patterns were observed in remaining places of sample MDFed up to 2 cycles. These features indicate that material fails in partially brittle manner under tearing mode, which is generally observed in severely deformed material due to dislocation strengthening and grain boundary strengthening. At higher cumulative strain of 1.8 (3 cycles) and 2.4 (4 cycles), fracture surface was completely perturbed with river markings, which can be seen in circular zone and rectangular zone in Fig. 5.1.14(c) and Fig. 5.1.14(d), respectively. These river markings correspond to the low energy fracture, which propagates along crystallographic plane known as cleavage plane. Fractographs corresponding to room temperature forged alloy is shown in Fig. 5.1.15(a)-(c). A comparative study of fractographs of room temperature MDFed alloy and cryo temperature MDFed alloy reveals that the fracture surface shows approximately same features after 3 point bend test for the all processing conditions. At a lower strain of 1.2, Fractographs (Fig.

191

5.1.15(a)) of MDFed alloy at room temperature shows a very few shallow elongated dimples with river patterns.
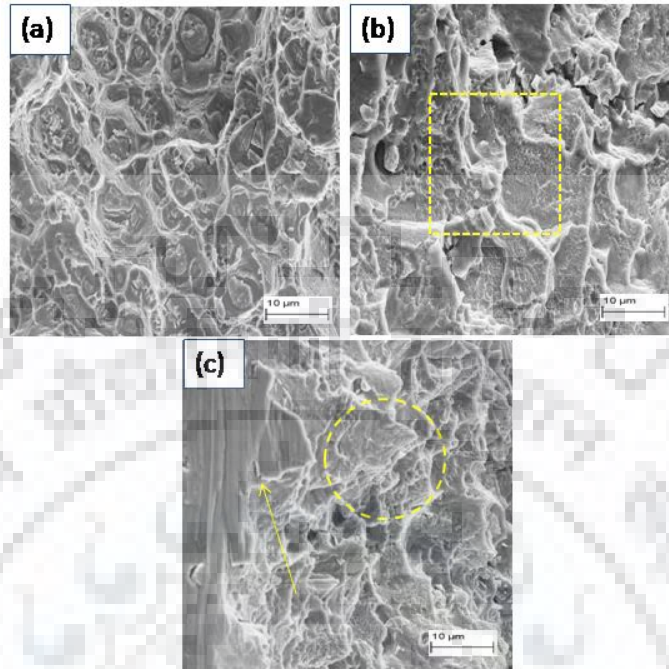
Figure 5.1.15: Fractographs of Room Temperature Forged Al 2014 Alloy after 3 Point Bend Test for various Processing Conditions : (a) 2 cycles ; (b) 3 Cycles; (c) 4 cycles

With increasing strain up to 1.8 and 2.4, fractographs of RT forged alloy reveals brittle facets (rectangular zone in Fig. 5.1.15 (b) and circular zone in Fig. 5.1.15 (c) with river markings. Mode of loading in 3-point bend test provides an interesting fracture surface for both conditions (at room temperature as well as cryogenic temperature) as compared to tensile test fractography, where loading is perpendicular to the fractured surface resulting equiaxed dimpled features. In the present investigation, calculated fracture toughness is very close for MDFed alloy at room temperature as well as cryogenic temperature, which elucidates approximately similar fracture appearance after 3 point bend test for both conditions. It is observed that the failure mechanism transforms from ductile tearing fracture to brittle fracture for solution treated to 4 cycles MDFed alloy, which substantiates the improvement in apparent fracture toughness (K_Q) with increasing strain steps at cryo as well as room temperature.

5.1.4 Conclusions

Mechanical Properties, microstructural evolution and fracture behavior of cryo as well as RT forged Al 2014 alloy has been investigated in present work. The following conclusions are made based on present study.

- The improvement in mechanical properties of cryoforged Al 2014 alloy was observed as compared to room temperature forged alloy due to effective retardation of dynamic recovery at cryogenic temperature. The cryoforged samples show an increment of 7% in tensile strength and 3% in yield strength over room temperature forged samples up to cumulative true strain of 2.4 (4 cycles).

- TEM investigations of RT forged Al 2014 alloy shows the reduced dislocation density and dislocation tangling zone due to dynamic recovery, compared to cryoforged alloy.

- Fractographs corresponding to 4 cycles cryoforged Al 2014 alloy after tensile testing show the mixed mode of fracture, while fractographs of RT forged Al 2014 alloy after 4 cycles exhibit the brittle fracture appearance.

- An increment of 60% is observed in apparent fracture toughness (K_Q) of cryoforged Al 2014 alloy as compared to solution treated alloy in 3-point bend test. Fracture mode of cryoforged as well as RT forged Al 2014 alloy after 3 point bend test changes from ductile tearing fracture to brittle fracture with increasing strain steps.

5.2   Influence of Annealing on Strain hardening behavior, Fracture mechanism, and Fracture toughness of Multidirectional Cryoforged (MDCFed) Al 2014 alloy

5.2.1 Introduction

It has been well established that grain refinement during multidirectional forging (MDF) derives from various dislocation mechanisms in metals/alloy with high or medium stacking fault energy (SFE) [5.54]. Grain is refined through accumulation, interaction (tangling), spatial distribution and rearrangement of dislocations. During the deformation at low strain, grains are divided in to large number of small elements, which are separated by geometrical necessary boundaries (GNBs) and incidental dislocation boundaries (IDBs) inside the grain as reported in the literature [5.55]. With increase in severe strain, these GNBs and IDBs are transformed in to high angle grain boundaries resulting in fine grain within the original coarser grain [5.56]. Recently, Sitdikov et al. [5.57] compared the microstructure of Al 7475 alloy processed through ECAP and MDF at 400°C and proposed the mechanism of

193

continuous dynamic recrystallisation (CDRX) occurring in the processed Al alloy. Exceptional grain fragmentation is achieved in both processes through the formation of deformation bands (GNBs) and microshear bands as reported in their work. Kobayashi et al. [5.40] studied the effect of multidirectional forging on copper at 195K and found that micro shear banding is primary mechanism for obtaining UFG at low strain, while mutual intersection of microshear bands is responsible for further refinement at high strain. Extensive studies on ferritic stainless steel, magnesium alloys AZ31 and AZ 61 subjected to MDF at warm temperatures are reported in the literature [5.16-5.18].

Recently, it has been generally agreed that grain fragmentation is not only depends upon the deformation strain but it is the deformation temperature especially cryogenic temperature, which plays a significant role in refining the grain size [5.26]. Rao et al. [5.38] performed the multidirectional forging (MDF) on Al 6061 alloy at cryogenic temperature and observed the significant improvement in strength (180 MPa- 388 MPa) and hardness (50 HV- 115 HV) as compared to solution treated (ST) alloy. Similar studies were made on cryogenically processed SPDed metals/alloy [5.58-5.60]. It has been reported that cryodeformed MDFed metals/alloy possesses significant amount of dislocation density due to suppression of dynamic recovery as compared to other SPD methods operated at room temperature or higher temperature [5.61]. In addition to this, cryogenically processed MDFed material shows poor work hardening rate due to inability to accumulate extra dislocations inside very fine grains [5.62- 5.63]. This limits the use of cryogenically processed MDFed metals/alloy for high strength structural/ industrial applications, where minimum ductility and formability is the key issue. Along with work hardening rate, it is essential to study the behavior of UFG metals/alloy produced by cryodeformed SPDed methods in presence of preexisting crack in order to use these materials safely in high strength structural applications [5.34]. Pre existing flaw/crack could initiate fracture in the material. Material resistance to failure in presence of pre-existing crack/flaw is determined by fracture toughness (K_{Ic} and J_{Ic}) [5.64]. Fracture toughness of cryodeformed SPDed material has been investigated in very few reports in past due to limitation in sample size obtained after SPD processing and complex testing procedures. Several past studies on fracture toughness of UFG metals/alloys is based on high pressure torsion (HPT) processed nickel (Ni) [5.34] , copper (Cu) [5.66], and iron (Fe) [5.45]. Ovid'ko et al. [5.21] made extensive study and proposed theoretical model for fracture toughness of ultrafine grained (UFG) and nanocrystalline (NC) materials and reported that crack tip blunting and crack

194

growth processes are influenced by the lattice dislocation emission from crack tip. Crack tip blunting is favored by grain boundaries (GBs) when lattice dislocations are stopped by it. The blunted crack tip and stress field of arrested dislocation further hinders the emission of lattice dislocation resulting significant suppression of crack tip blunting and enhance the crack growth mechanism as reported in their work [5.21]. The opposing trend of fracture toughness with decrease in grain size was observed in Ovid'ko's work

The studies on work hardening behavior and fracture toughness of age hardenable Al 2xxx series alloy processed through SPD methods, especially multidirectional forging at cryogenic temperature is very limited. Some of the earlier published work is based on the microstructure-properties correlations in UFG Al 6061, Al 6063, Al 7075 produced through cryorolling [5.67-5.69]. Aluminum 2014 alloy is one of the widely applied Al alloys in aerospace and high strength structural application due to its high strength to weight ratio and improved fatigue and fracture properties. The primary alloying elements in this alloy are Cu, Si, Mg, and Mn. The properties of this alloy can further be improved by producing ultrafine grains in its bulk counterparts and subsequently imparting thermal treatments such as annealing and aging. Such treatment not only provides strength but also a tensile ductility with improved fracture properties such as fracture toughness.

Based on the above discussions, the following studies are made on Al alloy i) Investigation of microstructural evolution in Al 2014 alloy subjected to multidirectional cryoforging (MDCF) and followed by post deformation annealing for 1 hour with the temperature varying from 150°C to 350°C. ii) Studies on the influence of second phase particle/precipitates on the work hardening, fracture mechanism, and fracture toughness of MDCFed Al 2014 alloy after annealing treatment. The mechanical properties such as tensile strength, uniform elongation, and fracture toughness are measured through tensile as well fracture toughness tests, while microstructural characterization is performed   by the help of optical microscopy, SEM and TEM.

5.2.2 Experimental Procedure

The chemical composition of Al 2014 alloy used in the present work is listed in Chapter 3 . The alloy was machined in the form of rectangular samples of dimension 33 mm x 30 mm x 27 mm and solutionised at 505°C for 2 hours followed by water quenching at room temperature. Solutionised samples were multidirectional cryoforged (MDCFed) by help of friction screw forging machine up to four cycles i.e cumulative strain $\sum \Delta\varepsilon = 2.4$. Here, one

cycle corresponds to 3 forging passes in three mutually perpendicular axis x, y, z. The first forging axis was parallel to the longest dimension (rolling direction) of the sample. The compressive strain of $\varepsilon = 0.2$ was exerted in each forging pass. To perform MDF at cryogenic temperature (-196°C), samples were dipped in liquid nitrogen filled box for 10 to 15 minutes before each forging pass. Initial dimension ratio is maintained by providing 90° rotations after each axial compression throughout the whole process. Schematic illustration of MDF procedure is shown in Fig. 5.2.1(a).
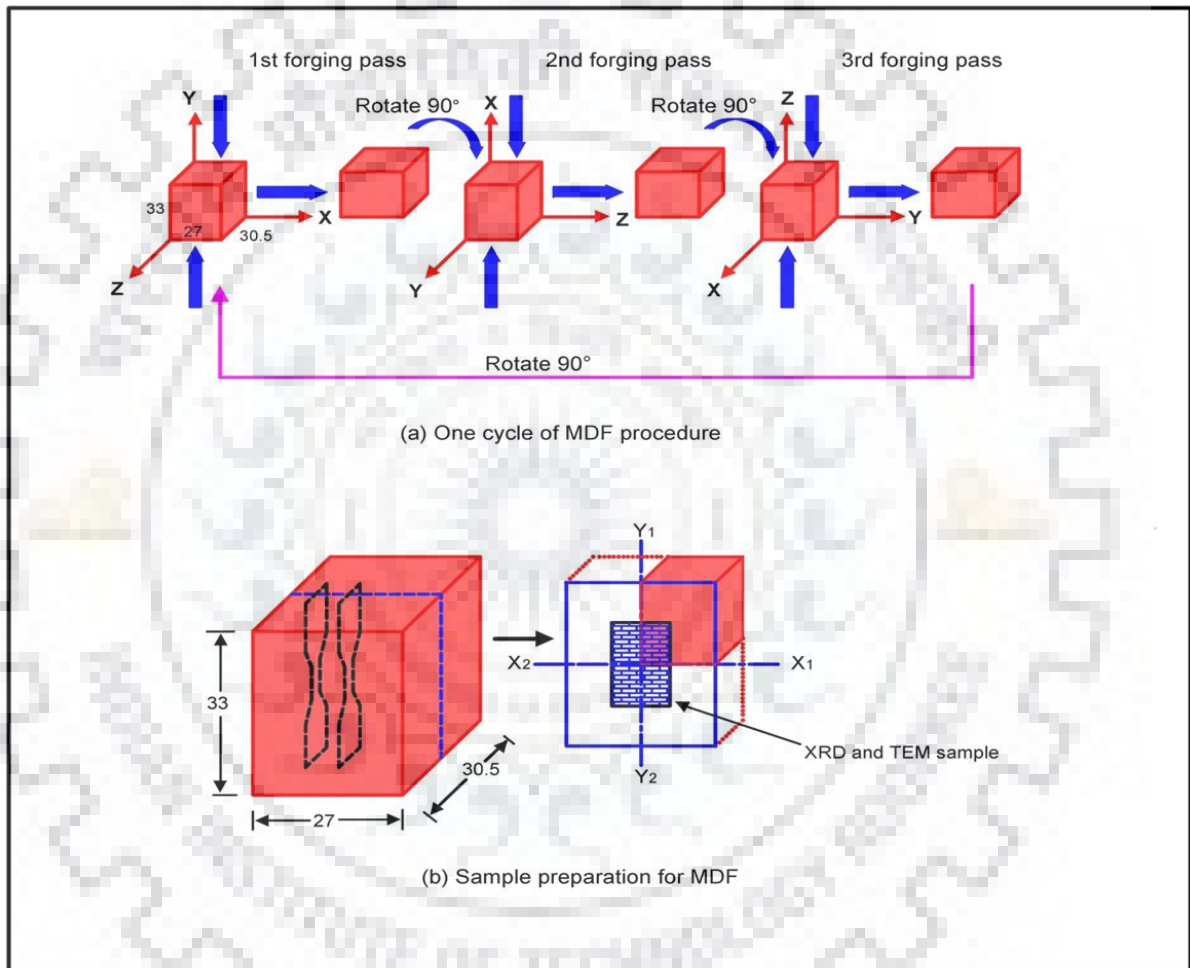
Figure 5.2.1: (a) one cycle of MDF procedure ; (b) Sample preparation for MDF

To investigate the effect of annealing on work hardening behavior, fracture mechanism and fracture toughness, the MDCFed (multidirectional cryoforged) Al 2014 alloy was annealed in the temperature ranging from 150°C to 350°C with the interval of 50°C for the time duration of 1 hour. Cryoforged and annealed samples were mechanically tested by tensile and fracture toughness tests (3-point bend test) on H25K-S Tinius Oslen tensile universal testing machine. Tensile samples were machined along the rolling direction (Fig. 5.2.1(b))

196

from the center of the processed samples with the gauge length of 10 mm and following the ASTM E-8 sub size specification. 3-point bend samples were prepared by following the ASTM E-399 standard. Sample dimension for 3-point bend specimen has been shown in our earlier published work [5.62] and Chapter 4.The microstructural characterizations were made by using optical microscopy and TEM. The details of TEM sample preparation are discussed in our earlier work [5.62] and discussed in Chapter 3. The fracture surface of tensile and 3-point bend sample was characterized by SEM.

5.2.3   Results

5.2.3.1 Microstructure

The microstructure of starting alloy, solutionised Al 2014 is characterized by using optical microscopy in the present work as depicted in Fig. 5.2.2(a).
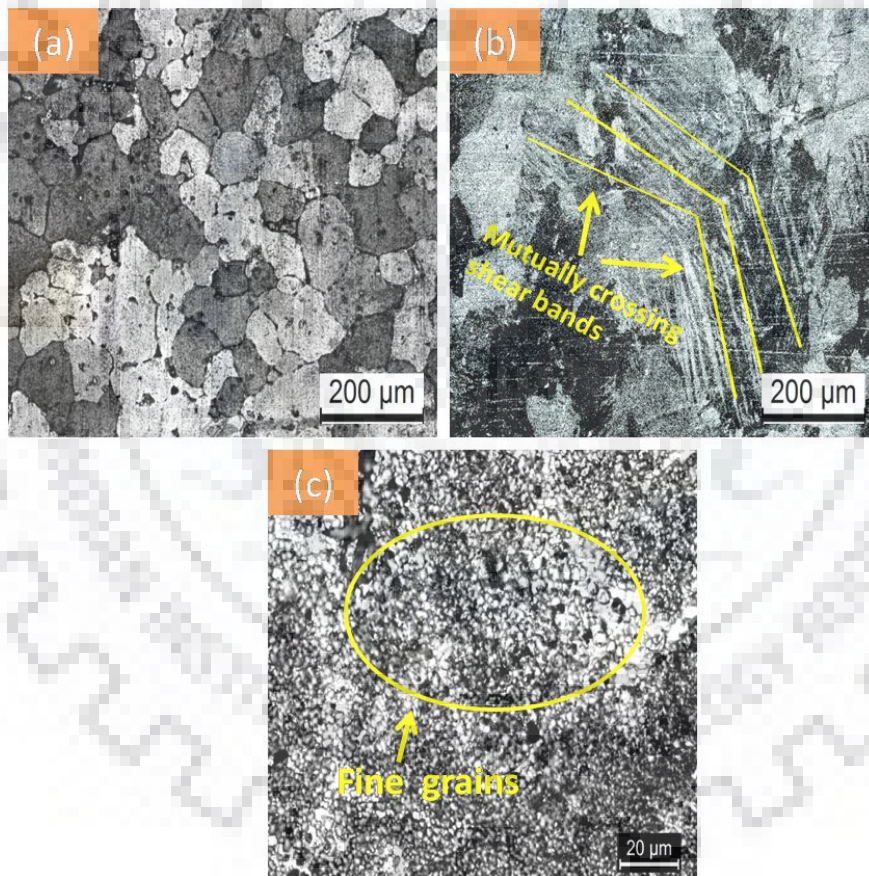
Figure 5.2.2: Optical Micrographs of MDCFed Al 2014 Alloy for various processing conditions: (a) Solution Treated; (b) 4 cycles; (c) 4 cycles at higher magnification

The starting materials consist of grain sizes in the range of 100 μm- 200μm as shown in Fig.5.2.2(a). Fig. 5.2.2 (b)-(c) are the optical micrographs of solution treated Al 2014, which is

subjected to multidirectional cryoforging (MDCF) up to cumulative strain of 2.4 (4 cycles). Numerous mutually intersecting shear bands (marked by yellow lines) can be visualized from Fig. 5.2.2(b). Higher magnification optical micrographs (Fig. 5.2.2(c)) corresponding to 4 cycles of MDCFed sample shows the evolution of fine grains. It has been observed that processed sample after multidirectional cryoforging does not depict the clear contrast of dislocation substructure/dislocation cell boundaries due to limitation of optical microscopy. Therefore, TEM studies are performed to investigate microstructural features in detail for MDCFed and MDCFed followed by annealed samples.

Microstructure of MDCFed sample after 4 cycles mainly consists of stretched structure along the shearing direction as observed from TEM micrographs (Fig. 5.2.3(a)).
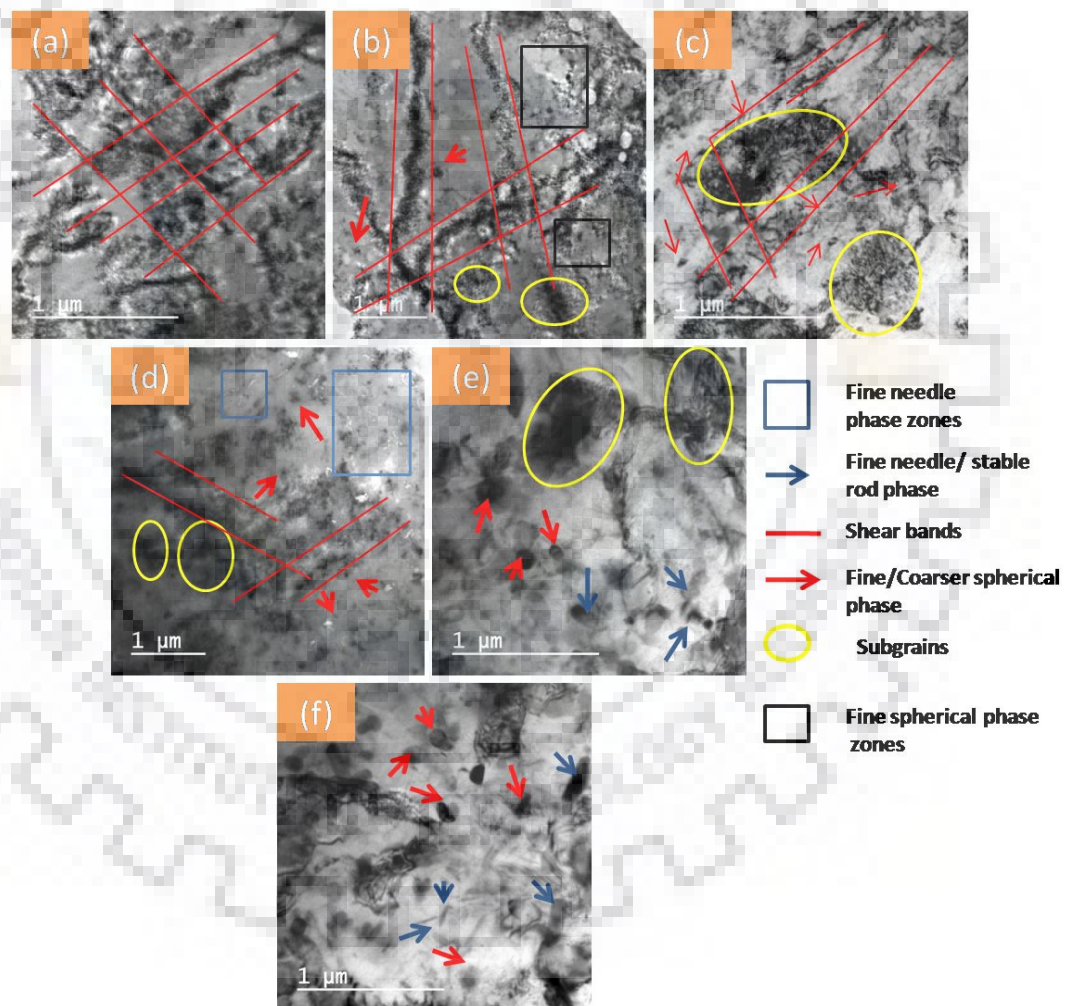
Figure 5.2.3: TEM micrograph of Al 2014 Alloy for various processing conditions : (a) 4 cycles (b) 4 cycles followed by annealed at 150°C ; (c) 4 cycles followed by annealed at 200°C; (d) 4 cycles followed by annealed at 250°C; (e) 4 cycles followed by annealed at 300°C; (f) 4 cycles followed by annealed at 350°C

This stretched structure has been reported as deformation/shear bands, which are intersecting to each other (marked by red lines in Fig. 5.2.3(a) [5.38]. Few fine subgrains were also observed in this condition at the point where these bands mutually crosses each other as observed from higher magnification TEM micrographs shown in Fig. 5.2.4(a)-(b). The SAED pattern corresponding to Fig. 5.2.4(a) is shown in Fig. 5.2.4(c). The elongated spots along with center brighter region can be seen in the SAED pattern of 4-cycles of cryoforged sample. These elongated spots substantiate the formation of ultrafine grains with higher misorientation after multidirectional cryoforging.
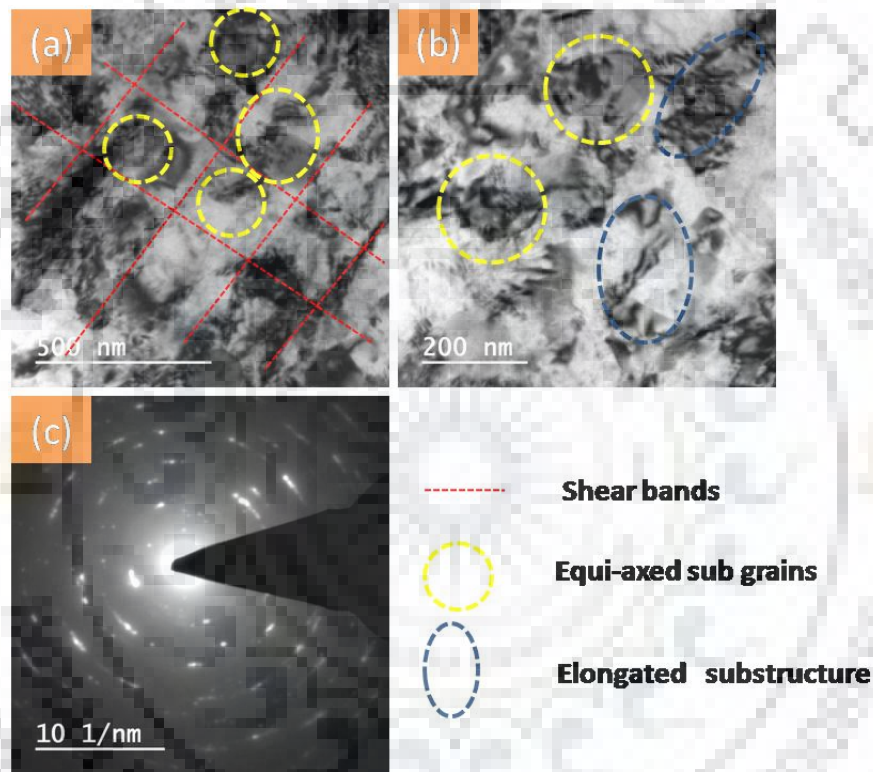
Figure 5.2.4: (a), (b) TEM micrographs of 4 cycles MDCFed alloy; (c) SAED pattern corresponding to 4 cycles MDCF

When MDCFed alloy is annealed at 150°C (MDCF+150°C), the slight recovery of the microstructure is observed with the evolution of fine spherical phase (highlighted by rectangular box and marked by red arrows in Fig. 5.2.3 (b). In addition to this, the density of shear bands is also slightly reduced as evident from the TEM micrograph Fig. 5.2.3(b) at this process condition. Fine dislocation cells (subgrains marked by yellow circle) away from shear bands are also observed at this annealed condition. To observe these precipitates more clearly, higher magnification TEM micrographs are also shown in Fig. 5.2.5(a)-(b). The SAED pattern of Fig.5.2.5(a) corresponding to sample annealed at 150°C is shown in Fig. 5.2.5(c). The

SAED pattern is nearly same as observed in MDCFed sample. However, the slight continuous rings are observed as compared to MDCFed sample along with elongated as well as broadened spots. Continuous rings might be present due to the reduction of dislocation density along with formation of subgrains, while some of the broadened spots may be due to the slight increase in grain size as compared to MDCFed sample.
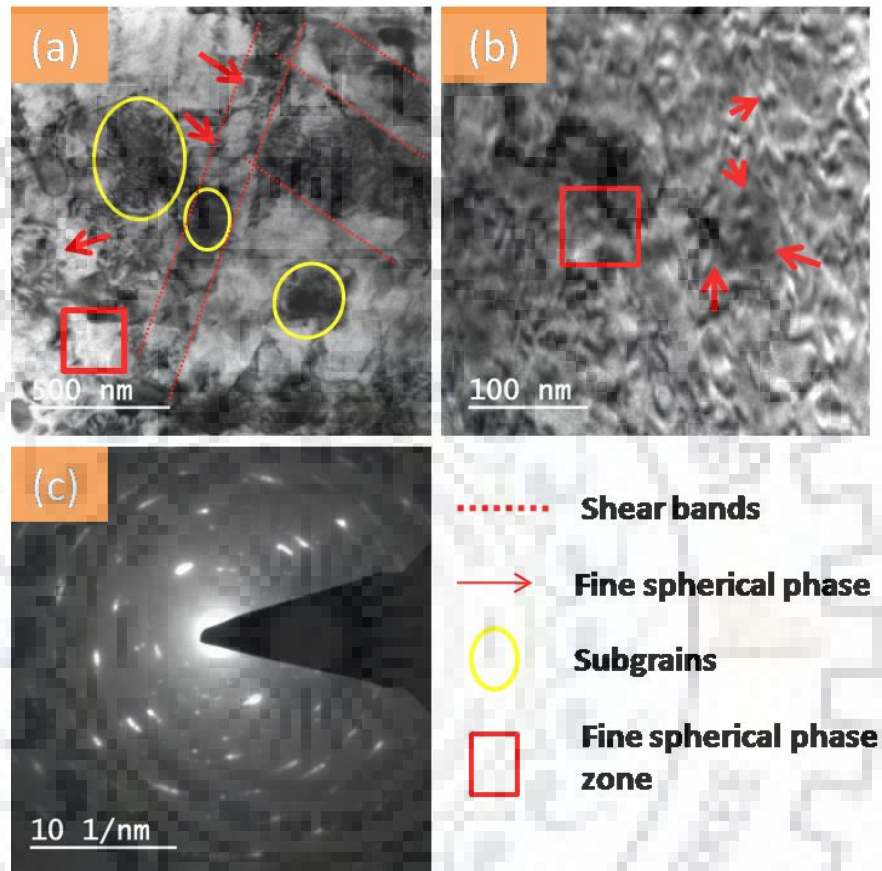
Figure 5.2.5: (a), (b) TEM micrographs of 4 cycles MDCFed alloy annealed at 150°C; (c) SAED pattern corresponding to 4 cycles MDCFed alloy annealed at 150°C

When MDCFed samples are annealed at 200°C, the dislocation density is gradually reduced along the shear bands and subgrains are much more prominent as depicted from lower and higher magnification TEM micrographs (Fig. 5.2.3(c)- Fig.5.2.6 (a)-(b)) at this condition. The same spherical phase seen at 150°C is also observed for MDCFed followed by annealed alloy at 200°C. However, the formation of subgrains is evident and spherical phase is slightly coarser as observed from higher magnification TEM micrographs (Fig. 5.2.6(a)-(b)) at this processing condition. The SAED pattern of Fig. 5.2.6(a) corresponding to this condition is shown in Fig. 5.2.6(c). The SAED ring pattern is continuous as compared to previous

conditions, which confirm that ill defined grain boundaries are transformed   in to well define sub grains at this conditions and recovery phenomenon is associated at this condition.
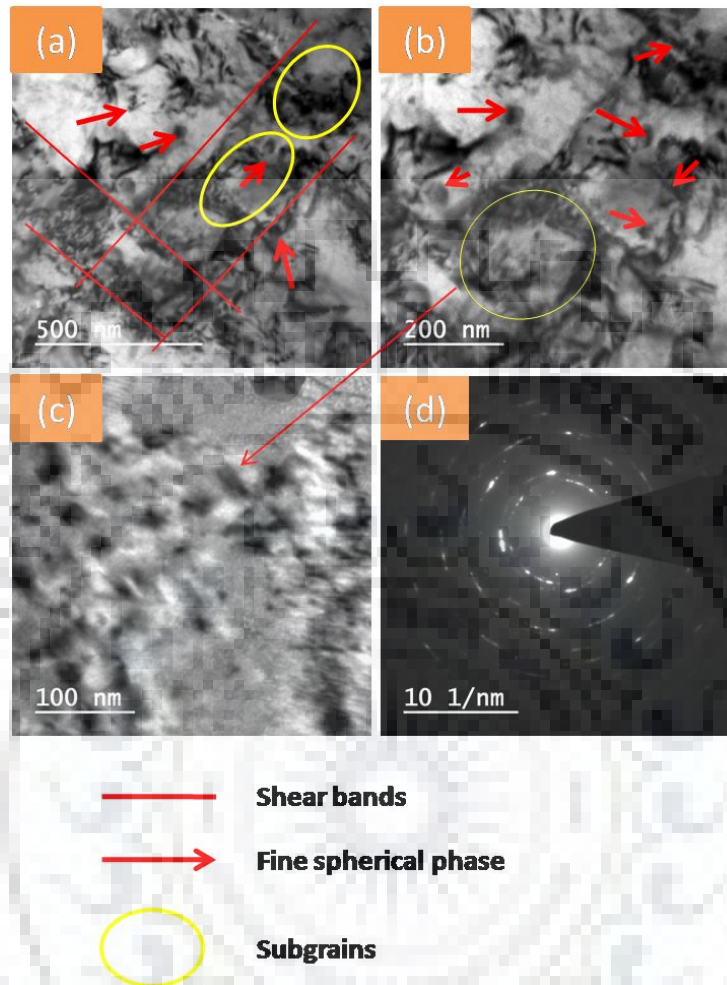
Figure 5.2.6: (a), (b), (c) TEM micrographs of 4 cycles MDCFed alloy annealed at 200°C; (d) SAED pattern corresponding to 4 cycles MDCFed alloy annealed at 200°C

The drastic change in the microstructure of MDCFed sample annealed at 250°C is observed as seen from Fig. 5.2.3(d) and Fig. 5.2. 7(a)-(d). Density of shear localization zone (shear bands) is observed to be less with evolution of large number of fine needle phase (highlighted in blue box) and very few spherical precipitates as seen from Fig. 5.2.3(d). Higher magnification micrographs are also shown in Fig. 5.2.7(a)-(d) to observe fine needle phase. It is also observed from these figures that subgrains formed at this temperature show a reduced dislocation interior and spherical phase is much coarser as compared to previous annealing condition (150°C, 200°C) samples. The SAED pattern of Fig.5.2.7(b) corresponding to this sample condition is shown in Fig. 5.2.7(e), which is slightly similar as in case of sample annealed at 200°C. The continuous rings along with some broadened spots were observed,

which is due to the fact that combined recovery and recrystallisation process occurs at this temperature.
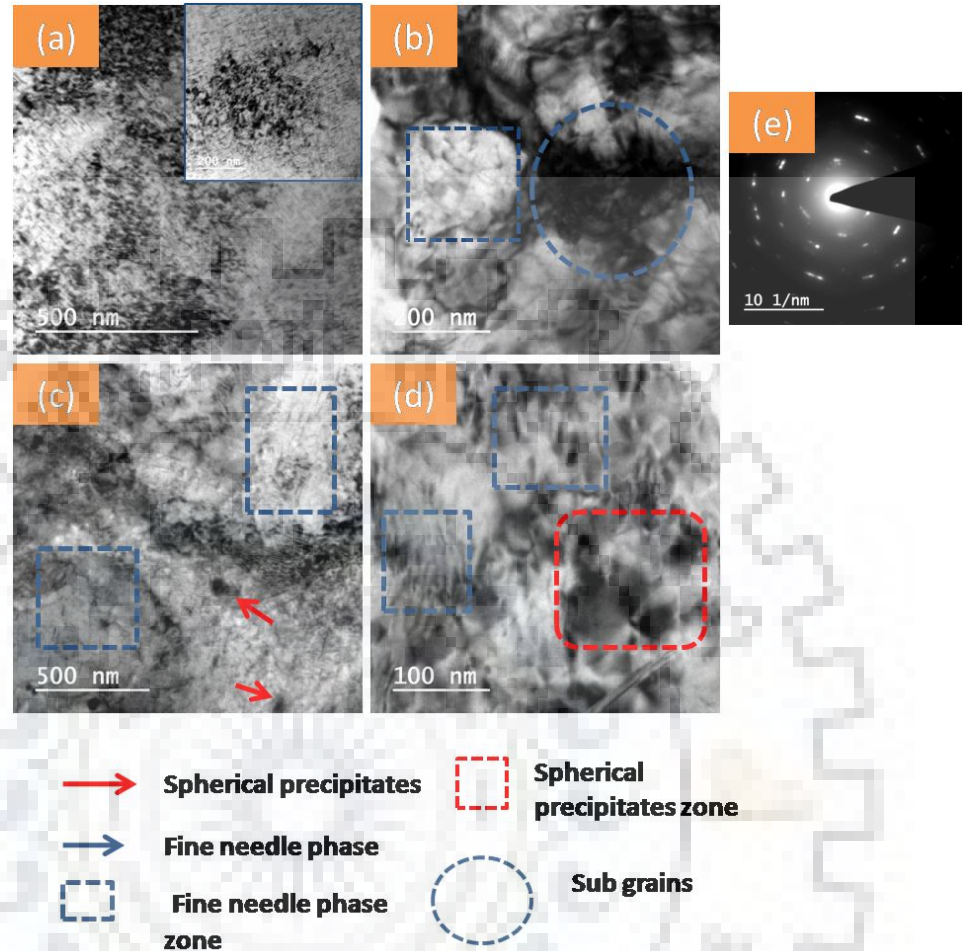
Figure 5.2.7: (a), (b), (c), (d) TEM micrographs of 4 cycles MDCFed alloy annealed at 250°C; (e) SAED pattern corresponding to 4 cycles MDCFed alloy annealed at 250°C

When MDCFed samples are annealed at temperatures of 300°C (Fig. 5.2.3(e)) and 350°C (Fig. 5.2.3(f)), the significant drop in dislocation density was observed from Fig. 5.2.3(e) and Fig. 5.2.3(f). Shear localization zones were almost annihilated with the evolution of coarser spherical phase and stable rod phase as seen from Fig. 5.2.3(e)-(f) and Fig. 5.2.8(a)-(d) at low/high magnification, respectively. Moreover, the size of spherical and rod phase is significantly increased with increasing annealing temperature. Along with this, the formation of dislocation free recrystallized grains was also observed. It shows that recrystallisation is much more prominent at these conditions (300°C and 350°C) with the transformation of fine spherical phase and fine needle phase in to coarser spherical and stable rod phase as evident from these figures. The SAED pattern corresponding to sample annealed at 300°C and 350°C

are shown in Fig. 5.2.8(c) and Fig. 5.2.8(d), respectively. The outer rings become much more wider and continuous along with central broadened spots observed at both condition as depicted from these figures. It confirms the coarsening of recrystallised grain and formation of bimodal microstructure at these conditions.
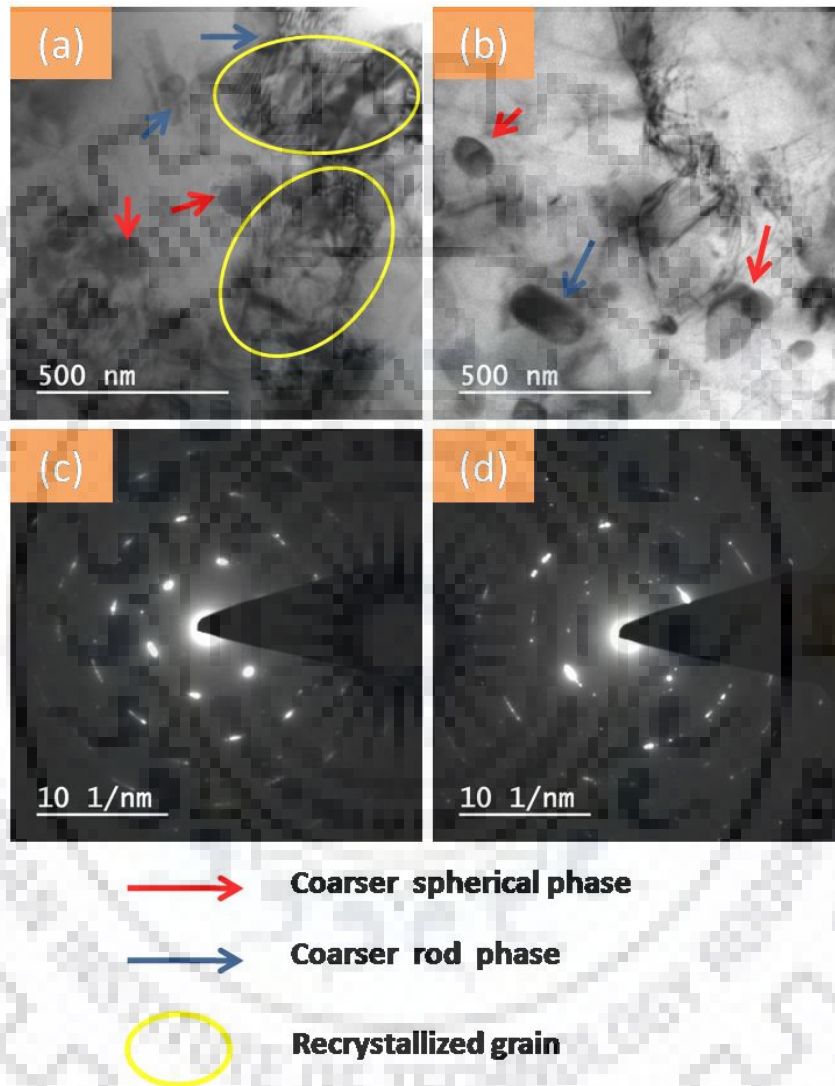
Figure 5.2.8: (a) TEM micrographs of 4 cycles MDCFed alloy annealed at 300°C; (b) TEM micrographs of 4 cycles MDCFed alloy annealed at 350°C (c) SAED pattern corresponding to 4 cycles MDCFed alloy annealed at 300°C (d) SAED pattern corresponding to 4 cycles MDCFed alloy annealed at 350°C

5.2.3.2 Tensile Properties

True stress-strain curve for all processed condition is shown in Fig. 5.2.9. The yield strength (YS) as well as tensile strength (TS) of cryoforged Al 2014 was observed to be 396 MPa and 497 MPa respectively.
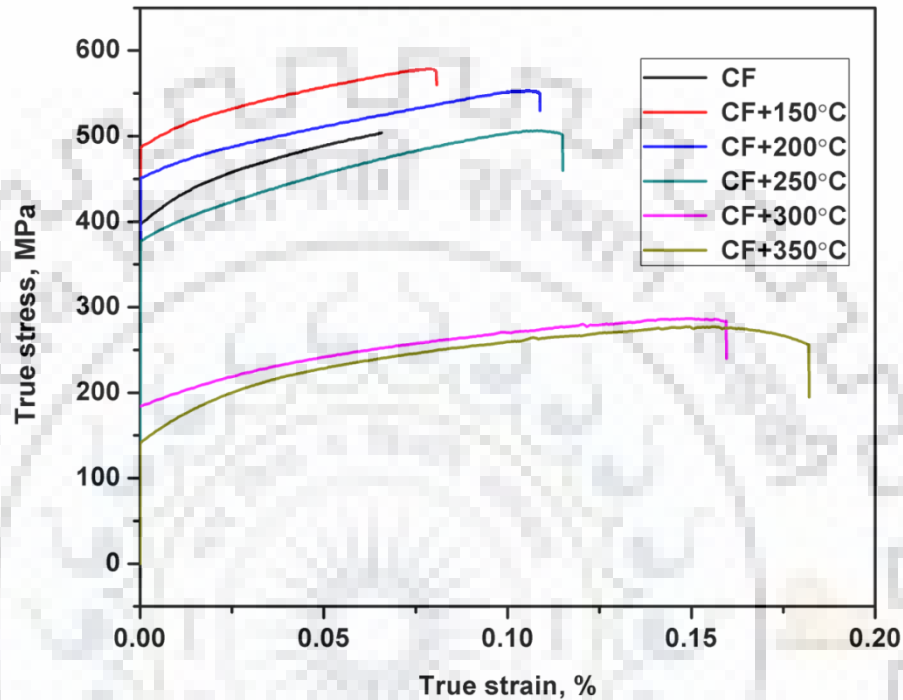
Figure 5.2.9: True stress vs True strain curves for MDCFed and MDCFed followed by annealed alloy at various temperatures

This is expected due to the Hall – Petch extrapolation after grain size reduction for MDCFed samples. These properties YS and UTS are further improved to 486 MPa and 579 MPa, respectively at annealing condition of 150°C. At annealing condition of 200°C, the yield and tensile strength are slightly decreasing to 450 MPa and 558, MPa respectively. With further increase in annealing temperature up to 250°C, the fall in yield strength (376 MPa) and tensile strength (505 MPa) is observed. At the annealing temperature of 300°C and 350°C, huge drop in yield strength (YS) and ultimate tensile strength (UTS) is observed. At 300°C, yield strength (YS) and tensile strength (UTS) has decreased to 183 MPa and 280 MPa, respectively, while these values become 140 MPa and 270 MPa on annealing at 350°C as noticed from Fig. 5.2.9.

The total % elongation of MDCFed Al 2014 alloy was observed to 6.7%. With increasing annealing temperature up to 250°C, the gradual increase in % elongation was observed and

204

reaches up to 11.4 %. The significant increase in % elongation was observed when MDCFed samples were annealed at 300°C (15.9%) and 350^{0}C (18.1%).

5.2.3.3 XRD Studies

The XRD results of MDCFed and MDCFed followed by annealed conditions are shown in Fig. 5.2.10 (a).
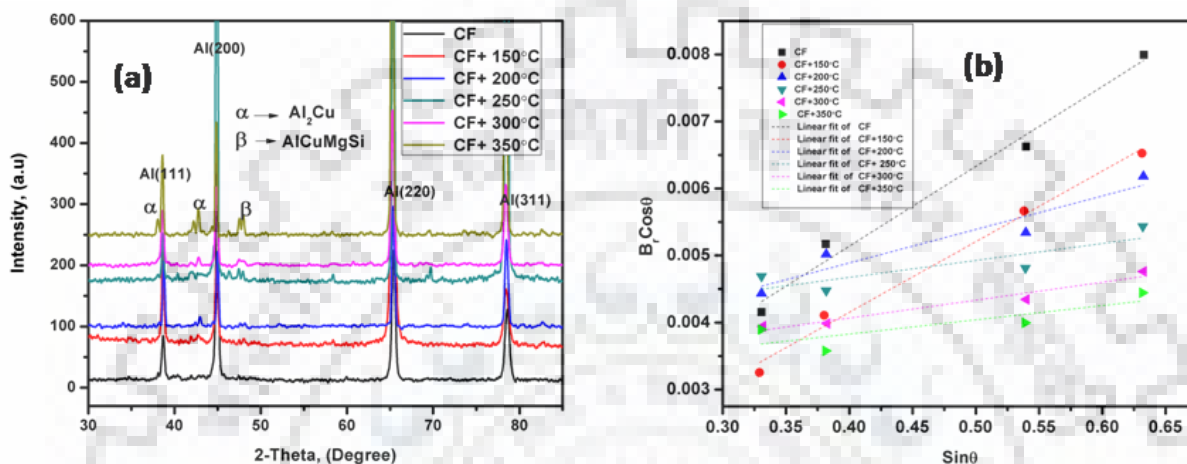
Figure 5.2.10: (a) XRD plot for MDCFed and MDCFed followed by annealed alloy at various temperatures (b) Williamson- Hall linear fit curves for MDCFed alloy for various processed conditions

XRD result of MDCFed Al 2014 alloy does not show any well defined peak which means after the solution treatment, solutes still remain inside the aluminum (Al) matrix. The peak pertaining to Al_2Cu phase is observed at the annealing condition of 150°C. However, its intensity observed is very less. This peak of Al_2Cu phase is observed in all annealing conditions with increasing annealing temperature from 150°C to 350°C. However, its intensity gradually increases up to 200°C. At 250°C, intensity of the peak corresponding to Al_2Cu phase slightly decreases, while new AlCuMgSi phase is also observed. With further annealing at 300°C, the peak intensity pertaining to Al_2Cu phase is further increased while peak intensity of AlCuMgSi phase is decreased. At 350°C, the intensity of both peaks, Al_2Cu and AlCuMgSi is increased as observed from Fig. 5.2.10(a). It is noted that intensity of second phase precipitates peak varies with various annealing temperature, which substantiates the complex precipitation behavior of MDCFed alloy at various annealing temperatures.

XRD data has also been used for evaluating the crystallite size 'd' and microstrain 'ε' of the processed samples using the Williamson-Hall method as per the following equation [5.69].

$$Bcos\theta_B = \frac{k\lambda}{d} + \varepsilon sin\theta_B \qquad\qquad (5.4)$$

Where λ is wavelength of Cu K$_\alpha$ radiation, which is 1.54A, k is constant and its value is 0.9, ε is microstrain, and θ_B is the Bragg angle [5.69]. The straight line is plotted between $Bcos\theta_B$ and $sin\theta_B$ by performing linear regression and values of crystallite size 'd' and microstrain 'ε' is calculated by measuring the slope and intercept of linear fit curves for various processed condition. Linear fit curve for various conditions is shown in Fig. 5.2.10 (b) in this work. The values of crystallite size 'd' and microstrain 'ε' for various processing condition is listed in Table 5.2.1. From the Table 5.2.1 it is clear that dislocation density and microstrain were observed to be maximum for MDCFed sample while with increasing annealing temperature from 150°C to 350°C these values decreases significantly.

Table 5.2.1: Estimation of Dislocation density, crystallite size and microstrain for various processing conditions

Processing condition	Dislocation density(m^{-2})	Crystallite size(nm)	Lattice microstrain
CF	4.32 X 10^{14}	140	.0053
CF+150^{0}C	2.76 X 10^{14}	175	.0041
CF+200^{0}C	2.59 X 10^{14}	142	.0035
CF+250^{0}C	2.01 X 10^{14}	175	.0029
CF+300^{0}C	8.65 X 10^{13}	210	.0023
CF+350^{0}C	5.2 X 10^{13}	230	.0011

5.2.3.4 Fracture toughness

Grain refinement mechanisms have been extensively studied in last two decades for improving the properties in terms of yield strength, tensile strength and % elongation. It has been seen in earlier investigations of various researchers that monotonic strength is improved at the cost of ductility after grain size reduction in the ultrafine regimes. Work hardening ability of metals/alloys detoriates with decrease in grain size in the range of 100 nm - 1µm as reported in various published work [5.12, 5.38]. Besides the total elongation, fracture toughness has been identified as one of the most significant property which makes the materials to be used for damage tolerance applications. The research work related to fracture toughness of UFG alloy fabricated by SPD processes is very limited because most of the processes does not provide sufficient material quantity/volume to conduct fracture toughness tests based on ASTM standards to satisfy sample dimensions. ASTM standards to assuring sample dimensions for valid fracture toughness tests are based on two methods. (i) LEFM (linear elastic fracture mechanics (ii) EPFM (elastic plastic fracture mechanics). Requirement of the sample dimensions in LEFM is quite complicative however measurement is quite

simple. On the hand requirements in EPFM are somewhat relaxed but measurement is very difficult as compared to LEFM. The general criterion for differentiating the LEFM and EPFM is based on plastic zone size. Plastic zone size near the pre existing crack is very small in LEFM approach while it is spreaded in EPFM approach. Therefore there must be some methods which accounts for close approximate of fracture toughness in UFG alloy processed by SPD methods due to limitation of sample dimensions obtained by these processes
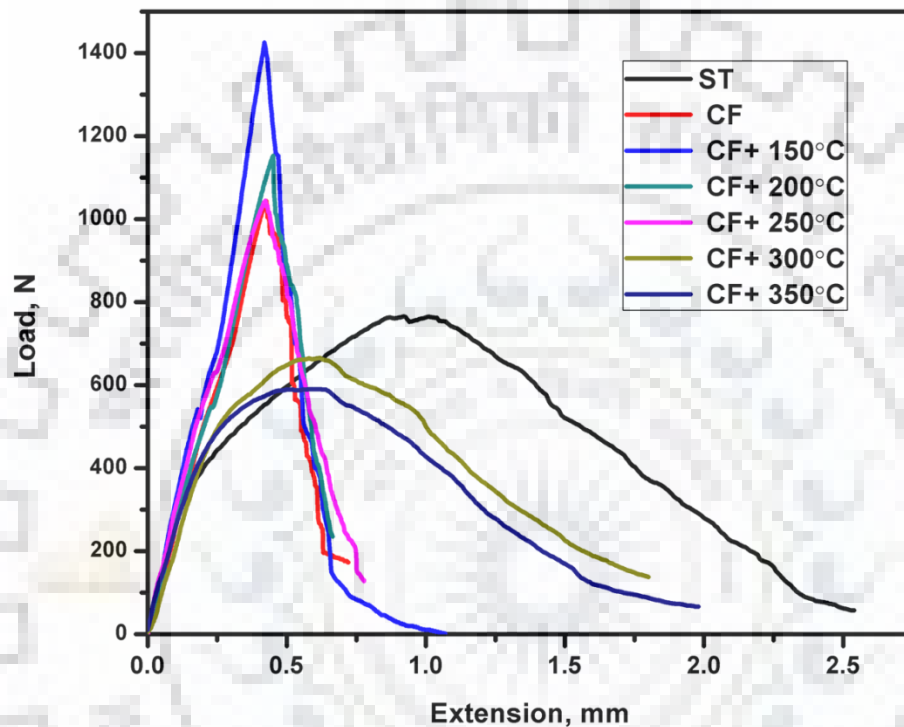
Figure 5.2.11: Load vs Extension curves after 3 point bend test for MDCFed alloy for various processed conditions

Various fracture toughness parameters have been evaluated for MDCFed and MDCF followed by annealed Al 2014 at various annealing temperature starting from 150°C to 350°C in the present work. The fracture parameters which are evaluated in the present work are given in following sections. 3-point bend specimens are machined from the center part of MDCFed and followed by annealed samples along the longest dimension as described in our earlier work [5.62] and discussed in Chapter 3/4. The small sizes of 3-point bend specimens are prepared following the ASTM 399 standard. The load extension curve for various processed condition after 3-point bend test is shown in Fig. 5.2.11.

5.2.3.4.1 Apparent fracture toughness (K_Q)

This fracture toughness parameter is used in linear elastic fracture mechanics (LEFM). In LEFM, crack tip is subjected to nearly plain strain condition with very small

207

plastic zone. Since tests are conducted in UTM (universal tensile testing machine), pre crack is developed by wire electric discharge machining (WEDM). A continuous measurement of load and extension of crack is recorded during the test. The detailed procedure for conducting the plain strain fracture toughness test has been discussed in Chapter 3 and our earlier published work [5.62]. However, the following two criterion must be satisfied for valid plain fracture toughness testing.

$$(i) \qquad \frac{P_{max}}{P_Q} \leq 1.10 \qquad\qquad\qquad (5.5)$$

$$(ii) \qquad a, B \geq 2.5 \left(\frac{K_Q}{\sigma_{ys}}\right) \qquad\qquad\qquad (5.6)$$

Where P_{max} = Maximum load, P_Q = Provisional load measured from 5% secant line, a = crack length, B = thickness of 3-point bend sample. The fracture toughness is measured from the following equation [5.71].

$$K_Q = \frac{P_{max}S}{BW^{\frac{3}{2}}} f\left(\frac{a}{W}\right) \qquad\qquad\qquad (5.7)$$

Where S = span length of 3-point bend sample, W = width of sample, $f\left(\frac{a}{W}\right)$ = function of $\left(\frac{a}{W}\right)$ for 3-point bend specimen as discussed in literature [5.71] . If above equations (5.5) and (5.6) are satisfied, the test is valid and K_Q measured from equation (5.7) is called plain strain fracture toughness (K_{IC}), otherwise it is called apparent fracture toughness K_Q. For small size MDCFed SENB samples, equation (5.5) and (5.6) are   not satisfied for all processed samples in this work, therefore, apparent fracture toughness (K_Q) is reported in this work. The variation of apparent fracture toughness (K_Q) with respect to different processing condition is shown in Fig. 5.2.12(a).

5.2.3.4.2   Equivalent energy fracture toughness (K_{ee})

It is well known that plain strain fracture toughness K_{IC} requires larger sample size to satisfy plain strain condition near crack tip. UFG materials produced by SPD methods are small in size due to which valid fracture toughness test is not possible in such metals/alloys. Equivalent energy methods are alternative methods for evaluating fracture toughness of small size specimen. The method is proposed by Witt which relates the fracture in larger size specimen with the geometrical similar small size model [5.47,5.72]. Lai [5.73] reported that fracture parameters of larger samples can be modeled by extrapolation of test data of small size specimen using equivalent energy method.
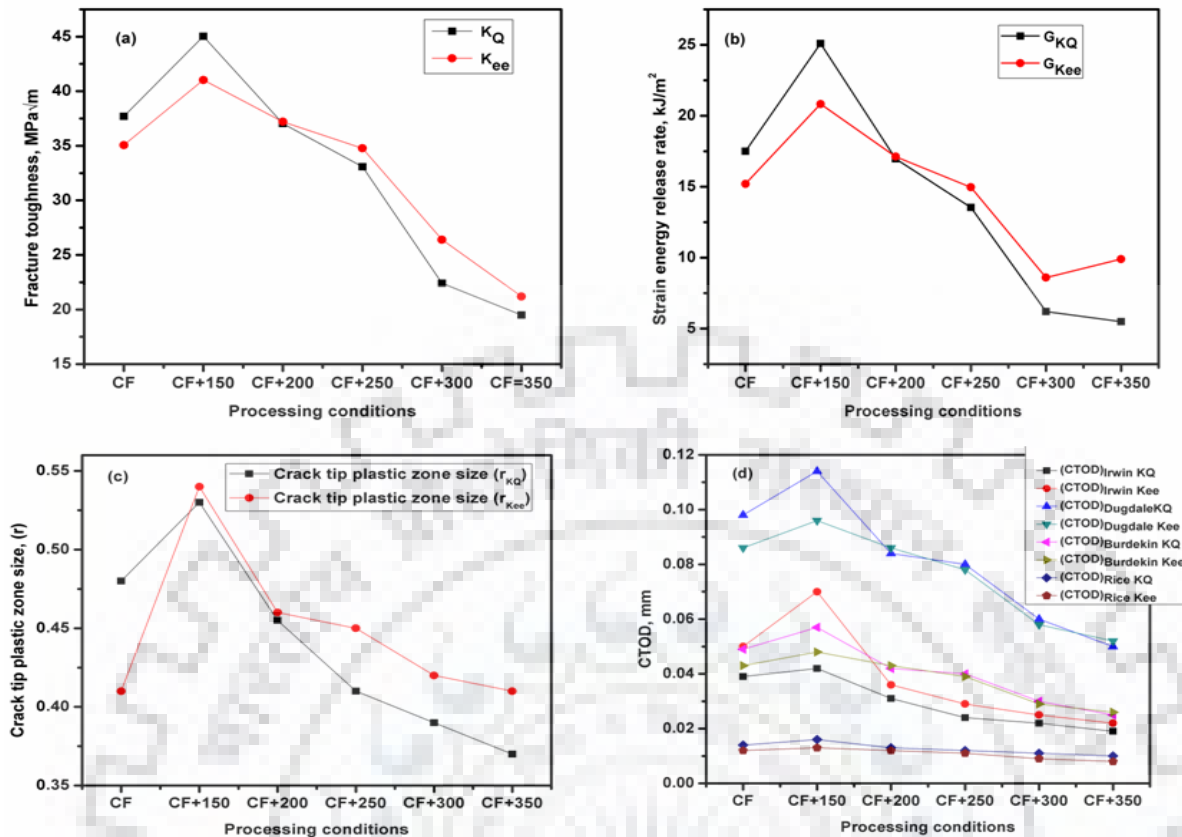
Figure 5.2.12: Variation of fracture toughness parameters for various processing conditions; (a) variation of apparent and equivalent energy fracture toughness; (b) variation of strain energy release rate; (c) variation of crack tip plastic zone size ; (d) variation of crack tip opening displacement (CTOD)

He reported that fracture toughness determined by energy method overestimate the fracture toughness that is measured by adopting the ASTM standards. Volumetric energy is the critical factor which is to be determined first for measuring the fracture toughness through this method as reported in literature. Area under the load-extension curve up to the maximum load in load-extension curve is termed as volumetric energy. Fracture toughness is obtained by dividing the volumetric energy ratio up to the maximum load to the volumetric energy ratio up to linear part of the curve. Lai [5.73] compared the fracture toughness of comsteel En 25 by two methods i.e ASTM standard 399 and equivalent energy method and found that K_{ee} overestimate the K_{IC} by 6% to 22%. Thus this method can be useful for severely deformed materials where it is very difficult to obtain larger size samples. On the basis of this we have attempted to evaluate the fracture toughness of MDCFed and MDCFed followed by annealed alloy by equivalent energy method. Detail procedure of finding the fracture toughness is discussed in our earlier published work [5.72] and discussed in Chapter 4.

Following equation has been used for finding the equivalent energy fracture toughness as reported in literature [5.72].

$$P_E = P_L \sqrt{\frac{A_T}{A_L}} \qquad (5.8)$$

$$K_{ee} = \frac{P_E}{B} \frac{S}{W^{3/2}} \, f(a/w) \qquad (5.9)$$

Where P_E = Equivalent load, P_L = Maximum load up to linear part, A_T = Area under the load-extension curve up to maximum load, K_{ee} = Equivalent energy fracture toughness, Other variables are same as in case of ASTM standard (5.50).
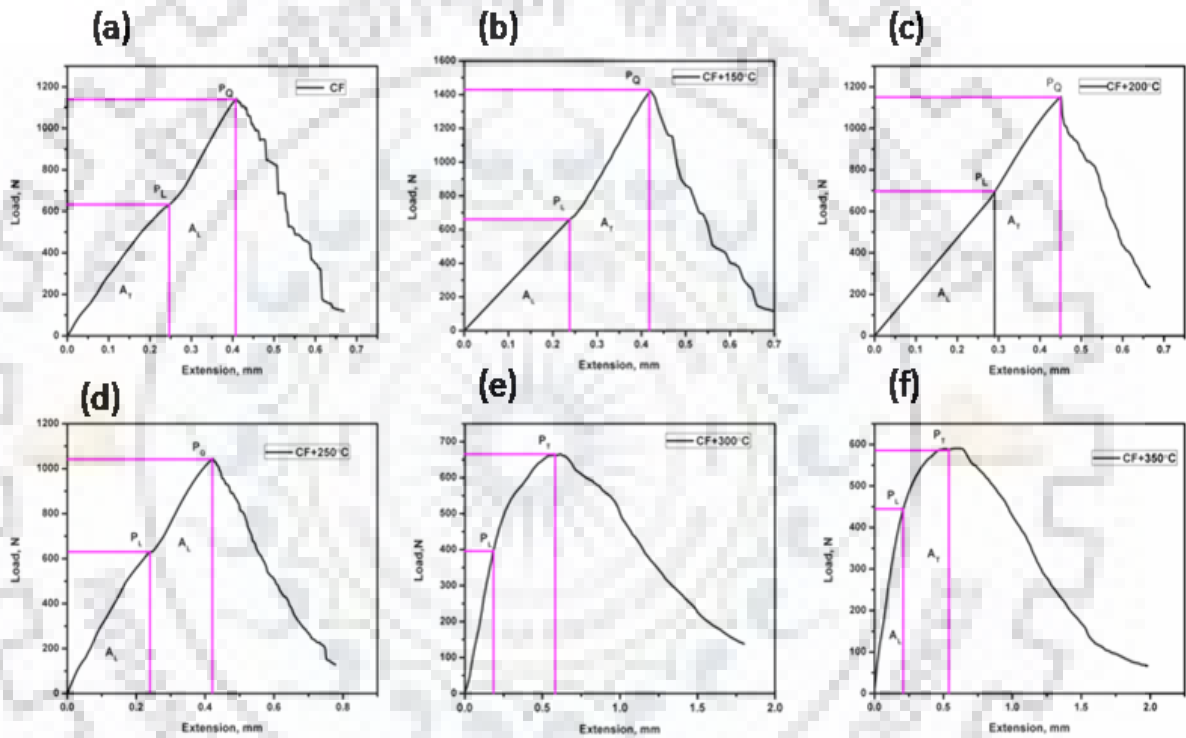
Figure 5.2.13: Evaluation of Equivalent energy fracture toughness (K_{ee}) for various processing conditions

The variation of equivalent energy fracture toughness K_{ee} with respect to various processing condition is shown in Fig. 5.2.12(a). The procedure for finding the equivalent energy fracture toughness of various processed sample condition in this work is shown in **Fig. 5.2.13**.

5.2.3.4.3 Strain energy release rate (G_I)

Strain energy release rate (G_I) is another fracture toughness parameter, which is widely used in linear elastic fracture mechanics (LEFM) [5.74]. It provides the material resistance to crack extension and represent the crack driving force. Strain energy release rate

equation is derived by Irwin and Orowan by modifying the Griffith's elastic surface energy equation by imposing a condition of plastic strain work near the crack tip. There is definite relationship between the strain energy release rate (G_I) and stress intensity factor (K_I) in LEFM as reported in the literature [5.71].

$$G_I = \frac{K_I{}^2}{E'} \qquad (5.10)$$

Where G_I = strain energy release rate, K_I = stress intensity factor, E' = modulus of elasticity and its value is $E' = \frac{E}{1-v^2}$ (in plain strain condition) while $E' = E$ in plain stress condition. Fracture toughness in terms of strain energy release rate (G_I) is represented by critical strain energy release rate (G_{IC}). The crack will move rapidly when $G_I \geq G_{IC}$. Based on above discussions, strain energy release rate has been calculated for various processed conditions in this work. For evaluating the critical strain energy release rate (G_{IC}), the values of apparent fracture toughness (K_Q) and equivalent energy fracture toughness (K_{ee}) has been used in equation (5.10) by assuming the plain strain condition near crack tip. Strain energy release rate obtained from apparent fracture toughness is denoted by G_{KQ} while strain energy release rate obtained from equivalent energy fracture toughness is represented by G_{Kee} in this work. Poisson's ratio (v) and modulus of elasticity for Al 2014 alloy is taken as 0.33 and 72 GPa as reported in literature [5.74]. Fig. 5.2.12(b) shows the variation of strain energy release rate (G) for various processed conditions.

5.2.3.4.4 Crack tip plastic zone size (r):

LEFM approach presumes that crack tip is subjected to infinite stress due to elastic nature. But inelastic deformation near the crack tip imparts the plasticity in the vicinity of crack tip due to yielding phenomenon associated around the crack tip [5.64, 5.71]. Consequently plastic zone is formed near the crack tip which contains defects, dislocation, or microvoids [5.24]. It can be said linear elastic fracture mechanics (LEFM) does not predicts the actual material behavior near the crack tip. Plastic zone size determines crack tip plasticity which further is utilized in predicting whether the existing crack will blunt or become sharper. If the crack tip becomes blunt the crack will propagate slowly while if it becomes sharp, crack will move rapidly resulting unstable failure. It may be mentioned that more the crack tip plastic zone more will be the crack tip plasticity and crack propagation will be retarded while crack propagation will be accelerated if plastic zone size is reduced.

Therefore we have tried to calculate crack tip plastic zone for different process conditions for MDCFed Al 2014 alloy by using preexisting Irwin's theoretical model as shown in Fig. 5.2.14(a). The distance r_1 in the Fig. 5.2.14(a) is the Irwin's plastic zone correction which is obtained by extending crack artificially up to r_1 distance. Plastic zone size r has been evaluated by using the Irwin's equation as described in literatures [5.50, 5.65, 5.71] which is given as

$$ r = \frac{1}{2\pi}\left(\frac{K_I}{\lambda\sigma_{ys}}\right)^2 \tag{5.11} $$

Where r = distance of crack tip plastic zone, K_1 = Plain strain fracture toughness, λ = constant known as Irwin's yielding factor and its value is 1 for plane stress problems while $\sqrt{3}$ for plain strain problems. Crack tip plastic zone r has been calculated by using the K_Q and K_{ee} in equation (5.11) for assuming plain strain condition. The trend of variation of crack tip plastic zone size with respect to various processing condition is shown in Fig. 5.2.12(c).
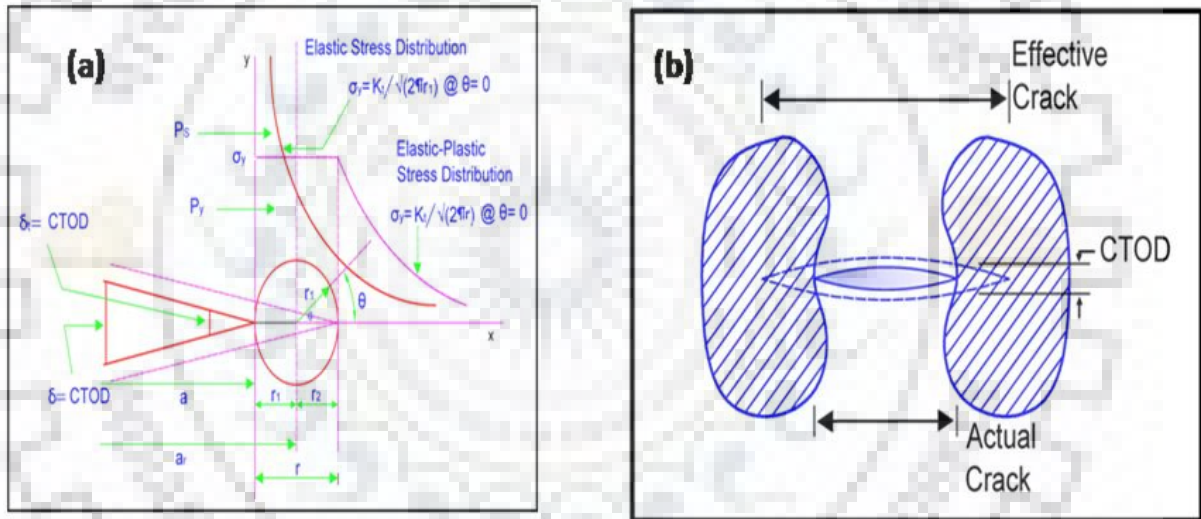
Figure 5.2.14: (a) Irwin's model showing the crack tip plastic zone near crack tip ; **(b)** illustration of crack tip opening displacement (CTOD)

5.2.3.4.5 Crack tip opening distance (CTOD):

Crack tip opening displacement (CTOD) is another fracture toughness parameter devised by Wells and Cottrell, which is used for characterizing crack in both LEFM and EPFM [5.50, 5.65, 5.71]. Crack tip opening displacement (CTOD) is an opening of effective crack which accounts the stress field and yielding in the vicinity of crack tip. Effective crack is longer than the actual crack as shown in Fig. 5.2.14(b). From this figure it is clear that an effective crack has some definite opening at the place of the actual crack tip which is called crack tip opening displacement (CTOD). CTOD determines the plasticity of the crack tip.

More the CTOD value more will be the crack tip plasticity and therefore crack propagation period. Based on this, experimental data is analyzed for evaluating crack tip opening displacement in the present work. The following models have been used to calculate crack tip opening displacement (CTOD) as described in literatures [5.50, 5.65, 5.71]

$$CTOD = \frac{4K_I{}^2}{\pi \lambda E \sigma_{ys}} \qquad \text{(Irwin's model)} \qquad (5.12)$$

$$CTOD = \frac{2K_I{}^2}{E \sigma_{ys}} \qquad \text{(Dugdale's model)} \qquad (5.13)$$

$$CTOD = \frac{K_I{}^2}{E \sigma_{ys}} \qquad \text{(Burdekin's model)} \qquad (5.14)$$

$$CTOD = \frac{(k+1)(1+v)K_I{}^2}{4\pi E \sigma_{ys}} \qquad \text{(Rice model)} \qquad (5.15)$$

Where symbols have usual meaning as defined earlier. However $k = 3 - 4v$ for the plain strain, while its value is $\frac{3-v}{1+v}$ for the plane stress condition. It is important to note that K_Q and K_{ee} is used in place of K_I for determining crack tip opening displacement (CTOD) from above equations. Fig. 5.2.12(d) shows the variation of CTOD with respect to various processed condition in the present work.

5.2.4 Discussions

5.2.4.1 Grain refinement mechanism

Grain refinement mechanism of multidirectional forging (MDF) has been well developed in the earlier published work [5.12, 5.18]. It is reported that continuous dynamic recrystallisation is main UFG formation mechanism in mutidirectionally forged (MDFed) metals/alloys [5.53,5.57]. Multidirectional forging at cryogenic temperature leads to huge increase in the dislocation density of Al 2014 alloy due to accumulation of large plastic strain in the sample. Cryogenic temperature reduces the mobility of dislocation by suppressing the dislocation cross slip and climb in high stacking fault energy (SFE) metals. The plastic strain induces the intense shear flow in metal in the form of deformation bands/shear bands. These shear bands are known as microshear bands (MSBs). From Section 5.1 it was observed that at low strain (up to 2 cycles) microshear bands (MSBs) are oriented along one direction with the evolution of low angle grain boundaries (LAGBs). Low angle boundaries (LAGBs) at low strain are formed due to inhomogenity of plastic flow in MDCFed samples, which are in the form of geometrical necessary boundaries (GNBs) and incidental grain boundaries (IDBs) [5.12, 5.55]. Due to change in strain path in MDCF procedure, shear gradient is not uniform in each part of sample. GNBs accommodate the inhomogenity in shear gradient in various part of

213

sample due to inhomogeneous plastic deformation [5.56]. IDBs are formed due to random trapping of accumulated dislocations during the more homogeneous plastic deformation. When plastic strain is increased, the density of microshear bands (MSBs) is increased and they are observed to intersect with each other and divide the original grain in to fine grains as observed in optical and TEM micrographs of 4-cycle MDCFed sample in this work. In addition to this, low angle boundaries (LAGBs) which are evolved at low strain (2 cycles, 3 cycles) are transformed in to high angle boundaries (HAGBs) at high strain sample (4 cycles MDCFed) sample. This is the basic mechanism of ultrafine grain formation in multidirectional cryo forging (MDCF). This mechanism has been reported as intersection of microshear bands (IMSD), which is shown in Fig. 5.2.15.
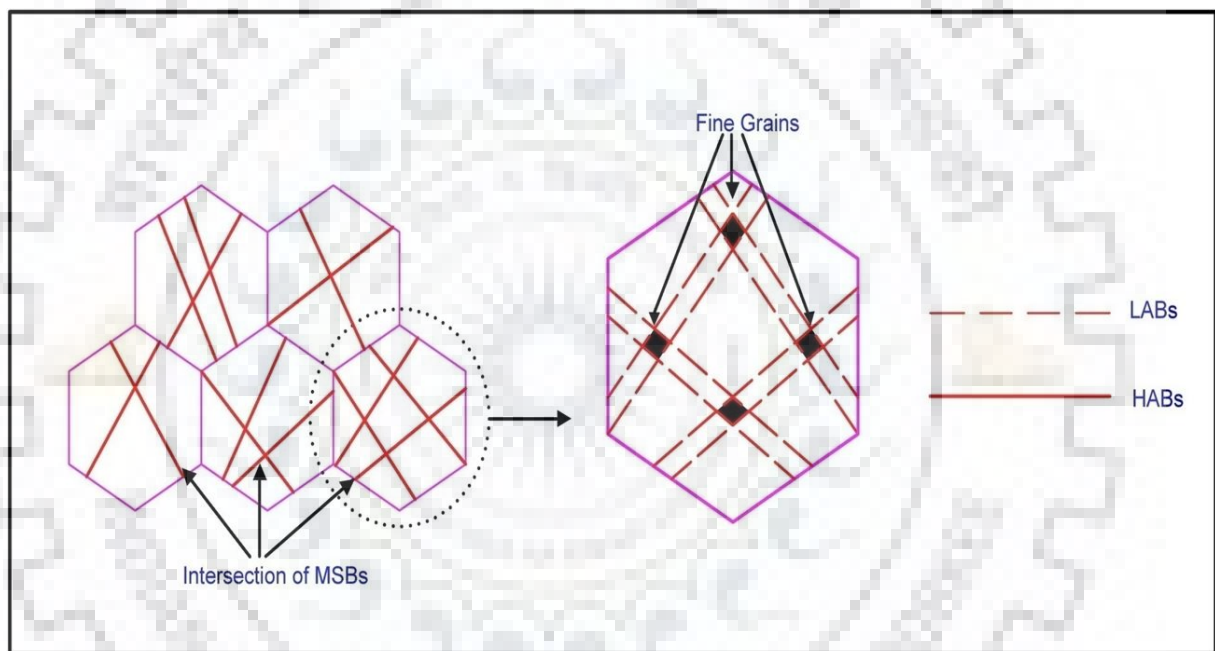
Figure 5.2.15: Mechanism showing the grain refinement in MDF

5.2.4.2   Factors Affecting strength

Effect of multidirectional cryoforging (MDCF) and subsequent annealing at various temperatures on tensile and yield strength has been investigated by performing tensile test in the present work. Variation of mechanical properties is shown in Fig. 5.2.9. It is observed that strength of MDCFed Al 2014 alloy is affected by accumulation of large number of dislocations and grain size reduction due to intense severe deformation. The yield strength of MDCFed Al 2014 alloy after 4 cycles is recorded as 396 MPa. The same alloy shows the yield strength of 176 MPa at solution treated (ST) condition. The significant rise in yield strength of the MDCFed alloy is attributed to (i) increase in dislocation density due to effective

suppression of dislocation mobility at cryogenic temperature. (ii) grain size reduction well below 1µm leading to grain boundary strengthening as described by Hall-Petch equation. After annealing at various temperatures, various types of precipitates are evolved that imparts additional strengthening to the MDCFed Al 2014. It may be mentioned that along with dislocation and grain boundary strengthening, the mechanical properties of annealed UFG alloy are influenced by precipitation hardening. On annealing at 150°C, fine spherical phase is observed in TEM micrographs of this condition. This phase is confirmed as semicoherent θ' phase that has a composition of Al_2Cu from XRD results. Similar phase is identified by Dhal et al [5.50] during annealing of Al 2014 alloy. Tensile and yield strength are significantly improved at this temperature, which is quite erratic trend by assuming the fact that these properties should be reduced at high temperature due to reduction in dislocation annihilation and slight recovery of microstructure as seen from TEM micrographs. However, these properties are significantly improved due to the obstruction of dislocation motion by these fine and semi coherent precipitates. With further annealing at 200°C, the slight drop in yield and tensile strength is observed. The dislocations along the shear bands are annihilating and some of the elongated subgrains are also seen away from the shear bands. However, these grains are not fully recrystallised as evident from the TEM micrographs at this condition. The spherical semi coherent precipitates which are evolved at 150°C, were also observed on annealing at 200°C with slight increase in size of spherical phase θ' as compared to sample annealed at previous conditions. It may be mentioned that due to annihilation of dislocation and slight coarsening of fine spherical semi coherent θ' phase, the observed strength is less at this temperature. On annealing at 250°C, the significant drop in yield strength is observed. Moreover, the nucleation of fine needle phase with very few slightly coarser spherical phase is observed from the corresponding TEM micrographs at this condition. This phase has been reported as semicoherent fine needle phase λ' in various earlier published literature [5.58, 5.72]. The composition of this phase is confirmed as AlCuMgSi as discussed in XRD results. The dislocation density along the shear bands has also significantly reduced due to high annealing temperature. It is seen in our earlier work [5.72] that hardening effect of needle phase is less as compared to fine spherical phase in this alloy. In addition to this, coherency of the precipitate is closely related to size and fineness of the precipitates as reported in the literature [5.72]. Lesser the size, higher will be the coherency and thereby strengthening effect. It is expected that at this annealing conditions, the spherical precipitates which are very fine at

150^0C might become slightly coarse and its volume fraction is also less as compared to needle phase at this condition. It may be illustrated that significant drop in dislocation density and evolution of slightly coarser spherical precipitate along with large number of fine needle phase at annealing condition of 250°C may give rise to the significant drop in tensile and yield strength at this condition. At the annealing condition of 300°C and 350°C, drastic decrease in tensile and yield strength was observed.TEM micrographs at these temperatures shows the evolution of coarser stable spherical phase θ and coarser stable rod phase λ along with dislocation free recrystallized grain sizes in the range of 500 nm- 1μm. Apart from this, dislocation density has significantly dropped at this condition. It is reported that in bigger/coarser particles, crack can easily penetrate, causing significant drop in the yield and tensile strength observed at these temperatures [5.24].

5.2.4.3 Work hardening response

Ductility and strain hardening response are the most important parameters for the operation like superplastic forming, and shaping processes for avoiding the sudden fracture in high load carrying application [5.76]. This information is very crucial for the UFG metals/alloy, which shows very limited tensile elongation to the failure due to which its application is limited in such sectors. Multidirectional cryoforged (MDCFed) Al 2014 alloy has shown the high strength (497MPa) after 4 cycles with limited % elongation of 6.7% in this work. Ma [5.76] and Dhal et al [5.24] reported the reasons for low tensile ductility of ultrafine grained metals/alloy. They reported that possible low tensile ductility might be due to processing flaw and artifacts, instability of crack nucleation and growth, and inability to accumulate extra dislocations due to fine grains [5.24, 5.76]. The similar reasons might account for the low tensile ductility of MDCFed Al 2014 alloy as the non equilibrium microstructure is not able to store large number of dislocation during the deformation. Early fracture in MDCFed Al 2014 alloy might be promoted by localized plastic deformation, which facilitates plastic instability in the form of catastrophic shear banding. To improve its tensile elongation and work hardening response, MDCFed Al 2014 alloy is annealed at various temperatures ranging from 100°C 350°C. However, due to the precipitation of various phases during annealing, its work hardening behavior is not straight forward as in case of non heat treatable Al alloys as combined recovery, recrystallisation along with precipitation is accompanied during annealing of this alloy. Therefore, true stress −strain curve is analysed by Hollomon's fitting equation [5.24]. In this equation, true stress and strain is expressed in the

216

form of power law and work hardening exponent is evaluated to measure the work hardening ability of metals/alloys.

Holloman's equation [5.24] is expressed as

$$\sigma = K_h \, \varepsilon^{n_h} \qquad\qquad (5.16)$$

Where K_h = Strength index measured from Hollomon's equation, n_h = Strain hardening index, σ, ε are the true stress and true strain, respectively.

Logarithmic form of above equation is

$$ln(\sigma) = ln(K_h) + n_h \, ln(\varepsilon) \qquad\qquad (5.17)$$

In a $ln(\sigma)$- $ln(\varepsilon)$ curve for above equation (5.17), n_h is the slope of curve, which is a measure of extent of strain hardening for metals/alloys. Fig. 5.2.16(a) shows the linear regression curves fitted as per the Hollomon's equation for MDCFed and MDCFed followed by annealed Al 2014 alloy for various processed condition. Strain hardening exponent using Hollomon's fit for various conditions are listed in Table. 5.2.2.

Modified differential Crussurd- Joul analysis has also been done which is based on swift stress-strain relation as expressed by following equation and reported in literature [5.24]

$$\varepsilon = \varepsilon_o + K_s \sigma^m \qquad\qquad (5.18)$$

Differential form of above equation is known as modified Crussard-Joul equation and represented by

$$ln\left(\frac{d\sigma}{d\varepsilon}\right) = (1 - m)ln(\sigma) + ln(K_s m) \qquad\qquad (5.19)$$

The slope of logarithmic plot between $\left(ln\left(\frac{d\sigma}{d\varepsilon}\right) \; vs \; ln(\sigma)\right)$ is $(1 - m)$. Strain hardening exponent m has been calculated by evaluating $(1 - m)$ for various processed condition using Modified Crussurd –Joul fit and shown in Fig.5.2.16(b).
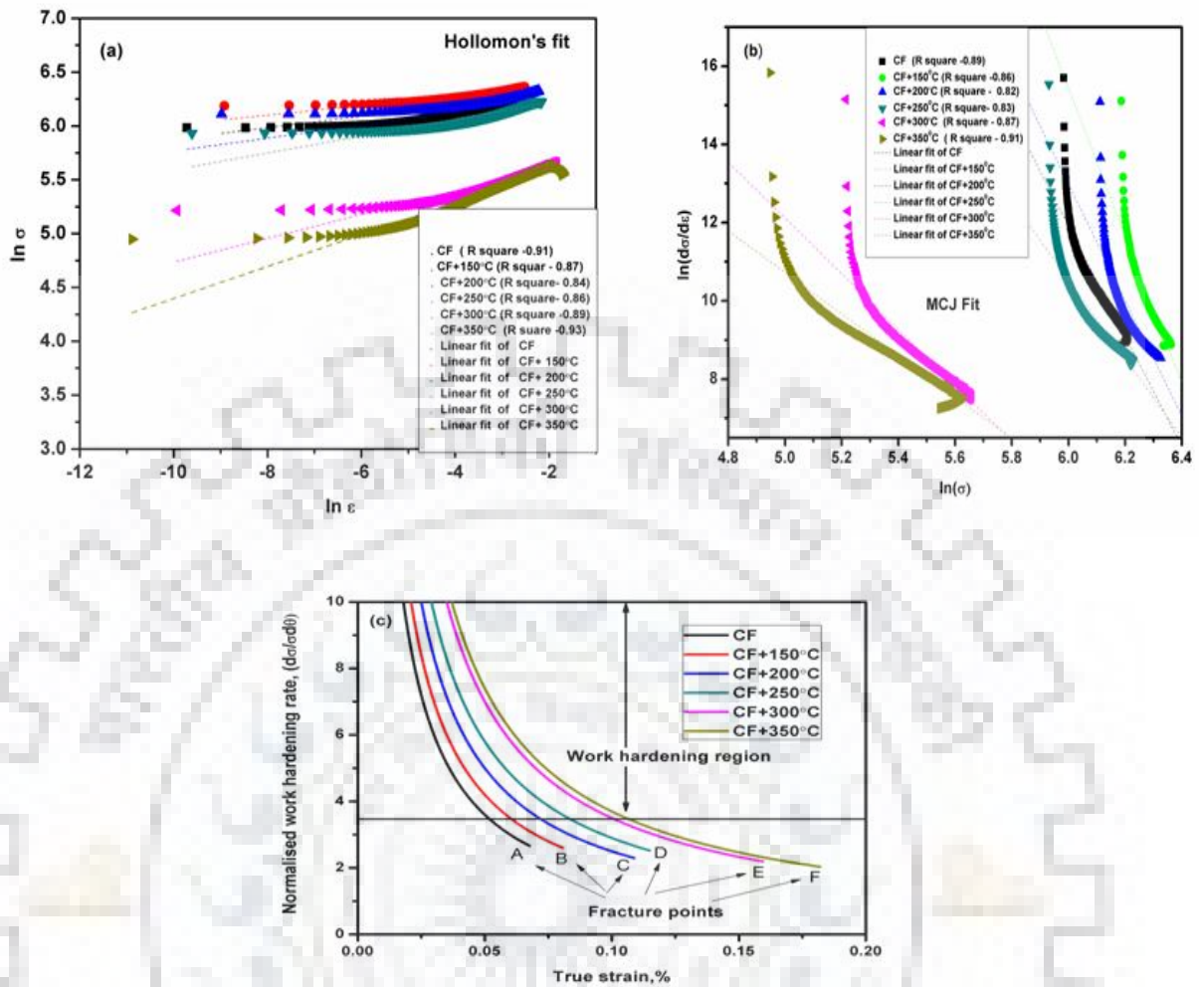
Figure 5.2.16: Evaluation of strain hardening exponent by (a) Hollomon's linear fitting curves; (b) Modified Crussurd Joul linear fitting curves; (c) Variation of normalized work hardening rate with respect to true strain for various processing conditions

Table 5.2.2: Values of strain hardening exponents using Hollomon's fit and modified Crussurd –Joul fit

Strain hardening exponants	CF	CF+150°C	CF+200°C	CF+250°C	CF+300°C	CF+350°C
Hollomon's fit/ m	.03	.05	.06	.07	.11	.14
Modified crussurd joul fit/ m	2.05	3.23	5.01	7.04	11.01	14.12

218

In the present investigation it was observed that trend of variation of strain hardening coefficient with respect to various annealing condition was same in both methods as seen from Table. 5.2.2. For multidirectional cryoforged (MDCFed) Al 2014 alloy, low value of m was observed. Gradual increase in strain hardening coefficient m was observed up to annealing temperature of 250°C while drastic improvement in strain hardening coefficient was observed beyond 250°C up to 350°C.

Normalised strain hardening rate (θ) has also been calculated for various processing conditions, which is expressed by following equation as reported in the various literature [5.24, 5.77].

$$\theta = \frac{1}{\sigma}\left(\frac{d\sigma}{d\varepsilon}\right) \tag{5.20}$$

Curve between normalized strain hardening rate and true strain has been plotted in Fig. 5.2.16(c). From these curves, it is evident that strain hardening rate (θ) is very small for MDCFed Al 2014 alloy. With further annealing from 150°C to 250°C, the curve shifts gradually to the right side, which means strain hardening rate has slightly improved. With annealing temperature of 300°C and 350°C, significant rise in strain hardening behavior is observed as compared to MDCFed Al 2014 alloy. The point A, B, C, D, E and F in Fig. 5.2.16(c) also suggest that fracture strain is also increasing with increasing annealing temperature. However, up to annealing of 250°C, the increase in strain hardening rate is slow, while above this temperature, strain hardening ability of material increases as seen from Fig. 5.2.16(c).

Based on above analysis performed by Hollmon's and Modified Crussurd - Joul methods, it may be mentioned that strain hardening response of multidirectional cryoforged (MDCFed) Al 2014 is very little. With further annealing at various temperatures, the strain hardening ability of material increases. MDCFed alloy shows a very low strain hardening ability due to presence of large numbers of mutually intersecting shear bands, which are precursor of crack initiation and provides catastrophic failure. In addition to this, grain size is very fine which can not store large amount of dislocation during cryoforging. When sample is annealed, slight recovery of microstructure begins and dislocations get annihilated due to which strain hardening response of bulk UFG alloy has increased. However, due to evolution of various phases during annealing, strain hardening response of material is gradually increased with slow pace at low annealing temperatures and sudden rise in strain hardening potential is observed at higher annealing temperatures. At first, fine spherical semicoherent phase is

evolved at temperature 150°C. This phase is coherent with the matrix and provides the additional sites for nucleation of extra dislocations during annealing. In addition to this, density of shear bands also decreased, resulting slight improvement in the strain hardening index. On annealing at 200°C, dislocation density is further reduced in the sample, while fine spherical phase is still observed but there volume fraction is observed more in this temperature. So, due to the recovery effect and large number of spherical fine phase, the nucleation sites for the dislocations increases, resulting further improvement in strain hardening response of MDCFed sample to some extent. With further annealing at 250°C, the fine needle phase λ' is observed with few coarser spherical θ phase due to dissolution of fine spherical θ' phase in the matrix. The shear bands are still seen but their density is significantly reduced at this temperature. The slight improvement in the strain hardening response of material might be due to the dislocation annihilation caused by recovery and fine needle phase λ', which provides additional nucleation sites for the dislocations. However, coarser spherical precipitate does not help in improving the strain hardening response because they are favorable sites of the crack initation. With further annealing at 300°C, fine spherical phase is completely dissolved and new stable spherical phase θ is evolved along with very few stable rod phase. The dislocation density is drastically decreased in the sample with evolution of dislocation free recrystallised grain, which is slightly bigger size as compared to previous conditions. The strain hardening response of material suddenly increases due to the formation of dislocation free recrystallized grain, which can accumulate large number of dislocations during deformation as reported in literature [5.26]. It is important to note that coarser stable precipitates do not contribute to the improvement in strain hardening ability. However, they promote early fracture due to their brittle nature but the rate of recrystallisation overcomes their effect and increases the strain hardening ability of material at this condition. The similar phenomenon is observed at the annealing condition of 350°C, where dislocations are completely annihilated with formation of dislocation free recrystalised grain along with stable and coarser θ and λ phases. These dislocation free grains whose size is slightly larger than the sample annealed at 300°C can accumulate more dislocations and raises the strain hardening ability of bulk UFG Al 2014 alloy up to maximum extent.

5.2.4.4 Macrographs and Fractographic observations after Tensile test

The macro-scale fracture surface of 4 cycles MDCFed and MDCFed with subsequent annealed samples after the tensile test is shown in Fig. 5.2.17.
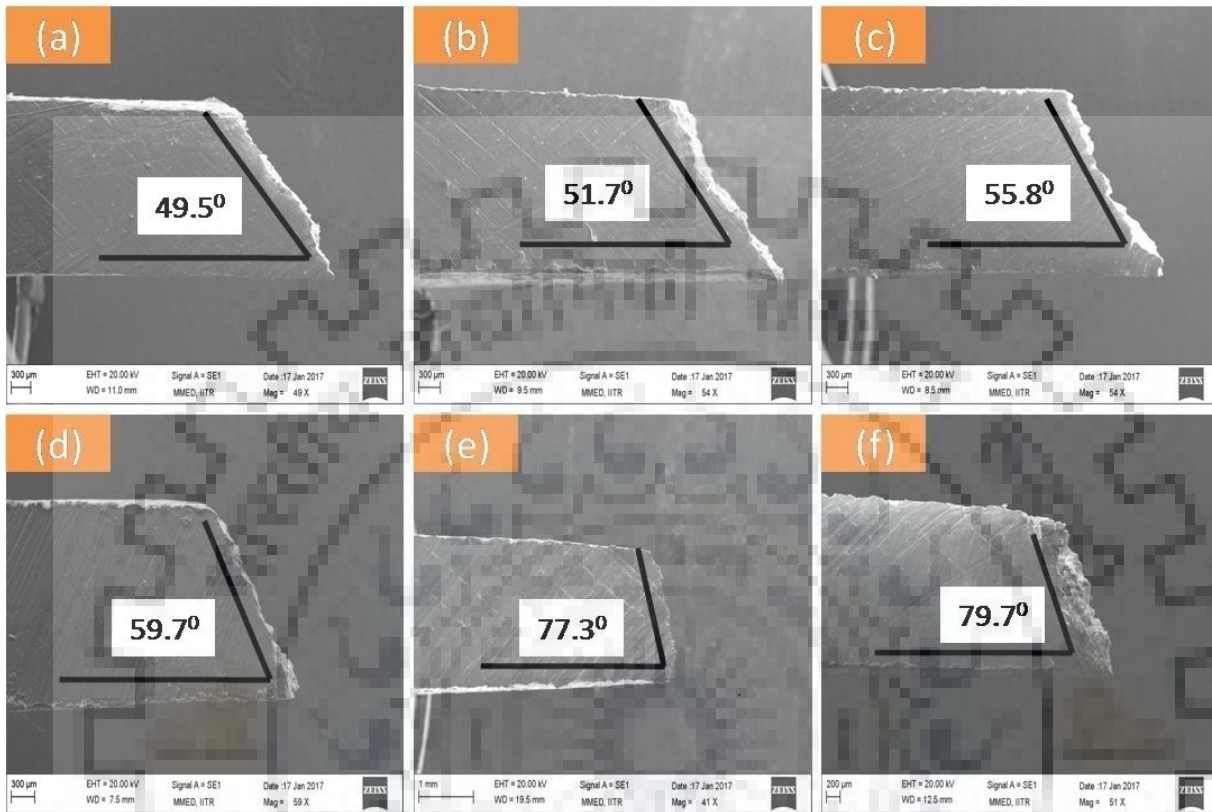
Figure 5.2.17: Macrographs showing the shear fracture angle for (a) MDCFed alloy; (b) MDCFed alloy annealed at 150°C; (c) MDCFed alloy annealed at 200°C; (d) MDCFed alloy annealed at 250°C; (e) MDCFed alloy annealed at 300°C; (f) MDCFed alloy annealed at 350°C

The post necking behavior of tensile tested fractured sample has been analysed by measuring the fracture angles for MDCFed and MDCFed followed by annealed alloy at various temperatures. After 4 cycles multidirectional cryoforging (MDCF), it is observed that the shear fracture plane makes an angle of 49.5° with respect to tensile loading direction as observed from Fig. 5.2.17(a). With increasing annealing temperatures from 150°C to 250°C, the gradual increase in the tensile shear fracture angles was observed and reached up to the 59.7° (Fig. 5.2.17(b)-(d)),while drastic increase in the tensile shear fracture angles (Fig. 5.2.17(e)-(f)) was seen for the temperatures 300°C (77.3°) and 350°C (79.7°). In fact, the trend of variation of tensile shear fracture angles was same in accordance with variation of strain hardening index with temperature in this work.

Fractographs of MDCFed samples and sample annealed at various temperatures starting from 150°C to 350°C are shown in Fig. 5.2.18.
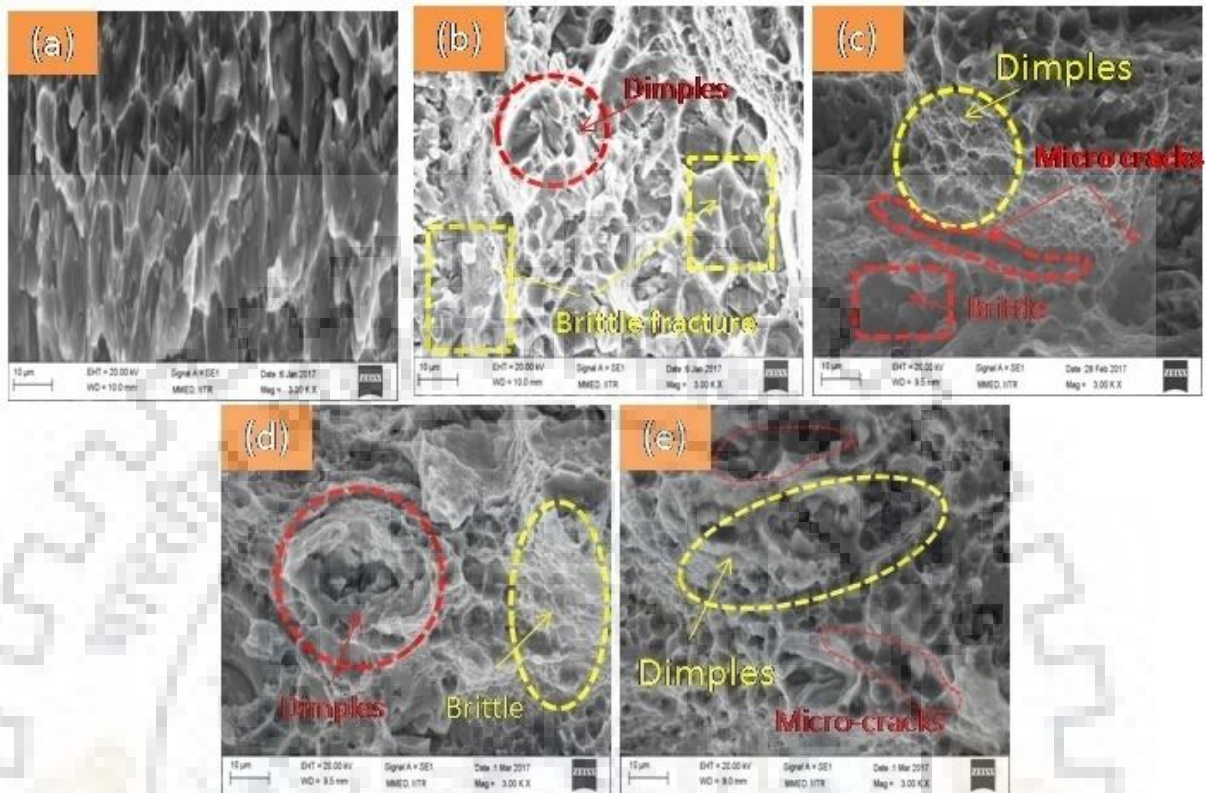
Figure 5.2.18: Fractographs after tensile test for (a) MDCFed alloy; (b) MDCFed alloy annealed at 150°C ; (c) MDCFed alloy annealed at 250°C; (d) MDCFed alloy annealed at 300°C; (e) MDCFed alloy annealed at 350°C

The fractograph of MDCFed sample after tensile test shows the sheared fracture surface as seen from Fig. 5.2.18(a). On annealing at 150°C, very few fine dimples (marked by red circle) can be observed, with majority of brittle surface (marked by yellow box) as seen from Fig. 5.2.18 (b). The similar fracture surface is observed for the annealing conditions 200°C and 250°C. However, volume fraction of dimples and its size has slightly increased up to temperature 250°C, which can be observed from the Fig. 5.2.18(c). The microcracks and brittle facets zone which are highlighted by red curves and red rectangular box can also be observed in Fig. 5.2.18(c) along with dimples for the sample annealed at 250°C. On annealing at 300°C and 350°C, the significant change in the fracture surface morphology is observed. The volume fraction of dimples has significantly increased in the sample at both temperatures with respect to previous conditions. Moreover, the dimples size has also increased with increasing annealing temperature from 300°C to 350°C and observed to be maximum for 350°C as seen from Fig. 5.2.18(d)-(e). In addition to this, along with dimpled features,

microcracks were also observed at both temperatures which substantiate that fracture process is not completely ductile, but mixed mode of fracture. It may be mentioned that fracture mode of MDCFed Al 2014 alloy was brittle while on annealing it, the fracture mode has transformed in to the quasi-cleavage (mix- mode) fracture. Moreover, at low annealing temperature up to 200°C, brittle fracture is dominant and the ductile fracture is dominant beyond this temperature.

5.2.4.5 Macroscopic Fracture Mechanism:

To understand tensile fracture mechanism of metals/alloys macroscopically, various failure theories have been well developed in the past. Some of important classical fracture theories are Maximum principal stress theory, Maximum shear stress theory (Tresca's theory), Mohr- coloumb theory, and Maximum distortion energy theory (Von-Mises theory) which are well reported in literature [5.78]. Maximum principal stress theory states that failure of the material will occur when maximum principal stress reaches a critical value of tensile stress obtained from simple tension test [5.78]. As per the Tresca's theory the failure will occur when maximum shear stress reaches a critical value of shear stress obtained from simple tension test. When a component is subjected to tensile stress σ_T, the normal stress σ and shear stress τ an any shear plane which makes an angle θ from the loading direction can be represented by the following equations as described in literature [5.78].

$$\sigma = \sigma_T \sin^2\theta \tag{5.21}$$

$$\tau = \sigma_T \sin\theta.\cos\theta \tag{5.22}$$

If σ_0 and τ_0 are the critical values of normal and shear stresses as obtained from tensile test , then the failure conditions as described by maximum principal stress and maximum shear stress (Tresca's theory) can be expressed mathematically by following equations.

$$\sigma_{max} \geq \sigma_0 \qquad \text{(Maximum principal stress theory)} \tag{5.23}$$

$$\tau_{max} \geq \tau_0 \qquad \text{(Maximum shear stress theory)} \tag{5.24}$$

It is obvious from above equations, that maximum normal stress and maximum shear stress occurs at an angle of 90^0 and 45^0 respectively from the tensile loading direction.

From above discussion it is clear that these two theories are very much suitable for the metals/alloys in which fracture occurs at an angle of 45^0 and 90^0. However in the present work shear fracture angles for MDCFed and MDCFed followed by annealed Al 2014 alloy for various processing conditions varies in the range beween 45^0 and 90^0 as seen from Fig. 5.2.17. This indicates the fracture of MDCFed alloy is controlled by both normal stress σ and shear

stress τ as described by the equation (5.21) and (5.22) respectively. In such cases there must be some another theories which can effectively predict the macroscopic fracture mechanism when fracture mode is dominated by both normal σ and shear stress τ. Two theories has been proposed by Zhang et al. for considering the above effect and these are

(i) Unified tensile fracture criterion or ellipse criterion [5.78, 5.79]

(ii) Modified ellipse criterion [5.80]
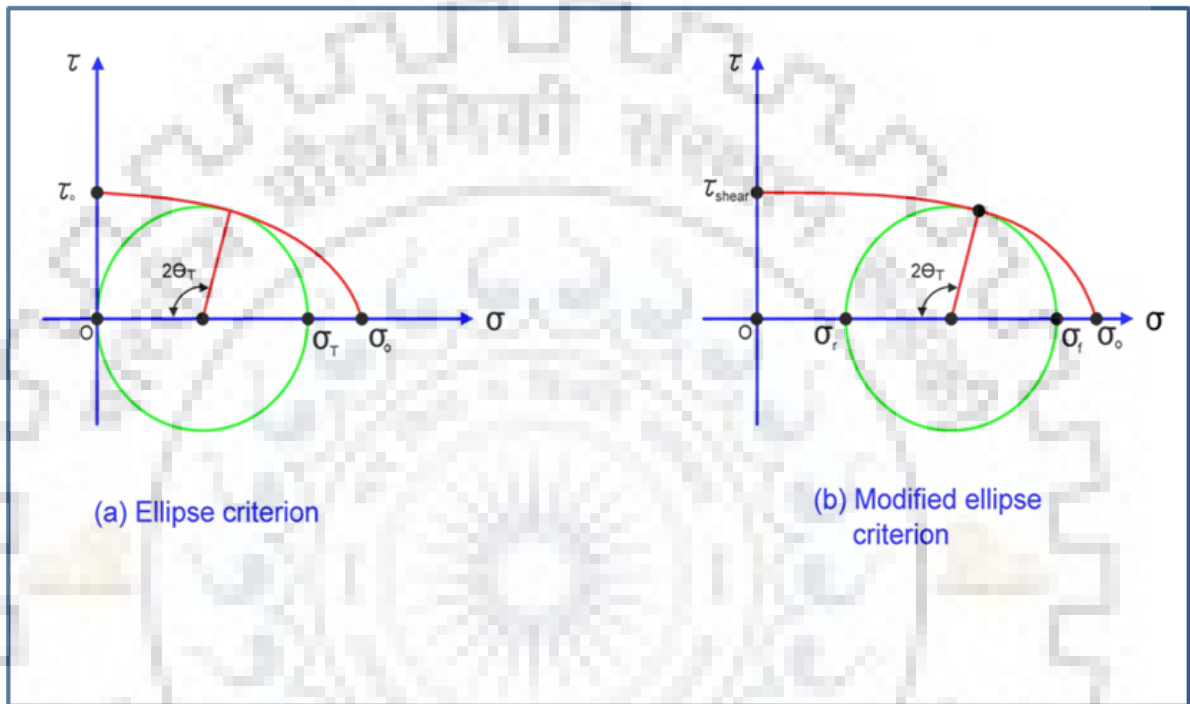
Figure 5.2.19: Macroscopic fracture criterion; (a) Ellipse criterion (b) Modified ellipse criterion

Unified tensile fracture criterion (ellipse criterion) is suggested by Zhang and coworkers [5.78)] and shown in Fig. 5.2.19 (a). This criterion can be expressed by the following equation as described in literature [5.78-5.79]

$$\left(\frac{\sigma_n}{\sigma_0}\right)^2 + \left(\frac{\tau_n}{\tau_0}\right)^2 = 1 \tag{5.25}$$

The critical value of normal σ_0 and shear stress τ_0 can be obtained from the following expression as reported in literature [5.78-5.79]

$$\sigma_T = 2\tau_0 \sqrt{1 - \alpha^2} \tag{5.26}$$

$$\theta_T = \frac{\pi}{2} - \frac{1}{2} arctan\left(\frac{\sqrt{1 - 2\alpha^2}}{\alpha^2}\right) \tag{5.27}$$

Where $\alpha = \frac{\tau_o}{\sigma_o}$ and known as fracture mode parameter which controls the macroscale fracture of metals/alloys. It is reported that shear fracture angle θ_T lies in between 45^0 and 90^0 if the value of fracture mode parameter α lies in between 0 and $\frac{\sqrt{2}}{2}$ [5.78-5.79].
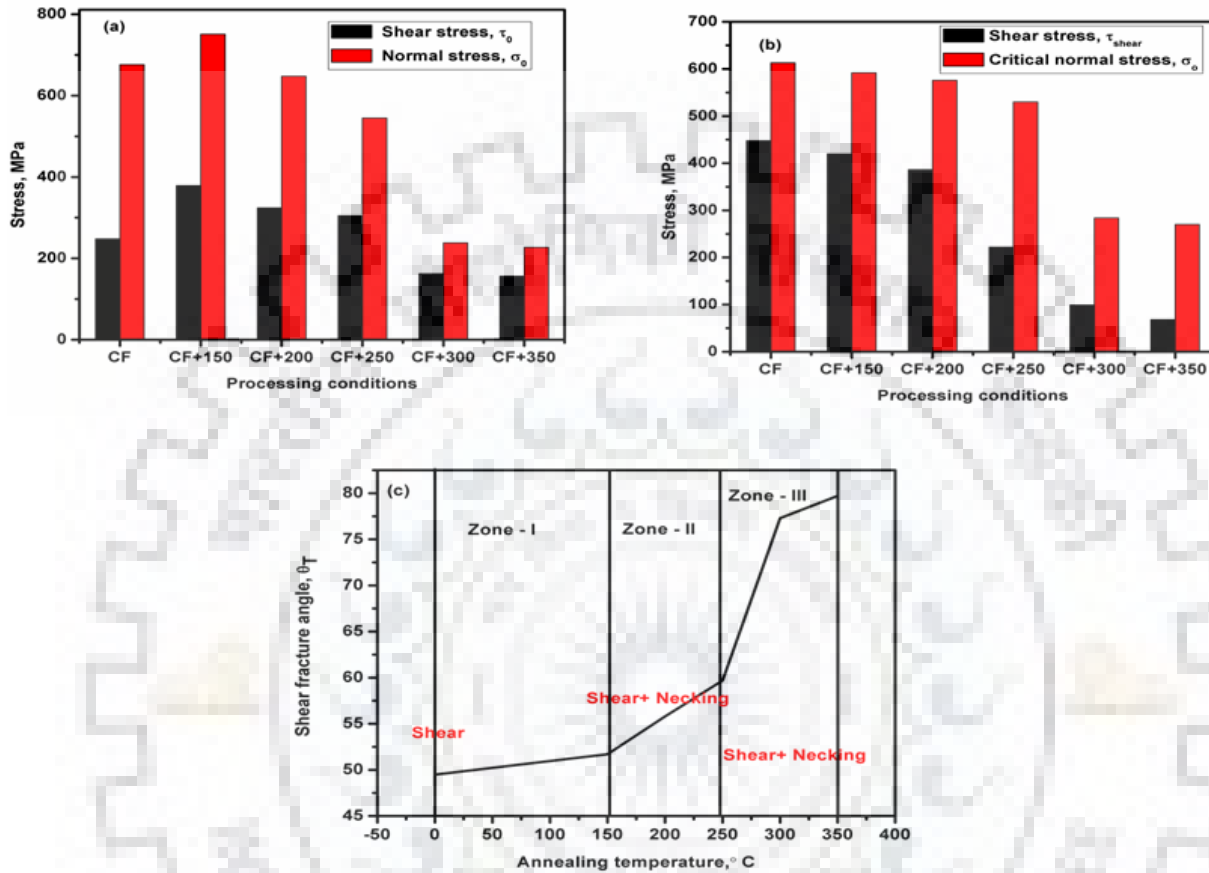
Figure 5.2.20: Variation of shear stress and normal stress with respect to various processing condition using (a) Ellipse criterion; (b) Modified ellipse criterion; (c) Variation of shear fracture angle with respect to annealing temperatures

The values of fracture mode parameter α has been calculated for various processed condition in this work and it is observed that fracture mode parameter α lies within the above mentioned range which substantiate the fracture is entirely governed by both normal and shear stresses. In addition to this the variation of critical shear stress τ_0 and critical normal stress σ_0 has also been plotted with respect to various processed condition in this work and shown in Fig. 5.2.20(a). The values of fracture mode parameter α with corresponding shear fracture angle θ_T has also been tabulated in Table. 5.2.3.

Table 5.2.3: Values of shear fracture angles for various processing condition using Ellipse and Modified Ellipse criterion

	CF	CF+150°C	CF+200°C	CF+250°C	CF+300°C	CF+350°C
Shear fracture angle θ_T (°)	49.5	51.7	55.8	59.7	77.3	79.7
Degree of necking ψ, (°)	0	12	16	21	37	41
Fracture mode factor, Ellipse criterion $\left(\alpha = \frac{\tau_0}{\sigma_0}\right)$	0.36	0.42	0.50	0.56	0.68	0.69
Fracture mode factor, modified ellipse criterion $\left(\alpha = \frac{\tau_{shear}}{\sigma_0}\right)$	0.73	0.71	0.67	0.42	0.35	0.24

From Table. 5.2.3, it is observed that value of fracture mode parameters α is minimum for multidirectional cryoforged samples and its value increases, on annealing the MDFCed samples from 150°C to 350°C and observed to be maximum for the MDCFed sample which is annealed at 350°C. In addition to this the values of critical normal stress σ_0 and critical shear stress τ_0 for annealed samples decreases gradually from the temperature 150°C to 250°C while drastic decrease is observed for the temperature 300°C and 350°C and observed to be minimum for sample annealed at 350°C (Fig. 5.2.20(a)).

Based on unified tensile criterion (ellipse criterion) it may be said that shear fracture angle θ_T largely depends upon the critical shear stress τ_0 and critical normal stress σ_0 and failure mode of the MDCFed sample changes from shear fracture to necking when MDCFed samples were annealed in the temperature range of 150°C to 350°C. The MDCFed sample have shown the lowest fracture angle because it has lowest value of fracture mode parameter α which means it has highest critical normal stress σ_0 due to which shear banding is promoted in MDCFed sample and necking is restricted. With further annealing in the temperature range from 150°C to 350°C fracture mode parameter α increases with continuous decrease in critical normal stress σ_0 and critical shear stress τ_0 due to which shear fracture angle θ_T increases. Subsequently dislocation pile up along the grain boundary is restricted and shear banding is suppressed which further promote the necking with increasing annealing temperature.

5.2.4.6 Modified ellipse criterion

Effect of stress-state is ignored in unified tensile criterion (ellipse criterion). However, Zhang et al [5.80] reported that state of stress before and after necking greatly affect the tensile fracture strength and related shear fracture angle because significant amount of stress triaxiality is imposed due to necking associated during tensile testing. In such a case, ellipse criterion is modified along with shifting of Mohr's circle (shown in Fig. 5.2.19(b)) in σ-τ plane as reported in literature [5.80]. Normal stress and shear stress can be expressed by following equations as described by modified ellipse criterion [5.80].

$$\sigma = (\sigma_f - \sigma_r)sin^2\theta + \sigma_r \qquad (5.28)$$

$$\tau = (\sigma_f - \sigma_r)sin\theta_T + cos\theta_T \qquad (5.29)$$

Where σ_f and σ_r are the maximum and minimum values of principal stresses due to necking and these are related with degree of necking by following equation.

$$tan\psi = \frac{\sigma_r}{\sigma_f} \qquad (5.30)$$

Where 'ψ' is the degree of necking. The fracture mode parameter in this case is given by the expression

$$\alpha = \frac{\tau_{shear}}{\sigma_o} \qquad (5.31)$$

From equation (5.25) and (5.28-5.31), the tensile fracture strength σ_f and shear fracture angle θ_T can be expressed by following equations

$$\sigma_f = \frac{2\tau_{shear}\sqrt{1-\alpha^2}}{\sqrt{tan^2\psi+2(2\alpha^2-1)tan\psi+1}} \qquad (5.32)$$

In the above equation value of α lies between 0 and $\left(\frac{\sqrt{2(1-tan\psi)}}{2}\right)$

$$\theta_T = arctan\sqrt{\frac{(2\alpha^2-1)tan\psi+1}{1-2\alpha^2-tan\psi}} \qquad (5.33)$$

Here, it is important to note that value of θ_T is equal to 90^0 when α is greater than $\left(\frac{\sqrt{2(1-tan\psi)}}{2}\right)$.

Based on above theory, fracture mode parameter α, critical normal stress σ_o and shear stress τ_{shear} are calculated for each processed condition in this work and it is observed that shear fracture angle θ_T increases with decrease in fracture mode parameter α which is just opposite to the unified tensile criterion as discussed earlier. The values of fracture mode parameter α and shear fracture angle θ_T using modified ellipse criterion is listed in Table 5.2.3. For MDCFed sample, the fracture mode parameter α was observed to be maximum while on

annealing in temperature range from 150°C to 350°C, its value continuously decreases and observed to minimum for the sample annealed at 350^{0}C. Fracture mode parameter α in modified ellipse criterion depends on τ_{shear} which is the shear stress required for the nucleation of shear bands in the material as reported in literature [5.80]. On the other hand, fracture mode parameter α in ellipse criterion depends on τ_0 which is critical value of shear stress. In addition to this, influence of necking is also considered in modified ellipse criterion. For the MDCFed sample, observed necking ψ was minimum because of nucleation of shear bands and reduced mobility of dislocations. Critical normal stress depends upon the bonding between the atoms and does not depend upon the microstructure [5.80]. So, the fracture mode parameter entirely depends upon the τ_{shear}. It can be seen that degree of necking decreases with increase in fracture mode parameter α which in turn depends upon the τ_{shear}. It is well known that plastic deformation takes place due to movement of dislocations. These dislocations are piled up at the grain boundaries (GBs) and induce concentrated stress [5.80]. If the grain size is large, piled up dislocations are moved from one grain to other grain by the concentrated stress and dislocation slip mechanism is favored while the dislocation pile up is not accommodated by the grain boundaries (GBs) when grain size is fine and in such cases grain boundary shear mechanism is favored and shear fracture is dominant [5.80]. The variation of shear fracture angle with respect to various processed condition can be seen by Fig. 5.2.20 (b). Fig. 5.2.21(a)-(e) represent the Mohr's circle for different processing conditions while Fig. 5.2.21 (f)-(g) represent the favorable mechanism for fine grain as well as annealed alloy. As discussed above for the annealed alloy grain size is sufficient to accommodate dislocation pile up due to which dislocation slip mechanism (Fig. 5.2.21 (f)) is favored. On the other hand for the 4 cycle cryo forged alloy grain size can not accommodate dislocation pile up resulting dislocation shear mechanism (Fig. 5.2.21(g)). In addition to this the difference between τ_{shear} and τ_{slip} is small for four cycle forged sample (Fig. 5.2.21(c)) due to which Mohr's circle will shift far from normal stress. With increasing annealing temperature from 150°C – 250°C, the difference between τ_{shear} and τ_{slip} will increase (Fig. 5.2.21(d)) slightly due to which Mohr's circle will slightly shift towards normal stress σ resulting slight increase in shear fracture angle. On further increase in annealing temperature from 250°C – 350°C, the significant increase in the difference between τ_{shear} and τ_{slip} is observed (Fig. 5.2.21(e)) resulting shifting of Mohr's circle very near to normal stress σ which increases the shear fracture angle

significantly in this annealing temperature range. Similar studies have already been done by Zhang et al. [5.80] for Cu and Cu-Zn alloy processed by ECAP.
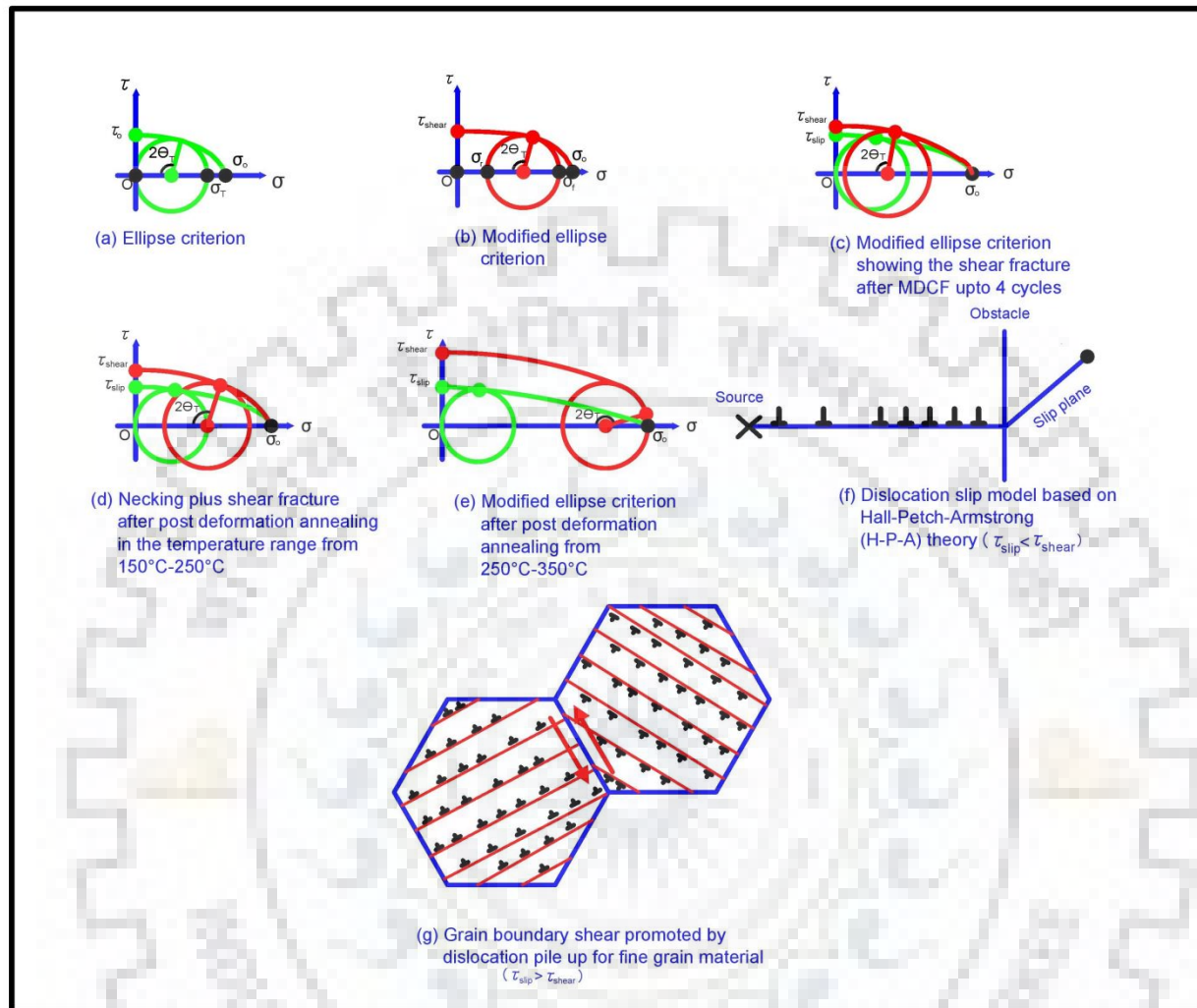
Figure 5.2.21: Mohr's circle for various processed conditions

For MDCFed sample, the nucleation of shear bands is easy due to high value of fracture mode parameter α which promotes the grain boundary glide mechanism (Fig. 5.2.21(g)), while for annealed sample, the fracture mode parameter α continuously decreases, resulting dislocation slip mechanism (Fig. 5.2.21(f)) as reported in the literature [5.80]. This might be the possible reason that MDCFed sample fails through the shear fracture with negligible necking. On annealing, dislocation density is slightly reduced up to 250°C and significantly reduced above this temperature, which promote the dislocation slip mechanism rather than shear mechanism, resulting transformation of shear fracture to necking behavior for annealed samples.

5.2.4.7 Microscopic versus macroscopic fracture mechanism

The variation of tensile fracture angle θ_T with respect to various processing condition is shown in Fig. 5.2.2(c) . This figure can be divided in to three zones.

Zone I : MDCFed sample and MDCFed sample annealed up to temperature 150°C

Zone II: MDCFed sample annealed at 150°C -250°C

Zone III: MDCFed sample annealed at 250°C -350°C

In Zone I, the tensile shear fracture angle varies in the range of 49^0 to 52^0. Tensile shear fracture angle of all the sample lies between 45^0 to 90^0, which means the fracture is not governed by maximum shear stress theory in which fracture essentially has to occur at an angle of 45^0. However, the increase in shear fracture angle of a MDCFed sample and sample annealed up to 150°C takes place with slow pace. For MDCFed sample, dislocation density is too high and grain size is very fine along with large density of shear bands as observed from TEM micrographs. Such type of microstructure can not effectively accumulate the dislocations due to which material experiences low work hardening rate resulting instant and catastrophic failure. Fractograph corresponding to this condition has also shown that MDCFed alloy fails through brittle fracture. When sample is annealed at 150°C, the slight recovery of microstructure takes place with reduction of shear bands density. The sharp and flat profile of MDCFed sample has been transformed in to slightly curved profile suggesting the occurrence of necking as observed from the macrograph of the sample annealed at 150°C. Shear fracture angle has also increased from 49.5^0 to 51.7^0 suggesting the slight improvement in work hardening rate. This might be due to the fact that on annealing, the density of microshear bands has reduced along with formation of subgrains. This microstructure can accumulate large number of dislocations during deformation due to which work hardening rate improves. The failure mode transforms to shear plus necking which has been confirmed by the corresponding fractograph showing the quasi cleavage (Mix-mode) fracture.

Zone II- On annealing at 200°C and 250°C, the subgrain size continuously increases with reduction of dislocation density and shear bands. So, the ability of accumulating dislocation improves on increasing annealing temperature due to which work hardenabilty and shear fracture angle is improved as compared to previous processing conditions and failure mode gradually transformed to shear and necking as compared to MDCFed sample. However, the shear fracture angle increase with slow pace up to 250°C. This might be due to the evolution of precipitates during annealing which imparts the pinning effect on the grain boundaries

230

(GBs) and restrict the grain growth as reported in various published work. This limits the dislocation storage ability of sub grains. However, this ability increase with increasing annealing conditions.

Zone III: on annealing at 300°C and 350°C, the significant improvement in the shear fracture angle was observed. On annealing at these temperatures, the dislocation density is significantly reduced and almost dislocation free recrystallized grains are formed whose size is more than 500 nm. Apart from this, shear bands density has also significantly decreased. Such type of microstructure can effectively accumulate large no of dislocations resulting drastic increase in shear fracture angle θ_T and work hardenabilty. The fractograph corresponding to this condition also proved that fracture is still shear plus necking. However, shear proportion is less prominent in the fracture surface. It is important to note that at such high temperature, shear fracture is still observed in the sample. It is due to the evolution of coarser and brittle stable spherical and rod phase, which act as a crack initiating source resulting shear fracture. From above discussion, it can be illustrated that fracture mechanism of MDCFed and MDCFed followed by annealed sample depends on the (i) Shear banding, dislocation density and grain size. Fine grain with numerous shear band promotes the stress localization with reduced necking ability and promote shear fracture (ii) second phase precipitates. Second phase precipitates restrict the grain growth and suppress the ability of dislocation accumulation, which restrict the ability of necking.

5.2.4.8 Fracture toughness and Fractographic observations after fracture toughness test

Fractographic observations has been made for MDCF and annealed alloy after 3-point bend test for correlating the fracture toughness with the fracture surface appearance in the present work. Fig. 5.2.22(a) shows the pre crack region which is machined by the help of WEDM. It has been reported that fracture toughness of precipitation hardenable Al alloy is influenced by many parameters such as second phase precipitates, grain size, crystal structure and precipitate free zones (PFZs) [5.81]. In this investigation, it has been observed that various fracture parameters viz. apparent fracture toughness, equivalent energy fracture toughness, strain energy release rate, crack tip plastic zone size, and crack tip opening displacement (CTOD) has been increased up to 150°C while these parameters have decreased beyond this temperature. The state of stress near crack tip largely influences the fracture toughness values due to variation of crack initiation phase and crack propagation phases for MDCFed and annealed alloy. Fig. 5.2.22(b) shows the fracture surface morphology of multidirectional

cryoforged (MDCFed) Al 2014 alloy after 3-point bend test. Fracture surface of MDCFed samples consists of very few fine dimples with flat facets showing the intergranular brittle fracture resulting rapid propagation of pre existing crack.
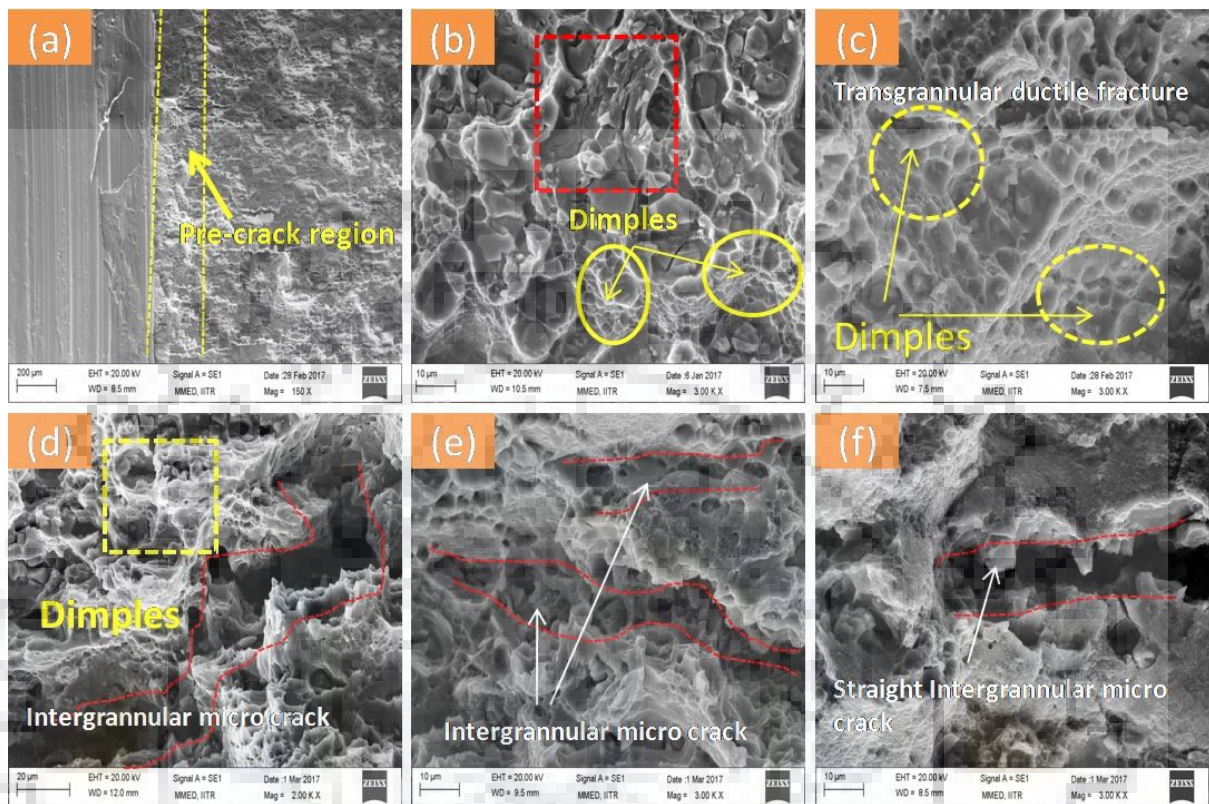
Figure 5.2.22: Fractographs after 3 point bend test (a) Pre - crack region; (b) MDCFed alloy; (c) MDCFed alloy annealed at 150°C; (d) MDCFed alloy annealed at 250°C; (e) MDCFed alloy annealed at 300°C; (f) MDCFed alloy annealed at 350°C

Fracture surface of MDCFed sample annealed at 150°C shows numerous fine and deep dimples as observed from SEM micrograph (Fig 5.2.22(c)) corresponding to this sample condition. The nucleation of void in front of pre existing crack might have produced the dimples as reported in literature [5.74]. At this condition, we observed the fine spherical semicoherent phase θ' (Al$_2$Cu) as discussed in earlier sections. This phase is semi coherent with the matrix and homogenously nucleated within the grain. Recently Li et al [5.81] reported that strength difference between matrix and grain boundaries controls the fracture mode of sample in presence of pre existing crack. The large number of coherent/semicoherent precipitates imparts the strength to the matrix while the precipitates at GBs provides the local stress concentration and reduces the fracture toughness as reported in their work. Similar phenomenon might occur for the sample annealed at 150°C due to homogeneous nucleation of semicoherent spherical phase θ' due to which significant improvement in all fracture

parameters are observed. The presence of fine dimples features in the fracture surface also substantiates the improvement in fracture toughness values as seen from SEM micrograph. On the basis of fracture toughness mechanism, it can be mentioned that lattice misfit between Al matrix and semicoherent phase θ' is minimum which provides the strength to the matrix resulting delaying in crack initiation phase due to which linear elastic fracture toughness parameters (strain energy release rate, K_Q and K_{ee}) observed to be maximum as compared to all other conditions. The improved crack tip plastic zone size (r) and crack tip opening displacement (CTOD) also substantiate that crack tip plasticity has significantly improved at this condition resulting delaying in crack propagation period and improved elastic plastic fracture toughness (EPFM) parameters at this condition.

The SEM micrograph of sample annealed at 250°C is shown in Fig. 5.2.22(d). The slight change in fracture surface morphology is observed as compared to sample annealed at 150°C as seen from Fig. 5.2.22(d). The volume fraction of dimples has decreased with respect to sample annealed at previous conditions. Some intergrannular microcrack (marked by red) with brittle facets were also observed as seen from this figure. This indicates that crack growth resistance for the sample annealed at 250°C has decreased resulting decrease in fracture toughness parameters at this condition. At this condition, we observed the metastable fine needle phase λ' and few slightly coarser stable precipitates θ as explained in the earlier sections. The meta stable needle precipitates λ' imparts the strength to matrix due to coherency associated with it. On the other hand, coarser spherical precipitates loses coherency due to increase in size. The fine dimples are observed where the fine needle metastable phase is nucleated while spherical phase act as a crack initiating sites. This might be the reason for mixed mode fracture surface (transgranular as well as intergranular fracture) at this sample condition. From the point of view of fracture toughness mechanism, it may be mentioned that the presence of spherical precipitates θ phase reduces the crack initiation as well as crack propagation period, resulting decrease in linear elastic fracture toughness (LEFM) parameters (strain energy release rate, K_Q, and K_{ee}) and elastic plastic fracture toughness (EPFM) parameters (crack tip plastic zone size, and CTOD) as compared to previous annealed conditions.

Fracture surface of sample annealed at 300°C and 350°C is shown in Fig. 5.2.22(e)-(f). The significant change in the fracture surface is observed in these conditions as compared to previous annealed condition and without annealed condition (MDCF sample). Dimple size has

slightly increased at annealing temperature of 300°C, however its volume fraction has significantly reduced as compared to previously annealed samples. Apart from this, wide curvature crack marked by red lines can also be observed in the fracture surface of sample annealed at 300°C. The larger size dimples are observed due to formation of larger size recrystallized grains at this condition. These both phases act as a crack initiating source due to which wide curvature macro cracks has been observed at this condition. These macro cracks easily initiate as well as rapidly propagate in the fracture surface resulting reduced fracture toughness parameters as compared to previous conditions. The crack tip plasticity has also decreased at this condition which substantiate the reduced crack growth resistance facilitated by coarser spherical and rod phases due to which significant decrease in EPFM fracture toughness parameters is observed. Similar fracture surface morphology is observed for sample annealed at 350°C (Fig. 5.2.22(f). However, the volume fraction of dimples has significantly decreased as compared to sample annealed at previous annealing conditions. In addition, a straight intergranular crack can also be observed from this figure. It is believed that wider straight intergranular crack moves rapidly as compared to curvature crack due to which the fracture toughness is minimum at this condition as compared to all other conditions. Crack opening is wider because evolution of coarser spherical and rod phase precipitates at this sample condition due to which all fracture toughness parameters have decreased.

On the basis of above discussion, it can be illustrated that fracture toughness of multidirectional cryoforged (MDCFed) Al 2014 alloy depends upon the size and nature of second phase precipitates and can be improved by improving the crack initiation and crack propagation period.

5.2.5 Conclusions

The effect of annealing on the strain hardening behavior, fracture mechanism,and fracture toughness of multidirectional cryoforged (MDCFed) and followed by annealed Al 2014 alloy has been investigated   in the present work. The following results are summarized based on present investigation.

- The multidirectional cryoforging (MDCF) is an effective approach for improving the mechanical properties such as tensile strength, yield strength and fracture toughness of coarser grain solution treated (ST) Al 2014 alloy due to development of UFG microstructure in the coarser grain Al 2014 alloy.

234

- The mechanical properties of bulk UFG Al 2014 alloy processed by multidirectional cryoforging (MDCF) can further be increased by employing the annealing treatment up to 250°C due to precipitation of semicoherent fine spherical phase θ' (Al$_2$Cu) and semicoherent fine needle phase λ' (AlCuMgSi).

- High temperature annealing treatments beyond 250°C are not suitable in high strength applications for the bulk UFG Al 2014 due to significant reduction in mechanical properties such as tensile, yield and fracture toughness at these temperatures resulting from combined recovery, recrystallisation and coarsening of metastable phases.

- The strain hardening exponent calculated from Hollomon's as well as modified Crussurd - Joul equation indicates that strain hardening rate for MDCFed and MDCFed followed by annealed alloy up to temperature 250°C increases with slow pace while beyond this temperature, strain hardening ability and strain hardening rate significantly increases.

- The macroscopic fracture mechanism for MDCFed alloy is dominated by shear localization with negligible necking while for annealed alloy up 350°C shows the mixed mode fracture mechanism, shear plus necking.

- Fracture surface of MDCFed Al 2014 after 3-point bend test has been dominated by intergranular brittle fracture with few fine dimpled features. The fracture behavior is transformed to transgranular ductile fracture upon annealing at 150°C, substantiating the improved fracture toughness at this temperature. Annealing beyond this temperature, the fracture surface is further transformed to the mix mode of fracture, intergranular as well as transgranular and with increasing annealing temperature, fracture surface is dominated by intergranular fracture resulting, a significant drop in fracture toughness values at high annealing temperature.

5.3 Strengthening Contributions from various Strengthening Mechanisms

Strengthening contributions to the yield strength from different strengthening mechanism has been evaluated in this work for the MDCFed and MDCFed followed by annealed Al 2014 alloy. It is well established that yield strength for UFG precipitation hardenable alloy is sum of solid solution strengthening, dislocation strengthening, grain boundary strengthening (Hall-Petch strengthening), and precipitation strengthening and can be expressed by following expression [5.82-5.83].

$$\sigma_y = \sigma_{ss} + \sigma_{Dis} + \sigma_{Gbs} + \sigma_{ps} \tag{5.34}$$

Where σ_{ss} = solid solution strengthening, σ_{Dis} = dislocation strengthening, σ_{Gbs} = Grain boundary strengthening and σ_{ps} = precipitation strengthening

For 4 cycles MDCFed Al 2014 alloy, we did not observe the precipitation of second phase in this work. It is proved by XRD results and TEM studies as discussed in section 5.2. Therefore, precipitation strengthening contribution is neglected for 4 cycles MDCFed samples. For annealed samples, evolution of precipitation of semicoherent spherical phase θ' and semicoherent fine needle phase λ' is observed up to 250°C, while these precipitates become coarser and stable spherical θ phase and stable rod phase λ at the annealing conditions 300⁰C and 350°C as discussed in the earlier section 5.2. So, the precipitation effect is considered in all annealing conditions. It is important to note that during the precipitation reaction, solute atom comes out in the form of precipitates due to which solid solution strengthening can be neglected for annealed MDCFed Al 2014 alloy.

5.3.1 Solid solution strengthening(σ_{ss}):

Solute atoms dissolved in the Al matrix creates local strain field by interacting with mobile dislocations and hinder their motion during deformation resulting an improvement in yield strength [5.70]. The major alloying elements in Al 2014 alloy are Cu = 4.5 % , Si = 0.77 %, Mg = 0.44 %, Mn = 0.71 %. The yield strength can be obtained by evaluating individually the solid solution strengthening contribution from individual atom and adding together as per following equations as discussed in literature [5.84].

$$\sigma_{ss} = \Delta\sigma_{Cu} + \Delta\sigma_{Si} + \Delta\sigma_{Mg} + \Delta\sigma_{Mn} \tag{5.35}$$

Where $\Delta\sigma_{Cu} = H_1 C^a$, $\Delta\sigma_{Si} = H_2 C^b$, $\Delta\sigma_{Mg} = H_3 C^c$, $\Delta\sigma_{Mn} = H_4 C^d$ as reported in literature [5.75,5.82,5.84].

Here, H_1 , H_2 , H_3 and H_4 are the rise in yield strength due to presence of Cu, Si, Mg, and Si respectively, and these values are listed in Table 5.3.1 C is the % content (in wt %) of the

respective atoms in the solid solution as described in reference [5.75,5.82,5.84].   , while a, b, c, and d are the constants and its values are listed in Table. 5.3.1. By substituting the values of individual strengthening components in equation (5.35), the yield strength increment in MDCFed Al 2014 is observed as 56.38 MPa. This strengthening effect is observed for only multidirectional cryoforged (MDCFed) Al 2014 alloy.

Table 5.3.1: Symbols and values of parameters used in equation (5.35)- (5.36)

Symbols	Meaning	Values	Unit	Reference
H_1	Strength increment factor due to Cu	7	MPa	[5.75,5.82,5.84].
H_2	Strength increment factor due to Si	8.8	MPa	[5.75,5.82,5.84].
H_3	Strength increment factor due to Mg	13.3	MPa	[5.75,5.82,5.84].
H_4	Strength increment factor due to Mn	10.1	MPa	[5.75,5.82,5.84].
C	Solute content	-	wt %	[5.74,5.82,5.84].
a, b, c, d	Exponents for Cu, Si, Mg, and Mn respectively	1, 1, 1.13, 1	Unit less	[5.74,5.82,5.84].

5.3.2 Grain boundary strengthening (σ_{Gbs}):

Multidirectional cryoforging (MDCF) leads to fine grains due to heavy deformation which creates a large volume fraction of grain boundaries (GBs). These grain boundaries (GBs) obstruct the dislocation movement during plastic deformation thereby significant improvement in the yield strength is observed. Grain boundary strengthening follows the Hall-Petch relationship and has been estimated by following expression as discussed in literature [5.84].

$$\Delta\sigma_{HP} = K^{HP} d^{\frac{-1}{2}}$$ (5.36)

Where K^{HP} the constant known as Hall- Petch is constant and its value is listed in Table 5.3.2, d is average grain size in nm, which has been calculated by measuring statistical distribution

of grain size in each processed condition from TEM micrographs. Grain boundary strengthening contribution to the yield strength is listed in Table. 5.3.3 for various processed conditions in the present work.

Table 5.3.2: Symbols and values of parameters used in equation (5.37)-(5.43)

Symbols	Meaning	Values	Unit	Reference
K^{HP}	Hall –Petch constant	0.12	MN/m$^{3/2}$	[5.75,5.82,5.84].
M	Mean orientation factor	3.06 for F.C.C	Unit less	[5.70]
α	Constant	0.2 for F.C.C	Unit less	[5.70]
G	Shear modulus for Al 2014 alloy	28	GPa	[5.75]
b	Burgers vector	.286 for F.C.C	nm	[5.70]
α_ε	Constant	2.6 for F.C.C	Unit less	[5.70]
r	Mean radius of spherical precipitates	30 nm at 300^{0}C 37 nm at 350^{0}C	nm	_
λ_p	Edge to edge inter precipitate distance for rod phase	83 nm at 300^{0}C 105 nm at 350^{0}C	nm	_

5.3.3 Dislocation strengthening (σ_{Dis}):

When Al 2014 alloy is MDCFed , the dislocation density is significantly increased in sample. These dislocations are interacting with each other and impede the motion of mobile dislocations further during the plastic deformation, resulting dislocation strengthening. Dislocation strengthening contribution to yield strength for the all processed condition in this work has been calculated using Bailey- Hirsch equation as discussed in literature [5.70].

$$\Delta\sigma_d = M\alpha Gb\rho^{\frac{1}{2}} \tag{5.37}$$

Various symbols and their corresponding values are listed in Table 5.3.2 and 5.3.3. The dislocation density (ρ) has been calculated by using the following equation as given in literature [5.69]

$$\rho = \frac{2\sqrt{3}\,\varepsilon}{db} \tag{5.38}$$

Where 'd' and 'ε' is the crystallite size and microstrain measured from XRD data, b is the Burger's vector and its value is 0.286 nm for Al . The values of 'd' and 'ε' have been calculated in XRD results of section 5.2. The dislocation strengthening contribution to the yield strength of Al 2014 alloy for various processing conditions is listed in Table. 5.3.3

Table 5.3.3: Strengthening contributions from various strengthening mechanisms

Strengthening contributions	CF	CF+150°C	CF+200°C	CF+250°C	CF+300°C	CF+350°C
Solid solution strengthening(σ_{ss}), MPa	56.38	-	-	-	-	-
Grain boundary strengthening (σ_{Gbs}), MPa	240	222	215	205	123	111
Dislocation strengthening(σ_{Dis}), MPa	90	81.49	78.87	69.48	35.5	11
Precipitation strengthening(σ_{ps}), MPa	-	183	156	101	20	6
Theoretical total yield strength, MPa	386	486.49 (approx)	449.87 (approx)	375.48 (approx)	178	128
Experimental yield strength MPa	396	486	450	376	183	140

5.3.4 Precipitation strengthening(σ_{ps}):

Precipitates offer the additional resistance to the dislocation motion thereby increasing the material strength. Precipitation strengthening is governed by two possible mechanisms as reported in literature [5.70, 5.85]. The first one is Orowan dislocation by passing mechanism and another is dislocation shearing mechanism. When the strength of precipitate particle is higher than the matrix strength, higher strength is applied to overcome the resistance offered by the precipitate. The dislocation shearing mechanisms are operative mechanisms [5.70, 5.83, 5.85]. On the other hand, when precipitates are coarser, dislocations are by passed by the particle. Dislocation by pass mechanism devised by Orowan is operative in such cases. Increase in yield strength due to by passing mechanism can be expressed by Orowan's equation [5.70, 5.83, 5.85] which is

$$\Delta\sigma_{orowan} = M \frac{.4Gb}{\pi\sqrt{1-v}} \frac{ln\left(\frac{2r'}{b}\right)}{\lambda_p} \tag{5.39}$$

Where r' = mean radius of spherical precipitates in random plane and its value is $\sqrt{\frac{2}{3r}}$.

Here 'r' is mean radius of precipitates. λ_p =Edge to edge inters precipitate distance. The other Symbols in above equation are defined in Table 5.3.2 and Table 5.3.3.

Ma et al. [5.70] reported that contribution in yield strength due to shearing mechanism is due to the three factors. (i) Strengthening due to the coherent precipitates $(\Delta\sigma_{cs})$, (ii) Strengthening due to mismatch of elastic modulas $(\Delta\sigma_{ms})$ and (iii) strengthening due to order strengthening $(\Delta\sigma_{os})$. Strength contributions due to these three factors can be expressed by following equations as reported in literature [5.70, 5.83, 5.86].

$$\Delta\sigma_{cs} = M\alpha_\varepsilon (G\varepsilon_c)^{\frac{3}{2}} \left(\frac{rf}{0.5Gb}\right)^{\frac{1}{2}} \tag{5.40}$$

$$\Delta\sigma_{ms} = M.0055(\Delta G)^{\frac{3}{2}} \left(\frac{2f}{G}\right)^{\frac{1}{2}} \left(\frac{r}{b}\right)^{\frac{3p}{2}-1} \tag{5.41}$$

$$\Delta\sigma_{os} = M0.81\frac{\gamma_{apb}}{2b} \left(\frac{3\pi f}{8}\right)^{\frac{1}{2}} \tag{5.42}$$

Where ΔG = mismatch modulus between matrix and precipitate, f = volume fraction of precipitates, ε_c = misfit due to difference in lattice parameter, γ_{apb} = free energy of antiphase boundary. Other symbols used in the above equation are listed in Table 5.3.2 and Table. 5.3.3. It is reported that when the precipitates are coherent or semi coherent, the precipitation strengthening mechanism is governed by dislocation shearing mechanism from equations 5.40-5.42 [5.70, 5.83, 5.85].From equation 5.39, it is also clear that dislocation by pass mechanism depends upon r' and λ_p, which the extrinsic parameters of the precipitates as discussed in literature [5.70, 5.83]. On the other hand, dislocation shearing mechanism expressed by equations 5.40-5.42 depends upon the materials intrinsic parameters such as composition, crystal structure etc. These parameters are extremely difficult to be calculated from TEM procedures [5.70, 5.83].

On the basis of above discussions, Orowan's by passing mechanism has been used for MDCFed alloy to evaluate contribution in yield strength for the incoherent stable precipitates which are evolved from temperature range 300°C and 350°C while precipitates in the temperature between 150°C to 250°C are semicoherent due to which Orowon's mechanism is not applicable. Mean radius (r) of spherical precipitates and edge to edge inter precipitates

distance λ_p for rod phase is calculated from image J software and its values are listed in Table 5.3.2. Moreover, strength contribution from dislocation shearing mechanism in the temperature range 150°C to 250°C is difficult and therefore precipitation hardening effect in this temperature range has been calculated by subtracting experimentally observed yield strength to the contribution of grain boundary strengthening and dislocation strengthening for MDCFed Al 2014 alloy annealed in the temperature range of 150°C to 250°C. The similar procedure is followed by Rao et al. [5.82] for the aged Al 6061 alloy processed by multidirectional cryoforging (MDCF). The strength contributions from precipitation hardening effect are listed in Table. 5.3.3 . For the annealing conditions 300°C and 350°C, the equation 5.39 described by Orowan has been used in the present work.

5.3.5 Conclusion

Assessment of the contribution of various strengthening mechanism to overall yield strength of MDCFed and MDCFed followed by annealed Al 2014 alloy has been investigated in this work . Based on the calculations of individual strengthening contributions to the yield strength, grain boundary strengthening (σ_{Gbs}), has significant contributions in raising the yield strength of MDCFed Al 2014 alloy, while for annealed samples up to the temperature range 250°C, the grain boundary (σ_{Gbs}) and precipitation strengthening (σ_{ps}) were observed to be maximum strength contributors to the yield strength.

References

[5.1]   R.Z. Valiev, A.V. Korznikov, and R.R. Mulyukov, Structure and Properties of Ultrafine-Grained Materials Produced by Severe Plastic Deformation, 1993, Mater.Sci. Eng.A, 168, pp. 141- 148.

[5.2]   Y. Estrin and A. Vinogradov, Extreme grain refinement by severe plastic deformation: a wealth of challenging science, 2013, Acta Mater, 61, pp. 782-817

[5.3]   R.Z. Valiev, Y. Estrin, Z. Horita, T.G. Langdon, M.J. Zechetbauer, and Y.T Zhu, Producing bulk ultrafine-grained materials by severe plastic deformation, 2006, J. Mater. Sci, 58, pp. 33-39.

[5.4]   Figueiredo, B. Roberto, and Terence G. Langdon, Using Severe Plastic Deformation for the Processing of Advanced Engineering Materials, Mater. Trans, 2009, 50, pp. 1613-1619.

[5.5]   V.M. Segal, Severe Plastic Deformation: Simple Shear versus Pure Shear, 2002, Mater.Sci. Eng.A, 338, pp. 331-344.

[5.6] R.Z. Valiev and T.G. Langdon, Principles of Equal-Channel Angular Pressing as a Processing Tool for Grain Refinement, 2006, Prog. Mater Sci, 51, pp. 881-981

[5.7] A.P. Zhilyaev and T.G. Langdon, Using High-Pressure Torsion for Metal Processing: Fundamentals and applications, 2008, Prog. Mater Sci, 53, pp. 893-979.

[5.8] Y. Saito, H. Utsunomiya, N. Tsuji, and T. Sakai, Novel Ultra-High Straining Process for Bulk Materials -Development of the Accumulative Roll-Bonding (ARB) Process, 1999, Acta Mater, 47, pp. 579-583.

[5.9] M. Richert, Q. Liu, and N. Hansen, Micro structural Evolution Over a Large Strain Range in Aluminium Deformed by Cyclic-Extrusion–Compression, 1999, Mater. Sci. Eng. A, 260, pp. 275-283.

[5.10] K. Nakamura, K. Neishi, K. Kaneko, M. Nakagaki, and Z. Horita, Development of Severe Torsion Straining Process for Rapid Continuous Grain Refinement, 2004, Mater Transac, 45, pp. 3338-3342.

[5.11] J.Y. Huang, Y.T. Zhu, H. Jiang, and T.C. Lowe, Microstructures and Dislocation Configurations in Nanostructured Cu Processed by Repetitive Corrugation and Straightening, 2001, Acta Mater, 49, pp. 1497-1505.

[5.12] D. Fuloria, S. Goel, R. Jayaganthan, D. Srivastava, G.K. Dey, and N. Saibaba, Mechanical Properties and Microstructural Evolution of Ultrafine Grained Zircaloy-4 Processed Through Multiaxial Forging at Cryogenic Temperature, 2015, T. Nonferr. Metal Soc, 25, pp. 2221-2229.

[5.13] O. Sitdikov, T. Sakai, A. Goloborodko, H. Miura, and R. Kaibyshev, Effect of Pass Strain on Grain Refinement in 7475 Al Alloy During Hot Multidirectional Forging,2004, Mater. Transac, 45, pp. 2232-2238.

[5.14] B. Cherukuri, and R. Srinivasan, Properties of AA6061 processed by multi-axial compressions/forging (MAC/F), 2006, Mater Manuf Process, 21, pp. 519-525.

[5.15] H. Miura, T. Maruoka, X. Yang, and J.J. Jonas, Microstructure and Mechanical Properties of Multi-Directionally Forged Mg–Al–Zn alloy, 2012, Scripta Mater, 66, pp. 49-51.

[5.16] X.S. Xia, C.H. Ming, F.Y. Fan, C.H. Zhu, J. Huang, T.Q. Deng, and S.F. Zhu, Microstructure and Mechanical Properties of Isothermal Multi-Axial Forging Formed AZ61 Mg Alloy,2013, T. Nonferr. Metal Soc, 23, pp. 3186-3192

[5.17] X.Y. Yang, Z.Y. Sun, X.I. Jie, H. Miura, and T. Sakai, Grain Size and Texture Changes of Magnesium Alloy AZ31 During Multi-Directional Forging, 2008, T. Nonferr. Metal Soc, 18, pp. 200-204

[5.18] T. Sakai, A. Belyakov, and H. Miura, Ultrafine Grain Formation in Ferritic Stainless Steel during Severe Plastic Deformation, 2008, Metall Mater Trans A, 39, pp. 2206-2214.

[5.19] A.Rezaee-Bazzaz, and S. Ahmadian, Modeling of Mechanical Behavior of Ultra Fine Grained Aluminum Produced by Multiple Compressions in a Channel Die, 2012, Mater. Des; 34, pp. 230-234

[5.20] R. Kapoor, A. Sarkar, R. Yogi, S.K. Shekhawat, I. Samajdar, and J.K. Chakravartty, Softening of Al during Multi-Axial Forging in a Channel Die, 2013, Mater. Sci. Eng. A, 560, pp. 404-412.

[5.21] I.A. Ovid'ko and A.G. Sheinerman, Grain Size effect on Crack Blunting in Nanocrystalline Materials, 2009, Scripta Mater, 60, pp. 627-630.

[5.22] X. Xu, Q. Zhang, N. Hu, Y. Huang, and T.G. Langdon, Using an Al–Cu Binary Alloy to Compare Processing by Multi-Axial Compression and High-Pressure Torsion, 2013, Mater. Sci. Eng. A, 588, pp. 280-287.

[5.23] C. Mallikarjuna, S.M. Shashidhara, and U.S. Mallik, Evaluation of Grain Refinement and Variation in Mechanical Properties of Equal-Channel Angular Pressed 2014 Aluminum Alloy, 2009, Mater. Des, 30, pp. 1638-1642.

[5.24] A. Dhal, S.K. Panigrahi, and M.S Shunmugam, Influence of Annealing on Stain Hardening Behaviour and Fracture Properties of a Cryorolled Al 2014 Alloy, 2015, Mater. Sci. Eng. A,645, pp. 383-392.

[5.25] P. Venkatachalam, S.R. Kumar, B. Ravisankar, V.T. Paul, and M. Vijayalakshmi, Effect of Processing Routes on Microstructure and Mechanical Properties of 2014 Al alloy Processed by Equal Channel Angular Pressing, 2010, T. Nonferr. Metal Soc, 20, pp. 1822-1828

[5.26] N. Rangaraju, T. Raghuram, B.V. Krishna, K.P. Rao, and P. Venugopal, Effect of Cryo-rolling and Annealing on Microstructure and Properties of Commercially Pure Aluminium, 2005, Mater. Sci. Eng. A, 398, pp. 246-251.

[5.27] Y. Wang, M. Chen, F. Zhou, and E. Ma, High Tensile Ductility in a Nanostructured Metal, 2002, Nature, 419, p 912-915.

[5.28] T. Shanmugasundaram , B.S. Murty , and V.S. Sarma , Development of ultrafine grained high strength Al–Cu alloy by cryorolling, 2006, Scripta Mater , 54, pp. 2013-2017.

[5.29] S.K. Panigrahi, and R. Jayaganthan, Effect of rolling temperature on microstructure and mechanical properties of 6063 Al alloy, 2008, Mater. Sci. Eng. A, 492, pp. 300-305.

[5.30] V.S. Sarma, K. Sivaprasad, D. Sturm, and M. Heilmaier , Microstructure and mechanical properties of ultra fine grained Cu–Zn and Cu–Al alloys produced by cryorolling and annealing, 2008, Mater. Sci. Eng. A , 489, pp. 253-258.

[5.31] A. Rollett, F.J. Humphreys, G.S. Rohrer, and M. Hatherly, Recrystallization and Related Annealing Phenomena, Elsevier, Pergamon, 2004

[5.32]   V.S. Sarma, J. Wang, W.W. Jian, A. Kauffmann, H. Conrad, J. Freudenberger, and Y.T. Zhu, Role of stacking fault energy in strengthening due to cryo-deformation of FCC metals, 2010, Mater. Sci. Eng. A, 527, pp. 7624-7630.

[5.33]   E.A. Starke and J.T. Staley, Application of Modern Aluminum Alloys to Aircraft, 1996, Prog Aerosp Sci, 32, pp. 131-172.

[5.34]   A. Hohenwarter and R. Pippan, Fracture Toughness Evaluation of Ultrafine-Grained Nickel, 2011, Scripta Mater, 64, pp. 982-985.

[5.35]   H. Somekawa and T. Mukai, Fracture Toughness in Ultra fine-Grained Magnesium Alloy, 2006, Mater Sci Forum, 503, pp. 155-160

[5.36]   A. Singh, L. Tang, M. Dao, L. Lu, and S. Suresh , Fracture Toughness and Fatigue Crack Growth Characteristics of Nanotwinned Copper, 2011, Acta Mater , 59 , pp. 2437-2446.

[5.37]   M. Gavgali and B. Aksakal, Effects of Various Homogenisation Treatments on the Hot Workability of Ingot Aluminium Alloy AA 2014, 1998, Mater. Sci. Eng. A, 254, pp. 189-199.

[5.38]   P.N. Rao, D. Singh, and R. Jayaganthan, Mechanical Properties and Micro structural Evolution of Al 6061 alloy Processed by Multidirectional Forging at Liquid Nitrogen Temperature, 2014, Mater. Des, 56, pp. 97-104

[5.39]   D.Kuhlmann-Wilsdorf, and N. Hansen, Geometrically Necessary, Incidental and Subgrain boundaries, 1991, Scripta Metall Mater, 25, pp. 1557-1562.

[5.40]   C. Kobayashi, T. Sakai, A. Belyakov, and H. Miura, Ultrafine Grain Development in Copper during Multidirectional Forging at 195 K, 2007, Phil Mag Lett, 87, pp. 751-766.

[5.41]   A. Chatterjee, G. Sharma, A. Sarkar, J.B. Singh, and J.K. Chakravartty, A Study on Cryogenic Temperature ECAP on the Microstructure and Mechanical Properties of Al–Mg alloy, 2012, Mater. Sci. Eng. A, 556, pp. 653-657.

[5.42]   N.N. Krishna, R. Tejas , K. Sivaprasad , and K. Venkateswarlu , Study on Cryorolled Al–Cu Alloy Using X-ray Diffraction Line Profile Analysis and Evaluation of Strengthening Mechanisms, 2013, Mater. Des, 52, pp. 785-790.

[5.43]   R.V. Stone, T.B. Cox, J.R. Low, and J.A. Psioda , Microstructural Aspects of Fracture by Dimpled Rupture, 1985, Int Met Rev, 30, pp. 157-180.

[5.44]   H. Toda , T. Kobayashi , and A. Takahashi , Micromechanism of Fracture in Wrought Aluminum Alloy Containing Coarse Inclusion Particles, 1999, Alum Trans, 1, p 109-116.

[5.45]   A. Hohenwarter, and R. Pippan, Anisotropic Fracture Behavior of Ultrafine-Grained Iron, 2010, Mater. Sci. Eng. A , 527, pp. 2649-2656.

[5.46]   F.J. MacMaster, K.S. Chan, S.C. Bergsma, and M.E. Kassner , Aluminum alloy 6069 part II: fracture toughness of 6061-T6 and 6069-T6 , 2000, Mater. Sci. Eng. A, 289, pp. 54-59.

[5.47]   ASTM E399-05 Standard Test Method for Plane-Strain Fracture Toughness of Metallic Materials, Annual Book of Astm Standards, Philadelphia PA, American Society for Testing and Materials, 2005.

[5.48]   P. Das, R. Jayaganthan, T. Chowdhury, and I. Singh, Improvement of Fracture Toughness (K1c) of 7075 Al Alloy by Cryorolling Process, 2011, Mater Sci Forum, 683, pp. 81-94

[5.49]   Handbook AS. Fractography, Materials Park (2nd printing, 1992), 12, 1987: 2217

[5.50]   A. Dhal, S.K. Panigrahi , and M.S. Shunmugam , Precipitation phenomena, thermal stability and grain growth kinetics in an ultra-fine grained Al 2014 alloy after annealing treatment, 2015, J. Alloy Compd, 649, pp. 229-238

[5.51]   R.Z. Valiev,   T.G. Langdon, Principles of Equal-Channel Angular Pressing as a Processing Tool for Grain Refinement, 2006, Prog. Mater Sci., 51, pp. 881-981.

[5.52]   Y.S. Li, N. R. Tao, K. Lu, Microstructural evolution and nanostructure formation in copper during dynamic plastic deformation at cryogenic temperatures, 2008, Acta Mater, 56, pp. 230-241.

[5.53]   T. Sakai, H. Miura, (2010). Mechanisms of ultrafine grain formation in severe plastic deformation, 2010, In Mater. Sci. Forum, 638, pp. 98-103.

[5.54]   Z. J. Zhang, Q. Duan, X. H. An, S. D. Wu, G. Yang , Z. F. Zhang, Microstructure and mechanical properties of Cu and Cu–Zn alloys produced by equal channel angular pressing, 2011, Mater. Sci Eng. : A, 528, pp. 4259-4267.

[5.55]   X. An, Q. Lin, S. Qu, G. Yang, S. Wu, F. Z. Zhang, Influence of stacking-fault energy on the accommodation of severe shear strain in Cu-Al alloys during equal-channel angular pressing, 2009, J. Mater. R,, 24, pp. 3636-3646.

[5.56]   X. H. An, Q. Y. Lin, S. D. Wu, F. Z. Zhang, (2010). Microstructural evolution and shear fracture of Cu–16at.% Al alloy induced by equal channel angular pressing, 2010, Mater. Sci Eng: A, 527, pp. 4510-4514.

[5.57]   O. S. Sitdikov, Comparative analysis of microstructures formed in highly alloyed aluminum alloy during high-temperature equal-channel angular pressing and multidirectional forging, 2016, Inorganic Materials: Applied Research , 7 , pp. 149-157.

[5.58]   A. Joshi, K. K Yogesha, R. Jayaganthan, . Influence of cryorolling and followed by annealing on high cycle fatigue behavior of ultrafine grained Al 2014 alloy, 2017, Mater. Char., 127, pp. 253-271

[5.59] K. K. Yogesha, A, Joshi, N. Kumar, R. Jayaganthan, Effect of cryo groove rolling followed by warm rolling (CGW) on the mechanical properties of 5052 Al alloy, 2016, Mater. Manuf. Process, 445, pp. 111-119.

[5.60] K. K. Yogesha, N. Kumar, A. Joshi, R. Jayaganthan , S. K. Nath, A Comparative Study on Tensile and Fracture Behavior of Al–Mg Alloy Processed Through Cryorolling and Cryo Groove Rolling, 2016, Metall. Micrstre. Ana. , 5 , pp. 251-.263.

[5.61] S. M. Dasharath, S. Mula, Mechanical properties and fracture mechanisms of ultrafine grained Cu-9.6% Zn alloy processed by multiaxial cryoforging, 2016, Mater Sci Eng: A, 675, pp. 403-414.

[5.62] A. Joshi, N. Kumar, K. K. Yogesha, R. Jayaganthan, S. K. Nath, Mechanical Properties and Microstructural Evolution in Al 2014 Alloy Processed Through Multidirectional Cryoforging, 2016, J. Matel. Eng. Perfm., 25, pp. 3031-3045.

[5.63] Y. M. Wang , E. Ma, Three strategies to achieve uniform tensile deformation in a nanostructured metal, 2004, Acta Mater, 52, pp. 1699-1709.

[5.64] A. Hohenwarter , R. Pippan, Fracture toughness evaluation of ultrafine-grained nickel, 2011, Script. Mater., 64, pp. 982-985.

[5.65] T. L. Anderson, T. L. Anderson, Fracture mechanics: fundamentals and applications. CRC presss (2005)

[5.66] A. Hohenwarter, R. Pippan, A comprehensive study on the damage tolerance of ultrafine-grained copper, 2012, Mater Science Eng. : A, 540, pp. 89-96.

[5.67] P. N. Rao , R. Jayaganthan, Effects of warm rolling and ageing after cryogenic rolling on mechanical properties and microstructure of Al 6061 alloy, 2012, Mater Des, 39, pp. 226-233.

[5.68] S. K. Panigrahi , R. Jayaganthan, A study on the mechanical properties of cryorolled Al–Mg–Si alloy, 2008, Mater Sci Eng: A ,480, pp. 299-305.

[5.69] S. K. Panigrahi, R. Jayaganthan, Development of ultrafine grained high strength age hardenable Al 7075 alloy by cryorolling, 2011, Mater. Des. 32, pp. 3150-3160.

[5.70] K. Ma, H. Wen, T. Hu, T. D. Topping, D. Isheim, D. N. Seidman , J. M Schoenung, Mechanical behavior and strengthening mechanisms in ultrafine grain precipitation-strengthened aluminum alloy, 2014, Act. Mater, 62, pp. 141-155.

[5.71] Broek, D. Elementary engineering fracture mechanics. Springer Science (2012).

[5.72] A. Joshi, K. K. Yogesha, N. Kumar, R. Jayaganthan, Influence of Annealing on Microstructural Evolution, Precipitation Sequence, and Fracture Toughness of Cryorolled Al–Cu–Si Alloy, 2016, Metall. Microstructure Ana., 5, pp. 540-556.

[5.73] M. O. Lai,   The equivalent energy method for KIC determination, 1987, Eng. Fract. Mech., 27, pp. 121-123.

[5.74] N. Perez,   Introduction to fracture mechanics. In Fracture Mechanics   Springer International Publishing (2017), pp. 53-77

[5.75] ASM Handbook: Properties and Selection: Nonferrous Alloys and Special-Purpose Materials, 1990, ASM international, 2 , pp. 889-896.

[5.76] E. Ma,. Instabilities and ductility of nanocrystalline and ultrafine-grained metals. 2003, Script. mater, 49 , pp. 663-668.

[5.77] P. Xue, B. L. Xiao , Y. Z. Ma, High tensile ductility via enhanced strain hardening in ultrafine-grained Cu, 2012, Mater Sci Eng: A , 532, pp. 106-110.

[5.78] F. Z. Zhang , J. Eckert, Unified tensile fracture criterion, 2005, Phy. review lett., 94 , 094301.

[5.79] D. R. Fang, Q. Duan, N. Q. Zhao, J. J. Li, S. D. Wu , F. Z. Zhang, Tensile properties and fracture mechanism of Al–Mg alloy subjected to equal channel angular pressing, 2007, Mater Sci Eng: A , 459, pp. 137-144.

[5.80]   P. Zhang, S. Qu, M. X. Yang, G. Yang, S. D. Wu, S. X. Li , Z. F. Zhang, . Varying tensile fracture mechanisms of Cu and Cu–Zn alloys with reduced grain size: From necking to shearing instability, 2014, Mater Sci Eng: A, 594, pp. 309-320

[5.81] B. Li, X.   Wang, X., H. Chen, J. Hu, C. Huang ,   G. Gou,   Influence of heat treatment on the strength and fracture toughness of 7N01 aluminum alloy, 2016, J. Alloys Compd, 678, pp. 160-166.

[5.82] P. N.Rao, D. Singh, H. G. Brokmeier, R. Jayaganthan, Effect of ageing on tensile behavior of ultrafine grained Al 6061 alloy, 2015, Mater. Sci. Eng: A, 641, pp. 391-401.

[5.83] N. N. Krishna, K. Sivaprasad, P. Susila,   Strengthening contributions in ultra-high strength cryorolled Al-4% Cu-3% TiB2 in situ composite, 2014, Transac. Nonferr. Metal. Soc. China, 24, pp. 641-647.

[5.84] N. N. Krishna, R. Tejas, K. Sivaprasad, K. Venkateswarlu, Study on cryorolled Al– Cu alloy using X-ray diffraction line profile analysis and evaluation of strengthening mechanisms, 2013, Mater. & Design, 52, pp. 785-790

[5.85] T. H. Courtney, (2005). Mechanical behavior of materials. Waveland Press.

[5.86] A. J. Ardell, Precipitation hardening, 1995, Metallurgical Transactions A, 16(12), pp. 2131-2165.

CONCLUSIONS & SUGGESTIONS FOR FUTURE WORK

This chapter discusses outcomes of the present research work and scope for future work. The influence of various processing routes such as Cryorolling (CR) and Multidirectional Cryoforging (MDCF) on microstructural evolution, tensile and fracture properties of Al 2014 alloy were investigated. The following conclusions are drawn based on the present work.

- Significant improvement in mechanical properties such as tensile strength (245 MPa-447 MPa) and yield strength (176 MPa-428 MPa) after cryorolling (CR) up to true strain of 2.3 was observed as compared to solution treated (ST) coarser grain alloy. However, the significant drop in % elongation (18.5 %- 4 %) of cryorolled (CR) alloy is noticed as compared to bulk solution treated (ST) alloy. The improvement in the strength of cryorolled (CR) alloy is attributed to the formation of UFG microstructure while the % elongation of cryorolled (CR) alloy is decreased due to lack of strain hardening ability after grain size reduction well below than 1 μm.

- After annealing in the temperature range of 100°C-350°C, tensile and yield strength were observed to be more at 100°C due to formation of coherent GP zones/fine coherent spherical phase (Al_2Cu); while annealing after 150^0C-350^0C, the drop in fracture toughness parameters was observed due to combined phenomenon of precipitation, softening due to dynamic recovery and recrystallisation.

- The improvement in the various fracture toughness parameters such as K_Q, K_{ee}, and J integral of cryorolled (CR) alloy was observed as compared to solution treated (ST) alloy due to delaying in crack initiation and crack propagation resulting from grain refinement, dislocation tangled zone and dislocation substructure.

- On annealing in the temperature range of 100°C -350°C, the fracture toughness parameters K_Q, K_{ee}, and J integral were observed to be more at 100°C while beyond this temperature, gradual decrease in these parameters were noticed and observed to be

minimum at 350°C. The improvement in the fracture toughness values at 100°C was attributed to the evolution of GP zones/fine coherent spherical precipitates during annealing, which imparts significant strengthening and improve the crack initiation as well as crack propagation stages..

- The failure mode of solution treated (ST) alloy during fracture toughness testing was observed to be typical ductile tearing fracture while upon annealing in the temperature range 100°C -250°C, the failure mechanism was transgranular ductile tearing fracture and it transforms in to transgranular brittle fracture in the temperature range of 250°C -350°C.

- The substantial improvement in the high cycle fatigue (HCF) strength from 72 MPa - 93 MPa was observed for the cryorolled (CR) alloy as compared to solution treated (ST) alloy. The improved high cycle fatigue properties of CR alloy as compared to ST alloy is attributed to the formation of UFG microstructure, which lead to reduced flaw size and increases the difficulty in imposing stress concentration near crack tip.

- On cryorolling and followed by annealing (CR+AN) in the temperature range 100°C - 250°C, the significant improvement in high cycle fatigue strength, was observed. However, the gradual decrease in high cycle fatigue strength was seen with increasing annealing temperature from 100°C to 200°C; while drastic decrease was observed for the annealed samples beyond 200°C. The improvement in high cycle fatigue properties of (CR+AN) alloy up to 200°C as compared to ST alloy observed is due to improvement in crack growth resistance facilitated by crack tip/precipitate interaction at grain boundaries (GBs). The high cycle fatigue strength gradually decreases with increasing annealing temperature from 100°C to 250°C, due to gradual coarsening of metastable precipitate (θ' phase) and transformed in to stable coarser precipitate 'θ' phase at 250°C.

- The fatigue crack growth rate (FCGR) test results for cryorolled alloy revealed that cryorolled (CR) alloy led to significant decrease in fatigue crack growth resistance in low stress intensity factor range as compared to coarser grain counterparts due to decrease level of crack closure in cryorolled (CR) alloy. The fatigue crack growth resistance of cryorolled (CR) alloy was improved in high stress intensity factor range

due to formation of UFG microstructure resulting fine striations as observed from fractographic studies.

- The post annealed sample at 100°C after cryorolling exhibited high fatigue crack growth resistance in low as well as high stress intensity factor range, and fine semicoherent spherical phase θ' was found to be responsible for affecting the fatigue crack growth resistance in low as well high stress intensity factor range.

- Microstructural evolutions in MDFed alloy at cryogenic temperature were associated with the significant amount of shear/deformation banding with the applied strain. The intersection of deformation bands of several types led to the grain refinement during multidirectional cryoforging.

- Multidirectional cryoforging (MDCF) up to a cumulative strain 2.4 shows an improvement of tensile strength, hardness and apparent fracture toughness (K_Q) from 276 MPa to 470 MPa, 115 HV to 171 HV, and 23.93 MPa$\sqrt{m}$ to 37.7 MPa$\sqrt{m}$, respectively, with decrease in ductility from 18.5 % to 6% as compared with solution treated alloy. The cryoforged Al 2014 alloy exhibits an increment of 7% in tensile strength, 3% in yield strength and 3% in hardness up to cumulative true strain of 2.4 as compared to the samples forged at room temperature. The improvement in tensile properties of MDFed alloy is attributed to dislocation strengthening and grain boundary strengthening effect at both temperatures. The effective suppression of cross slip and climb at liquid nitrogen temperature improves the strength of cryo forged sample better than that of room temperature forged alloy.

- The studies on multidirectional cryoforging (MDCF) and followed by annealed alloy in the temperature range 150°C -350°C revealed that strain hardening ability, fracture mechanisms and fracture toughness of deformed and post annealed samples is influenced by the shear banding, combined recovery/recrystallisation process, and evolution of second phase precipitates during annealing treatment at various temperatures.

- Macroscopic fracture mechanism of MDCFed sample was dominated by shear fracture while upon annealing it gradually transformed to shear plus necking.

250

- On investigating the tensile and fracture toughness properties such as apparent fracture toughness, equivalent energy fracture toughness, crack tip opening displacement (COD), and crack tip plastic zone size (r_p) of MDCFed and followed by annealed alloy, it was observed that these are retained up to the annealing temperature of 250°C, while above this temperature, a significant drop in these properties was observed. Finally, it was concluded that fine spherical semicoherent phase θ' is responsible for improving the mechanical properties of bulk UFG Al 2014 alloy.

- The strain hardening exponent calculated from Hollomon's equation and modified Crussurd-Joul analysis follows the similar trend for both MDCFed and followed by annealed alloy. It indicates that strain hardening rate for MDCFed and MDCFed followed by annealed alloy up to temperature 250°C increases with slow pace, while beyond 250°C strain hardening ability and strain hardening rate significantly increases.

- The results of strengthening mechanism calculations for MDCFed and followed by annealed alloy revealed that grain boundary strengthening (σ_{Gbs}), has significant contributions in raising the yield strength of MDCFed Al 2014 alloy, while for annealed samples up to the temperature range 250°C, the grain boundary (σ_{Gbs}) and precipitation strengthening (σ_{ps}) were observed to be maximum strength contributors to the yield strength.

- Summary of mechanical properties by three different processes is listed in Table 6.1 shown in next page.

Table 6.1: Summary of mechanical Properties of Al 2014 alloy

Al Alloy	Processing method	UTS (MPa)	YS (MPa)	% Elong.	Fracture toughness (K_{ee})	HCF (MPa)	References
Al 2014	ECAP	250	220	7 %	Not Reported	Not Reported	Venkat et al [2.122]
Al 2014	CR	447	428	4 %	37.8	93	Present Work
Al 2014	CR+150°C (Optimised)	511	456	7.5 %	47.05	113	Present Work
Al 2014	MDF	470	396	6 %	35.5	Not Reported	Present Work
Al 2014	MDF+150°C (Optimised)	535	486	8.4 %	43.04	Not Reported	Present Work

Suggestions for Future Work

- In the present work, influence of annealing on the tensile, fracture toughness, high cycle fatigue (HCF) and fatigue crack growth properties of bulk UFG Al 2014 alloy fabricated by cryorolling (CR) has been investigated. However, the influence of pre and post natural and artificial aging on fatigue and fracture properties of cryorolled Al alloy requires detailed investigation.

- The precipitation behaviour of cryorolled/multidirectional cryoforged alloy and followed by annealed alloy can be studied in detail through HRTEM and low temperature DSC studies.

- In present investigation, multidirectional cryoforged Al alloy was studied for tensile properties, fracture mechanism and fracture toughness testing. The fatigue properties were not studied due to small size specimen after processing in this work. However, the influence of multidirectional cryoforging on the high cycle fatigue (HCF) and fatigue crack growth rate (FCGR) testing requires detailed investigation by using small size specimen.

- In addition to the experimental results of cryoforging and cryorolling in Al 2014 alloy, Finite element methods and numerical simulations can be used to understand the deformation behaviour of UFG Al alloys.

- Combination of techniques such as cryoforging followed by cryorolling, cryoforging followed by RT rolling and cryoforging followed by warm rolling can be performed and compared for achieving better combination of strength, ductility, fatigue and fracture properties of bulk UFG Al 2014 alloy.